Universitat de Girona

DEVELOPMENT OF EFFICIENT TESTING METHODS AND COHESIVE ZONE MODELS FOR ANALYZING FATIGUE-DRIVEN DELAMINATION IN 3D LAMINATED COMPOSITE STRUCTURES

Laura Carreras Blasco

Doctoral Thesis

Development of efficient testing methods and cohesive zone models for analyzing fatigue-driven delamination in 3D laminated composite structures

Laura Carreras Blasco

2018

Universitat de Girona

Doctoral Thesis

Development of efficient testing methods and cohesive zone models for analyzing fatigue-driven delamination in 3D laminated composite structures

Author:
Laura Carreras Blasco

Advisors:
Dr. Albert Turon Travesa
University of Girona
Dr. Jordi Renart Canalias
University of Girona
Dr. Brian Lau Verndal Bak
Aalborg University

2018

Doctoral Program in Technology

Thesis submitted to the University of Girona
for the degree of Doctor of Philosophy

Laura Carreras Blasco
Development of efficient testing methods and cohesive zone models for analyzing fatigue-driven delamination in 3D laminated composite structures
Doctoral Thesis, 2018
Doctoral Program in Technology
Advisors: Dr. Albert Turon Travesa, Dr. Jordi Renart Canalias and Dr. Brian Lau Verndal Bak
3rd Party Advisor: Dr. Esben Lindgaard

Universitat de Girona
AMADE Research Group
Escola Politècnica Superior
Carrer Universitat de Girona, 4
17003 Girona

> *Meno: I feel, somehow, that I like what you are saying.*
> *Socrates: And I, Meno, like what I am saying. Some things I have said of which I am not altogether confident. But that we shall be better and braver and less helpless if we think that we ought to enquire, than we should have been if we indulged in the idle fancy that there was no knowing and no use in seeking to know what we do not know; — that is a theme upon which I am ready to fight, in word and deed, to the utmost of my power.*
>
> — **Plato**

> *Every concept arises from the equation of unequal things. Just as it is certain that one leaf is never totally the same as another, so it is certain that the concept "leaf" is formed by arbitrarily discarding these individual differences and by forgetting the distinguishing aspects.*
>
> — **Friedrich Nietzsche**

Acknowledgements

I would like to express my gratitude to my advisors, family, friends and AMADE research team.

També m'agradaria agrair al Dr. Pere Roura per haver despertat el meu interès per la recerca.

The work contained in this Ph.D. thesis was conducted in the AMADE research group (Department of Mechanical Engineering and Industrial Construction, University of Girona, Spain). The thesis was carried out under the grant CBRGR_IF. Part of the research presented in this thesis was developed during the Ph.D. candidate's stay at Aalborg University, which was funded by the University of Girona through the grant MOB16.

List of Publications

The present Ph. D. thesis has been prepared as a compendium of peer-reviewed journal papers, according to the regulations of the Universitat de Girona. The thesis is comprised of the following papers:

- L. Carreras, J. Renart, A. Turon, J. Costa, Y. Essa, F. Martin de la Escalera. An efficient methodology for the experimental characterization of mode II delamination growth under fatigue loading. *International Journal of Fatigue* 2017; 95:185-193.
  doi:10.1016/j.ijfatigue.2016.10.017
  ISSN: 0142-1123, Impact Factor: 2.899, ranked 19/130 in the category of *Engineering, Mechanical* (1^{st} quartile)[1].

- L. Carreras, B.L.V. Bak, A. Turon, J. Renart, E. Lindgaard. Point-wise evaluation of the growth driving direction for arbitrarily shaped delamination fronts using cohesive elements. *European Journal of Mechanics / A Solids* (In press).
  doi:10.1016/j.euromechsol.2018.05.006
  ISSN: 0997-7538, Impact Factor: 2.846, ranked 17/133 in the category of *Mechanics* (1^{st} quartile) [1].

- L. Carreras, E. Lindgaard, J. Renart, B.L.V. Bak, A. Turon. Evaluation of the mode-decomposed energy release rates for arbitrarily shaped delamination fronts using cohesive elements. *Submitted to Journal of the Mechanics and Physics of Solids*
  ISSN: 0022-5096, Impact Factor: 4.255, ranked 49/275 in the category of

[1] According to the 2016 Journal Citation Reports

Materials Science, Multidisciplinary (1^{st} quartile), ranked 5/133 in the category of *Mechanics* (1^{st} quartile) [1].

Other publications that have been derived from this thesis but are not included in this document are listed below:

- I. Jaeck, L. Carreras, J. Renart, A. Turon, F. Martin de la Escalera, Y. Essa. Experimental methodology for obtaining fatigue crack growth rate curves in mixed-mode I-II by means of variable cyclic displacement tests. *International Journal of Fatigue* 2018; 110:63-70.
  doi:10.1016/j.ijfatigue.2018.01.016
  ISSN: 0142-1123, Impact Factor: 2.899, ranked 19/130 in the category of *Engineering, Mechanical* (1^{st} quartile) [1].

- J. Renart, S. Budhe, L. Carreras, J.A. Mayugo, J. Costa. A new testing device to simultaneously measure the fatigue delamination behaviour of a batch of specimens. *Submitted to International Journal of Fatigue*
  ISSN: 0142-1123, Impact Factor: 2.899, ranked 19/130 in the category of *Engineering, Mechanical* (1^{st} quartile) [1].

Conference Proceedings

- J. Renart, L. Carreras, J. Costa, A. Turon. Determination of Crack Growth Rate Curves in Mode II Tests by Means of the Compliance Real Time Monitoring. 7^{th} International Conference on Composites Testing and Model Identification (COMPTEST 2015). Madrid (Spain).
  International Conference. Oral presentation.

- L. Carreras, J. Renart, J. Costa, A. Turon. Obtención de curvas continuas de crecimiento de grieta en ensayos ENF a fatiga mediante la determinación de la flexibilidad en tiempo real. 11^{th} Congreso Nacional de Materiales Compuestos (MATCOMP 2015). Madrid (Spain).
  National Conference. Oral presentation.

- L. Carreras, A. Turon, J. Renart, J. Costa, Y. Essa, F. Martin de la Escalera, B.L.V. Bak, E. Lingaard. Formulation of a cohesive zone model to simulate fatigue delamination in laminated structures. 5^{th} Thematic Conference on Mechanical Response of Composites (ECCOMAS 2015). Bristol (United Kingdom of Great Britain and Northern Ireland).
  International Conference. Oral presentation.

- A. Turon, L. Carreras, J. Renart, B.L.V. Bak, E. Lingaard, Y. Essa, F. Martin de la Escalera. Simulation of fatigue delamination in composite structures. 6^{th} International Conference on Innovation in European Aeronautics Research (EASN 2016). Porto (Portugal).
  International Conference. Oral presentation.

- E. Lingaard, L. Carreras, B.L.V. Bak, A. Turon, J. Renart. Evaluation of the decomposed J-integral in 3D crack fronts using cohesive elements. 7^{th} International Conference on Composites Testing and Model Identification (COMPTEST 2017). Leuven (Belgium).
  International Conference. Poster.

- L. Carreras, B.L.V. Bak, A. Turon, E. Lingaard, J. Renart, Y. Essa, F. Martin de la Escalera. Methodology for the simulation of fatigue-driven delamination in 3D composite structures. 7^{th} International Conference on Composites Testing and Model Identification (COMPTEST 2017). Leuven (Belgium).
  International Conference. Poster.

- L. Carreras, J. Renart, I. Jaeck, A. Turon, Y. Essa, F. Martin de la Escalera. An efficient methodology for the experimental characterization of mode II and mixed-mode I+II delamination growth under fatigue loading. 14^{th} International Conference on Fracture (ICF 2017). Rhodes (Greece).
  International Conference. Oral presentation.

- E. Lindgaard, L. Carreras, B.L.V. Bak, J. Renart, A. Turon. Mode decomposed J-integral for 3D crack problems using a cohesive zone model. 6^{th} Thematic Conference on Mechanical Response of Composites (ECCOMAS 2017). Eindhoven (The Netherlands).
  International Conference. Oral presentation.

- A. Turon, L. Carreras, B.L.V. Bak, E. Lindgaard, J. Renart, Y. Essa, F. Martin de la Escalera. Simulation of delamination in 3D composite structures under fatigue loading. 6^{th} Thematic Conference on Mechanical Response of Composites (ECCOMAS 2017). Eindhoven (The Netherlands).
  International Conference. Oral presentation.

Universitat de Girona

Dr. Albert Turon Travesa, Associate Professor at the University of Girona,

Dr. Jordi Renart Canalias, Associate Professor at the University of Girona,

and

Dr. Brian Lau Verndal Bak, Assistant Professor at Aalborg University,

hereby CERTIFY that

The work entitled *Development of efficient testing methods and cohesive zone models for analyzing fatigue-driven delamination in 3D laminated composite structures*, submitted for the doctoral degree by Laura Carreras Blasco, has been conducted under their supervision and that it fulfills the requirements to aim for the *International Mention*.

Girona, July 2018.

Albert Turon Travesa	Jordi Renart Canalias	Brian Lau Verndal Bak
University of Girona	University of Girona	Aalborg University

List of Figures

List of Tables

Contents

Abstract

The overall purpose of this Ph.D. thesis is to contribute to the reliable design of composite structures subjected to fatigue-driven delamination. The aim is motivated by a wish to reduce the amount of experimental testing needed in the dimensioning of real components and to anticipate the mechanical response of layered structures undergoing fatigue delamination.

From a review of the methods based on the cohesive zone model approach available in the literature, it is detected that most of them are either limited to two dimensional (2D) applications or they have not been fully validated in three dimensional (3D) problems. In order to extend the general applicability of the existing methods, both new analysis and experimental data of 3D delamination propagation are needed. In the case of the model taken as the point of departure of the present Ph.D. thesis, an efficient identification of the crack propagation direction and an accurate means of calculating the energy release rate in three-dimensional structures are needed for the 3D extension.

In the cohesive element framework, the propagation direction is computed as the normal direction to the damage isolines. The damage isolines tracking requires exchange of information between neighboring elements, thus post-processing global data, which is computationally expensive. A novel approach for the evaluation of the growth driving direction, only using local element information, has been derived. The method can be directly implemented in a user-defined element subroutine and be evaluated at the execution time of the analysis.

On the other hand, the computation of the mode-decomposed energy release rates in 3D problems involving delaminations, modeled using a cohesive zone model approach, has not been previously investigated. The J-integral is a suitable method for calculating them, since its domain-independence can be employed to shrink the integration domain to the cohesive interface, and reduce it to a line integral. A numerical procedure to evaluate the mode-decomposed J-integral in curved delamination fronts is presented. The growth driving direction criterion is used to track the integration path along the cohesive zone and to decompose the energy release rate.

Moreover, the fatigue damage rate model is based on the link between the damage rate and the crack growth rate. Therefore, efficient tools to characterize the crack growth rate curves under different loading conditions are needed to feed the numerical method. The existing methodologies for mode II fatigue testing using three-point bending end-notched flexure (3-ENF) under constant cyclic displacement conditions yield discontinuous delamination growth rate curves, therefore requiring a batch of several specimens to be tested under different severity conditions in order to fully characterize the crack growth. A variable cyclic displacement test procedure is presented which allows the crack growth rate to be measured for the desired range of severities with a single specimen. With this methodology, human intervention during the test is avoided.

Finally, a benchmark test for fatigue-driven 3D crack growth has been used for model validation. A full characterization, at the coupon level, of the interlaminar properties of the demonstrator material has been performed. The developed fatigue method provides accurate predictions for the fatigue benchmark tests.

Resum

L'objectiu general d'aquesta tesi doctoral és contribuir al disseny fiable d'estructures de materials compòsits en capes sotmeses a delaminació provocada per la fatiga. Per una banda, es pretén reduir la quantitat de proves experimentals necessàries en el procés de disseny de components i, per l'altra, anticipar la resposta mecànica de les estructures que pateixen delaminació a fatiga.

A partir d'una revisió dels mètodes disponibles a la bibliografia, es detecta que la majoria d'ells es limiten a aplicacions en dues dimensions (2D) o no han estat plenament validats en tres dimensions (3D). Per tal d'ampliar l'aplicabilitat dels mètodes existents, es necessiten dades experimentals de propagació de la delaminació en 3D i el desenvolupament de nous mètodes. En el cas del model que es pren com a punt de partida de la present tesi doctoral, es necessiten dos nous conceptes: un mètode eficaç d'identificació de la direcció de propagació d'esquerda i un mitjà precís de calcular l'energia disponible per a la fractura en estructures tridimensionals.

En el marc dels elements cohesius, la direcció de propagació es pot calcular com la direcció normal a les isolínies de dany. No obstant, per tal de traçar les isolínies de dany, es requereix intercanviar informació entre elements veïns i, per tant, post processar dades de forma global, que resulta computacionalment car. Es proposa un enfocament nou per tal d'avaluar la direcció de creixement d'esquerda utilitzant, només, la informació disponible localment a nivell d'element. El mètode es pot implementar directament en una subrutina d'usuari d'elements finits i ser avaluada durant l'execució de l'anàlisi.

D'altra banda, el càlcul de l'energia disponible per a la fractura descomposta en modes en problemes 3D que impliquen delaminacions, modelades utilitzant un model de zona cohesiva, no s'ha investigat prèviament. La integral-J és un mètode adequat per calcular-la, ja que és independent del domini d'integració i permet reduir-lo a la interfície cohesiva i, així, avaluar-la com una integral de línia. Es presenta un procediment numèric per avaluar la integral-J descomposta en modes en fronts de delaminació corbats. El criteri de direcció de creixement d'esquerda s'utilitza per dibuixar el camí d'integració al llarg de la zona cohesiva i descompondre l'energia disponible per a la fractura en modes.

El model de creixement del dany a fatiga es basa en el vincle entre la velocitat creixement del dany i la velocitat de propagació d'esquerda. Per tant, es necessiten eines eficients per caracteritzar les corbes de velocitat de propagació d'esquerda sota diferents condicions de càrrega per alimentar el mètode numèric. Les metodologies existents per assajos a fatiga en mode II basats en la configuració d'assaig a flexió amb recolzament a tres punts i entalla final (3-ENF) sota condicions de desplaçament cíclic constant produeixen corbes discontínues de la velocitat de propagació d'esquerda. Per això, es necessita assajar un lot de diverses provetes a diferents severitats de càrrega per caracteritzar completament la corba de velocitat de propagació d'esquerda. Es presenta un procediment d'assaig basat en l'aplicació d'un desplaçament cíclic variable que permet mesurar la velocitat de propagació d'esquerda per al rang desitjat de severitats de càrrega usant una sola proveta. Amb aquesta metodologia, s'evita la necessitat d'intervenir durant l'assaig.

Finalment, per tal de validar el model a fatiga, s'ha dissenyat una configuració d'assaig per obtenir dades de propagació de la delaminació en estructures 3D. S'ha dut a terme una campanya experimental de l'assaig validador. A més, s'ha realitzat una caracterització completa de les propietats interlaminars del material validador a nivell de proveta. El mètode de fatiga desenvolupat proporciona prediccions precises per als assajos de referència.

Resumen

El objetivo general de esta tesis doctoral es contribuir al diseño fiable de estructuras de materiales compuestos en capas sometidas a deslaminación provocada por la fatiga. Por un lado, se pretende reducir la cantidad de pruebas experimentales necesarias en el proceso de diseño de componentes y, por otro, anticipar la respuesta mecánica de las estructuras que sufren deslaminación a fatiga.

A partir de una revisión de los métodos disponibles en la bibliografía, se detecta que la mayoría de ellos se limitan a aplicaciones en dos dimensiones (2D) o no han sido plenamente validados en tres dimensiones (3D). Con el fin de ampliar la aplicabilidad de los métodos existentes, se necesitan datos experimentales de propagación de la deslaminación en 3D y el desarrollo de nuevos métodos. En el caso del modelo que se toma como punto de partida de la presente tesis doctoral, se necesitan dos nuevos conceptos: un método eficaz de identificación de la dirección de propagación de grieta y un medio preciso de calcular la energía disponible para a la fractura en estructuras tridimensionales.

En el marco de los elementos cohesivos, la dirección de propagación se puede calcular como la dirección normal a las isolíneas de daño. No obstante, con el fin de trazar las isolíneas de daño, se requiere intercambiar información entre elementos vecinos y, por tanto, post procesar datos de forma global, que resulta computacionalmente caro. Se propone un enfoque nuevo para evaluar la dirección de crecimiento de grieta utilizando, sólo, la información disponible localmente a nivel de elemento. El método se puede implementar directamente en una subrutina de usuario de elementos finitos y ser evaluada durante la ejecución del análisis.

Por otra parte, el cálculo de la energía disponible para la fractura descompuesta en modos en problemas 3D que implican deslaminaciones, moldeadas utilizando un modelo de zona cohesiva, no se ha investigado previamente. La integral- J es un método adecuado para calcularla, ya que es independiente del dominio de integración y permite reducirlo a la interfaz cohesiva y, así, evaluar como una integral de línea. Se presenta un procedimiento numérico para evaluar la integral- J descompuesta en modos en frentes de deslaminación curvados. El criterio de dirección de crecimiento de grieta se utiliza para dibujar el camino de integración a lo largo de la zona cohesiva y descomponer la energía disponible para la fractura en modos.

El modelo de crecimiento del daño a fatiga se basa en el vínculo entre la velocidad crecimiento del daño y la velocidad de propagación de grieta. Por tanto, se necesitan herramientas eficientes para caracterizar las curvas de velocidad de propagación de grieta bajo diferentes condiciones de carga para alimentar el método numérico. Las metodologías existentes para ensayos a fatiga en modo II basados en la configuración de ensayo a flexión con apoyo en tres puntos y entalla final (3-ENF) bajo condiciones de desplazamiento cíclico constante producen curvas discontinuas de la velocidad de propagación de grieta. Por ello, se necesita ensayar un lote de varias probetas a diferentes severidades de carga para caracterizar completamente la curva de velocidad de propagación de grieta. Se presenta un procedimiento de ensayo basado en la aplicación de un desplazamiento cíclico variable que permite medir la velocidad de propagación de grieta para el rango deseado de severidades de carga usando una sola probeta. Con esta metodología, se evita la necesidad de intervenir durante el ensayo.

Finalmente, a fin de validar el modelo a fatiga, se ha diseñado una configuración de ensayo para obtener datos de propagación de la deslaminación en estructuras 3D. Se ha llevado a cabo una campaña experimental del ensayo validador. Además, se ha realizado una caracterización completa de las propiedades interlaminares del material validador a nivel de probeta. El método de fatiga desarrollado proporciona predicciones precisas para los ensayos de referencia.

1 Introduction

1.1 Contextual background

Composite materials are a combination of one or more constituents acting as reinforcements embedded in a matrix that bind them together. The advantage of composites is that they can be tailored so that their properties are superior to those of their components separately. However, they must be manufactured so that the dispersion of one constituent to the other is controlled in order to achieve optimum properties. Some of the factors that must be controlled are the interface acting as the bond between constituents, the reinforcement relative volume, the uniformity of the composite system or the orientation of the constituents.

Composites can be classified in many ways depending on different factors such as the nature of the constituents or the arrangement of the reinforcement in the matrix. The most influential factors are the reinforcement (particles and whiskers, discontinuous fibers or continuous long fibers), the laminate configuration (single unidirectional lamina, laminate with some laminae which have the same or different fiber orientation, or bulk composites) and hybrid structures (different material in various laminae or different reinforcements in a lamina) [26].

In particular, laminated composites are layered materials produced by stacking plies which contain long continuous fibers. Fibers supply stiffness and strength to the material in the laminate plane. Although laminated composite structures are designed so that the highest stresses are in the fiber direction, out-of-plane stresses may also occur in service at many types of geometric discontinuities such as ply drops, skin-stiffener terminations, intersections, sandwich panels, free edges, holes, cut-outs, flanges, bonded and bolted joints or impacted zones. These load cases may damage the interface between plies (interlaminar damage), causing the failure mechanism called delamination. Delamination is often considered the most detrimental failure mechanism in laminated composite structures because it occurs at relatively low load levels but still entails significant reduction of the structure's load carrying capacity [123].

As an example of practical appliaction, civil aircrafts recently released (i.e., Airbus A380, Airbus A350XWB, Boeing 787, Embraer E-Jet, Embraer E-Jet E2, Bombardier CRJ NextGen) make use of fiber reinforced laminated composites in the aircraft primary structure. Composites' unparalleled by any other material specific stiffness and strength (stiffness and strength to weight ratio) is behind their selection to produce light-weight structural components, thus leading to aircraft lower operational costs. The companies also advertise a superior fatigue performance due to the use of composites. The no-growth criterion and the damage tolerance approach are two alternatives to deal with fatigue-driven delamination in aircraft design [144]. The first aims to ensure that no crack propagation will ever occur over the lifetime of the component. Conversely, the damage tolerance approach is based on a structure's remaining capacity to safely sustain in-service loads, even with the presence of sub-critical sized delaminations. By allowing damage growth, lighter weight structures can be achieved while higher load levels are acceptable.

However, the technologies associated to composites are, in general, not as mature as for other material systems such as metals. This is even more evident when dealing with delamination. The technology related to tests and computational tools to deal with simulation of delamination in composite structures under static loads, is in the Technology Readiness Level (TRL) 5 [102, 101], which means that the technology has been validated at component level in a relevant environment. However, the existing simulation tools and characterization methods for fatigue-driven delamination are even less mature. In this case, they can be classified as TRL2-TRL3 [102, 101], this meaning that they are not yet fully validated in laboratory environment. This enforces the reliance on empirical procedures for life verification rather than life prediction of real application structures. Indeed, the certification of an airplane is basically based on extensive, and very costly, fatigue testing; from small components to large substructures or full-scale. These tests are aimed in ensuring that no catastrophic failure occurs during the service life of the aircraft. To give just an example, in 2015, the Boeing 787 Dreamliner's carbon composite structure was tested during 165,000 flight cycles (five-year fatigue test) equivalent to 75 years of service (c.f. Figure 1.1) [39].

Fig. 1.1.: Full-scale fatigue test on Boeing 787 [39].

1.2 Motivation

Multiple models exist in the literature to deal with fatigue-driven delamination. However, although they succeed in reproducing the fatigue behavior at coupon level, most of them are not applicable or have not been validated for simulating larger structures. Thus, there is a need for efficient and reliable technologies and design methodologies to account for delamination in complex layered composite structures under fatigue loading. On the one hand, these methodologies are needed for a proper dimensioning of the components (thus reducing the number of manufactured specimens needed for a trial and error optimization) and, on the other hand, to be able to anticipate the mechanical response to different infringed damage forms. In this regard, adopting a simulation-based design approach, also called Virtual Mechanical Testing, is a key point to achieve a reduction of development costs.

Moreover, simulation tools may also have a key role during service. If advanced computational tools capable to predict fatigue damage growth behavior with accuracy are available, an inspection schedule that enable detection of damage before it becomes critical can be reliably programmed. Consequently, a damage tolerance approach can be adopted, enabling lighter and more efficient aircraft designs.

1.3 Objectives

The aim of the present thesis is to attain an integral approach to fatigue loading (experimental procedures and simulation tools) which could be accepted by certification bodies in partial replacement of expensive and time consuming fatigue tests. The overall objectives of the thesis are:

- To investigate the existing simulation methods for fatigue-driven delamination, with special attention to their 3D capabilities.
- To develop a new methodology to simulate fatigue-driven delamination based on the findings of the investigation and implement it into a commercial finite element framework.
- To devise an experimental methodology to obtain the material card that feeds the simulation method.
- To validate the proposed methodology by comparing computational and experimental tests of a demonstrator representative of arbitrarily shaped delamination growth in a real structural component.

1.4 Thesis structure and content

Even though the present thesis has been prepared as a compendium of publications, this document has been written as a whole. The reader is guided through an overall view of the contributions done, while referred to the appendices when needed of detailed descriptions. This means that the content of the publications is not entirely included in the main body, but only some parts. Moreover, some additional information has been included, such as the material card definition, the design and description of the experimental procedure on the demonstrator specimen and the comparison of the computational and experimental results, which are not published elsewhere.

Taking into account the aforementioned, the thesis is structured as follows:

Chapter 2 gives an review on the observed phenomenology of delamination under fatigue loads in composite laminates. An overview of the existing computation methods is presented. Special focus is given to those based on a cohesive zone model approach. Moreover, an introduction to the selected cohesive zone model for the simulation of high-cycle fatigue-driven delamination, which forms the basis of the formulation developed in the framework of this thesis, is provided. The chapter concludes with a review on the procedures for the experimental characterization of interlaminar properties.

Chapter 3 deals with the improvements on the applied fatigue cohesive zone model which consists of extending its applicability to three-dimensional analysis. To this end, both a point-wise evaluation of the growth driving direction and a methodology to evaluate the mode decomposed energy release rates in three-dimensional structures, are developed. Then, the presented tools are used in combination with a damage rate model for the simulation of fatigue-driven delamination in complex three-dimensional structures.

Chapter 4 describes an efficient methodology for the experimental characterization of delamination growth under pure mode II fatigue loading conditions. Few insights into the application of the proposed methodology under mixed-mode fatigue loading conditions are also given.

Chapter 5 contains the results of the material card definition.

In Chapter 6 the proposed fatigue simulation method is validated. The design of a demonstrator specimen undergoing varying crack front shape to obtain experimental data at coupon level is defined. Quasi-static and fatigue tests results on the demonstrator are provided and compared to numerical predictions.

Chapter 7 contains a summary of the overall conclusions.

The impact of the contributions of the thesis is highlighted in Chapter 8.

Finally, suggestions for future work are given in Chapter 9.

State-of-the-art

2

2.1 Delaminations understood as cracks in the material

A crack can be understood as a strong discontinuous singular surface, S, which divides a body into two sub-domains. Bounding the crack surface, there are two initially coincident surfaces: the S^+, associated with the upper sub-domain, Ω^+, and S^-, associated with the lower sub-domain, Ω^- (c.f. Figure 2.1). S^+ and S^- represent the crack faces and they independently translate, rotate and stretch, though their motion is constrained by the constitutive law used to describe the interface behavior.

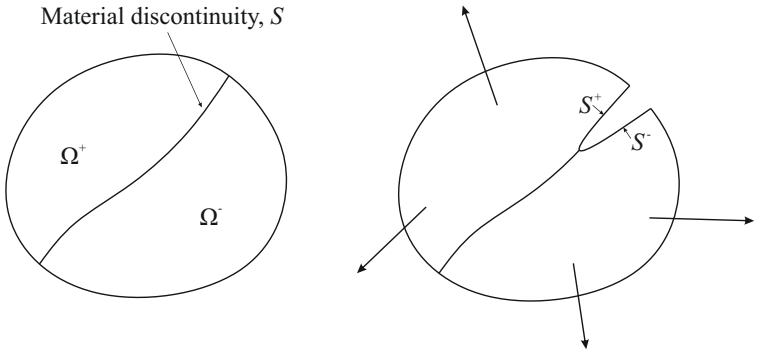

Fig. 2.1.: Crack modeled as a strong discontinuous singular surface, S, dividing a body into two sub-domains, Ω^+ and Ω^-.

In this regard, delaminations are cracks within the interface between adjacent layers which, generally, are confined to propagate in the interface. Then, a laminated structure can be split into several sub-domains, Ω_1, Ω_2..., each one constituting a ply, separated by the potential crack paths, S_1, S_2..., which are the interfaces between layers.

2.1.1 Fracture modes

Crack propagation can be described through three basic fracture modes [71] (c.f. Figure 2.2):

- Mode I: normal opening to the crack plane
- Mode II: in-plane shear opening
- Mode III: out-of-plane shear opening

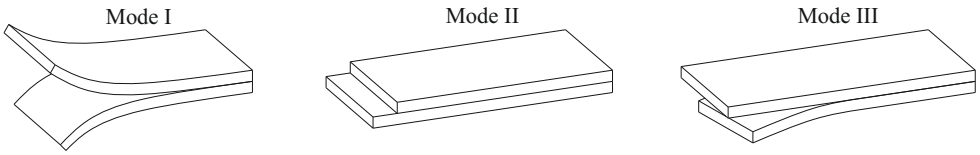

Fig. 2.2.: The three basic fracture modes.

In homogeneous materials, such as metals, a crack loaded in a combination of mode shear modes, tends to deviate in order to keep growing under mode I conditions, which is the fracture mode that dissipates the least energy. However, this is not the case for delaminations in layered composite materials, where, in most cases, the crack is restricted to grow in the interface between plies. Thus, crack propagation can occur under any fracture mode condition, or a combination of them, depending on the geometry of the specimen and loads. The fracture mode is then referred to as mixed-mode.

2.2 Delamination modeling under static loading

The most common methods for the prediction of interlaminar failure can be divided into two main approaches: Methods purely based on fracture mechanics and methods based on the cohesive zone model (CZM) concept [49, 27], the latter combining the framework of fracture mechanics and damage mechanics.

In the fracture mechanics approach, usually a local Griffith's criterion [58] is used to predict delamination growth: the energy release rate, $\mathcal{G}$, is compared to the interlaminar fracture toughness, $\mathcal{G}_c$, which is considered to be a constant material property. Then, applying Griffith's criterion, delamination propagation occurs at the points where $\mathcal{G} \geq \mathcal{G}_c$. This local energy balance criterion implies negligible fracture process zone.

Conversely, CZMs can capture fracture energy dissipation mechanisms of quasi-brittle materials, such as the formation of micro cracks ahead of the crack tip before complete separation of the crack faces. Therefore, the CZM approach is a suitable means of predicting delamination propagation when a nonnegligible fracture process zone is present. The stress singularity at the tip of a sharp crack is removed by accounting for a cohesive zone (CZ), where the material undergoes degradation until complete decohesion. The mechanical behavior of the interface is usually modeled by means of a damage variable, which is a measure of the degradation of the mechanical properties of the material ahead of the crack tip. When the damage variable reaches its maximum value, new crack surface is created.

A more recent approach, presented by Van der Meer et al. [174], uses the level set method to describe the crack front location. It is a fracture mechanics based approach. Furthermore, its variant for large process zone simulation [173] makes use of a stiffness degrading damage variable that allows a band of damaged material with predefined width. Conversely to most of the existing CZM formulations, the damage variable is not a function of the local properties but it is determined by the distance to the crack front, where the crack front is defined as the line that separates the damage process zone and the completely damaged interface.

Since this thesis is based on the cohesive zone model approach, the concept of cohesive law is further introduced in the following.

2.2.1 Introduction to the cohesive law

Linear elastic fracture mechanics (LEFM) was the first approach to the analysis and modeling of cracks. As a consequence of using linear elasticity and infinitely sharp crack tips, LEFM leads to an unrealistic phenomenon: the presence of a stress singularity at the crack tip. However, no material is capable to withstand

infinite stresses. Thus, Irwin [71] introduced a modification for ductile materials which consists of considering a non-linear zone ahead of the crack tip where the material undergoes plastic deformation.

Later, Dugdale [49] and Barenblatt [27] independently introduced the concept of cohesive zone model. The models from Dugdale and Barenblatt account for a fracture process zone (FPZ), called the cohesive zone (CZ), where cohesive tractions act on the separating surfaces, thus avoiding stress singularities at the tip of sharp cracks. In Dugdale's model, cohesive stresses are caused by yielding of the material and they are constant along the cohesive zone. In Barenblatt's model, cohesive stresses are the molecular cohesion forces, and they are a function of the separation length between atoms. Barenblatt assumed that the length of the CZ is constant and material specific and that the distribution of the cohesive stresses throughout the CZ is independent on the fracture mode.

The first to apply the concept of cohesive zone model to a Finite Element framework were Hilleborg et al. [62]. The model from Hilleborg et al. describes a micro-cracked FPZ capable of transferring stress until complete separation. Similar to current cohesive zone models, the distribution of cohesive stresses, $\sigma(\delta)$, is a function of the separation between crack faces, δ, usually referred to as displacement jump (c.f. Figure 2.3.a). The process of fracture initiates when the stress at the crack tip reaches the interfacial strength, σ_o. Then, the cohesive law describes a stress-softening behavior. With increasing displacement jump, δ, cohesive stresses, σ, decrease. The amount of energy dissipated per unit of newly created crack area in the opening process (from 0 to the critical displacement jump, δ_c) is the fracture toughness, $\mathcal{G}_c$:

$$\mathcal{G}_c = \int_0^{\delta_c} \sigma(\delta) \mathrm{d}\delta \tag{2.1}$$

The cohesive law can not be defined uniquely by the fracture toughness, $\mathcal{G}_c$, and the interfacial strength, σ_o. One of the determining factors for accuracy in the mechanical response is the cohesive law shape. Different interpretations have been made of the physical processes underlying at the micro-scale that may determine its shape, such as fiber bridging [8, 61, 155, 156], small cale yielding [49], the formation of micro cracks [62, 175] or polymer crazing/bridging [177]. The exact

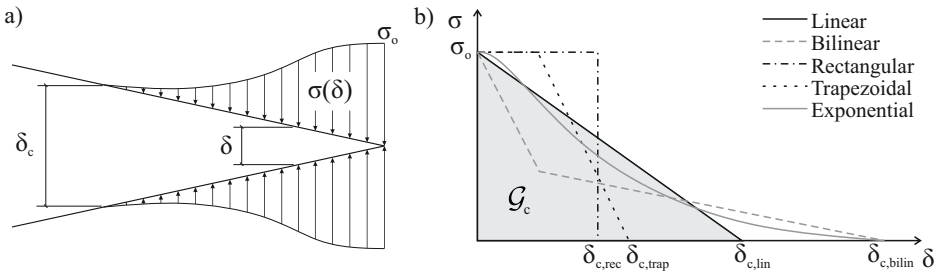

Fig. 2.3.: a) Cohesive stress distribution, $\sigma(\delta)$, throughout the CZ. b) Common cohesive law shapes with the same interfacial strength, σ_o, and different critical displacement jumps: $\delta_{c,rec}$ (rectangular), $\delta_{c,trap}$ (trapezoidal), $\delta_{c,lin}$ (linear), $\delta_{c,bilin}$ (bilinear). $\delta_{c,exp}$ (exponential)= ∞ and, therefore, is not represented. The critical energy release rate, $\mathcal{G}_c$, of the linear cohesive law is the area represented in gray color.

shape of the cohesive law can be extracted from experimental tests, either by a direct measurement [159, 155, 94, 145], or by indirect methods [120], although there does not exist any standardized procedure. In practice, the shape of the cohesive law may also affect the performance of the numerical solution procedure [9]. If the shape of the cohesive law have not been obtained experimentally and there is no previous experience on the most appropriate selection, the simplest approach is to assume linear softening [170].

Irreversibility of the softening process

Current cohesive zone models are formulated within the framework of damage mechanics to ensure irreversible crack propagation [121, 10, 36, 57, 167, 168]. In continuum damage mechanics, damage is understood as the creation of micro-surfaces of discontinuities in a continuum body [77, 82], and it is coupled with elasticity or plasticity. Thus, it makes use of state variables, which are usually related to the crack density and evolve monotonically with time, to degrade a macroscopic property. On the other hand, in interface damage mechanics, the damage parameter acts to prevent the restoration of the previous cohesive state between the interfacial surfaces. In this regard, a thermodynamical interpretation of the irreversible process of interlaminar fracture can be established by definition of the damage as the fraction of dissipated specific energy, ω_d to the energy necessary to create a unit of new

surface, $\mathcal{G}_c$ (c.f. Figure 2.4.a for an schematic representation using a linear cohesive law).

$$\mathcal{D}^e = \frac{\omega_d}{\mathcal{G}_c} \tag{2.2}$$

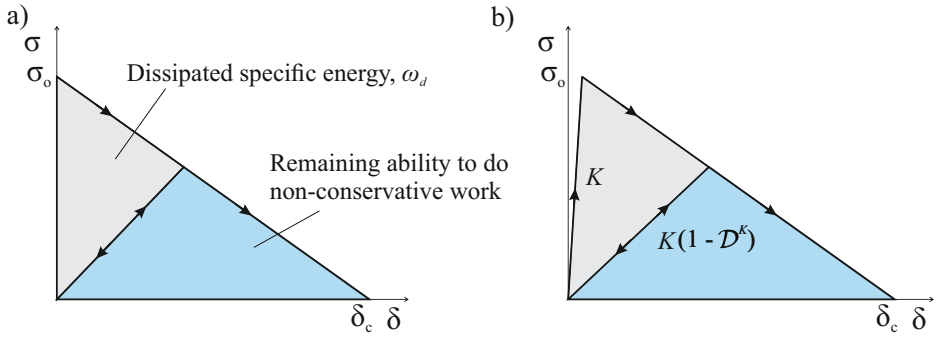

Fig. 2.4.: a) Physical interpretation of the irreversible linear cohesive law and b) irreversible linear cohesive law implemented in the cohesive element formulation.

The evolution of the energy-based damage variable, $\mathcal{D}^e$, depends on the interfacial strength, σ_o, the fracture toughness, $\mathcal{G}_c$, and the shape of the cohesive law. If the softening is assumed linear, a linear dependence of $\mathcal{D}^e$ with the displacement jump, δ, is obtained [99] (c.f. Figure 2.5).

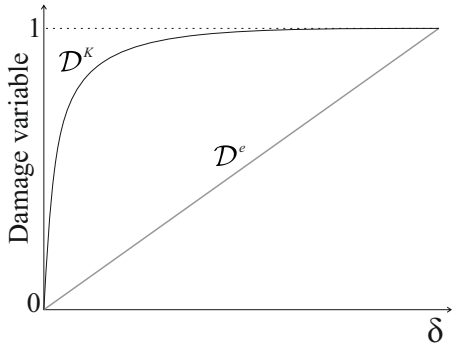

Fig. 2.5.: Evolution of the damage variables with the displacement jump.

On the other side, in the numerical implementation of cohesive zone models in a finite element framework using cohesive elements, a finite interfacial stiffness is needed. Therefore, an elastic region is introduced before the initiation of the

degradation process. This elastic region is defined by a penalty stiffness, K, as shown in Figure 2.4.b. Then, in most of the existing formulations [170] a stiffness degrading damage variable, $\mathcal{D}^K$ is defined to ensure the irreversibility of the softening process. The evolution of this stiffness degrading damage variable, $\mathcal{D}^K$, however, is highly nonlinear with the displacement jump, δ (c.f. Figure 2.5) and depends on the penalty stiffness, K, which is a non-physical parameter.

2.3 Delamination under fatigue loading

2.3.1 Fatigue loading characterization

Real structures, in service conditions, are subjected to a complex, and in some cases, random sequence of loads of different amplitude. However, the loading spectrum introduces complexity in the experimental characterization and modeling of the fatigue behavior. Thus, there exist several cyclic-counting algorithms (commonly called rain-flow algorithms [107]) for reducing a spectrum of varying loading to a load cycle histogram. Then, fatigue analysis of delamination in composites is usually done by assuming that the fatigue load is defined as a sinusoidal cyclic load of a given frequency and amplitude [25, 126], although other cycle shapes (square, triangle) may occur in technical applications, such as mechanical, electrical or architectural.

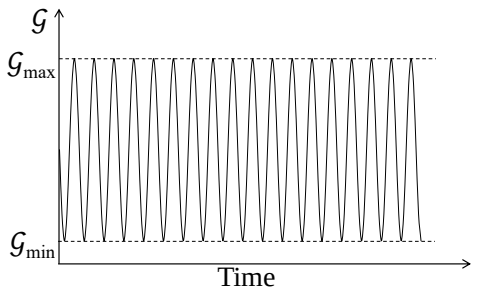

Fig. 2.6.: Sinusoidal loading cycles defined by the maximum and the minimum energy release rates, $\mathcal{G}_{max}$ and $\mathcal{G}_{min}$.

The load is usually expressed in terms of a fracture mechanics parameter [24, 126], normally, the stress intensity factor (SIF) or the energy release rate, $\mathcal{G}$. Then, a load cycle is completely defined by two independent parameters among the load level (maximum or minimum load), the mean value, the load amplitude and the load ratio, defined as:

$$R = \frac{K_{min}}{K_{max}} = \sqrt{\frac{\mathcal{G}_{min}}{\mathcal{G}_{max}}} \tag{2.3}$$

where K_{max} and K_{min} are the maximum and minimum cyclic stress intensity factors and $\mathcal{G}_{max}$ and $\mathcal{G}_{min}$ are the corresponding the minimum and maximum energy release rates (c.f. Figure 2.6).

The use of fracture mechanics parameters for the characterization of the fatigue loading is highly motivated by Paris and co-workers' achievements in the characterization of fatigue crack growth in metals [125, 124]. Moreover, since the calculation of the SIF in inhomogeneous materials, such as laminated composites, may be challenging [126], the energy release rate $\mathcal{G}$ has become the preferred parameter for the modeling of delamination growth. Nevertheless, both parameters are equivalent.

During experimental testing, $\mathcal{G}$ can be obtained by measuring the change of compliance with crack length, $\mathrm{d}C/\mathrm{d}a$. On the other hand, for delamination modeling, $\mathcal{G}$ may be either calculated analytically (only in simple specimen configurations) or by means of numerical tools. Thus, for the analysis of delamination in structures of complex geometry or loading, finite element analysis has become an indispensable tool.

Two of the most common extraction methods for the energy release rate (also called the crack extension force) are the virtual crack closure technique (VCCT) [88] and the J-integral approach [136].

The virtual crack closure technique (VCCT) is the most widely used FE techniques [86]. However, its application to realistic three-dimensional geometries with arbitrarily shaped crack front requires a continuous adaptive meshing technique in order to get a smooth front that fits with the instantaneous crack front curvature [54, 149, 70]. Alternative methods, that allow the use of stationary meshes, consist of tracing a

smooth virtual front around the stepped front [178, 97, 98]. These techniques require the use of algorithms to determine the normal direction to the virtual delamination front using global information (or 18-noded elements as in [178]). This direction is used to compute the virtually closed area and to define a local coordinate system that enables to calculate the energy release rate components according to it.

In the context of the VCCT, Zou et al. [182, 181] used laminate theory to eliminate high order gradients from the through thickness variations in displacement, leading to discontinuities in stress (and strain). The stress resultant jumps and the derivatives of the displacement jumps between the delamination surfaces are used to evaluate the total energy release rate and its individual components. However, as it is a VCCT based method, it still requires that the delamination front is located on the element edges. In a more recent work, van der Meer et al. [174, 122], also working under the assumption that higher order variations through the thickness are eliminated, makes use of the jump in Eshelby momentum tensor over the interface between uncracked and cracked parts to obtain the energy release rate. They use a level set model for progressive delamination, with which the front can be located inside the elements. Both methods are applicable to three-dimensional delamination analysis, but the mesh requirements related to the VCCT are avoided using the level set method.

On the other hand, the path-independence of the two-dimensional J-integral makes it very attractive in practice. For this reason, much effort has been devoted to extend the applicability of the J-integral to three-dimensional domains [13, 48, 113, 95, 150, 68, 38, 139, 138, 55, 96]. The published extensions of the J-integral for its evaluation in three-dimensional problems, where the crack extension force may change along the crack front, is commonly done by means of two approaches. The first is a point-wise evaluation of the J-integral on a cross-section of the crack surface, resulting in a combination of a contour integral and a surface integral defined over the area enclosed by the contour. See [138] for a detailed description. The second approach is the equivalent domain integral over a finite volume surrounding the crack front [95, 150]. Regardless, the applicability of most of these J-integral extensions to three-dimensional domains is restricted to certain assumptions such as plane-strain/stress, i.e. at the vicinity of the crack tip, or planar cracks. By employing curvilinear coordinates, Eriksson [50] and Fernlund et al. [52] obtained generalized expressions applicable to curved cracks with non-planar crack surfaces. In [50], a volume-independent integral expression for the evaluation of the crack extension force is derived from the principle of virtual work. In [52], the decrease of

the potential energy with crack extension is employed to obtain a general path-area independent J-integral expression for non-planar cracks with curved crack fronts. In both cases, the mode-decomposition is not addressed.

It must be noted that, in all the aforementioned approaches for the computation of the energy release rate in three-dimensional problems, the fracture process zone is considered negligible. Conversely, in [92], a thick level set interface method is presented. The model accounts for a band of damaged material of predefined thickness. The fatigue energy release rate is calculated non-locally by numerical integration of the variation of the free energy in the level set direction throughout the damaged band. Nevertheless, the computation of the mode-decomposed energy release rate in three-dimensional delamination models based on the CZM approach has not been reported in the literature up to now.

2.3.2 Experimental observations

Much effort as been made towards a clear understanding of the factors that can affect the behavior of delamination under fatigue loading, such as the characteristics of the fatigue load (load ratio [106, 65, 64, 104, 161, 105, 12], mode mixity [19, 153, 118, 117, 119, 104, 46, 80, 18, 180, 11], load frequency [7], cyclic load sequence [176]), environmental factors (temperature [153, 66, 151, 110], moisture [90, 115], radiation [89], corrosion [63]), the fiber orientation at the interface [28, 128] or the influence of fiber-bridging [180, 69], among others.

Recently, in 2014, Bak and co-workers presented a review on the observed phenomenology and computational methods for delamination under fatigue loading [25]. They divided the existing experimental tests in three main groups: delamination initiation, onset and propagation tests, based on the stages of fatigue-induced damage. Initiation tests deal with the emergence of delaminations in pristine laminates. It can be compared with the nucleation stage in metals. However, the existence of initiation studies for laminated composites in the literature is very scarce. This is, probably, due to the inhomogeneous micro-structure and the presence of flaws and manufacturing defects in composites, which act as already "nucleated" delaminations.

In delamination onset studies, the delamination already exists (it is often created by a Teflon insert or it is made by a static pre-crack) and the information being sought is the number of cycles, N, required to make the delamination grow under a certain load [42] (c.f. Figure 2.7.a).

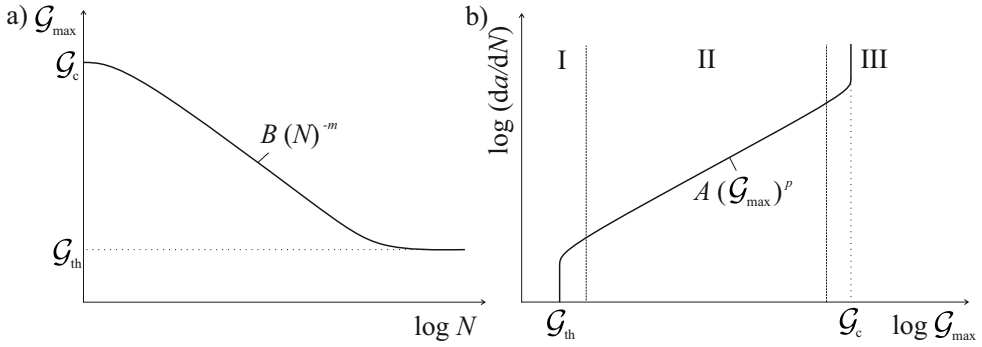

Fig. 2.7.: Qualitative representations of typical a) onset curve, and b) propagation curve.

Onset data can be fitted, as proposed by Krueger [84], by an expression of the kind:

$$\mathcal{G}_{max} = B \cdot (N)^{-m} \tag{2.4}$$

where B and m are fitting parameters.

On the other hand, delamination propagation tests evaluate the crack growth rate, $\frac{\mathrm{d}a}{\mathrm{d}N}$, as a function of the load. In Figure 2.7.b, an sketch of a typical propagation curve is represented. Three regions can be clearly identified: I) propagation arrest, bordering the threshold value, $\mathcal{G}_{th}$, (the load below which the crack growth becomes inappreciable); II) log-linear crack growth, governed by a Paris' law-based expression, such as [46, 18]:

$$\frac{\mathrm{d}a}{\mathrm{d}N} = A \cdot (\mathcal{G}_{max})^p \tag{2.5}$$

where A and p are fitting parameters; and III) fast growth, where the maximum cyclic energy release rate, $\mathcal{G}_{max}$, approaches the critical value, $\mathcal{G}_c$.

Among all the aforementioned factors that may influence the fatigue behavior of delamination, the two governing parameters that have been most widely investigated are the load ratio and the mode mixity. It is worth mentioning that little work has been done on the analysis of mode III fracture properties. Thus, since mode III fracture toughness is often higher than that of mode II loading [103], as a conservative approach, the fracture properties of mode II are generally attributed to any combination of shear mode. Then, fatigue tests under mixed-mode loading conditions are usually performed under a combination of mode I and mode II, and the mode mixity is defined as the amount of mode II energy release rate over the total energy release rate:

$$\Phi = \frac{\mathcal{G}_{II}}{\mathcal{G}_I + \mathcal{G}_{II}} \tag{2.6}$$

Mode II fracture toughness, $\mathcal{G}_{IIc}$, is, in most composite materials, notably higher than that of mode I, $\mathcal{G}_{Ic}$. This is explained by the different fracture mechanisms that take place under each loading mode, which result in different interlaminar crack morphologies [75]. Thus, it is reasonable that, when $\mathcal{G}_{max}$ is close to $\mathcal{G}_c$, since the delamination grows in similar conditions as those of quasi-stating growing, differences in fatigue behavior between mode loadings exist. However, these differences diminish at low levels of fatigue loading. The effect of the mode mixity, Φ, on the onset and propagation curves is qualitatively represented in [25] (and here reproduced in Figure 2.8.a), based on the behavior observed in [153] for carbon/epoxy laminates. After review of [66, 19, 153, 161, 119, 104, 180], among others, it is concluded that the fitting exponents in equations (2.4) and (2.5) vary nonmonotonically with the mode mixity. In addition, it is also stated that the fatigue threshold, $\mathcal{G}_{th}$, is independent of the mode mixity, based on the convergence of the fatigue curves at low load levels.

It is noteworthy that the identification of the energy release rate thresholds in fiber reinforced epoxies is difficult from an experimental point of view [33], because the near-threshold crack growth rates may be below the sensitivity of the measurements devices employed in the tests. Moreover, there does not exist any standardized criteria for the identification of the threshold values. Therefore, the thresholds are usually defined as the energy release rate value below which a minimum detectable increment of crack length is not exceeded during a certain number of cycles [104].

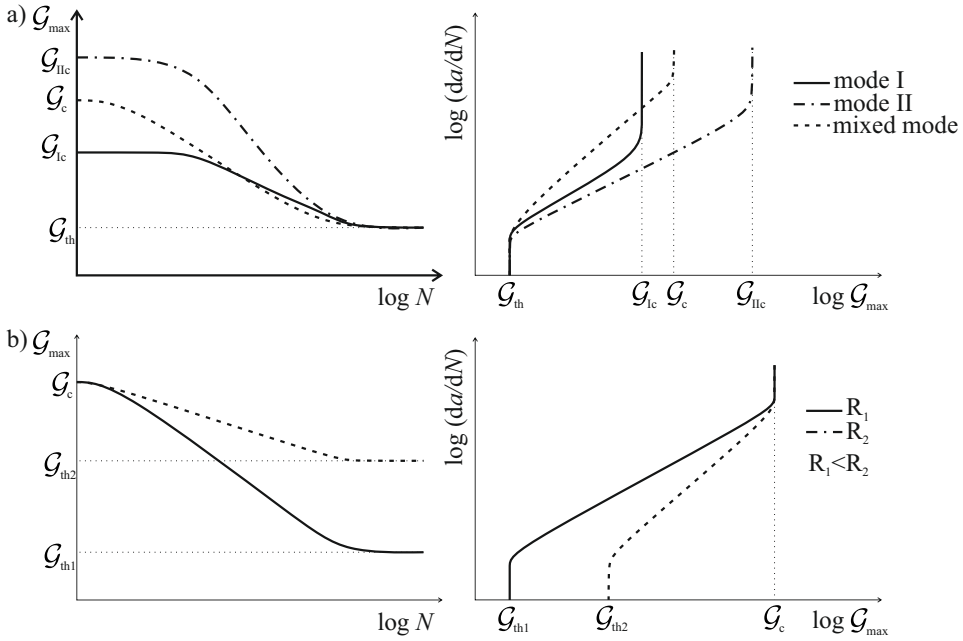

Fig. 2.8.: a) Qualitative representation of the influence of the mode mixity in delamination onset and propagation curves. b) Qualitative representation of the influence of the load ratio in delamination onset and propagation curves. Figure extracted from [22].

In practice, this number of cycles usually depends on the specific engineering application considered.

The influence of the load ratio, R, for a given maxim load, $\mathcal{G}_{max}$, is also reported in [25]. From the review of different experimental studies, such as [106, 65, 64, 104, 7, 161], the behavior described by the onset and propagation curves is summarized as depicted in Figure 2.8.b. The effect of the load ratio, R, is attenuated as $\mathcal{G}_{max}$ increases. This is because, when the delamination grows in conditions close to those of quasi-static growing, the amplitude of the fatigue load appears to be insignificant. Moreover, the fitting exponents in equations (2.4) and (2.5), and the fatigue threshold, $\mathcal{G}_{th}$, increase with R.

The effect of the mode mixity and the load ratio is accounted in several phenomenological models for fatigue delamination growth. Most of them are formulated to

describe the log-linear region of the propagation curve (region II in Figure 2.7.b), while a few of them also capture the near-threshold (region I) and near-critical (region III) propagation regimes. In [25], the capabilities of the existing models are summarized in a table, which is here reproduced in Table 2.1. All the listed phenomenological models are modifications of the Paris' law [125, 124], where the crack growth rate, $\frac{\mathrm{d}a}{\mathrm{d}N}$, is expressed a function of the energy release rate, $\mathcal{G}$.

Tab. 2.1.: Summary of the capabilities of the phenomenological models for fatigue crack growth rate presented in [25].

Phenomenological model	Parameters accounted for in the model				
	Mode mixity, Φ	Load ratio, R	Maximum load, $\mathcal{G}_{max}$	Fatigue threshold, $\mathcal{G}_{th}$	Near-critical propagation, $\mathcal{G}_c$
Ramkumar and Whitcomb [132]	✓(1)	-	✓	-	-
Gustafson and Hojo [59]	✓(1)	✓	-	-	-
Russell and Street [142]	✓(2)	✓	✓	-	-
Dahlen and Springer [46]	✓(2)	✓	✓	-	-
Kardomateas et al. [78]	✓(3)	✓	-	✓	-
Kenane and Benzeggagh [80]	✓(3)	✓	-	-	-
Blanco et al. [31]	✓(3)	✓	-	-	-
Hojo et al. [65]	-	✓	✓	-	-
Andersons et al. [17]	-	✓	✓	✓	✓
Allegri et al. [12]	-	✓	✓	-	-
Allegri et al. [11]	✓(3)	✓	✓	-	-
Martin and Murri [104]	-	-	✓	✓	✓
Shivakumar et al. [152]	-	-	✓	✓	✓

(1) Uncoupled mixed-mode behavior. The total crack growth rate is the sum of the crack growth rate of each pure mode.

(2) Coupled but not experimentally adjustable mixed-mode behavior. The interaction between models is fixed.

(3) Coupled and experimentally adjustable mixed-mode behavior.

Finally, it should be emphasized that the experimental studies available in the literature are mainly focused on one-dimensional propagation. Thus, the experimental research on arbitrarily shaped delamination fronts in three-dimensional specimens is very scarce. In this regard, Pradhan and Tay [35] conducted experiments in notched laminated under compressive fatigue loading. The delamination front was monitored with C-scan pictures. Four batches of three specimens were employed. Each batch was fatigued up to a certain number of cycles and each specimen was used for a single delaminated area measurement. More recently, Sachse et al. [143] presented an experimental and numerical study on the application of a rivetless nut plate joint to arrest fatigue crack growth in hybrid adhesive-mechanical composite joints. During propagation, the crack front shape and location were monitored in-situ using an

automated air-coupled ultrasonic measurement system. During the inspections, the fatigue test was stopeed and a reduced static load was applied. The crack front curved and slowed significantly as it approached the bolt. Nevertheless, a set of benchmark examples for fatigue propagation in three-dimensional problems to obtain data for model calibration is still remaining.

2.3.3 Simulation methods for prediction of fatigue delamination growth

One of the most recent reviews of simulation methods for delamination propagation, by Bak et al. [25], splits them into two categories: linear elastic fracture mechanics (LEFM) and cohesive zone model (CZM) based methods. Another very recent review, by Pascoe [126], adds the categories of stress/strain and extended finite element method (XFEM) based models. However, on the one hand, the two reported expression where stress is used to describe delamination growth [133, 131], are phenomenological models which can be rewritten in therms of LEFM parameters. On the other hand, only two XFEM approaches [30, 21] are described in [126]. Both resort to LEFM to define the load: in [30], the basic form of the Paris' law is expressed in terms of the stress intensity factor; in [21], the VCCT is used to compute the energy release rate. Moreover, any cohesive law formulation accounting for a damage variable that evolves under fatigue loading is potentially implementable into a XFEM framework, even though there is not any work published in the literature. However, some examples using quasi-static cohesive law formulations are already available [37, 111]. In view of the aforementioned, attention will be focused on LEFM and CZM based simulation methods.

In general terms, the LEFM based methods [35, 83] directly apply any of the Paris' law based expressions (c.f. Table 2.1) evaluated using VCCT [87, 88], or any other technique for determining the energy release rate (as described in Section 2.3.1). The strength of such methods is that, since they use a phenomenological expression for the crack growth, any experimental evidence of the effect of the load ratio, R, and/or the mode mixity, Φ, are easily included in the simulation (provided that the method for characterizing the load is capable to measure R and Φ). The weaknesses are the mesh requirements associated to the VCCT [86].

Regarding the methods based on the CZM approach, most of the fatigue formulations are extensions of the cohesive laws for quasi-static loading accounting for an additional criterion for the development of the damage due to fatigue loading. In contrast with VCCT, the cohesive zone model approach avoids the need for re-meshing and, moreover, no initial crack is needed. In addition, the CZM approach accounts for a nonnegligible fracture process zone (FPZ). On the other hand, due to its, generally, point-wise implementation into the finite element method framework, a local computation of the mode mixity, B, is introduced which varies along the length of the cohesive zone. Due to the lack of efficient formulations for determining the crack growth direction, the shear modes are not disaggregated. The cohesive zone models for fatigue delamination can be divided in two main groups: the loading-unloading hysteresis models, which simulate the whole load cycle to compute the evolution of the damage variable, and the envelope load models, which only model the maximum cyclic load.

One of the main advantages of the loading-unloading hysteresis models is that they are capable to model variable loading spectra. In return, the models become computationally unfeasible for high cycle fatigue simulation. Thus, they are typically only found in low-cycle fatigue applications. On the other hand, most of the existing loading-unloading hysteresis models are damage mechanics based models [179, 116, 141, 100, 5, 140, 166], in which the damage evolution laws are calibrated by fitting with experimental results and the predictive capabilities are subjected to the problem configuration. Conversely, a recently developed loading-unloading hysteresis model [157], links the fatigue damage law with a Paris' law based expression. The model requires the length of the cohesive zone, which is evaluated non-locally during the simulation. In this way, the model does not make use of any fitting parameter. The energy release rate is also computed non-locally using the two-dimensional J-integral formulation presented in [136]. It is worth mentioning that, in order to enable the simulation of three-dimensional structures, an extended J-integral formulation for three dimensional cohesive interfaces is needed.

In envelope load methods, the number of cycles is discretized and the damage variable, $\mathcal{D}$, is updated for each equilibrium sub-step. The damage at a given number of cycles, $\mathcal{D}(N_n + \Delta N)$ is determined by integration of the damage rate, $\frac{\mathrm{d}\mathcal{D}}{\mathrm{d}N}$:

$$\mathcal{D}\left(N_n + \Delta N\right) = \mathcal{D}\left(N_n\right) + \int_{N_n}^{N_n+\Delta N} \frac{\mathrm{d}\mathcal{D}}{\mathrm{d}N} \mathrm{d}N \tag{2.7}$$

where N_n is the current number of cycles and ΔN is the increment in cycles for the next equilibrium substep. Since $\frac{\mathrm{d}\mathcal{D}}{\mathrm{d}N}$ is unknown for $N \in]N_n, N_n + \Delta N]$, the integral of $\frac{\mathrm{d}\mathcal{D}}{\mathrm{d}N}$ is numerically approximated, either using 2 point Newton-Cotes quadrature (whenever $\frac{\mathrm{d}\mathcal{D}}{\mathrm{d}N}\big|_{N_n}$ and $\frac{\mathrm{d}\mathcal{D}}{\mathrm{d}N}\big|_{N_n+\Delta N}$ are both known [140, 166, 23]), or using 1 point Newton-Cotes quadrature (if only $\frac{\mathrm{d}\mathcal{D}}{\mathrm{d}N}\big|_{N_n}$ is known [172, 129, 81, 108, 60, 114, 109, 112, 79, 90, 163, 164]). These strategies make more efficient the simulation of high-cycle fatigue. Moreover, Turon et al. [172] incorporated a link between the damage rate and the crack growth rate, which was later followed by other authors [129, 60, 114, 79, 90, 23, 163, 164]. Thus, using this approach, any Paris law' based expression can be used. The general problematics of these CZMs is concerned to the accurate calculation of the energy release, although different solutions are proposed. A description of the fatigue damage rate models presented in [140, 166, 172, 129, 60, 81, 79, 23, 163, 164, 14] is given a few lines further down.

Another recent approach is the level set interface method for fatigue modeling [91]. This method is based on the envelope load approach. The crack growth rate is used to update the level set function in each time step. Therefore, any Paris' law based expression can be introduced in the model. Moreover, an accurate means of calculating the energy release rate is used. It is based on the jump in Eshelby momentum tensor at the location of the crack front when shell theory is assumed [174, 122]. Another advantage of this technique is that it allows the use of coarser meshes than those needed for the other methods covered in this state-of-the-art review. However, one limitation is that negligible FPZ must be assumed, which is not always possible. In this regard, the authors developed a thick level set interface method [93], which uses interface elements with a constitutive behavior controlled by a damage variable. The damage ranges from 0 (intact) to 1 (fully damaged) as a function of the distance to the front. This results in a band of damaged material of a predefined width. A Paris' law based expression is used to advance the level set. The energy release rate, $\mathcal{G}$, and mode mixity, Φ, are defined non-locally, and

only vary in the direction along the front (in three-dimensional analysis), but not perpendicular to it.

Finally, a combination of CZM and level set method is presented in [15]. The model skips the limitation of the level set to thin structures using the CZM to calculate the energy release rate. This is done by integrating the area under the quasi-static cohesive law. The level set front location is updated using a Paris' law based expression. A quasi-static cohesive law works in the interface elements until the level set reaches a given integration point. When this occurs, the damage at such integration point is suddenly set to 1. In [15], it is shown that a fine mesh is needed in order to avoid oscillations in the energy release rate values computed at the nodes when the crack front falls inside the elements and is influenced by the shape of the element boundaries.

Fatigue damage rate cohesive zone models

The basic features of the models found in the literature using a load envelope approach are described in the following. Note that the symbols used by the original authors in the equations that will be quoted have been replaced by a uniform nomenclature for comparison purposes between different models.

The first fatigue damage rate model to appear for delamination propagation in laminated composite materials was developed by Robinson et al. [140]. This model was based on the continuum damage mechanics fatigue model proposed by Peerlings et al. [127]. In [140], an exponential function containing three fitting parameters, C_1, C_2 and C_3 were used to describe the damage rate:

$$\frac{\mathrm{d}\mathcal{D}}{\mathrm{d}N} = \frac{C_1}{1+C_2} e^{C_3 \mathcal{D}} \left(\frac{\delta}{\delta_c} \right)^{C_2} \tag{2.8}$$

The parameters C_1, C_2 and C_3 had to be adjusted, for each fracture mode, by a trial and error approach to fit the experimentally determined crack growth rate data. Later, Tumino and Capello [166] incorporate a variable mixed-mode adaptation by defining an interpolation rule for the fitting parameters C_1 and C_2 (C_3 was eliminated), which

has to be determined a priori. The damage variable, $\mathcal{D}$, was a stiffness degrading variable (previously denoted in Section 2.2.1 as $\mathcal{D}^K$).

Khoramishad et al. [81] proposed a new formulation based on the model developed by Peerlings et al. [127]. The damage evolution is related to the principal strain and it acts to degrade the initial onset traction, τ_o. Likewise the former models, it relies on fitting parameters that need to be calibrated with experimental tests. This model is the only one reviewed here which is implemented in non-zero thickness interface elements. Another noteworthy characteristic of the model by Khoramishad et al. [81] is that it is based on separate damage variables for quasi-static and fatigue.

Turon et al. [172] were the first to link fracture mechanics and damage mechanics by expressing the stiffness degrading damage rate as a function of the crack growth rate:

$$\frac{\mathrm{d}\mathcal{D}}{\mathrm{d}N} = \frac{1}{l_{cz}} \frac{\left(\delta_c \left(1-\mathcal{D}\right) + \mathcal{D}\delta_o\right)^2}{\delta_c \delta_o} \frac{\mathrm{d}a}{\mathrm{d}N} \tag{2.9}$$

where δ_o is the displacement jump at the onset of damage and l_{cz} is an analytical estimation of the cohesive zone length, which initially was based on Rice's solution for mode I [137], and latter was updated for linear orthotropic materials as a function of the mode mixity [171]. The crack growth rate is calculated by any variant of the Paris' law such as the ones listed in Table 2.1. Thus, any influence of mode mixity and load ratio on the crack growth rate is included in the model by means of the chosen phenomenological model for the crack growth rate. The energy release rate, needed to evaluate the Paris' law based expression, is calculated as the total specific work, ω_{tot}. It is computed as the area under the quasi-static law, using instantaneous local information at each point, but not integrating the complete failure path in the traction-separation response. This approach leads to inaccurate computation of the crack growth rate; the reason is explained as follows. At the beginning of each time sub-step, static equilibrium exists. Due to an increment of the number of cycles, the damage variable is updated integrating the damage rate in Equation (2.9). This reduces the magnitude of the cohesive tractions in the fracture process zone, so that the crack driving force is no longer balanced. Thus, a quasi-static damage evolution is needed to recover the equilibrium again. This unintended static damage leads to a non-vertical failure path, meaning the complete failure response and the total

dissipated energy can not be computed using instantaneous information. Moreover, the approach used in [172] implies that there is a different crack growth rate value, $\frac{\mathrm{d}a}{\mathrm{d}N}$, for each point in the cohesive zone which can be difficult to interpret physically. Also, the mode mixity is evaluated locally (the local mode mixity is denoted as B) and it changes throughout the length of the cohesive zone. Nevertheless, the model offers the advantage of being point-wise evaluable, which, in turn, makes it readily applicable as a simulation tool for delamination propagation in 3D problems.

Later, the approach used by Turon et al. was adopted and simplified by Pirondi and Moroni [129, 112]:

$$\frac{\mathrm{d}\mathcal{D}}{\mathrm{d}N} = \frac{1}{l_{cz}} \frac{\mathrm{d}a}{\mathrm{d}N} \tag{2.10}$$

In this case, the energy release rate is determined by the J-integral, which leads to a constant $\frac{\mathrm{d}a}{\mathrm{d}N}$ value in the cohesive zone. As a counterpart, the model of Pirondi and Moroni [129] relies on spatial information. In addition, there can not be found in the literature any formulation for computing the mode-decomposed J-integral value in three-dimensional analysis using a CZM approach.

In the method developed by Harper and Hallett [60] the internal variable is a traction degrading damage variable. The damage rate is related to the crack growth rate:

$$\frac{\mathrm{d}\mathcal{D}}{\mathrm{d}N} = \frac{1 - \mathcal{D}_s - \mathcal{D}_{f,u}}{l_{fat}} \frac{\mathrm{d}a}{\mathrm{d}N} \tag{2.11}$$

where l_{fat} is the length of the cohesive zone under fatigue loading, which is related to that extracted from quasi-static simulations. The cohesive zone is split into two parts: a zone which only accumulates static damage and a zone undergoing fatigue damage updated by integration of Equation (2.11). $\mathcal{D}_s$ refers to the damage accumulated in the static part of the cohesive zone and $\mathcal{D}_{f,u}$ refers to the unintended static damage accumulated in the fatigue part of the cohesive zone. Likewise in the model of Turon et al. [172], the energy release rate is computed as the total specific work. Due to the unintended contribution of $\mathcal{D}_{f,u}$, inaccurate computation of the crack growth rate is obtained.

In [79], Kawashita and Hallett proposed a model where fatigue damage is only applied to the element at the crack tip. The model is based on calculating the jump in number of cycles needed for the crack propagate the length of the element at the crack tip, l_e, at the velocity of the crack growth rate, $\frac{\mathrm{d}a}{\mathrm{d}N}$:

$$\frac{\mathrm{d}\mathcal{D}}{\mathrm{d}N} = \frac{1-\mathcal{D}_s}{l_e}\frac{\mathrm{d}a}{\mathrm{d}N} \tag{2.12}$$

Even though it is not required to calculate the length of the cohesive zone, a non-local algorithm to identify the elements located at the crack tip is needed. Moreover, l_e is length associated to an integration point in the crack propagation direction. The original model [79] accounts for five possible in-plane propagation directions, which are based on the state of the neighbouring integration points. The maximum crack length increment is limited to l_e. In addition, a novel approach is used for the calculation of the energy release rate. It is done by integration of the traction-separation response of the most open point in the cohesive zone. This strategy assumes that crack growth occurs under self-similar condition, i.e. the variation of energy release rate between consecutive cohesive elements is small. The method leads to accurate results when short target increments in crack length are used [25]. However, it requires post-processing global data. Recently, the authors presented a method [164] based on the implementation of the model into four integration-point interface elements (the model was originally implemented into single-integration-point elements). This offers the advantage of exchanging spacial information within the element domain, thus making the formulation evaluable at element level.

Tao et al. [163] incorporated two modifications to the original model of Kawashita et al. [79]: a virtual fatigue damage variable to identify the crack tip elements using local element information, and a strain energy release rate correction method to enable the use of coarser meshes. This correction method uses an estimation of the cohesive zone length extracted from quasi-static simulations.

Bak et al. [23] developed a method which avoids making use of any fitting parameter in the link between the crack growth rate, $\frac{\mathrm{d}a}{\mathrm{d}N}$, which is a scalar variable, and the damage rate, $\frac{\mathrm{d}\mathcal{D}}{\mathrm{d}N}$, which is a field variable. This is achieved by application of two conditions: 1) the relation between tractions and displacement jumps is determined

by the quasi-static cohesive law during fatigue propagation, and 2) the damage changes discontinuously to 1 when the criterion for full damage is met:

$$\text{if} \quad \omega_{tot} > \mathcal{G} \quad \text{then} \quad \mathcal{D} = 1 \tag{2.13}$$

These two conditions imply that the distributions of cohesive tractions and displacement jumps, δ, within the damage process zone are unchanged in the shift between quasi-static loading and fatigue loading. Thus, the unwanted increase in the extracted total specific work [172, 60, 163] is eliminated and this field quantity can be determined accurately using instantaneous local information. On the other hand, the maximum cyclic energy release rate, $\mathcal{G}$, is a scalar variable determined using the J-integral method, i.e. using global information. The lack of formulations for three-dimensional mode-decomposed J-integral prevents the model of being applicable to three-dimensional analysis.

Taking into consideration condition 1), the damage rate model can be derived by making use of the dependencies of the variables in the quasi-static CZM. Then, by application of the chain rule, the damage rate is written as:

$$\frac{\mathrm{d}\mathcal{D}}{\mathrm{d}N} = \left(\frac{\partial \mathcal{D}}{\partial B} \frac{\partial B}{\partial a} + \frac{\partial \mathcal{D}}{\partial \delta} \frac{\partial \delta}{\partial a} \right) \frac{\mathrm{d}a}{\mathrm{d}N} \tag{2.14}$$

In [23], the slopes of local mode mixity and displacement jump with crack growth, $\frac{\partial B}{\partial a}$ and $\frac{\partial \delta}{\partial a}$ are calculated, assuming self-similar crack growth, as the slopes of mode mixity and displacement jump along the propagation direction. Thus, in three-dimensional analysis, the crack propagation direction must be identified in order to compute them. Current formulations for identification of the propagation direction require post-processing global information, which is computationally expensive. Thus, an efficient algorithm to determine the direction of crack growth is needed.

A more simpler approach than that used by Bak et al. [23] is used in [14], where the damage rate is calculated as:

$$\frac{\mathrm{d}\mathcal{D}}{\mathrm{d}N} = \frac{\partial \mathcal{D}}{\partial \delta}\frac{\partial \delta}{\partial a}\frac{\mathrm{d}a}{\mathrm{d}N} \tag{2.15}$$

Thus, the effect of the change in local mode mixity, B, during crack propagation is not taken into account. Moreover, in [14], condition 2) is changed to:

$$\text{if} \quad \mathcal{D}\left(N_n\right) + \int_{N_n}^{N_n+\Delta N} \frac{\mathrm{d}\mathcal{D}}{\mathrm{d}N}\mathrm{d}N > \mathcal{D}_s^{max} \quad \text{then} \quad \mathcal{D}\left(N_n + \Delta N\right) = 1 \tag{2.16}$$

where $\mathcal{D}_s^{max}$ is the quasi-static damage at the element at the crack tip, obtained by applying the maximum value of the cyclic load. The energy release rate is computed as the area under the traction-separation curve at the crack tip element. This measure is used for the rest of elements forming the cohesive zone, thus leading to a single value of crack growth rate. This strategy implies assuming self-similar crack growth. Moreover, it remains to define an strategy for three-dimensional analysis, where the energy release rate changes along the direction of the crack front.

In [22], benchmark studies of six of the presented computational methods [23, 172, 140, 130, 60, 79] are analyzed. The accuracy of the predicted crack growth rate is studied and compared. It is shown that the method of Bak et al. [23] leads in terms of robustness and accuracy. Some of the most recent methods [163, 14, 164] were not benchmarked in [22]. Nevertheless, either they are based on any of the previous models or they are not formulated for their applicability to 3D structures.

2.4 Introduction to the applied cohesive zone model for the simulation of high-cycle fatigue-driven delamination

The point of departure of the formulation developed in this Ph.D. thesis is the simulation method for high-cycle fatigue-driven delamination of Bak et al. [23]. The method was formulated for its applicability to 2D structures. This thesis is aimed at extending the original formulation to 3D. The method presented in [23] is, in turn, an extension of the CZM for quasi-static loading proposed by Turon et al. [167, 168]. Since they form the basis of the 3D fatigue damage formulation developed in this Ph.D. thesis, the quasi-static CZM and the 2D fatigue damage model from the original works [167, 168, 23], and their finite element implementation, are outlined in the following.

Kinematics of the cohesive interface

The CZM reduces the cohesive behavior to the mid-surface, $\overline{S}$, between the upper surface S^+, and the lower surface, and S^- (c.f. Figure 2.9). The deformed mid-surface, $\overline{S}$, is defined in the global Cartesian coordinates, $\boldsymbol{X}$, as the average distance between two initially coincident points,

$$\overline{\boldsymbol{x}} = \boldsymbol{X} + \frac{1}{2}\left(\boldsymbol{u}^+ + \boldsymbol{u}^-\right) \tag{2.17}$$

where $\boldsymbol{u}^\pm$ are the displacements of the two material points on $S^\pm$.

Defining a local Cartesian coordinate system $(\hat{\boldsymbol{e}}_1, \hat{\boldsymbol{e}}_2, \hat{\boldsymbol{e}}_3)$ on $\overline{S}$, the displacement jump across the material discontinuity $(\boldsymbol{u}^+ - \boldsymbol{u}^-)$ can be expressed according to the local normal and tangential directions of the midsurface:

$$\boldsymbol{\delta} = \boldsymbol{\Theta}\left(\boldsymbol{u}^+ - \boldsymbol{u}^-\right) \tag{2.18}$$

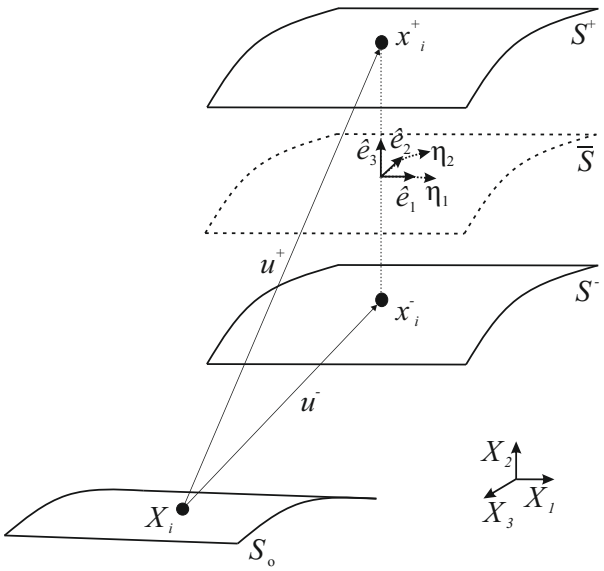

Fig. 2.9.: Description of the deformed element midsurface, $\overline{S}$.

where $\boldsymbol{\Theta}$ is the transformation tensor that relates the global to the local coordinate system:

$$\boldsymbol{\Theta} = [\hat{\boldsymbol{e}}_1, \hat{\boldsymbol{e}}_2, \hat{\boldsymbol{e}}_3]^T \tag{2.19}$$

Let η_1 and η_2 be isoparamteric curvilinear coordinates located on $\overline{S}$, as represented in Figure 2.9 (note that the isoparametric representation of the physical space is reduced to the interfacial element midsurface). Then, the two vectors tangential to the deformed midsurface are established as:

$$\boldsymbol{e}'_{\mathbf{1}} = \frac{\partial \overline{x}_i}{\partial \eta_1} \qquad \boldsymbol{e}'_{\mathbf{2}} = \frac{\partial \overline{x}_i}{\partial \eta_2} \tag{2.20}$$

and the direction cosines of the local Cartesian coordinate system, which are the normal, $\hat{e}_3$, and tangential, $\hat{e}_1$ and $\hat{e}_2$, unit vectors to $\overline{S}$, can be derived from the Equation (2.20) as follows:

$$\hat{\boldsymbol{e}}_{\mathbf{1}} = \frac{\boldsymbol{e}'_{\mathbf{1}}}{|\boldsymbol{e}'_{\mathbf{1}}|} \qquad \hat{\boldsymbol{e}}_{\mathbf{3}} = \frac{\boldsymbol{e}'_{\mathbf{1}} \times \boldsymbol{e}'_{\mathbf{2}}}{|\boldsymbol{e}'_{\mathbf{1}} \times \boldsymbol{e}'_{\mathbf{2}}|} \qquad \hat{\boldsymbol{e}}_{\mathbf{2}} = \hat{\boldsymbol{e}}_{\mathbf{3}} \times \hat{\boldsymbol{e}}_{\mathbf{1}} \tag{2.21}$$

Quasi-static constitutive model

The constitutive relation between the displacement jumps, $\boldsymbol{\delta}$, and the tractions, $\boldsymbol{\tau}$, between crack faces is defined as:

$$\begin{aligned} \tau_j &= \left(1 - \mathcal{D}^K\right) K \delta_j \qquad \text{for} \qquad j = 1, 2 \\ \tau_3 &= \left(1 - \mathcal{D}^K\right) K \delta_3 - \mathcal{D}^K K \langle -\delta_3 \rangle \end{aligned} \tag{2.22}$$

where $\mathcal{D}^K \in [0, 1]$ is a scalar damage variable reducing the penalty stiffness, K, and $\langle\,\rangle$ are the Macaulay brackets defined as $\langle x \rangle = (x + |x|)$. Note that, as interpenetration of crack faces is physically prevented by contact, negative normal opening values are avoided.

The evolution of the stiffness degrading damage variable, $\mathcal{D}^K$ is governed by an equivalent one-dimensional cohesive law and a damage criterion (c.f. Figure 2.10). For the formulation of this equivalent one-dimensional cohesive law, and so that different stages of the degrading process can be compared under changing mixed-mode loading conditions, a non-negative scalar displacement jump is defined:

$$\lambda = \sqrt{(\delta_I)^2 + (\delta_s)^2} \tag{2.23}$$

where δ_I is the mode I opening, associated to the displacement jump in the normal direction to the midsurface, and δ_s is the shear sliding resultant of the displacement jumps in the tangential directions to the midsurface.

$$\delta_I = \langle \delta_3 \rangle, \qquad \delta_s = \sqrt{(\delta_1)^2 + (\delta_2)^2} \tag{2.24}$$

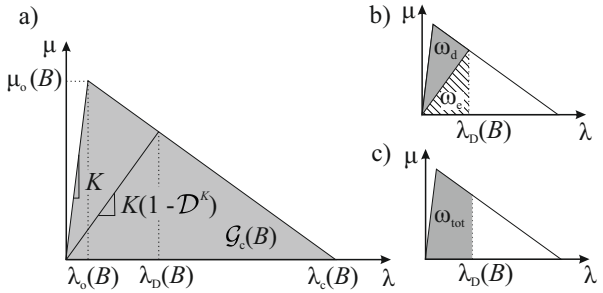

Fig. 2.10.: Equivalent one-dimensional cohesive law for a given mode-mixity, B. The shadowed area in a) represents the fracture toughness, $\mathcal{G}_c$, in b), the specific dissipated energy, ω_d, and the specific elastic energy, ω_e, and in c), the total specific work, ω_{tot}, for a given state of damage.

Note that the two tangential (orthogonal among each other) displacement jumps, δ_1 and δ_2, are reduced to an equivalent shear displacement jump, δ_s. It is worth mentioning that this is due to the incapability of the original formulation [167, 168] to distinguish into modes II and III, mainly attributed to the hitherto lack of computationally-efficient crack front tracking algorithms.

The equivalent one-dimensional interface traction, μ, is related to the equivalent one-dimensional displacement jump, λ, with

$$\mu = \left(1 - \mathcal{D}^K\right) K \lambda \tag{2.25}$$

With increasing displacement jump, the traction increases to a peak value, μ_o, corresponding to the interfacial strength, and then decreases until complete decohesion. To ensure the correct energy dissipation during the process of fracture, the total area under the traction-displacement jump curve is set equal to the fracture toughness, $\mathcal{G}_c$. Both the interfacial strength and the fracture toughness are material parameters

that depend on the opening mode-mixity, B, and, together with the penalty stiffness, K, define the shape of the constitutive law. The local mode-mixity, B, is defined in terms of the displacement jump as:

$$B = \frac{\delta_s^2}{\delta_I^2 + \delta_s^2} \tag{2.26}$$

and it is equivalent to the amount of total specific work related to shear mode over the entire total specific work, ω_{tot} (see Figure 2.10 for an schematic representation of ω_{tot}).

The fracture toughness, $\mathcal{G}_c$, for a given mode-mixity, is determined using the expression proposed in [29],

$$\mathcal{G}_c = \mathcal{G}_{Ic} + (\mathcal{G}_{IIc} - \mathcal{G}_{Ic})\, B^{\eta} \tag{2.27}$$

where subscripts I and II denote the pure modes I and II values, respectively, and η is an experimentally determined mode interaction parameter. Even though the hypothesis of a constant shear fracture toughness is not supported by any physical evidence, shear opening mode is, conservatively [103], treated as mode II.

Similarly to the intepolation of the fracture toughness, the interfacial strength, μ_o, for a given mode-mixity is defined as:

$$\mu_o = \sqrt{(\tau_{Io})^2 + [(\tau_{IIo} - \tau_{Io})]\, B^{\eta}} \tag{2.28}$$

where τ_{Io} and τ_{IIo} are the tensile and shear interfacial strengths. If it is assumed that the penalty stiffness of the model is mode independent. The interfacial shear strength is set as a function of the other material properties [168]:

$$\tau_{IIo} = \tau_{Io}\sqrt{\frac{\mathcal{G}_{IIo}}{\mathcal{G}_{Io}}} \tag{2.29}$$

In terms of the displacement jump, the onset, λ_o, and propagation, λ_c, of delamination are related to the parameters of the cohesive law:

$$\lambda_o = \frac{\mu_o}{K}, \qquad \lambda_c = \frac{2\mathcal{G}_c}{\mu_o} \tag{2.30}$$

The damage criterion is formulated ensuring damage irreversibility, such that the damage variable at the current time is determined as

$$\mathcal{D}^K = \min\left(\max\left(0, \frac{\lambda_c^t\left(\lambda^t - \lambda_o^t\right)}{\lambda^t\left(\lambda_c^t - \lambda_o^t\right)}\right), 1\right) \qquad \forall\, t \in [0, t_c] \tag{2.31}$$

Thus, the mixed-mode displacement jump associated to the current damage state is:

$$\lambda_{\mathcal{D}} = \frac{\lambda_o \lambda_c}{\lambda_c - \mathcal{D}^K\left(\lambda_c - \lambda_o\right)} \tag{2.32}$$

As shown in Section 2.2.1, the stiffness degrading damage variable, $\mathcal{D}^K$, is strongly nonlinear in terms of $\lambda_{\mathcal{D}}$. This might hinder the performance of the numerical method [23]. Conversely, an energy-based damage variable, $\mathcal{D}^e$, exhibits linear dependency with $\lambda_{\mathcal{D}}$. $\mathcal{D}^e$ is defined in [168] and [23] as the specific dissipated energy due to fracture, ω_d, over the fracture toughness, $\mathcal{G}_c$, during degradation ($\lambda_o \leq \lambda_{\mathcal{D}} \leq \lambda_c$):

$$\begin{cases} \mathcal{D}^e = 0 & \text{for} \quad \lambda_{\mathcal{D}} \leq \lambda_o \\ \mathcal{D}^e = \dfrac{\omega_d}{\mathcal{G}_c} & \text{for} \quad \lambda_o \leq \lambda_{\mathcal{D}} \leq \lambda_c \\ \mathcal{D}^e = 1 & \text{for} \quad \lambda_{\mathcal{D}} \geq \lambda_c \end{cases} \tag{2.33}$$

where ω_d is, in terms of the displacement jump, given as:

$$\omega_d = \max\left\{0, \frac{1}{2} K \lambda_o \lambda_c \frac{\lambda_o - \lambda_{\mathcal{D}}}{\lambda_o - \lambda_c}\right\} \tag{2.34}$$

The damage variables $\mathcal{D}^K$ and $\mathcal{D}^e$ are related by:

$$\mathcal{D}^e = 1 - \frac{\lambda_c \left(1 - \mathcal{D}^K\right) K \lambda_{\mathcal{D}}}{2\mathcal{G}_c} \tag{2.35}$$

Finally, the total specific work associated to the current damage state can also be determined in terms of the displacement jump:

$$\omega_{tot} = \frac{1}{2} K \lambda_o \left(\lambda_c - \frac{\left(\lambda_c - \lambda_{\mathcal{D}}\right)^2}{\lambda_c - \lambda_o} \right) \tag{2.36}$$

Note that, during crack propagation, the μ-λ relation follows the equivalent one-dimensional cohesive law, i.e.:

$$\lambda_{\mathcal{D}} = \lambda \tag{2.37}$$

and that before damage initiation ($\lambda \leq \lambda_o$), no energy is dissipated and the total specific work corresponds to the specific elastic energy:

$$\omega_{tot} = \frac{1}{2} K \lambda^2 \tag{2.38}$$

Fatigue damage model

The method presented in [23] for the simulation of fatigue-driven delamination is based on an envelope load approach. Thus, the damage after a given number of cycles is determined by integration of the damage rate, $\frac{\mathrm{d}\mathcal{D}}{\mathrm{d}N}$, at discrete increments in cycles, ΔN. The cycle integration scheme is further developed in the finite element implementation.

Since there does not exist any methodology for the experimental characterization of the fatigue cohesive law in the literature, most of the existing models are linked to or calibrated using the crack growth rate, $\frac{\mathrm{d}a}{\mathrm{d}N}$ [172, 60, 130, 79, 163]. The main challenge handled by the method from [23] is avoiding making use of any fitting parameter in the link between the crack growth rate, $\frac{\mathrm{d}a}{\mathrm{d}N}$, which is a scalar variable, and the energy-based damage rate, $\frac{\mathrm{d}\mathcal{D}}{\mathrm{d}N}$, which is a field variable. This is achieved by 1) maintaining that the quasi-static relationship between tractions, $\boldsymbol{\tau}$, and displacement jumps, $\boldsymbol{\delta}$, during fatigue propagation, and 2) setting the damage to 1 when the criterion for full damage is met (c.f. Equation (2.13)).

The rate of energy-based damage, $\frac{\mathrm{d}\mathcal{D}^e}{\mathrm{d}N}$, is better used instead of the rate of stiffness degrading damage variable, $\frac{\mathrm{d}\mathcal{D}^K}{\mathrm{d}N}$, the reason being that $\mathcal{D}^e$ changes linearly with the displacement jump, unlike $\mathcal{D}^K$ (see Section 2.2.1). Thus, Equation (2.14) is rewritten as:

$$\frac{\mathrm{d}\mathcal{D}^e}{\mathrm{d}N} = \left(\frac{\partial \mathcal{D}^e}{\partial B} \frac{\partial B}{\partial a} + \frac{\partial \mathcal{D}^e}{\partial \lambda} \frac{\partial \lambda}{\partial a} \right) \frac{\mathrm{d}a}{\mathrm{d}N} \tag{2.39}$$

Each of the partial derivatives in Equation (2.39) are addressed in the following. The derivative of the energy-based damage with respect to the mode mixity, $\frac{\partial \mathcal{D}^e}{\partial B}$, and the derivative of the energy-based damage with respect to the mixed-mode displacement jump, $\frac{\partial \mathcal{D}^e}{\partial \lambda}$, are scalar factors derived, by successive application of the chain rule, as:

$$\begin{aligned}
\frac{\partial \mathcal{D}^e}{\partial B} &= \frac{\partial \left(\frac{\omega_d}{\mathcal{G}_c} \right)}{\partial \omega_d} \left(\frac{\partial \omega_d}{\partial \lambda_o} \frac{\partial \lambda_o}{\partial \mu_o} + \frac{\partial \omega_d}{\partial \lambda_c} \frac{\partial \lambda_c}{\partial \mu_o} \right) \frac{\partial \mu_o}{\partial B} + \left(\frac{\partial \left(\frac{\omega_d}{\mathcal{G}_c} \right)}{\partial \omega_d} \frac{\partial \omega_d}{\partial \lambda_c} \frac{\partial \lambda_c}{\partial \mathcal{G}_c} + \frac{\partial \left(\frac{\omega_d}{\mathcal{G}_c} \right)}{\partial \mathcal{G}_c} \right) \frac{\partial \mathcal{G}_c}{\partial B} \\
\frac{\partial \mathcal{D}^e}{\partial \lambda} &= \frac{\partial \left(\frac{\omega_d}{\mathcal{G}_c} \right)}{\partial \omega_d} \frac{\partial \omega_d}{\partial \lambda}
\end{aligned} \tag{2.40}$$

Note that, in the original work [23], $\mathcal{G}_c - \omega_r$ is used instead of ω_d. Nevertheless, both expressions are equivalent.

Due to condition 1), the partial derivatives in Equation (2.40) can be obtained using the quasi-static dependencies. The partial derivatives are solved for the particular application of the CZM from [167, 168] and listed in Table 2.2. The expression for $\frac{\partial \mathcal{D}^e}{\partial B}$, obtained after substituting the partial derivatives in Equation (2.40) by the expressions listed in Table 2.2 is:

$$\frac{\partial \mathcal{D}^e}{\partial B} = \frac{\eta \left(\mathcal{G}_{IIc} - \mathcal{G}_{Ic}\right) B^{(\eta-1)} \lambda}{K \lambda_c \lambda_o \left(\lambda_o - \lambda_c\right)} = F_B \tag{2.41}$$

Similarly, the expression for $\frac{\partial \mathcal{D}^e}{\partial \lambda}$ reads:

$$\frac{\partial \mathcal{D}^e}{\partial \lambda} = \frac{1}{\lambda_c - \lambda_o} = F_\lambda \tag{2.42}$$

The rates $\frac{\partial B}{\partial a}$ and $\frac{\partial \lambda}{\partial a}$ in Equation (2.39) are the local point-wise change of the local mode-mixity and the mixed-mode displacement jump with the crack propagation. In a self-similar crack growth, $\frac{\partial B}{\partial a}$ and $\frac{\partial \lambda}{\partial a}$ can be interpreted as the slopes of the local mode-mixity and the mixed-mode displacement jump along the direction of crack propagation (for further details on this assumption, the reader is referred to the original paper [23] describing the method). Thus, being x_1 the crack growth coordinate, $\frac{\partial B}{\partial a}$ and $\frac{\partial \lambda}{\partial a}$ can be computed as:

$$\begin{aligned} \frac{\partial B}{\partial a} &\approx \frac{\partial B}{\partial x_1} \\ \frac{\partial \lambda}{\partial a} &\approx \frac{\partial \lambda}{\partial x_1} \end{aligned} \tag{2.53}$$

Note that, in order to compute $\frac{\partial B}{\partial x_1}$ and $\frac{\partial \lambda}{\partial x_1}$ in a three-dimensional model, the propagation direction must be identified.

The last term in Equation 2.39, $\frac{\mathrm{d}a}{\mathrm{d}N}$, is the crack growth rate, which can be expressed by any variant of the Paris' law [125] based on the energy release rate, $\mathcal{G}$. Thus, any experimentally observed effect on the crack growth rate, such as the effect of the

Tab. 2.2.: Dependencies and partial derivatives of the variables in the system using the CZM presented in [167, 168].

Dependencies	Partial derivatives	
$\lambda_o(\mu_o)$	$\dfrac{\partial \lambda_o}{\partial \mu_o} = \dfrac{1}{K}$	(2.43)
$\lambda_c(\mu_o, \mathcal{G}_c)$	$\dfrac{\partial \lambda_c}{\partial \mu_o} = -\dfrac{2\mathcal{G}_c}{\mu_o^2}$	(2.44)
	$\dfrac{\partial \lambda_c}{\partial \mathcal{G}_c} = \dfrac{2}{\mu_o}$	(2.45)
$\mu_o(B)$	$\dfrac{\partial \mu_o}{\partial B} = \dfrac{\eta\left(\tau_{IIo}^2 - \tau_{Io}^2\right) B^{\eta-1}}{2\mu_o}$	(2.46)
$\mathcal{G}_c(B)$	$\dfrac{\partial \mathcal{G}_c}{\partial B} = \eta\left(\mathcal{G}_{IIc} - \mathcal{G}_{Ic}\right) B^{\eta-1}$	(2.47)
$\omega_d(\lambda_o, \lambda_c, \lambda)$	$\dfrac{\partial \omega_d}{\partial \lambda_o} = \dfrac{1}{2} K \lambda_c \dfrac{\lambda_o^2 - 2\lambda_c\lambda_o + \lambda_c\lambda}{\left(\lambda_o - \lambda_c\right)^2}$	(2.48)
	$\dfrac{\partial \omega_d}{\partial \lambda_c} = \dfrac{1}{2} K \lambda_o^2 \dfrac{\lambda_o - \lambda}{\left(\lambda_o - \lambda_c\right)^2}$	(2.49)
	$\dfrac{\partial \omega_d}{\partial \lambda} = \dfrac{1}{2} K \lambda_o \lambda_c \dfrac{1}{\left(\lambda_c - \lambda_o\right)}$	(2.50)
$\mathcal{D}^e(\omega_d, \mathcal{G}_c)$	$\dfrac{\partial\left(\frac{\omega_d}{\mathcal{G}_c}\right)}{\partial \omega_d} = \dfrac{1}{\mathcal{G}_c}$	(2.51)
	$\dfrac{\partial\left(\frac{\omega_d}{\mathcal{G}_c}\right)}{\partial \mathcal{G}_c} = \dfrac{-\omega_d}{\mathcal{G}_c^2}$	(2.52)

mode mixity or the load ratio, can be included in the fatigue damage model. In this thesis, the crack growth rate, $\mathrm{d}a/\mathrm{d}N = f(\mathcal{G}_{max}, R, \Phi)$, is assumed to depend on the maximum cyclic energy release rate, $\mathcal{G}_{max}$, the load ratio, R, and the global mode mixity, Φ, which is defined as

$$\Phi = \frac{\mathcal{G}_{II}}{\mathcal{G}_I + \mathcal{G}_{II}} \tag{2.54}$$

where subscript II denotes the shear component of the energy release rate. Note that, likewise in the quasi-static model [167, 168], the modes II and III are not disaggregated. Also note the difference between the displacement jump based mode mixity, B, expressed in Equation (2.26) as a local quantity, and the energy release rate-based mode mixity, Φ, which is extracted from global information.

For a given load ratio, R, the Paris' law [125] like expression reads:

$$\frac{\mathrm{d}a}{\mathrm{d}N} = \begin{cases} A\left(\mathcal{G}_{max}\right)^p & \text{for} \quad \mathcal{G}_{th} < \mathcal{G} < \mathcal{G}_c \\ 0 & \text{for} \quad \mathcal{G} \leq \mathcal{G}_{th} \end{cases} \tag{2.55}$$

where the exponent, $p(\Phi)$, and coefficient, $A(\Phi)$, are mode-dependent parameters determined by [31]:

$$\begin{aligned} p &= \Phi^2\left(p_{II} - p_I - p_m\right) + \Phi p_m + p_I \\ logA &= \Phi^2\left(\frac{A_{II}}{A_m A_I}\right) + \Phi log\left(A_m\right) + log\left(A_I\right) \end{aligned} \tag{2.56}$$

and p_I and A_I are the Paris' law like parameters for pure mode I, p_{II} and A_{II} are the Paris' law like parameters for pure mode II, p_m and A_m are mode interpolation parameters, and $\mathcal{G}_{th}$ is the energy release rate threshold below which it is considered

that no propagation occurs. Its dependence with the mode mixity is assumed to follow a Benzeggagh-Kenane-based [29] expression, as stated in [172]:

$$\mathcal{G}_{th} = \mathcal{G}_{Ith} + (\mathcal{G}_{IIth} - \mathcal{G}_{Ith})\, \Phi^{\eta_2} \tag{2.57}$$

The maximum cyclic energy release rate, $\mathcal{G}_{max}$, and the global mode mixity, Φ, are computed using the J-integral method. The original model presented in [23], is developed for 2D analysis. In this case, the crack growth direction is defined naturally as the only possible direction confined in the interface. Then, making use of the path independence of the J-integral [136], the integration path domain is defined along the crack growth direction coordinate, x_1, extending the length of the CZ. However, for the extension of the fatigue model to the analysis of delamination propagation in 3D structures, the formulation of the J-integral must be reformulated.

Finite element implementation

The analysis of delamination propagation leads to a system of nonlinear equations that can only be solved using a numerical method. In this regard, most of the recently developed CZMs have been implemented in a finite element framework. By discretization into finite elements, the geometric and material nonlinearities of the system compounded by the bulk body and the interfacial crack can be addressed. The CZM presented in [167, 168, 23] is implemented into an 8-noded zero-thickness user-defined element (c.f. Figure 2.11) in the commercial code ABAQUS/Standard [160]. This interface element is compatible with three dimensional continuum elements that may form the upper and lower part of the bulk body containing the singularity.

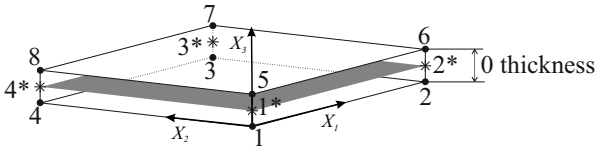

Fig. 2.11.: Sketch of the undeformed cohesive element. The nodes are represented as black dots and numbered from 1 to 8 and the integration points are represented as asterisks and numbered from 1* to 4*.

The nodal coordinates of the undeformed interface element are arranged in vector $\boldsymbol{C}$ in such a way that:

$$\boldsymbol{C} = \left\{\boldsymbol{C}^{-}, \boldsymbol{C}^{+}\right\} \tag{2.58}$$

$\boldsymbol{C}^{-} = \left\{X_1^1, X_2^1, X_3^1, ..., X_1^4, X_2^4, X_3^4\right\}^T$ and $\boldsymbol{C}^{+} = \left\{X_1^5, X_2^5, X_3^5, ..., X_1^8, X_2^8, X_3^8\right\}^T$ are the global coordinates of the nodes at the lower and upper interfaces, respectively, where X_i^n is the i-th coordinate of the n-th node.

The nodal displacements, relative to the global coordinates, are arranged in vector $\boldsymbol{Q}$ similarly to the nodal coordinates, i.e. the nodal displacements of the lower interface, $\boldsymbol{Q}^{-} = \left\{u_1^1, u_2^1, u_3^1, ..., u_1^4, u_2^4, u_3^4\right\}^T$, are numbered first, and the nodal displacements of the upper interface, $\boldsymbol{Q}^{+} = \left\{u_1^5, u_2^5, u_3^5, ..., u_1^8, u_2^8, u_3^8\right\}^T$, are numbered second:

$$\boldsymbol{Q} = \left\{\boldsymbol{Q}^{-}, \boldsymbol{Q}^{+}\right\} \tag{2.59}$$

The material coordinates and the displacement fields are interpolated within the domain of the cohesive element using isoparametric bilinear shape functions,

$$\begin{aligned} L_1 &= \frac{1}{2}\left(1-\eta_1\right)\left(1-\eta_2\right); \qquad L_2 = \frac{1}{2}\left(1+\eta_1\right)\left(1-\eta_2\right) \\ L_3 &= \frac{1}{2}\left(1+\eta_1\right)\left(1+\eta_2\right); \qquad L_4 = \frac{1}{2}\left(1-\eta_1\right)\left(1+\eta_2\right) \end{aligned} \tag{2.60}$$

organized in matrix the shape function matrix, $\boldsymbol{N}$, as follows:

$$\boldsymbol{N} = \begin{bmatrix} L_1 & 0 & 0 & & L_4 & 0 & 0 \\ 0 & L_1 & 0 & ... & 0 & L_4 & 0 \\ 0 & 0 & L_1 & & 0 & 0 & L_4 \end{bmatrix} \tag{2.61}$$

According to Equation (2.17) and making use of equations (2.58)-(2.61), the coordinates of the interfacial deformed midsurface are:

$$\overline{\boldsymbol{x}} = \frac{1}{2}\boldsymbol{N}\left(\boldsymbol{C}^{+} + \boldsymbol{C}^{-} + \boldsymbol{Q}^{+} + \boldsymbol{Q}^{-}\right) \tag{2.62}$$

The tangential vectors to the interfacial midsurface defined in Equation (2.20), are arranged in the Jacobian matrix:

$$\boldsymbol{\mathcal{J}} = [\boldsymbol{e}_1', \boldsymbol{e}_2'] \qquad \text{where} \qquad \boldsymbol{\mathcal{J}} = \frac{1}{2}\frac{\partial \boldsymbol{N}}{\partial \boldsymbol{\eta}}\left(\boldsymbol{C}^{+} + \boldsymbol{C}^{-} + \boldsymbol{Q}^{+} + \boldsymbol{Q}^{-}\right) \tag{2.63}$$

Hence, the unit vectors, $\hat{\boldsymbol{e}}_1$, $\hat{\boldsymbol{e}}_2$, $\hat{\boldsymbol{e}}_3$, corresponding to the direction cosines of the local Cartesian coordinate system, can be derived from $\boldsymbol{\mathcal{J}}$ following equation (2.21).

The transformation matrix, $\boldsymbol{M}$, computes the displacement jump in global coordinates of two initially coinciding points from the nodal global displacement vector:

$$\boldsymbol{u}^{+} - \boldsymbol{u}^{-} = \boldsymbol{M}\boldsymbol{Q} \tag{2.64}$$

where $\boldsymbol{M}$ is defined as:

$$\boldsymbol{M} = [-\boldsymbol{N}\ \boldsymbol{N}] \tag{2.65}$$

Thus, from Equation (2.18), the displacement jump in local coordinates reads:

$$\boldsymbol{\delta} = \boldsymbol{\Theta}\boldsymbol{M}\boldsymbol{Q} \tag{2.66}$$

The interface element internal force vector isderived from the principle of virtual work at each of the sub-domains in which the body is divided by the cohesive interface

and assuming that the resultant of the cohesive tractions must be continuous by Newton's Third Law [56]:

$$\boldsymbol{f} = \int_{\bar{S}_e} \boldsymbol{N}^T \boldsymbol{\Theta}^T \boldsymbol{\tau} \mathrm{d}\bar{S}_e = \int_{-1}^{1}\int_{-1}^{1} \boldsymbol{N}^T \boldsymbol{\Theta}^T \boldsymbol{\tau} |\boldsymbol{e_1'} \times \boldsymbol{e_2'}| \mathrm{d}\eta_1 \eta_2 \tag{2.67}$$

where $\bar{S}_e$ is the mid-surface of the interface element in the deformed configuration. The element tangent stiffness matrix, $\boldsymbol{K}_f$, reads:

$$\boldsymbol{K}_f \approx \int_{\bar{S}_e} \boldsymbol{N}^T \boldsymbol{\Theta}^T \boldsymbol{D}^{tan} \boldsymbol{\Theta} \boldsymbol{N} \mathrm{d}\bar{S}_e = \int_{-1}^{1}\int_{-1}^{1} \boldsymbol{N}^T \boldsymbol{\Theta}^T \boldsymbol{D}^{tan} \boldsymbol{\Theta} \boldsymbol{N} |\boldsymbol{e_1'} \times \boldsymbol{e_2'}| \mathrm{d}\eta_1 \eta_2 \tag{2.68}$$

where $\boldsymbol{D}^{tan}$ is the constitutive tangent stiffness matrix [167]:

$$D_{ij}^{tan} = \begin{cases} K \left[\bar{\delta}_{ij} \left(1 - \mathcal{D}^K - \mathcal{D}^K \bar{\delta}_{3j} \dfrac{\langle -\delta_3 \rangle}{\delta_3} \right) - \left(1 + \bar{\delta}_{3j} \dfrac{\langle -\delta_3 \rangle}{\delta_3} \right) \cdot \right. \\ \left. \left(1 + \bar{\delta}_{3j} \dfrac{\langle -\delta_3 \rangle}{\delta_3} \right) \dfrac{\lambda_c \lambda_o \delta_i \delta_j}{\delta_3 \left(\lambda_c - \lambda_o \right)} \right], & \text{for} \quad \lambda_{\mathcal{D}} < \lambda < \lambda_c \\ \\ \bar{\delta}_{ij} K \left(1 - \mathcal{D}^K - \mathcal{D}^K \dfrac{\langle -\delta_3 \rangle}{\delta_3} \right), & \text{for} \quad \lambda < \lambda_{\mathcal{D}} < \lambda_c \quad \text{or} \quad \lambda > \lambda_c \end{cases} \tag{2.69}$$

where $\bar{\delta}_{ij}$ is the Kronecker delta and $i, j = 1, 2, 3$.

During fatigue loading, the number of cycles is discretized and the energy-based damage, $\mathcal{D}^e$, is updated for each equilibrium substep. Then, the updated $\mathcal{D}^e$ after an increment ΔN in number of cycles is obtained as:

$$\mathcal{D}^e \left(N_n + \Delta N \right) = \mathcal{D}^e \left(N_n \right) + \int_{N_n}^{N_n + \Delta N} \frac{\mathrm{d}\mathcal{D}^e}{\mathrm{d}N} \mathrm{d}N = \mathcal{D}^e \left(N_n \right) + \Delta \mathcal{D}_f^e \tag{2.70}$$

Since $\frac{\mathrm{d}\mathcal{D}^e}{\mathrm{d}N}$ is unknown for $N \in]N, N+\Delta N]$, the integral of $\frac{\mathrm{d}\mathcal{D}^e}{\mathrm{d}N}$ is approximated using the trapezoidal rule:

$$\Delta\mathcal{D}_f^e \approx \frac{1}{2}\left(\frac{\mathrm{d}\mathcal{D}^e}{\mathrm{d}N}\,|_{N_n} + \frac{\mathrm{d}\mathcal{D}^e}{\mathrm{d}N}\,|_{N_n+\Delta N}\right)\Delta N \tag{2.71}$$

The increment in cycles for the next equilibrium substep is determined in [23] using a target increment in crack length, Δa_t, and the crack growth rate, $\frac{\mathrm{d}a}{\mathrm{d}N}$, from Equation (2.55) at the current number of cycles, N_n:

$$\Delta N = \frac{\Delta a_t}{\frac{\mathrm{d}a}{\mathrm{d}N}} \tag{2.72}$$

However, Equation (2.70) provides accurate results only when the delamination propagates in a self-similar way and when a very fine mesh is used. The reason being the error committed due to the calculation of the rates $\frac{\partial B}{\partial a}$ and $\frac{\partial \lambda}{\partial a}$ as $\frac{\partial B}{\partial x_1}$ and $\frac{\partial \lambda}{\partial x_1}$, respectively (c.f. Equation (2.53)). This error produces inaccurate computation of the increment of the damage due to fatigue loading, $\Delta\mathcal{D}_f^e$, implying that an unintended increment of the damage, $\Delta\mathcal{D}_s^e$, evolves to ensure static equilibrium. Thus, the updated energy-based damage is given as:

$$\mathcal{D}^e\left(N_n + \Delta N\right) = \mathcal{D}^e\left(N_n\right) + \Delta\mathcal{D}_f^e + \Delta\mathcal{D}_s^e \qquad \text{(non-self-similar crack growth)} \tag{2.73}$$

The contribution of the quasi-static term implies that the predicted energy-based damage, $\mathcal{D}^e$, does not correspond to the number of cycles elapsed. In order to overcome this situation, an adaptive cycle integration (ACI) approach, which enables the use of coarse meshes, is proposed in [23]. The ACI approach incorporates a point-wise modification of the cycle integration limits in Equation (2.70) and a point-wise modification of the criterion for full damage in Equation (2.13). By using the ACI approach, the overestimated crack growth rate caused by the unindented increment of quasi-static damage, $\Delta\mathcal{D}_s^e$, is reduced. Further details on the ACI implementation are given in [23].

2.5 Experimental characterization of interlaminar properties

The material card that feeds both parts of the damage model, the quasi-static and the fatigue parts, includes the parameters listed in Table 2.3. Additionally, the penalty stiffness, K, and the load ratio, R, are input parameters that must be defined by the user. In the following, the existing experimental methodologies to obtain the parameters listed in Table 2.3 are presented.

Tab. 2.3.: Material card.

Nomenclature	Property
$\mathcal{G}_{Ic}, \mathcal{G}_{IIc}$:	Mode I and mode II fracture toughnesses
η :	Benzeggagh-Kenane mode interpolation parameter of the fracture toughness [29]
τ_{Io}:	Interfacial tensile strength
p_I, A_I :	Exponent and coefficient of the Paris' law-like expression of Equation (2.55) under pure mode I loading conditions
p_{II}, A_{II} :	Exponent and coefficient of the Paris' law-like expression of Equation (2.55) under pure mode II loading conditions
p_m, A_m :	Mode interpolation parameters of Equation (2.56)
$\mathcal{G}_{Ith}, \mathcal{G}_{IIth}$:	Mode I and mode II energy release rate thresholds
η_2 :	Benzeggagh-Kenane mode interpolation parameter of the energy release rate threshold [29, 172]

A review of the test methods for delamination resistance or fracture toughness of fiber-reinforced polymer-matrix laminated composites was done in 1998 by Davies et al. [47], later in 2003 by Tay [165] and more recently, in 2008 by Brunner at al. [32]. Significant progress within the last ten years can be noted and some of the tests methods presented in [47, 165, 32] have been yet standardized, or are being considered for standardization.

For the determination of mode I interlaminar fracture toughness, $\mathcal{G}_{Ic}$, of unidirectional carbon or glass fiber-reinforced composites, the standard procedures ISO 15024 [1] and ASTM D5528 [41] are based on the double cantilever beam (DCB) specimen and are technically equivalent. A similar mode I standard test method by the JSA was edited in conjunction with a mode II procedure, the JIS K7086 [76]. In addition, for both carbon fiber composites manufactured from unidirectional tape or woven

fabric, the standard EN 6033 [3], also based on the DCB specimen, was approved in 2015 for aerospace applications.

For mode II fracture toughness, $\mathcal{G}_{IIc}$, of unidirectional carbon or glass fiber-reinforced composites, the standard JIS K7086 [76] was the first issued. In [76], an stabilized three-point bending end notch flexure (SENF) is proposed. It provides stable propagation, though it requires a complex test set-up since the applied displacement is controlled using the real-time measurement of the shear displacement at the cracked end of the specimen. Later, the standard ASTM D7905 [45], for unidirectional fiber arrangements, and the standard EN 6034 [4] for unidirectional and woven fabric-made composites for aerospace applications, proposed the use of the three-point bending end notch flexure (3ENF). However, since the ENF-test is essentially unstable, only initiation values but not propagation data can be obtained. Another standardized mode II test configuration, which exhibit stable crack propagation, is the End Loaded Split (ELS). In this regard, the standard ISO 15114 [2] uses the ELS configuration and specifies an experimental procedure to calibrate the compliance to crack length relationship. Thus, the crack length is estimated and its measurement can be avoided.

For mixed mode I/II fracture toughness of unidirectional carbon or glass fiber-reinforced composites, the standard procedure ASTM D6671 [41] is based on the mixed mode bending (MMB) test configuration.

For interfacial tensile strength, τ_{Io}, of fiber-reinforced polymer-matrix composites there are two standards: the ASTM D7291 [44], based on producing an interlaminar tensile stress by directly applying an out-of-plane tensile load to a flat specimen, and the ASTM D6415 [43], based on generating an interlaminar tensile stress by applying bending moments to curved beam specimens (four-point bend loading configuration). Note in Equation (2.29) that, using the CZM presented in [168], the number of interlaminar properties is reduced so that the interfacial shear strength, τ_{IIo}, is expressed as a function of τ_{Io}, $\mathcal{G}_{Ic}$ and $\mathcal{G}_{IIc}$. Optionally, τ_{IIo} may be measured instead of τ_{Io}. Then, the interfacial shear strength, τ_{IIo}, can be determined following the standard procedure ASTM D2344 [40] for short-beam strength of high-modulus fiber-reinforced composite materials.

Some test parameters that are currently out of the scope of the standards, such as high and low temperature, humidity, other types of lay-ups or other types of loading

(pi.e. mode III or higher rates) are being extensively investigated or developed into standard procedures. Fatigue loading is also excluded from the standard procedures, with the only exception of the standard ASTM D6115 [42], which is a means of determining the delamination growth onset in unidirectional fiber-reinforced laminates under mode I fatigue loading. However, fatigue crack propagation is not considered in the ASTM D6115 [42] procedure.

Focusing on the fatigue characterization techniques, Brunner et al. [33] published a round robin exercise on mode I fatigue delamination testing with the aim of developing a standardized test procedure for crack growth rate data extraction. The testing procedure was based on the DCB specimen. For a DCB fatigue test conducted under displacement control and constant displacement amplitude, the energy release rate decreases as the crack grows. That is, the crack growth rate curve (c.f. Figure 2.7.b) sweeps from right to left until the propagation becomes unnoticeable (near threshold-region). Thus, the selection of the testing parameters is not critical.

In order to compute the crack growth rate, the crack length over the number of cycles is required. Monitoring specimen crack length may be either optically done with a traveling microscope or be estimated through the specimen's compliance [33]. In [134], Renart et al. developed a methodology to measure the specimen's compliance in real time (referred to as "dynamic compliance") and, thus, enabling to obtain a continuous curve for the evolution of the crack length with the number of cycles. Furthermore, in [135], a new test rig and an associated methodology is presented which, in combination with the real time monitoring of the compliance, enables to test several DCB specimens simultaneously in a universal testing machine (c.f. Figure 2.12). The novelty of the solution relies on being able to test several specimens at different levels of load ratio and energy release rates in a single run.

Regarding mode II fatigue testing, there is an open discussion about which is the best suited rig. In the round robin exercise presented in [34], both 3-ENF and CELS test rigs were used and the Paris' law-like fitting parameters (p_{II} and A_{II}) of the data from both configurations clearly differed. They attributed the problems in the 3-ENF configuration to the specimen shifting and the compressive stresses in the region under the loading arm, while, for the C-ELS test, to the effects of variation in clamping (different torques applied to the screws). In addition, the C-ELS test involves large vertical deflections which may create the need for a correction in the data reduction scheme to account for them and it may also entail inertial effects

Fig. 2.12.: Multi-fatigue test device with 6 specimens.

related to the heavy weight of the clamping rig, which describes a cyclic movement in conjunction with the specimen. Therefore, only detailed data analysis will reveal whether 3-ENF or C-ELS is better suited for cyclic mode II fatigue delamination characterization.

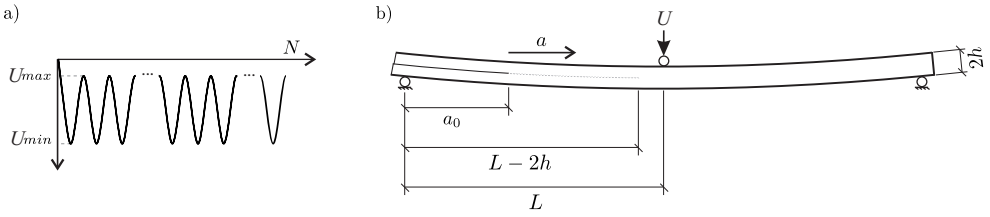

Fig. 2.13.: a) Sinusoidal shaped loading cycles with constant displacement. b) 3-ENF test configuration, where L is the mid-span length, a is the crack length, a_0 is the initial crack length and $2h$ is the specimen's total thickness of the specimen.

For mode II 3-ENF fatigue tests, the range of the crack growth rate curve swept in a single test under constant cyclic displacement is very narrow. This results from

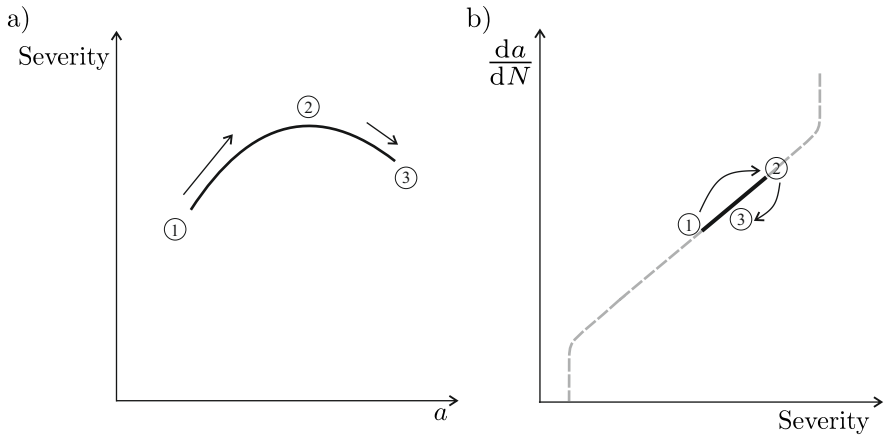

Fig. 2.14.: a) Maximum energy release rate applied to the 3-ENF test as a function of the crack length. b) Crack growth rate curve segment analyzed in a single test with constant cyclic displacement.

the dependence of the energy release rate on the geometry of the specimen and the configuration of the test. Indeed, in 3-ENF tests the region available for crack propagation spans between the support and the vicinity of the loading roller, where the through thickness compression arrests crack propagation (c.f. Figure 2.13). The energy release rate does not evolve monotonically with the crack extension but, as the cracks extends, it increases and then decreases, as shown in Figure 2.14.a. Thus, only a small segment of the crack growth curve is covered by a single test. In fact, the same segment of the curve is tracked twice: first upward and then downward (c.f. Figure 2.14.b). Hence, to construct the entire crack growth curve requires various constant cyclic displacement tests at different load intensities. The alternative to performing multiple tests is to implement a test with a proper variation of the displacement. Only Tanaka and Tanaka [161], Matsubara et al. [105] and Hojo et al. [67, 65] carried out 3-ENF fatigue tests with fiber reinforced polymer specimens by decreasing the applied peak load as the crack propagates. In [161] the authors conducted fatigue tests under either a constant or decreasing stress intensity range, ΔK, to graphite/epoxy composite specimens. The same data on crack growth rate, $\mathrm{d}a/\mathrm{d}N$, with crack extension was obtained in the ΔK-constant tests. Tanaka and Tanaka determined that fiber bridging had no influence on Mode II crack propagation and concluded that crack growth is independent of crack extension history. Matsubara et al. [105] used a decreasing-load test procedure based on the

ASTM standard for metals [20]. This methodology enables the crack growth rate for a broader range of the load intensity factor to be determined and also to approach the low-rate region, near the threshold, by decreasing the applied load. The load shedding can be done manually at selected crack size intervals or, alternatively, by continuously reducing the force to adjust the normalized K-gradient, $(1/K)\mathrm{d}K/\mathrm{d}a$, to a fixed value. They conducted constant- and decreasing- load tests with glass fibre reinforced polymer specimens and obtained identical results, confirming that crack growth rate is independent of crack extension history. Similarly, Hojo et al. [67, 65] carried out fatigue tests under constant normalized gradient of energy release rate, $(1/\mathcal{G})\mathrm{d}\mathcal{G}/\mathrm{d}a$, by measuring the specimen's compliance and decreasing the peak load accordingly.

In practice, incrementally shedding the force with increasing crack size requires the continuous intervention of a technician. On the other hand, computer-controlled stress intensity or, equivalently, energy release rate gradient techniques [147, 148], require the crack length to be monitored in real-time, usually by means of the specimen's compliance. Indeed, the use of the compliance to control the machine, or any other behavioral-based control technology, can lead to unexpected load setpoints, i.e. unpredictable responses from the test machine.

On the other hand, onset curves (c.f. Figure 2.7.a) are built by measuring the number of cycles required for fatigue propagation for different levels of severity of load. The severity of load is usually defined as the ratio of the maximum cyclic energy release rate, $\mathcal{G}_{max}$, to the quasi-static fracture toughness, $\mathcal{G}_c$. According to the ASTM 6115 standard [42], the onset point for each specimen can be identified either by visual inspection of the crack length or by an increase of the specimen's compliance. Regarding the latter, two different criteria are recommended in [42]: a 1% and a 5% increase of the specimen's compliance relative to the initial value. In practice, running these tests is not only costly and time consuming, but also leads to scattered results. If the increment in crack length criterion is used, it requires stopping the test periodically to carry out crack length inspection. On the other hand, if the increment of the specimen's compliance criterion is used, it requires also stopping the test periodically to perform quasi-static tests on the linear region of the material. Thus, the accuracy in determining the onset point depends on the frequency of the stops, and requires the continuous intervention of a technician. In this regard, the methodology presented in [134] can be used to obtain a continuous curve for the evolution of the specimen's compliance with the number of cycles. In

Figure 2.15, the dynamic compliance [134] of a DCB specimen is plotted against the number of cycles for a test performed with an initial severity of 60%. The dynamic compliance is measured during the fatigue test at a sampling rate of 1 data/cycle. Thus, by using the real time monitoring of the specimen compliance, the identification of the onset point is done with a precision of 1 cycle.

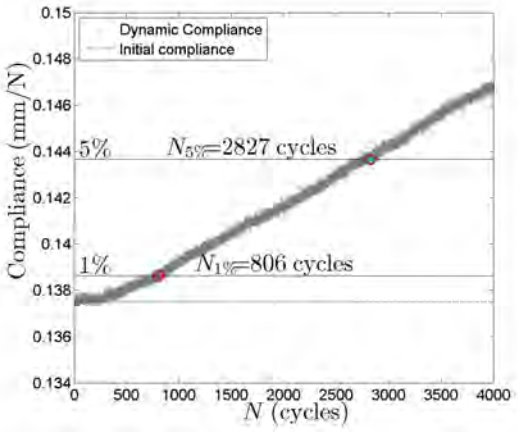

Fig. 2.15.: Specimen curves of the dynamic compliance [134] versus the number of cycles. The curve indicates the number of cycles for which the compliance increases by 1%, and 5%. The reference value of the compliance has been obtained from the first cycles.

Moreover, onset curves can be used to obtain a "fatigue limit": an energy release rate value, $\mathcal{G}_{th}$, below which no onset of propagation occurs.

3 Extension of the simulation method for fatigue-driven delamination in 3D structures

Based on the formulation reviewed in Section 2.4, there are two main requirements that must be met in order to extend the method presented in [23] for its three-dimensional application:

- Develop an efficient algorithm to determine the direction of crack propagation.
- Formulate a three-dimensional J-integral applicable to cohesive interfaces for the determination of the mode-decomposed energy release rates.

In this chapter, both tools are provided together with the details of the extension of the cohesive zone model for 3D structures undergoing fatigue delamination.

3.1 Point-wise evaluation of the growth driving direction for arbitrarily shaped delamination fronts using cohesive elements

In this section, a local algorithm to determine the growth driving direction in CZM is presented. It can be evaluated at any point within the cohesive zone at the same time the damage state is being computed. Therefore, it can be used to enhance the cohesive element formulation under static loading, preserving the local nature of the formulation. Moreover, it is an efficient alternative to the existing nonlocal propagation direction algorithms used in the methods for fatigue simulation.

3.1.1 Determination of the growth driving direction

In the framework of LEFM, the propagation direction is assumed to be the normal direction to the crack front, where the crack front is the line separating the uncracked and cracked parts (see Figure 3.1.a). In contrast to LEFM, the CZM technique accounts for a band of damaged interface of variable length, called the fracture process zone, FPZ (light grey band in Figure 3.1.b). Therefore, the propagation direction, understood as the normal to the crack front line, can not be defined in the CZM framework. In this work, the concept of "growth driving direction" is introduced for CZM as the analogous to the propagation direction. It is assumed to be normal to a given damage isoline and it can be calculated at any point within the FPZ. This definition follows naturally from the LEFM definition and provides the exact same result in the limiting case where the length of the fracture process zone goes to zero.

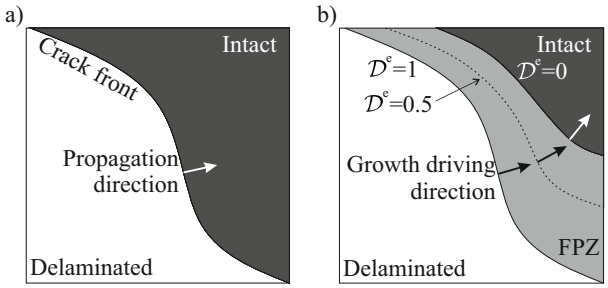

Fig. 3.1.: a) The propagation direction is assumed to be the normal direction to the crack front in the LEFM framework. b) The growth driving direction is assumed to be the normal direction to a damage isoline in the CZM framework. The energy-based damage variable, $\mathcal{D}^e$.

Growth driving direction using cohesive elements

Consider a laminated structure undergoing a delamination crack restricted to propagate in the interface between two adjacent plies. The degradation process of the material ahead of the crack tip is modeled using the bilinear CZM formulation developed in [167, 168]. As detailed in 2.4, the process of the degradation of the interface properties is governed by an energy-based damage variable, $\mathcal{D}^e$, defined in Equation (2.33) as the ratio between the specific dissipated energy, ω_d, and the

fracture toughness, $\mathcal{G}_c$. Thus, $\mathcal{D}^e$ is a scalar quantity that measures the degree of crack development: when $\mathcal{D}^e$ equals 0, the degradation process is yet to start, while, when $\mathcal{D}^e$ equals 1, the crack is completely developed. The total specific work, ω_{tot}, corresponding to a given state of damage is the sum of the specific dissipated energy, ω_d, and the specific elastic energy, ω_e.

To ensure the proper energy dissipation under mixed-mode conditions, a one-dimensional cohesive law relates the equivalent mixed-mode traction, μ, to the equivalent mixed-mode displacement jump, λ. Such constitutive law is formed by an initial elastic region, before damage initiation, and a softening region. When the area under the one-dimensional traction-displacement jump curve is equal to the fracture toughness, $\mathcal{G}_c$, a new crack surface is formed. The Benzeggagh-Kenane criterion [29] is used to define the mixed-mode displacement jumps at which the onset of damage, λ_o, and propagation, λ_c, occur. A sketch of the equivalent one dimensional bilinear law is represented in Figure 2.10 for a given mode-mixity, B.

Complying with the cohesive element definition, the interfacial tractions and displacement jumps are evaluated at the interfacial deformed midsurface, $\overline{S}$, and determined by its local orientation. Thus, the normal and tangential traction components, acting on a unit deformed interfacial midsurface area, are conjugated to the normal and tangential displacement jumps across the material discontinuity. For the analysis of delamination propagation in three-dimensional structures, the interfacial midsurface is defined by the Cartesian coordinates $\overline{x}_i$, with $i = 1, 2, 3$. The local Cartesian coordinate system located on the deformed midsurface is defined by two tangential unit vectors, $\hat{\boldsymbol{e}}_1$ and $\hat{\boldsymbol{e}}_2$, and a normal unit vector, $\hat{\boldsymbol{e}}_3$. Assuming that the crack propagation is confined to the interface, the vector defining the growth driving direction must belong to the plane spanned by the tangential vectors $\hat{\boldsymbol{e}}_1$ and $\hat{\boldsymbol{e}}_2$ at the point $\overline{p}_i$ where the direction is evaluated. Thus, the three-dimensional problem, can be solved in a two-dimensional space defined by the local Cartesian coordinates (e_1, e_2), where e_l, with $l = 1, 2$, are the coordinates spanned by the unit vectors $\hat{\boldsymbol{e}}_l$.

Then, for any given distribution of $\mathcal{D}^e\,(e_1, e_2)$, the growth driving direction at any point on the midsurface is assumed normal to the damage isolines, following the discussion related to Figure 3.1, i.e. is given by the negative of the gradient vector:

$$-\nabla \mathcal{D}^e\,(e_1, e_2) \tag{3.1}$$

Growth driving direction criteria

The growth driving direction at any point $\overline{p}_i$, contained in $\overline{S}$, is defined in this work as the one that provides the largest rate of decrease of $\mathcal{D}^e$. This is the direction of the negative gradient of $\mathcal{D}^e$, defined in the local Cartesian coordinate system (e_1, e_2) with origin at $\overline{p}_i$ (see Equation (3.1)). However, polar coordinates are most appropriate when looking for a direction from a pole (See Figure 3.2). Thus, the growth driving direction can be found by identifying the angle φ that minimizes the slope of $\mathcal{D}^e$ with respect to the radial coordinate, ρ:

$$\min_{\varphi} \frac{\partial \mathcal{D}^e}{\partial \rho} \tag{3.2}$$

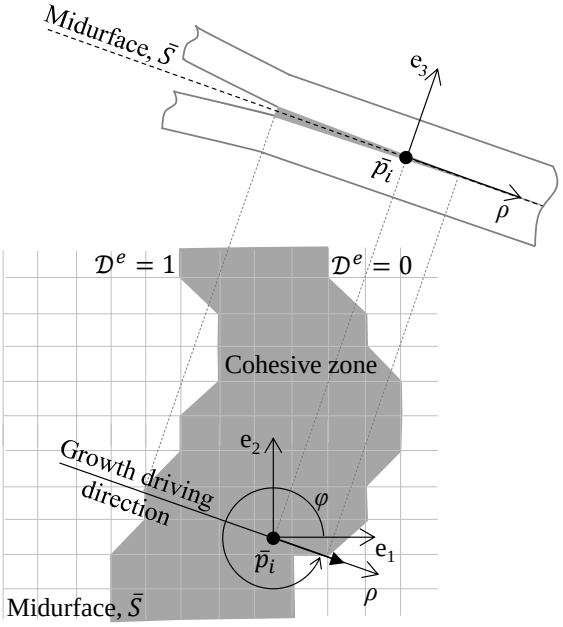

Fig. 3.2.: The growth driving direction evaluated at point $\overline{p}_i$ is embedded in the tangential plane spanned by the local Cartesian coordinates e_1 and e_2.

Considering the energy-based damage, $\mathcal{D}^e$, dependent on both the mode mixity, B, and the mixed-mode displacement jump, λ, and by application of the chain rule, the angle φ that minimizes Equation (3.2) can be found by solving:

$$\frac{\partial}{\partial \varphi}\frac{\partial \mathcal{D}^e\left(B,\lambda\right)}{\partial \rho} = \frac{\partial}{\partial \varphi}\left(\frac{\partial \mathcal{D}^e}{\partial B}\frac{\partial B}{\partial \rho} + \frac{\partial \mathcal{D}^e}{\partial \lambda}\frac{\partial \lambda}{\partial \rho}\right) = 0 \tag{3.3}$$

and by checking its convexity:

$$\frac{\partial^2}{\partial \varphi^2}\frac{\partial \mathcal{D}^e\left(B,\lambda\right)}{\partial \rho} = \frac{\partial^2}{\partial \varphi^2}\left(\frac{\partial \mathcal{D}^e}{\partial B}\frac{\partial B}{\partial \rho} + \frac{\partial \mathcal{D}^e}{\partial \lambda}\frac{\partial \lambda}{\partial \rho}\right) > 0 \tag{3.4}$$

However, equations (3.3) and (3.4) are equal to zero in the elastic regime ($\lambda \in [0, \lambda_o]$), since the energy based damage variable, $\mathcal{D}^e$, is also equal to zero (see Equation (2.33). In order to compute the growth driving direction before the initiation of the degradation process, another criterion, based on the ratio between the total specific work, ω_{tot} and the fracture toughness, $\mathcal{G}_c$, can be formulated such that the growth driving direction can be found by solving:

$$\min_{\varphi} \frac{\partial\left(\frac{\omega_{tot}}{\mathcal{G}_c}\left(B,\lambda\right)\right)}{\partial \rho} \tag{3.5}$$

Note that, similarly to the energy-based damage, $\mathcal{D}^e$, the ratio between the total specific work and the fracture toughness, $\frac{\omega_{tot}}{\mathcal{G}_c}$, is dependent on both the mode mixity, B, and the mixed-mode displacement jump, λ.

Finally, for the sake of simplicity, a third criterion, which is also active before damage initiation, can be formulated only taking into account the mixed-mode displacement jump field, λ:

$$\min_{\varphi} \frac{\partial \lambda}{\partial \rho} \tag{3.6}$$

The general expressions to solve for each of the criteria are listed in Appendix A.

In summary, three different criteria are presented depending on the quantity being analyzed: the energy-based damage, $\mathcal{D}^e$, (Criterion 1), the total specific work over the fracture toughness, $\frac{\omega_{tot}}{\mathcal{G}_c}$ (Criterion 2), and the mixed-mode displacement jump, λ, (Criterion 3). The evolution of these quantities along the growth driving direction are sketched in Figure 3.3 for an interface opened under pure mode I conditions. The three criteria are listed in Table 3.1 and presented in the following.

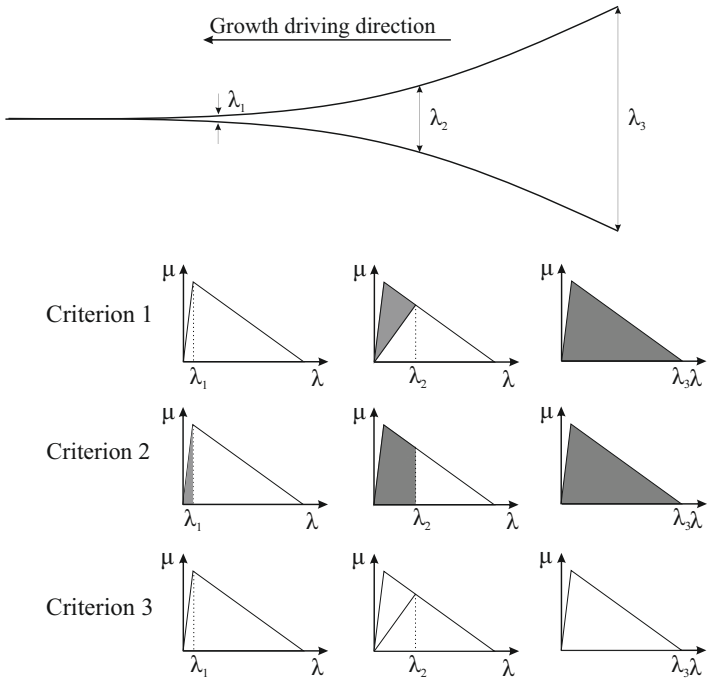

Fig. 3.3.: Quantities being minimized in each criterion for a pure mode I opened interface.

Criterion 1. The growth driving direction is defined by the negative gradient of the energy-based damage variable, $\mathcal{D}^e$. This is equivalent to computing the negative gradient of the ratio between the specific dissipated energy, ω_d (see Figure 2.10.b), and the fracture toughness, $\mathcal{G}_c$. Since Criterion 1 is based on the energy-based damage distribution, $\mathcal{D}^e$, it is only active once the degradation process is already initiated. Moreover, Criterion 1 is an energy-based approach that depends on the kinematics and the constitutive law of the cohesive element. Since the cohesive law

Tab. 3.1.: Summary of the criteria to determine the growth driving direction.

Criterion ID	Function to solve	Nomenclature	Approach	Limitations
1	$-\nabla\mathcal{D}^e$	$\mathcal{D}^e$: Energy-based damage	Energy-based	Not active in elastic regime
2	$-\nabla\frac{\omega_{tot}}{\mathcal{G}_c}$	ω_{tot}: total specific work $\mathcal{G}_c$: fracture toughness	Energy-based	May depend on the specific elastic energy in CZM
3	$-\nabla\lambda$	λ: mixed-mode opening displacement	Geometrical	Independent of interface properties

is usually mode-dependent, an uneven distribution of mode-mixity, B, can affect the gradient vector.

Criterion 2. The growth driving direction is defined by the negative gradient of the ratio between the total specific work, ω_{tot} (see Figure 2.10.c), and the fracture toughness, $\mathcal{G}_c$. Thus, both the specific dissipated energy, ω_d, and the specific elastic energy, ω_e, are included in the computation of Criterion 2. Since, as soon as two initially coinciding points separate from each other some elastic energy is stored, Criterion 2 is active before any energy dissipation due to fracture takes place. Moreover, this approach depends on both the kinematics and the constitutive law of the cohesive element and, therefore, can be affected by the variation in mode-mixity, B, with the direction.

It is worth to mention that, with the constitutive model used in this work, presented in 2.4, criteria 1 and 2 lead to the same growth driving direction results. However, since both the conservative and non-conservative work are computed in Criterion 2, in contrast to Criterion 1, in which only the non-conservative work is quantified, both criteria might provide different results when using other CZ formulations that allow the definition of mode-dependent penalty stiffness, K [169].

Criterion 3. The growth driving direction is defined by the negative gradient of the mixed-mode displacement jump, λ. This is a pure geometrical approach, since the only governing parameter is the mixed-mode displacement jump. Thus, the solution only depends on the kinematics of the cohesive element. Indeed, changes in the cohesive law due to variation in mode-mixity, B, with direction are not affecting Criterion 3.

Formulation of Criterion 1 for the identification of the growth driving direction

A complete description of the derivation of Criterion 1 is presented in this section. Moreover, the formulation for the evaluation of the growth driving direction using criteria 2 and 3 is given in Appendix A.

It can be seen, from equations (3.3) and (3.4), that, in order to find the growth driving direction using Criterion 1, the radial slope of the energy-based damage, $\frac{\partial \mathcal{D}^e}{\partial \rho}$, must be minimized as a function of the angle φ. Each of the terms in equations (3.3) and (3.4) are addressed in the following.

The derivative of the energy-based damage with respect to the mode mixity, $\frac{\partial \mathcal{D}^e}{\partial B}$, and the derivative of the energy-based damage with respect to the mixed-mode displacement jump, $\frac{\partial \mathcal{D}^e}{\partial \lambda}$, are expressed in equations (2.41) and (2.42).

Furthermore, the radial slope of the mixed-mode displacement jump, $\frac{\partial \lambda}{\partial \rho}$, in equations (3.3) and (3.4) is addressed in the following. Taking into account the dependency of the mixed-mode displacement jump, λ (Equation (2.23)), on the normal and tangential displacement jumps, arranged in vector δ_i, and by application of the chain rule, the following expression is obtained:

$$\frac{\partial \lambda}{\partial \rho} = \frac{\partial \lambda}{\partial \delta_j} \frac{\partial \delta_j}{\partial \rho} \tag{3.7}$$

The first term in the right hand side of Equation (3.7) reads:

$$\frac{\partial \lambda}{\partial \delta_j} = \left\{ \frac{\delta_1}{\lambda}, \frac{\delta_2}{\lambda}, \frac{\langle \delta_3 \rangle}{\lambda} \right\}^T = A_j \tag{3.8}$$

and the second term in the right hand side of Equation (3.7) is the derivative of the displacement jumps, δ_j, with respect to the radial coordinate, ρ, which is obtained as follows:

$$\frac{\partial \delta_j}{\partial \rho} = \frac{\partial \Theta_{ji}}{\partial \rho} M_{im} Q_m + \Theta_{ji} \frac{\partial M_{im}}{\partial \rho} Q_m \tag{3.9}$$

where Θ_{ji} is the rotation matrix that relates the global to the local Cartesian coordinate system and M_{im} is the transformation matrix that relates the global displacement jump with the nodal global displacement, Q_m.

The derivative of the rotation matrix, Θ_{ji}, with respect to the radial coordinate, ρ, can be approximated to zero, by assuming that the curvature of the interface within the element domain is small. Moreover, its derivation leads to a complex expression that would increase the difficulty of the formulation and its further implementation into FE without a substantial improvement in the accuracy of the solution. For the sake of simplicity, in the following it is assumed that $\frac{\partial \Theta_{ji}}{\partial \rho} = 0$. Therefore, only the second summand in the right hand side of Equation (3.9) is addressed.

The derivative of the transformation matrix, M_{im}, with respect to the local polar coordinate, ρ, is obtained by successive application of the chain rule:

$$\frac{\partial M_{im}}{\partial \rho} = \frac{\partial M_{im}}{\partial \eta_\alpha} \frac{\partial \eta_\alpha}{\partial e_l} \frac{\partial e_l}{\partial \rho} \tag{3.10}$$

The first partial derivative in the right hand side of Equation (3.10) is the variation of the transformation matrix, M_{im}, with the isoparametric coordinates of the cohesive element formulation, η_α:

$$\frac{\partial M_{im}}{\partial \eta_\alpha} = \left[-\frac{\partial N_{ik}}{\partial \eta_\alpha},\ \frac{\partial N_{ik}}{\partial \eta_\alpha} \right] = E_{im\alpha} \tag{3.11}$$

where N_{ik} is the shape function matrix and the subscript k runs from 1 to the number of degrees of freedom of each of top and bottom surface of the cohesive element. In case of an eight-noded element, $k = 1...12$.

The derivative $\frac{\partial \eta_\alpha}{\partial e_l}$ is the inverse matrix of the two vectors tangential to the deformed midsurface, described in Equation (2.20) and expressed in local tangential coordinates, these being:

$$\frac{\partial e_l}{\partial \eta_\alpha} = \Theta_{li} \frac{1}{2} \frac{\partial N_{ik}}{\partial \eta_\alpha} \left(C_k^+ + C_k^- + Q_k^+ + Q_k^- \right) = \Theta_{li} \mathcal{J}_{i\alpha} \tag{3.12}$$

where $\mathcal{J}_{i\alpha}$ is the Jacobian matrix defined in Equation (2.63). Thus, let matrix $G_{\alpha l}$ be defined as:

$$G_{\alpha l} = (\Theta_{li} \mathcal{J}_{i\alpha})^{-1} = \begin{bmatrix} \frac{\partial \eta_1}{\partial e_1} & \frac{\partial \eta_2}{\partial e_1} \\ \frac{\partial \eta_1}{\partial e_2} & \frac{\partial \eta_2}{\partial e_2} \end{bmatrix} \tag{3.13}$$

Using the following transformation relation:

$$\begin{bmatrix} e_1 \\ e_2 \end{bmatrix} = \begin{bmatrix} \rho\ \cos(\varphi) \\ \rho\ \sin(\varphi) \end{bmatrix} \tag{3.14}$$

the derivative of the local Cartesian coordinates, e_l, with respect to the radial coordinate, ρ, reads:

$$\frac{\partial e_l}{\partial \rho} = \begin{bmatrix} \cos(\varphi) \\ \sin(\varphi) \end{bmatrix} \tag{3.15}$$

Then, the slope of the mixed-mode displacement jump, λ, with respect to the radial coordinate, ρ, is obtained using equations (3.8)-(3.15) in Equation (3.7):

$$\frac{\partial \lambda}{\partial \rho} = A_j \Theta_{ji} E_{im\alpha} \left(G_{\alpha 1} \left(\cos \varphi \right) + G_{\alpha 2} \left(\sin \varphi \right) \right) Q_m \tag{3.16}$$

The same procedure can be applied to find the radial slope of the mode mixity, $\frac{\partial B}{\partial \rho}$, in equations (3.3) and (3.4). Taking into account the dependency of the mode mixity, B, defined in Equation (2.26), on the displacement jumps, δ_j, the radial slope $\frac{\partial B}{\partial \rho}$ is obtained by applying the chain rule as:

$$\frac{\partial B}{\partial \rho} = \frac{\partial B}{\partial \delta_j} \frac{\partial \delta_j}{\partial \rho} \tag{3.17}$$

where the derivative of the mode mixity, B, with respect to the displacement jumps, δ_j, reads:

$$\frac{\partial B}{\partial \delta_j} = \left\{ \frac{2\delta_1 \langle \delta_3 \rangle^2}{\lambda^4}, \ \frac{2\delta_2 \langle \delta_3 \rangle^2}{\lambda^4}, \ -\frac{2\delta_s^2 \langle \delta_3 \rangle}{\lambda^4} \right\}^T = O_j \tag{3.18}$$

and $\frac{\partial \delta_j}{\partial \rho}$ is developed through equations (3.9)-(3.15). Hence, the radial slope $\frac{\partial B}{\partial \rho}$ is given by:

$$\frac{\partial B}{\partial \rho} = O_j \Theta_{ji} E_{im\alpha} \left(G_{\alpha 1} \left(\cos \varphi \right) + G_{\alpha 2} \left(\sin \varphi \right) \right) Q_m \tag{3.19}$$

Finally, let matrix V_α be:

$$V_\alpha = F_B O_j \Theta_{ji} E_{im\alpha} Q_m \tag{3.20}$$

and matrix W_α be:

$$W_\alpha = F_\lambda A_j \Theta_{ji} E_{im\alpha} Q_m \tag{3.21}$$

then, the growth driving direction according to Criterion 1 is found using equations (3.16) and (3.19)-(3.21) in Equation (3.3), solving for the angular coordinate, φ:

$$\varphi = \text{atan}\left(-\frac{(V_1 + W_1)\, G_{11} + (V_2 + W_2)\, G_{21}}{(V_1 + W_1)\, G_{12} + (V_2 + W_2)\, G_{22}}\right) \tag{3.22}$$

and fulfilling the condition for convexity (Equation (3.4)):

$$(V_\alpha + W_\alpha)\left(G_{\alpha 1}\left(-\cos\varphi\right) + G_{\alpha 2}\left(-\sin\varphi\right)\right) > 0 \tag{3.23}$$

Once φ is identified, the transformation of the global Cartesian coordinates, X_i, into the local Cartesian coordinates that are located on the midsurface and oriented according to the growth driving direction is done by means of the following rotation matrix:

$$R_{ri} = T_{rj} \Theta_{ji} \tag{3.24}$$

where T_{rj} is:

$$T_{rj} = \begin{bmatrix} \cos\varphi & -\sin\varphi & 0 \\ \sin\varphi & \cos\varphi & 0 \\ 0 & 0 & 1 \end{bmatrix} \tag{3.25}$$

As shown, all the information necessary to evaluate Criterion 1 (and also criteria 2 and 3, as demonstrated in Appendix A) are the global nodal coordinates, C_m and displacements Q_m. Using the cohesive element formulation in [167, 168], this information is available at the element level and, thus, the presented growth driving direction algorithms can be implemented into a user-defined element subroutine and evaluated at any point in the cohesive zone without any additional post-processing or non-local information.

3.1.2 One-element validation examples

The following one-element studies serve to validate the formulation of the growth driving direction criteria presented in Section 3.1.1. The proposed method has been implemented in a MATLAB program. The eight-noded cohesive element used is illustrated in Figure 2.11. The kinematics and constitutive law associated to the element are detailed in 2.4. Newton-Cotes integration scheme is used, with 2x2 integration points located at the midsurface vertexes. The undeformed element is 0.1 mm wide, 0.1 mm long and has zero thickness. The cohesive properties are listed in Table 3.2. Three different loading cases (A, B and C) have been analyzed. The applied nodal displacements are listed in Table 3.3 for each case. The growth driving direction is calculated at a point $\overline{\boldsymbol{p}}\,(\eta_1, \eta_2)$ located on the midsurface, with natural coordinates $(-0.5, -0.5)$. The results of the angle φ obtained in each case are listed in Table 3.3 for the three criteria.

Case A is a pure mode I-opened element. The distribution of the mixed-mode displacement jump, λ, along the element midsurface is projected on the deformed element midsurface in Figure 3.4, where the point $\overline{\boldsymbol{p}}$ is highlighted in white. Integation points 1 and 2 have the lowest λ value, while points 3 and 4 are the most opened. As illustrated, the growth driving direction according to Criterion 3 is determined by the greatest rate of decrease of λ. The other quantities being analyzed in criteria

Tab. 3.2.: Cohesive law properties used in the one-element case studies.

Interface properties		
$\mathcal{G}_{Ic}$: Mode I fracture toughness	0.3	N/mm
$\mathcal{G}_{IIc}$: Shear mode fracture toughness	0.7	N/mm
τ_{Ic}: Mode I interlaminar strength	50	MPa
τ_{IIc}: Shear mode interlaminar strengths	76.4	MPa
η: Benzeggagh-Kenane's interpolation parameter [29]	2	-
K: penalty stiffness	1E5	N/mm^3

Tab. 3.3.: Loading conditions and growth driving direction results at point $\overline{\boldsymbol{p}}$ from the one-element case studies.

Case ID	Loading conditions	Nodal displacements (mm)	φ at point $\overline{\boldsymbol{p}}$ (deg) Crit. 1	Crit. 2	Crit. 3
A	Pure mode I B constant	$u_3^5 = 0.005$ $u_3^6 = 0.005$ $u_3^7 = 0.01$ $u_3^8 = 0.01$	270.0	270.0	270.0
B	Mixed mode I-shear B constant	$u_1^5 = u_2^5 = u_3^5 = 0.001$ $u_1^6 = u_2^6 = u_3^6 = 0.002$ $u_1^7 = u_2^7 = u_3^7 = 0.003$ $u_1^8 = u_2^8 = u_3^8 = 0.002$	225.3	225.3	225.3
C	Mixed mode I-shear same λ at nodes	$u_1^5 = \sqrt{2 \cdot 0.008}$ $u_1^6 = u_3^6 = 0.008$ $u_3^7 = \sqrt{2 \cdot 0.008}$ $u_1^8 = u_3^8 = 0.008$	225.0	225.0	45.0

1 and 2, $\mathcal{D}^e$ and $\frac{\omega_{tot}}{\mathcal{G}_c}$ respectively, are represented in Figure 3.5, as well as the mode-mixity, B. Like the B-distribution along the element midsurface is constant, the growth driving direction is only defined by the direction that minimizes the slope of the mixed-mode displacement jump. Therefore, in Case A only, the kinematics of the element governs the growth driving direction, independently of which criteria is used.

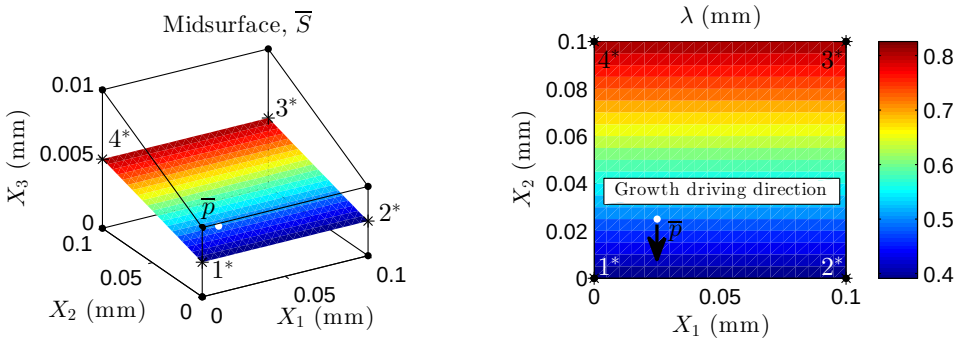

Fig. 3.4.: Mixed-mode displacement jump distribution at the element midsurface for Case A loading conditions. The growth driving direction is analyzed at point $\overline{p}$, indicated with a white circle, and the result is listed in Table 3.3.

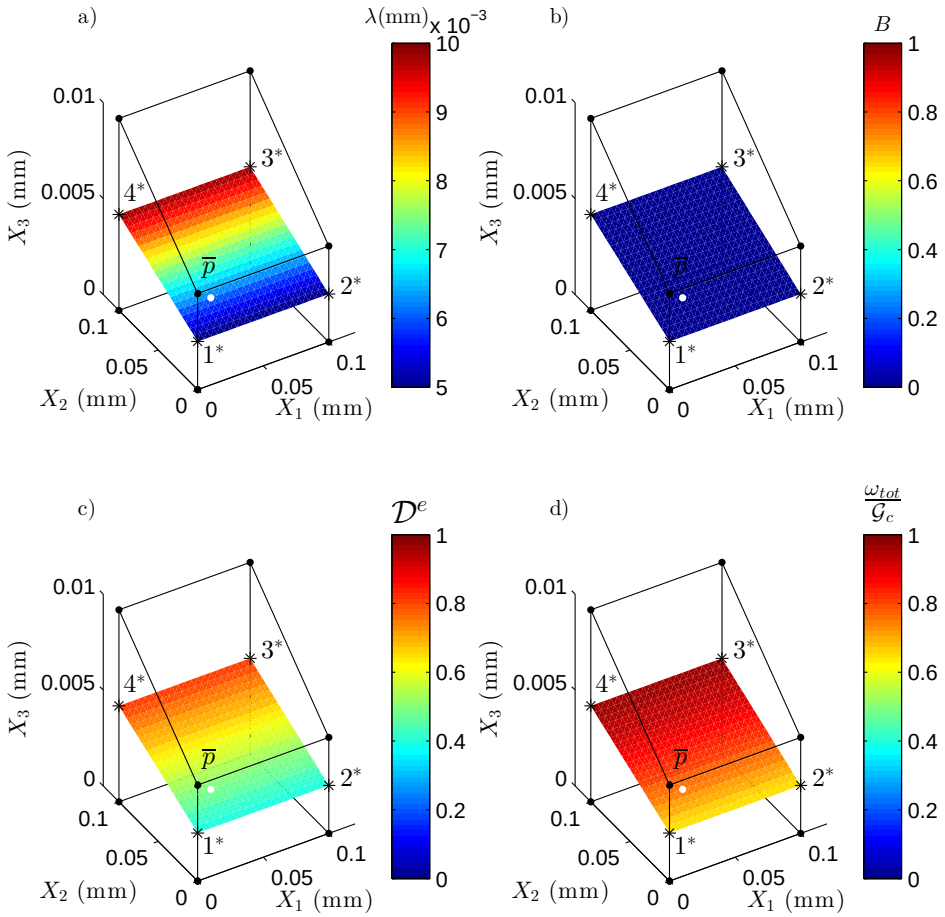

Fig. 3.5.: a) Mixed-mode displacement jump, λ, b) mode-mixity, B, c) energy-based damage, $\mathcal{D}^e$, and d) total specific work over the fracture toughness, $\frac{\omega_{tot}}{\mathcal{G}_c}$, distributions at the element midsurface for Case A loading conditions. The point $\overline{\boldsymbol{p}}$, where the growth driving direction is analyzed, is indicated with a white circle.

On the other hand, in Case B, the element is opened under constant mixed mode I-shear opening conditions (See Figure 3.6). In this case, λ linearly increases along the midsurface diagonal direction, from integration point 1 to integration point 3. However, B is constant and, thus, also the constitutive law associated to it. Again, in Case B, the growth driving direction is only defined by the direction that minimizes the slope of the mixed-mode displacement jump, λ. Therefore, it is governed by the kinematics of the cohesive element and there is agreement between the three criteria.

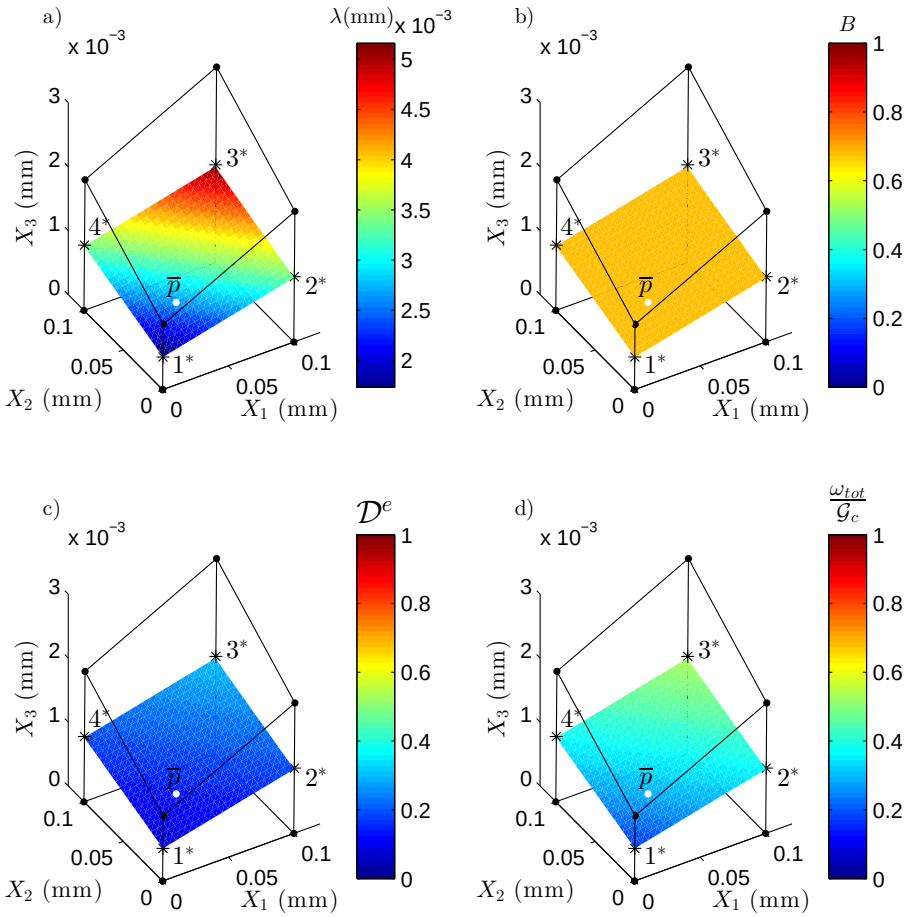

Fig. 3.6.: a) Mixed-mode displacement jump, λ, b) mode-mixity, B, c) energy-based damage, $\mathcal{D}^e$, and d) total specific work over the fracture toughness, $\frac{\omega_{tot}}{\mathcal{G}_c}$, distributions at the element midsurface for Case B loading conditions. The point $\overline{\boldsymbol{p}}$, where the growth driving direction is analyzed, is indicated with a white circle.

Finally, in Case C, all the integration points have the same λ-value, although the mode-mixity, B, changes from 0 to 1 along the midsurface diagonal direction (See Figure 3.7). At integration point 1, only shear sliding displacement is applied, while at the opposite corner, at integration point 3, there is only mode I opening. At the integration points 2 and 4, there is 50% mixed-mode opening. On the other hand, λ is lower at the center part of the element midsurface than at the corners and its distribution is determined by the interpolation functions. Criterion 3 is only affected by the λ-interpolation and results in the direction that points to the center of the element. Furthermore, due to the uneven B-distribution, the constitutive law is not constant. With the cohesive properties used in these studies, the direction of steepest negative slopes of $\mathcal{D}^e$ and $\frac{\omega_{tot}}{\mathcal{G}_c}$ coincides with the direction that maximizes the rate of increase of B. Note that, when evaluated at point $\overline{\boldsymbol{p}}$, this is the direction of largest slope of λ. Therefore, Criterion 3 and criteria 1 and 2 point to opposite directions.

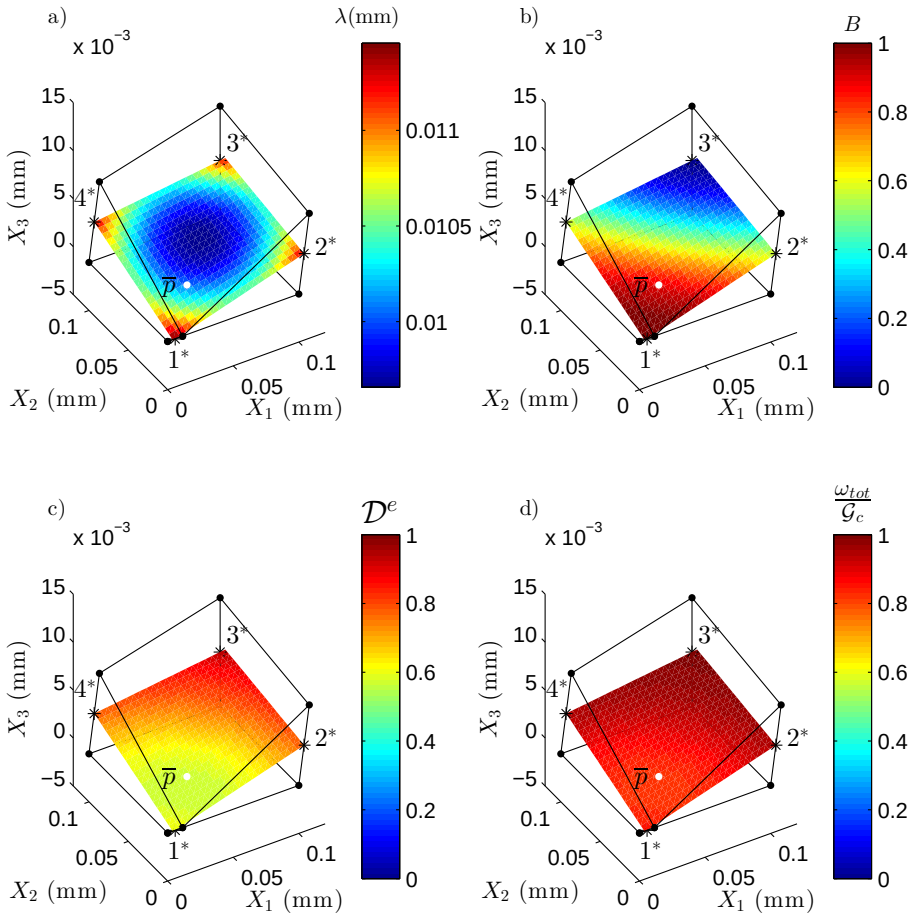

Fig. 3.7.: a) Mixed-mode displacement jump, λ, b) mode-mixity, B, c) energy-based damage, $\mathcal{D}^e$, and d) total specific work over the fracture toughness, $\frac{\omega_{tot}}{\mathcal{G}_c}$, distributions at the element midsurface for Case C loading conditions. The point $\overline{\boldsymbol{p}}$, where the growth driving direction is analyzed, is indicated with a white circle.

In addition, the slopes $\frac{\Delta \mathcal{D}^e}{\Delta \rho}$, $\frac{\Delta(\omega_{tot}/\mathcal{G}_c)}{\Delta \rho}$ and $\frac{\Delta \lambda}{\Delta \rho}$ have been numerically evaluated using a central difference at every 1 degree at point $\overline{\boldsymbol{p}}$ under Case C loading conditions using a perturbation size for the radius of ρ =0.001 mm. Thus, the slope of any quantity $f(\rho, \varphi)$ has been calculated as:

$$\frac{\Delta f}{\Delta \rho} = \frac{f(0.001, \varphi) - f(-0.001, \varphi)}{2 \cdot 0.001} \tag{3.26}$$

The resulting slopes are represented in Figure 3.8. The disagreement between Criterion 3 and criteria 1 and 2 can be observed. For Criterion 3, the angle φ that minimizes $\frac{\Delta \lambda}{\Delta \rho}$ is 45 degrees, while for criteria 1 and 2, the angle that minimizes $\frac{\Delta \mathcal{D}^e}{\Delta \rho}$ and $\frac{\Delta(\omega_{tot}/\mathcal{G}_c)}{\Delta \rho}$, respectively, amounts 225 degrees. Note that these results are in agreement with the results obtained by implementing the formulation developed in Section 3.1.1.

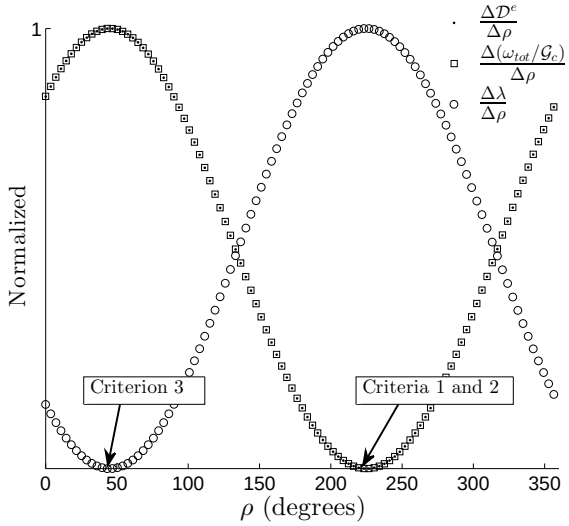

Fig. 3.8.: Slopes in the radial direction, ρ, of the energy-based damage, $\mathcal{D}^e$, the total specific work over the fracture toughness, $\frac{\omega_{tot}}{\mathcal{G}_c}$, and the mixed-mode displacement jump, λ, as a function of the angle φ evaluated at point $\overline{\boldsymbol{p}}$ for Case C loading conditions. The slopes have been calculated using a central difference with a perturbation for the radius of 0.001 mm. The values $\frac{\Delta \mathcal{D}^e}{\Delta \rho}$, $\frac{\Delta(\omega_{tot}/\mathcal{G}_c)}{\Delta \rho}$ and $\frac{\Delta \lambda}{\Delta \rho}$ have been normalized by their maximum value.

Tab. 3.4.: Laminate properties used in the partially reinforced ELS simulation study.

Laminate properties		
E_{11}: Longitudinal Young's modulus	154	GPa
$E_{22} = E_{33}$: Transversal Young's modulus	8.5	GPa
$G_{12} = G_{13}$: Shear modulus in the longitudinal planes	4.2	GPa
G_{23}: Shear modulus in the transversal plane	3.036	GPa
$\mu_{12} = \mu_{13}$: Poison's coefficient in the longitudinal planes	0.35	-
μ_{23}: Poison's coefficient in the transversal plane	0.4	-

Tab. 3.5.: Interface properties used in the partially reinforced ELS simulation study. The nomenclature of the interface properties is defined in 2.4.

Interface properties		
$\mathcal{G}_{Ic}$: Mode I fracture toughness	0.3	N/mm
$\mathcal{G}_{IIc}$: Shear mode fracture toughness	3	N/mm
τ_{Ic}: Mode I interlaminar strength	10	MPa
τ_{IIc}: Shear mode interlaminar strengths	31.62	MPa
η: Benzeggagh-Kenane's interpolation parameter [29]	2	-
K: penalty stiffness	1E5	N/mm^3

3.1.3 Three-Dimensional application

To exemplify the applicability of the presented formulation, a three-dimensional model with a non-straight crack front is used. The test configuration is a End-Loaded Split (ELS) test on a symmetric run-out specimen with a midplane initial defect. A Teflon insert acts as an initial straight delamination (see Figure 3.9). Moreover, the middle width of the specimen is stiffened by bonding CFRP reinforcements on the upper and lower faces. During propagation, the crack front shape changes when it approaches the reinforced region. The formulation presented in Section 3.1.1 can be used to evaluate the growth driving criteria at any given loading state during the quasi-static simulation. To this end, the method in [167, 168] has been enhanced with the growth driving direction calculation and implemented in ABAQUS [160] as a UEL subroutine. The user-defined cohesive elements that model the middle interface are 0.2 mm x 0.5 mm. The laminate and interface properties used in the simulation are listed in tables 3.4 and 3.5.

The historical evolution of the 0.5-valued damage isoline is plotted in Figure 3.10.a. The energy-based damage, $\mathcal{D}^e$, distribution is projected on the deformed midsurface,

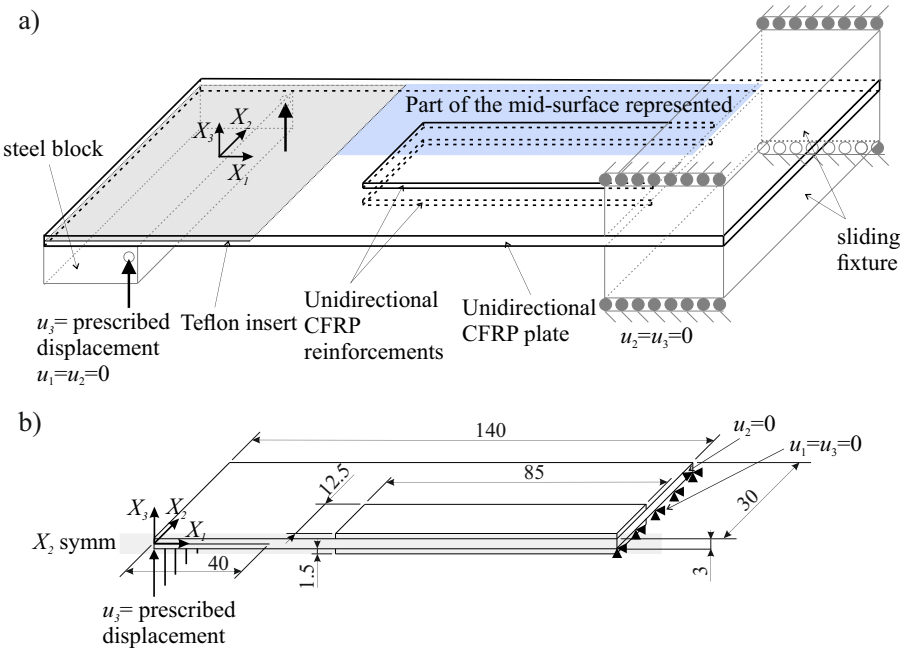

Fig. 3.9.: a) Sketch of the partially reinforced ELS specimen. The grey-shadowed area represents the Teflon insert. The blue-shadowed area is the area represented in figures 3.10.b, 3.11 and 3.16. b) Simplified model for FE simulation and dimensions (units in mm).

in Figure 3.10.c, for a prescribed displacement of 32.55 mm. Only the blue-shadowed area in Figure 3.9 is represented. The crack growth direction is evaluated at each integration point within the FPZ using criteria 1, 2 and 3, and represented in Figure 3.11. Note that criteria 1 (Figure 3.11.a) and 2 (Figure 3.11.b) are coincident except from at the elastic region, where no results from Criterion 1 can be obtained. By comparison of figures 3.11.b and 3.11.c, it can be observed that Criterion 3 only differs from criteria 1 and 2 at a region located at the upper left part of the cohesive zone ($X_1 < 85$ mm and $X_2 > 10$ mm). Indeed, the mode-mixity, B, is constant and equal to 1 in the entire cohesive zone, except for this region, where it locally decreases to 0.6 (see Figure 3.11.d). As demonstrated in Section 3.1.2, under constant B conditions, the growth driving direction is only governed by the kinematics of the cohesive elements. Therefore, evaluating any of the three criteria results in the same growth driving direction solution. On the other hand, only criteria 1 and 2 are affected by changes in the mode-dependent constitutive law, leading to

different results, if compared to Criterion 3, at the region where the mode-mixity, B, varies.

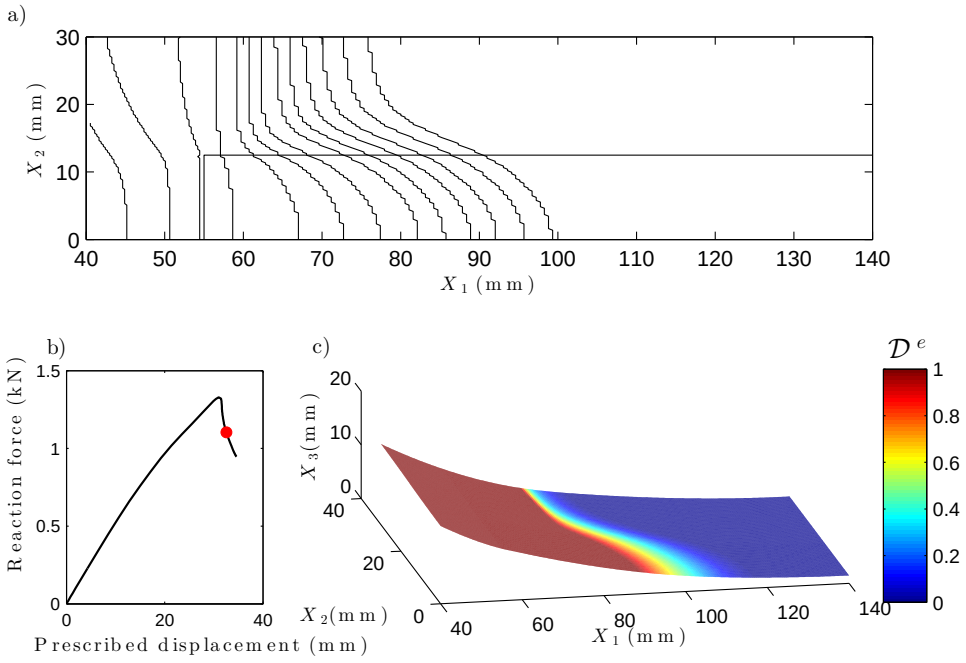

Fig. 3.10.: a) Historical evolution of the 0.5-valued damage isoline. b) Reaction force vs prescribed displacement curve with the current loading state highlighted in red. c) Energy-based damage projected on the deformed midsurface.

In addition, four damage isolines have been traced. The damage isolines are constructed by connecting integration points with the same damage value. The first damage isoline, represented in Figure 3.12.a, is the line connecting the completely damaged integration points adjacent to the damage process zone. At each point on the damage isoline, the geometrical normal direction has been approximated by the normal to the slope of a second degree polynomial expression fitted to five consecutive points represented in white in Figure 3.12.a): the current point and the two preceding and the two succeeding points. Therefore, the approximated normal direction is computed by post-processing global information and it is heavily affected by the discretization and the choice of the fitting function. The results are compared to the local growth driving direction criteria developed in Section 3.1.1 in Figure 3.12.b. The same analysis is done with a 0.5-valued damage isoline (Figure 3.13),

a 0.1-valued damage isoline (Figure 3.14) and the line connecting the undamaged integration points adjacent to the damage process zone (Figure 3.15). Note that, although for comparison purposes the growth driving direction is evaluated in a discrete manner at the same points where the approximated normal direction is computed, it is a continuous field that can be evaluated at any point, as shown in Figure 3.11.

Finally, three different FE models with element sizes 0.5 x 0.2 mm, 1 x 1.25 mm and 2.5 x 2.5 mm (see Figure 3.16) are used to compare the element size effect on both the approximated normal direction to the 1-valued damage isoline, evaluated by using global information, and the predicted growth driving direction using Criterion 1, evaluated point-wise at the element level. The results are obtained using the information of the points on the 1-valued damage isoline traced in Figure 3.17 for the three meshes. The direction obtained along the damage isoline using both methods is plotted in Figure 3.18.

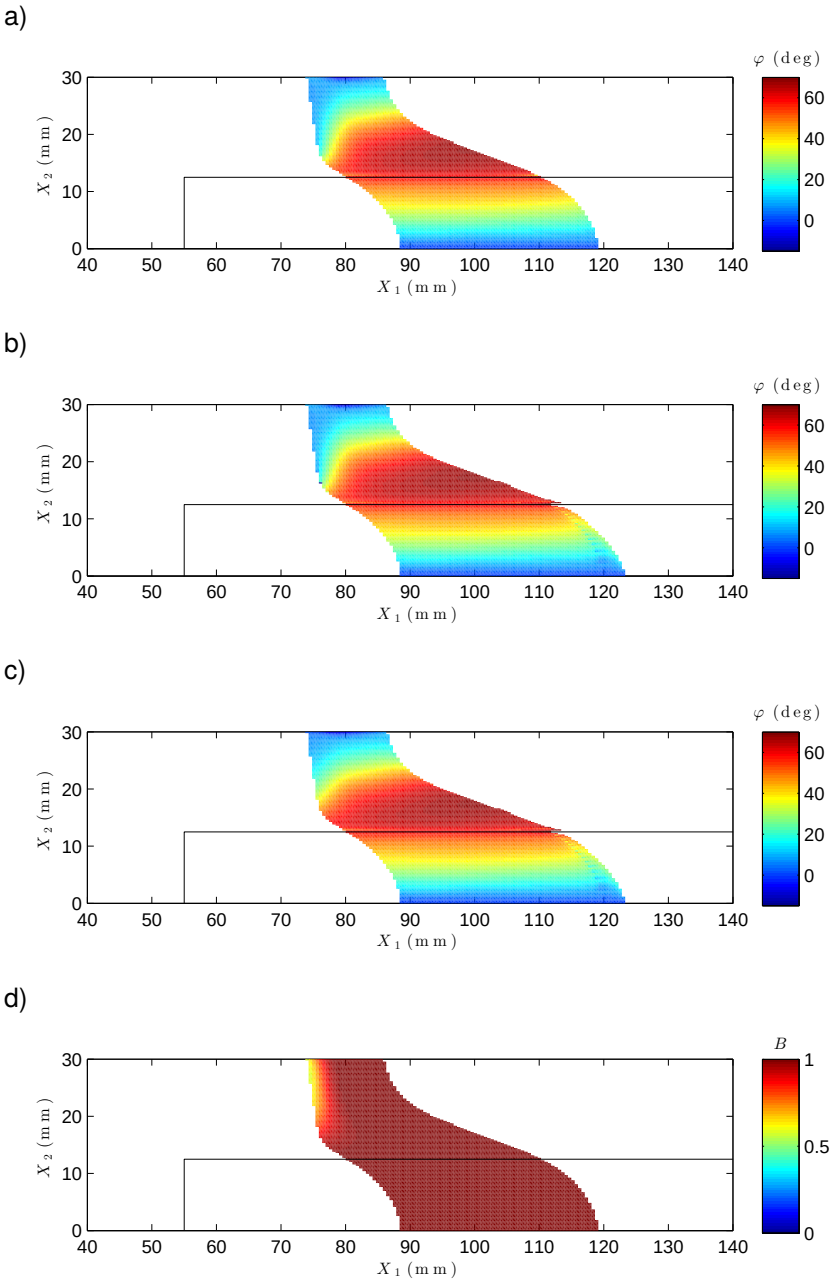

Fig. 3.11.: a) Growth driving direction resulting from the evaluation of Criterion 1. b) Growth driving direction resulting from the evaluation of Criterion 2. c) Growth driving direction resulting from the evaluation of Criterion 3. d) Mode mixity, B. The black line marks the reinforcements.

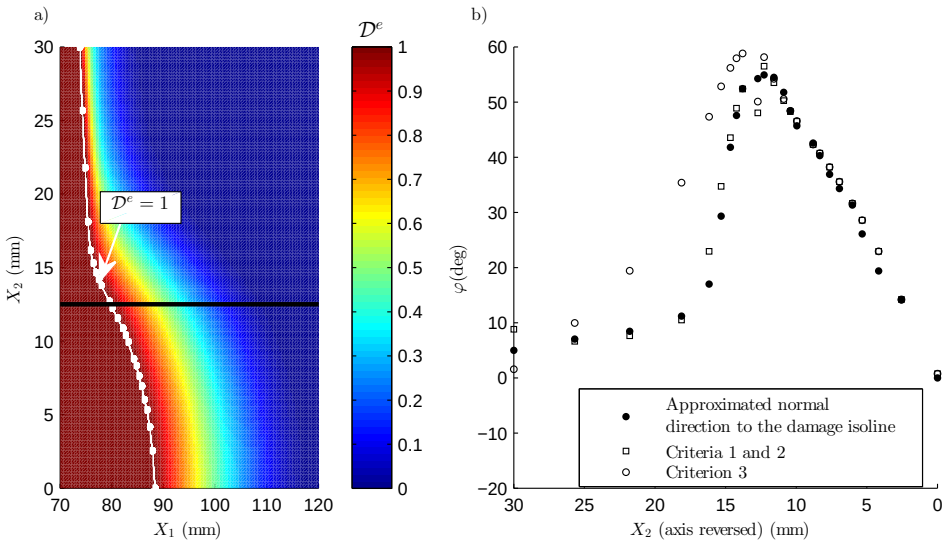

Fig. 3.12.: a) Energy-based damage, $\mathcal{D}^e$, distribution along the cohesive zone. The points forming the 1-valued damage isoline are highlighted in white. The thick black solid line marks the reinforcements border. b) Comparison of the angle φ obtained at the 1-valued damage front by computing the normal direction using global information and by locally evaluating the growth driving direction criteria. Criteria 1 and 2 are represented by the same marker because they lead to identical growth driving direction results.

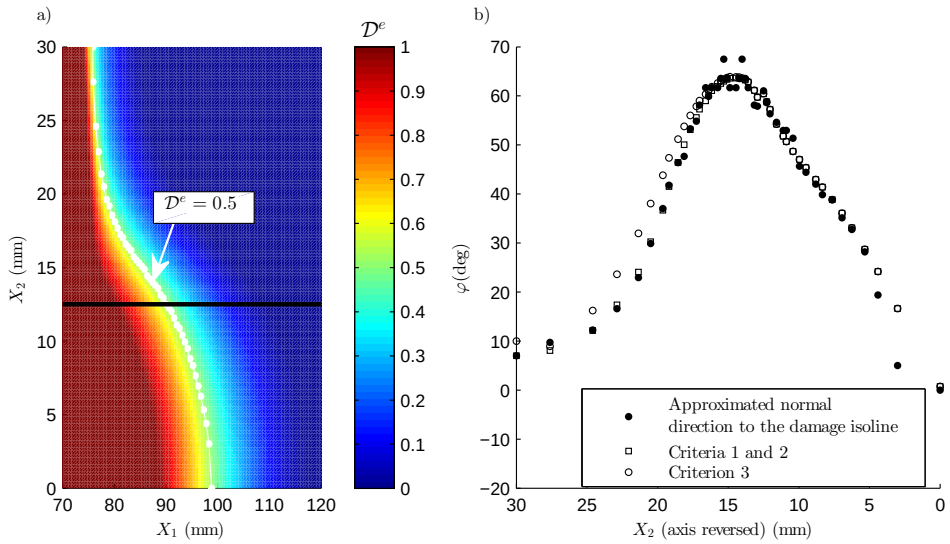

Fig. 3.13.: a) Energy-based damage, $\mathcal{D}^e$, distribution along the cohesive zone. The points forming the 0.5-valued damage isoline are highlighted in white. The thick black solid line marks the reinforcements border. b) Comparison of the angle φ obtained at the 0.5-valued damage front by computing the normal direction using global information and by locally evaluating the growth driving direction criteria. Criteria 1 and 2 are represented by the same marker because they lead to identical growth driving direction results.

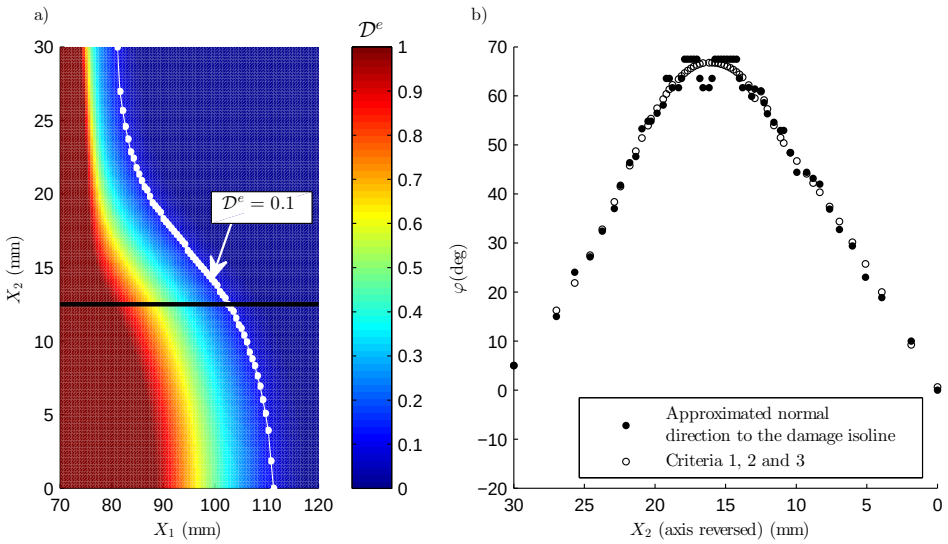

Fig. 3.14.: a) Energy-based damage, $\mathcal{D}^e$, distribution along the cohesive zone. The points forming the 0.1-valued damage isoline are highlighted in white. The thick black solid line marks the reinforcements border. b) Comparison of the angle φ obtained at the 0.1-valued damage front by computing the normal direction using global information and by locally evaluating the growth driving direction criteria. Criteria 1, 2 and 3 are represented by the same marker because they lead to identical growth driving direction results.

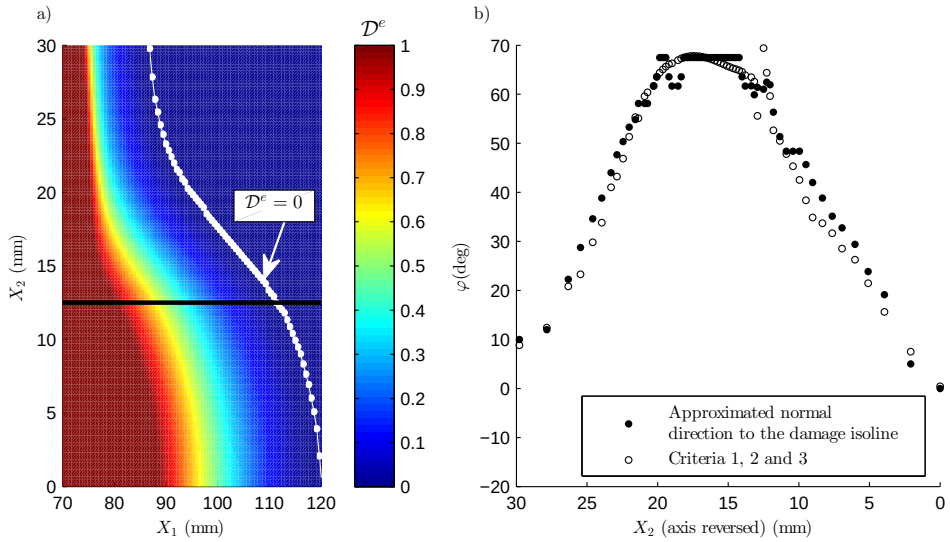

Fig. 3.15.: a) Energy-based damage, $\mathcal{D}^e$, distribution along the cohesive zone. The points forming the line connecting the undamaged integration points adjacent to the damage process zone are highlighted in white. The thick black solid line marks the reinforcements border. b) Comparison of the angle φ obtained at the 0-valued damage front by computing the normal direction using global information and by locally evaluating the growth driving direction criteria. Criteria 1, 2 and 3 are represented by the same marker because they lead to identical growth driving direction results.

a) Element size: 0.5 x 0.2 mm

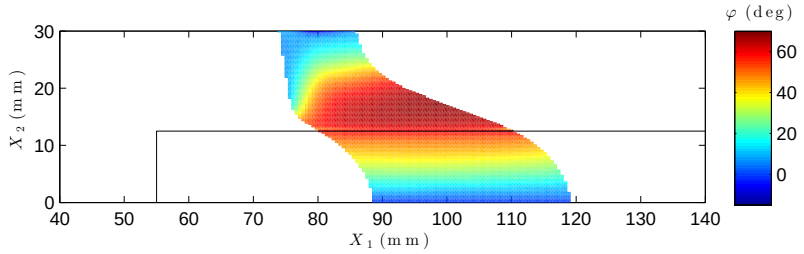

b) Element size: 1 x 1.25 mm

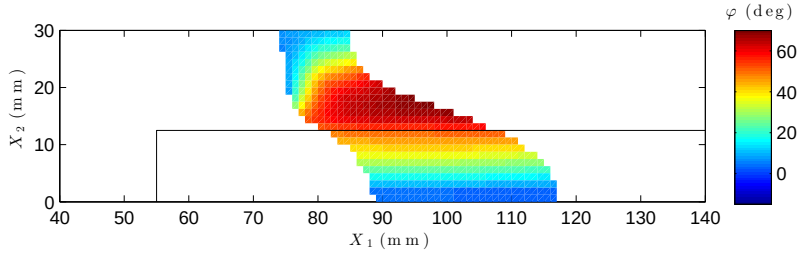

c) Element size: 2.5 x 2.5 mm

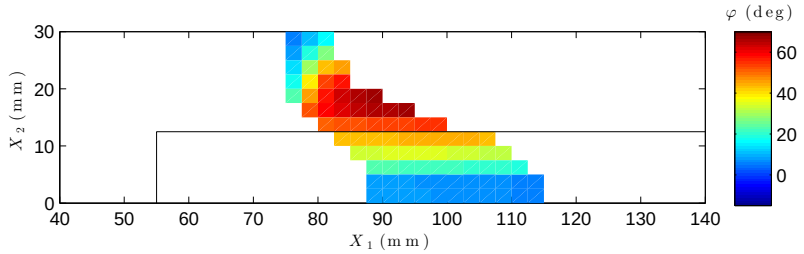

Fig. 3.16.: Growth driving direction resulting from the evaluation of Criterion 1 using three different element sizes.

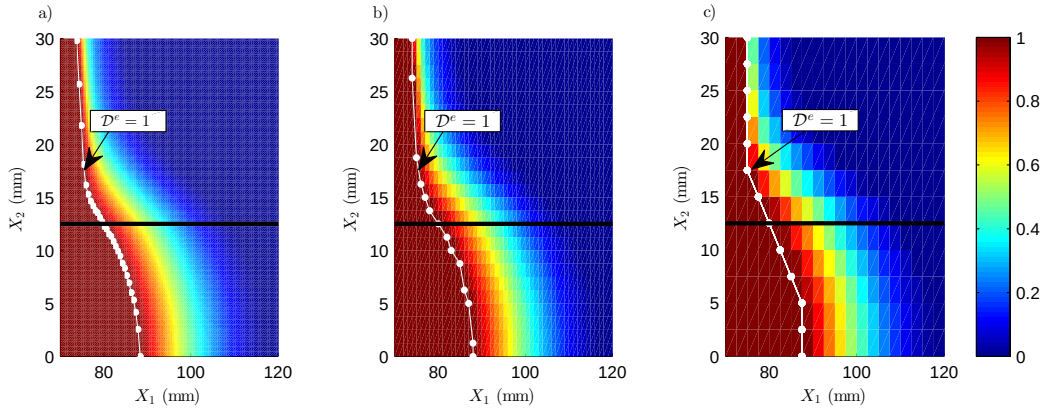

Fig. 3.17.: 1-valued damage fronts using different element sizes: a) 0.2 x 0.5 mm. b) 1 x 1.25 mm. c) 2.5 x 2.5 mm.

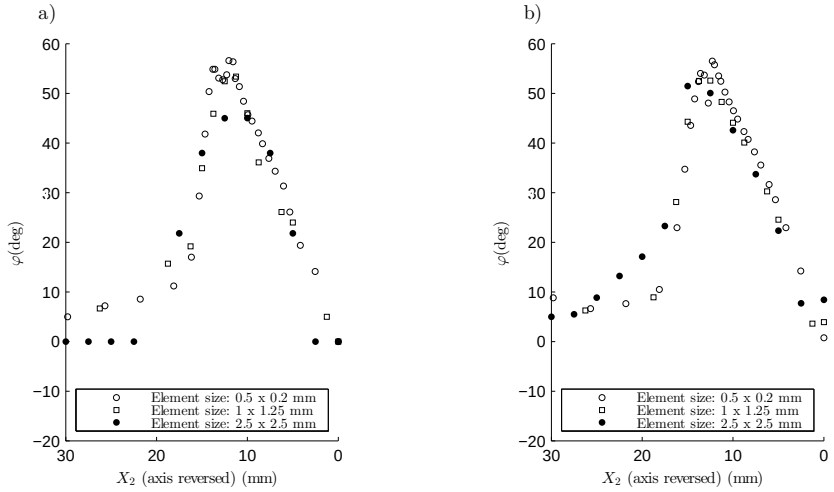

Fig. 3.18.: Comparison of the angle φ obtained at the 1-valued damage isoline using three different element sizes by a) computing the normal direction to the crack front using global information and b) evaluating Criterion 1.

3.1.4 Discussion

Three different growth driving direction criteria have been proposed as element-level algorithms, that can be evaluated at any point within the cohesive zone. Criteria 1 and 2 are energetically-based formulations that account for both the kinematics and the constitutive law of the interface element. On the other hand, Criterion 3 is a geometrical approach, which only accounts for the kinematics of the interface element. Therefore, when the mode-mixity, B, is not constant, criteria 1 and 2 are the most appropriate. Moreover, Criterion 2 computes the rate of decrease of both the specific elastic energy, ω_e, and the dissipated energy, ω_d, normalized to the fracture toughness, $\mathcal{G}_c$. On the contrary, Criterion 1 only computes the rate of decrease of the dissipated energy, ω_d, normalized to the fracture toughness, $\mathcal{G}_c$, which is equivalent to computing the rate of decrease of the energy-based damage, $\mathcal{D}^e$. On this basis, Criterion 1 is not active before damage initiation, while Criterion 2 can be computed as soon as some separation between two initially coinciding points at the interface occurs. The three criteria have been presented for completeness, since they can be developed for other CZM formulations following the methodology described in Section 3.1.1. With the CZM used in this work, criteria 1 and 2 lead to the same growth driving direction solution at the damaged region. However, different results may be obtained if a mode-dependent penalty-stiffness is used, which could render the specific elastic energy of Criterion 2 dependent on growth driving direction.

The implementation of the formulation for the proposed growth driving direction criteria has been validated with one-element case studies in Section 3.1.2. The distribution of the quantities being analyzed have been projected on the element midsurface for visual verification (see figures 3.5-3.7 for different loading cases). In addition, the slopes of such quantities have been numerically evaluated at different orientations around a given evaluation point under Case C loading conditions (Figure 3.8). The orientation that results in lowest slopes coincides with the angle of growth driving direction predicted by each criteria, respectively.

Finally, the capabilities of the presented formulation are demonstrated in Section 3.1.3 using a three-dimensional run-out specimen loaded under ELS test conditions (Figure 3.9). The crack front propagates with non-straight shape due to the reinforcements bonded at the middle width of the specimen Figure 3.10. The growth driving direction criteria are evaluated at all the integration points within the cohesive

zone for a given loading state with large deformations (Figure 3.11). The results from the three criteria differ only at those regions where the mode-mixity, B, is not constant, as already demonstrated in Section 3.1.2. Moreover, the resulting crack growth driving direction is compared with the geometrical normal direction of four different damage isolines computed by post-processing global information (figures 3.12-3.15). Both results are in good agreement, although the agreement is higher between the geometrical normal direction to the damage isolines derived from global information and the results from criteria 1 and 2, than from Criterion 3, specially at the non-constant mode-mixity, B, region. It is noteworthy that the global description of the damage isoline is highly dependent on the methodology used to compute it, mainly the number of points taken into account and its fitting. Therefore, in a FE framework, the computation of the approximated normal direction to the damage isoline using global information may, in some cases, misrepresent the actual normal direction. Indeed, the local computation of the negative gradient of the energy-based damage, $\mathcal{D}^e$, by means of Criterion 1 is the exact normal to the damage isolines. The fitting of the points forming the damage isoline, that leads to an approximate global description of it, is only used to validate the implementation of the formulation presented. To close, the effect of the mesh size on the determination of the normal direction to the 1-valued damage isoline is analyzed using both methods (Figure 3.18): the approximated normal direction using global information and the growth driving direction obtained by evaluating Criterion 1. The results show that the growth driving direction, evaluated locally, shows less sensitivity to the element size. Indeed, the growth driving direction is a continuum field which does not explicitly depend on the mesh size, but it implicitly does, due to discretization of the displacement field in the FEM [24].

3.2 Evaluation of the mode-decomposed energy release rates for arbitrarily shaped delamination fronts using cohesive elements

3.2.1 Formulation of the mode-decomposed energy release rates

In this section, the formulation of the mode-decomposed energy release rates in three-dimensional delaminations, modeled using a cohesive zone model approach, is presented. The point of departure is the generalized J-integral for non-planar curved cracks obtained by Fernlund et al. [52].

Assessment of the energy release rate by means of the J-integral formulation in curvilinear coordinates

Consider an elastic body (c.f. Figure 3.19), with a crack, subjected to prescribed tractions, T, and displacements, u, along parts of its boundary surface (Note that T and u are physical entities which are not yet described in any particular coordinate basis). In a general three dimensional domain, both the crack surfaces and the crack front may be curved. Let θ^i, $i = 1, 2, 3$, be an orthogonal curvilinear coordinate system with origin at a given point P along the crack front. This local coordinate system is oriented such that, at point P, θ^3 is normal to the crack surface in the undeformed configuration where the crack surfaces are coinciding, θ^2 is the coordinate along the crack front and θ^1 is the direction of crack propagation, which is always tangent to the crack surface and perpendicular to θ^2 and θ^3.

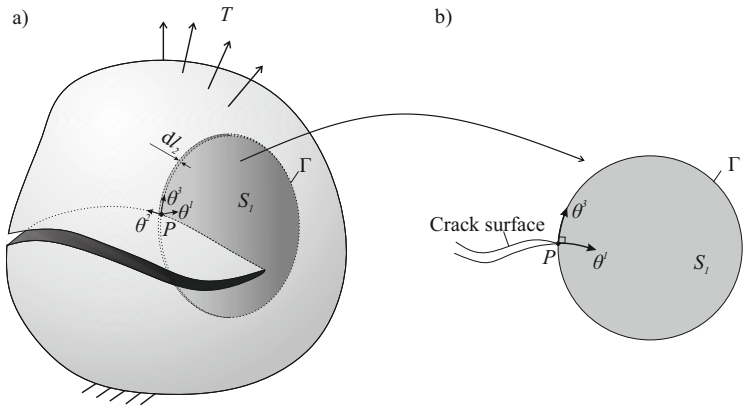

Fig. 3.19.: a) Three-dimensional body undergoing a delamination with curved front and non-planar crack surfaces. b) The integration domain is a slice of infinitesimal thickness, $\mathrm{d}l_2$.

Let us focus on a thin slice of elemental thickness, $\mathrm{d}l_2$, of the cracked body, which contains P (c.f. Figure 3.19). Note that an infinitesimal length segment, $\mathrm{d}l_i$ along a curvilinear axis, θ^i is given by:

$$\mathrm{d}l_i = \sqrt{g_{ii}}\mathrm{d}\theta^i \tag{3.27}$$

where g_{ij} is the covariant metric tensor. In the absence of body forces, the change in potential energy, Π, per unit of newly created crack area is [52]:

$$-\frac{\mathrm{d}\Pi}{\mathrm{d}A} = -\int_V \frac{\mathrm{d}W}{\mathrm{d}A}\mathrm{d}V + \int_S T^i \frac{\mathrm{d}u_i}{\mathrm{d}A}\mathrm{d}S \tag{3.28}$$

where $\mathrm{d}A$ is the elemental crack area extension, V the volume of the slice, S is the surface surrounding V, W is the strain energy density, T^i are the contravariant components of the traction vector and u_i are the covariant components of the displacement vector.

The infinitesimal thickness of the slice, allows to lump the three-dimensional slice into a surface S_1, defined by $\theta^2 = 0$ ($\mathrm{d}l_2 \to 0$). Then, by application of Green's

theorem, and under the assumption of small deformations, elastic material behavior, symmetry of the stress tensor and equilibrium conditions, the decrease in potential energy per unit area extension is expressed, in [52], as a contour integral and an area integral on the surface S_1:

$$J = -\frac{\mathrm{d}\Pi}{\mathrm{d}A} = \frac{1}{\sqrt{g_{11}}} \oint_{\Gamma} \left(W n_1 - T^i \frac{\partial u_i}{\partial \theta^1} \right) \mathrm{d}\Gamma - \frac{1}{\sqrt{g_{11} g_{22}}} \int_{S_1} \frac{\partial}{\partial \theta^2} \left(\sigma^{i2} \frac{\partial u_i}{\partial \theta^1} \right) \mathrm{d}S \tag{3.29}$$

where Γ is the contour enclosing S_1 in the clockwise direction and n_j is the outward unit normal vector on Γ. Note that in [52], the curvilinear coordinate system is rotated 90° around the θ^1-coordinate.

The J-integral is equivalent to the energy release rate, $\mathcal{G}$, for an elastic material response. In a three-dimensional body, the energy release rate may vary along the crack front. Therefore, in order to assess the delamination extension force in three-dimensional problems, it is customary to compute the point-wise value of J as a function of the crack front position, P.

Application to cohesive interfaces

When applied to delamination modeling in laminated composite materials, the cohesive behavior is lumped into the interface between subsequent plies. In [52], it is demonstrated that the J-integral of Equation (3.29), generalized in terms of curvilinear coordinates for cracks with curved front and non-planar crack surfaces, is path-area-independent. Then, for the measurement of the delamination extension force in 3D laminated structures modeled using a CZM approach, the path-area-independence of Equation (3.29) can be employed to shrink the contour Γ to the upper and lower crack surfaces (c.f. Figure 3.20), similarly to what is done with the two-dimensional form of the J-integral [136]. Therefore, the term related to the surface in Equation (3.29) vanishes due to the zero-thickness of the cohesive

interface. Moreover, the contribution from the strain energy term within the cohesive interface also vanishes and Equation (3.29) is reduced to:

$$J = -\frac{1}{\sqrt{g_{11}}} \oint_{\Gamma} \left(T^i \frac{\partial u_i}{\partial \theta^1} \right) \mathrm{d}\Gamma \tag{3.30}$$

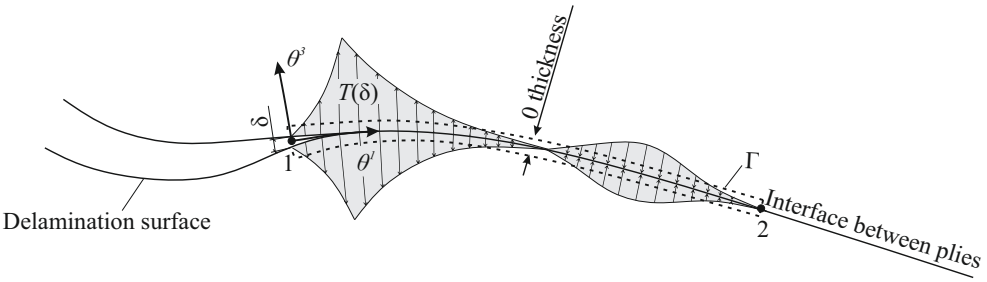

Fig. 3.20.: The integration path, Γ, is reduced to the cohesive interface.

Let σ^{ij} be the contravariant components of the cohesive stress tensor. Then, the contravariant traction vector at the crack faces is given by:

$$T^i = \sigma^{ij} n_j \tag{3.31}$$

being n_j is the outward unit normal vector on the contour Γ, i.e. on the crack surfaces. Thus, n_j vanishes for $j \neq 3$, and Equation (3.30) reads:

$$J = -\frac{1}{\sqrt{g_{11}}} \int_{\Gamma} \left(\sigma^{i3} \frac{\partial u_i^+}{\partial \theta^1} + \sigma^{i3} \frac{\partial u_i^-}{\partial \theta^1} \right) \mathrm{d}\theta^1 \tag{3.32}$$

where u^+ and u^- are the displacements at the upper $(^+)$ and lower $(^-)$ crack surfaces, respectively. Finally, introducing the displacement jump as the separation of two initially coinciding points on the interface, defined as:

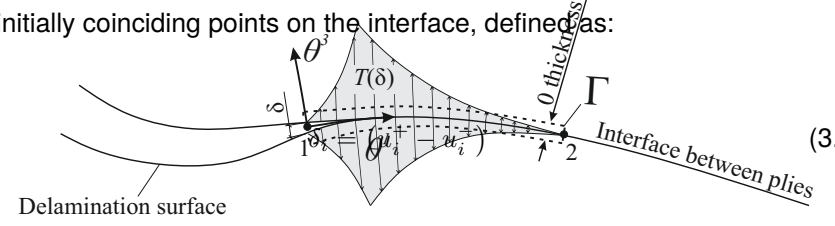

$$\delta_i = (u_i^+ - u_i^-) \tag{3.33}$$

the curvilinear CZ J-integral, when applied to cohesive interfaces, can be expressed as:

$$J = -\frac{1}{\sqrt{g_{11}}} \int_{CZ} \left(\sigma^{i3} \frac{\partial \delta_i}{\partial \theta^1} \right) \mathrm{d}\theta^1 \tag{3.34}$$

Observe, in Figure 3.20, that the integration path is the entire CZ so that all the cohesive stresses contribute to the CZ J-integral.

Integration paths

As demonstrated in Section 3.2.1, the integration domain of the curvilinear CZ J-integral applied to cohesive interfaces is a slice of infinitesimal thickness, $\mathrm{d}l_2$, lumped into the delamination interface. Thus, the integration domain is reduced to a path contained in the delamination interface which follows the direction of crack propagation, θ^1. In order to compute the J-distribution in three-dimensional structures, the interface can be divided into infinite slices. Obviously, the J-value of each slice is unique, and is obtained when the integration path is covered in its entirety, i.e. going through the entire cohesive zone, from the completely damaged zone (point 1 in Figure 3.20, with zero cohesive stress) until the end of the zone in elastic regime (point 2 in Figure 3.20, with zero cohesive stress).

In LEFM, the propagation direction, θ^1, is assumed to be the normal to the crack front at the point P, where the crack front is the line separating the damaged and undamaged parts (c.f. Figure 3.21.a). However, the definition of the propagation direction as the normal to the crack front does not apply for CZM, due to existence of a cohesive zone of variable length. Making use of Criterion 2 for growth driving direction (GDD) presented in Section 3.1, θ^1 can be defined according to the GDD. In this way, the integration paths, defined along the θ^1-coordinate, never intersect and the three-dimensional structure can be understood as the aggregation of infinite individual slices of infinitesimal thickness which contain a crack propagating in the GDD. It is worth to mention that the damage isolines may not be parallel along the CZ, leading to slices with double curvature if, in addition, the cohesive interface mid-surface is non-planar.

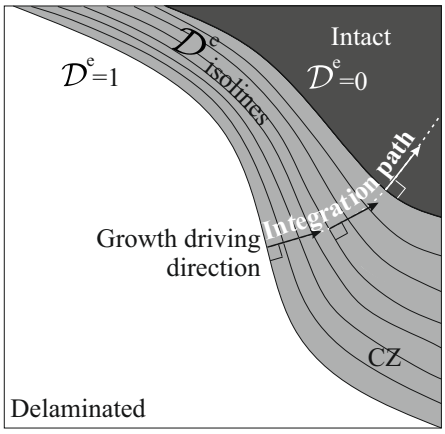

Fig. 3.21.: The growth driving direction is assumed to be the normal direction to the energy-based damage isolines in the CZM framework. The integration paths are tangent at the local GDD direction.

It is noted that, for the computation of the J-value in cohesive interfaces using Equation (3.34), the contribution of the stress, σ^{i3}, and displacement jump slope in the GDD direction, $\frac{\partial \delta_i}{\partial \theta^1}$, in the elastic regime is needed. Criterion 2 is chosen over Criterion 1 because it is also active in the elastic regime. Both the conservative and the non-conservative work are computed using Criterion 2. Thus, since, as soon as two initially coinciding points separate from each other some elastic energy is stored, this criterion is active before any energy dissipation due to fracture takes place. Moreover, using the CZM presented in [168] once the damage is initiated, both criteria lead to the same GDD solution.

Mode-decomposition of the CZ J-integral for its application to cohesive interfaces

Mode I is defined normal to the cohesive interface mid-surface, mode II, tangent to the mid-surface in the propagation direction and mode III, tangent to the mid-surface and perpendicular to mode II. Moreover, it is assumed that the GDD is defined as the direction equivalent to crack propagation direction when a CZM approach is used. Thus, the mode II direction is defined coincident to the GDD, whereas the mode III direction is defined perpendicular to it. Indeed, since θ^i are orthogonal curvilinear

coordinates, the local covariant and contravariant basis vectors are coincident. The local basis vectors are aligned with the three loading modes directions, since θ^1 is locally coincident with the GDD (i.e. tangent to the mid-surface), θ^3 is normal to the mid-surface, and θ^2 is normal to θ^1 and θ^3.

At an interface modeled using a CZM approach, only three uncoupled components of cohesive stresses (σ^{13}, σ^{23} and σ^{33}) result from the displacements jumps between crack faces (δ_1, δ_2, δ_3). Stresses are expressed in the local contravariant basis vectors and displacements jumps in the local covariant basis vectors of the curvilinear crack coordinate system, θ^i. Therefore, necessarily, the quantities σ^{13} and $\frac{\partial \delta_1}{\partial \theta_1}$ contribute to mode II, σ^{23} and $\frac{\partial \delta_2}{\partial \theta_1}$, to mode III, and σ^{33} and $\frac{\partial \delta_3}{\partial \theta_1}$, to mode I crack loading. Hence, the mode-decomposed CZ J-integrals are defined according to the local θ^i coordinate system such that the terms with $i = 3$ are attributed to Mode I, the terms with $i = 1$, to Mode II and the terms with $i = 2$, to Mode III:

$$\begin{aligned} J_I &= -\frac{1}{\sqrt{g_{11}}} \int_{CZ} \left(\sigma^{33} \frac{\partial \delta_3}{\partial \theta^1} \right) \mathrm{d}\theta^1 \\ J_{II} &= -\frac{1}{\sqrt{g_{11}}} \int_{CZ} \left(\sigma^{13} \frac{\partial \delta_1}{\partial \theta^1} \right) \mathrm{d}\theta^1 \\ J_{III} &= -\frac{1}{\sqrt{g_{11}}} \int_{CZ} \left(\sigma^{23} \frac{\partial \delta_2}{\partial \theta^1} \right) \mathrm{d}\theta^1 \end{aligned} \tag{3.35}$$

For 3D planar cracks, described by a rectangular Cartesian coordinate system, the mode decomposed CZ J-integrals in Equation (3.35) evaluated at the cohesive interface, are in agreement with that in [138, 51].

3.2.2 Discretization with the Finite Element Method

To numerically integrate Equation (3.35), trapezoidal integration is employed (although any other numerical integration method could be used). Thus, the curved integration pathline is discretized into small linear subintervals tangent to the curvilinear coordinate θ^1. The quantities in the integrand of Equation (3.35) must, thereby, be defined according to the local Cartesian coordinate system, x_i. The coordinates x_i are oriented in such a way that x_1 and x_2 are the tangential and normal coordi-

nates to the GDD, respectively, with locally coincident direction with the covariant and contravariant basis vectors of the orthogonal curvilinear coordinate system, θ^i. The tracking of the integration path, as well as its limits, are further addressed.

The derivative of the displacement jumps, δ_i, with respect to x_1, the local Cartesian coordinate aligned with the GDD, is addressed in the following. X_j is the Cartesian reference system, x_i is the local Cartesian coordinate system and R_{ij} is the transformation tensor which relates the global to the local coordinate system. By assuming that the derivative of R_{ij} with respect to x_1 can be omitted, the derivative $\frac{\partial \delta_i}{\partial x_1}$ reads:

$$\frac{\partial \delta_i}{\partial x_1} = R_{ij} \frac{\partial M_{jm}}{\partial x_1} Q_m \tag{3.36}$$

The derivative of the transformation matrix, M_{jm}, with respect to the local coordinate, x_1, is obtained by application of the chain rule:

$$\frac{\partial M_{jm}}{\partial x_1} = \frac{\partial M_{jm}}{\partial \eta_\alpha} \frac{\partial \eta_\alpha}{\partial x_1} \tag{3.37}$$

The first partial derivative in the right hand side of Equation (3.37) is the variation of the transformation matrix, M_{jm}, with the isoparametric coordinates of the cohesive element formulation, η_α (α=1,2), which is addressed in Section 3.1.1.

Finally, the derivatives $\frac{\partial \eta_\alpha}{\partial x_1}$ are the inverse of the derivatives of the local coordinate, x_1, with respect to the isoparametric coordinates, η_α, defined as:

$$\frac{\partial x_1}{\partial \eta_\alpha} = R_{1j} \frac{1}{2} \frac{\partial N_{jk}}{\partial \eta_\alpha} \left(C_k^+ + C_k^- + Q_k^+ + Q_k^- \right) \tag{3.38}$$

Tracking of the integration paths

Using the formulation described above, the delamination extension force, which may vary for every slice, can be evaluated everywhere within the CZ. Moreover, any point within the CZ belongs to a single slice, i.e. to a single integration path, which is defined according to the local GDD. Therefore, one can randomly select any location of the CZ and, by means of the GDD, identify the tangent to the integration pathline at that point in order to move, either forward or backward, along the integration path. The delamination extension force corresponding to such slice is obtained when the path is tracked in its entirety.

Consider a point, P^k, belonging to the CZ. In order to assess the delamination extension force at the slice which the point P^k belongs to, the numerical integration of Equation (3.35) is performed along the integration path, defined tangent to the local GDD direction and limited by vanishing stress conditions at both ends (c.f. Figure 3.20). In the general case, the initial point P^k is not located at one end of the integration path, i.e. point P^k is located in the middle of the CZ. In this case, the path will be tracked from P^k in the GDD and in the opposite direction to GDD: In the positive GDD until vanishing elastic stress is reached (point 2 in Figure 3.20); in the negative GDD until the intersection with the 1-valued energy-based damage isoline, where the cohesive stress also equals zero (point 1 in Figure 3.20).

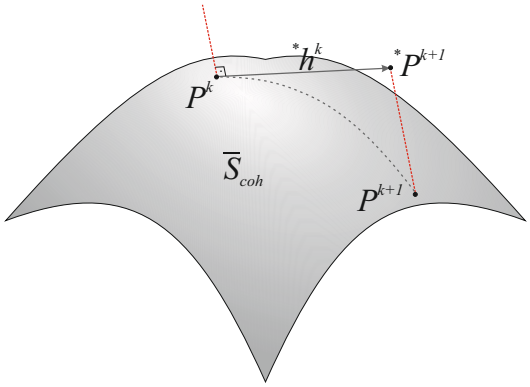

Fig. 3.22.: Point P^k is a point on the integration path of a curved cohesive interface, $\bar{S}_{coh}$. The following point on the integration path, P^{k+1}, is found by projecting point $^*P^{k+1}$ along the normal direction to the interface at point P^k. Point $^*P^{k+1}$ is at a $^*h$ distance from P^k in the tangential GDD.

In order to move along the integration path, the following procedure is applied. Starting from P^k, the next point along the integration path is established by moving in a straight line a ${}^*h^k$-length step further in the local GDD, which is tangent to the cohesive interface mid-surface, $\bar{S}_{coh}$, at P^k. Then, a new point, ${}^*P^{k+1}$, in the space is found. Nevertheless, ${}^*P^{k+1}$ is not necessarily placed on the mid-surface, $\bar{S}_{coh}$. This becomes evident when $\bar{S}_{coh}$ is highly non-planar (c.f. Figure 3.22). Thus, the real next point constituting the integration path, P^{k+1}, is found by performing the projection of ${}^*P^{k+1}$ on $\bar{S}_{coh}$ in the normal x_3-direction of point P^k.

FE-discretized mode-decomposed CZ J-integral

After discretization of the cohesive interface into FE, the numerical integration of Equation (3.35), performed by means of the trapezoidal rule, reads:

$$\begin{aligned} J_I &\backsimeq \sum_k \left[h^k \left(\frac{\sigma_{33}^k \frac{\partial \delta_3^k}{\partial x_1} + \sigma_{33}^{k+1} \frac{\partial \delta_3^{k+1}}{\partial x_1}}{2} \right) \right] \\ J_{II} &\backsimeq \sum_k \left[h^k \left(\frac{\sigma_{13}^k \frac{\partial \delta_1^k}{\partial x_1} + \sigma_{13}^{k+1} \frac{\partial \delta_1^{k+1}}{\partial x_1}}{2} \right) \right] \\ J_{III} &\backsimeq \sum_k \left[h^k \left(\frac{\sigma_{23}^k \frac{\partial \delta_2^k}{\partial x_1} + \sigma_{23}^{k+1} \frac{\partial \delta_2^{k+1}}{\partial x_1}}{2} \right) \right] \end{aligned} \tag{3.39}$$

where h^k is the integration interval length, approximated to the Euclidean distance between two consecutive points along the integration path, P^k and P^{k+1}.

3.2.3 Comparison with mode-decomposed energy release rates extracted by VCCT

The capabilities of the presented CZ J-integral formulation are assessed by comparison with the energy release rate mode-components of a moment-loaded DCB

model obtained by VCCT. The unidirectional composite specimen is 30 mm long, 6 mm wide and 3 mm thick (Figure 3.23). The elastic properties of the laminate and the fracture properties of the interface are listed in Tables 3.6 and 3.7, respectively. The specimen arms are modeled in the commercial FE code ABAQUS [160] using C3D8I hexahedral elements. The undeformed elements are 0.4 mm wide, 0.2 mm long and 0.5 mm thick. The delamination front is completely straight and located at the mid-surface at a distance of 15.1 mm from the loading application edges. A combined I, II and III fracture mode is created by application of four force couples (Figure 3.23). $M1$ and $M2$ generate uneven opening Y-moments at the upper and lower arms, respectively. $M3$ and $M4$ generate even tearing Z-moments at both arms. The resultant bending moments are listed in Table 3.8.

Tab. 3.6.: Elastic properties of the laminate used in the simulation studies of the moment-loaded DCB and the ELS specimens.

Laminate properties		
E_{11}: Longitudinal Young's modulus	154	GPa
$E_{22} = E_{33}$: transversal Young's modulus	8.5	GPa
$G_{12} = G_{13}$: Shear modulus in the longitudinal planes	4.2	GPa
G_{23}: Shear modulus in the transversal plane	3.0	GPa
$\mu_{12} = \mu_{13}$: Poison's coefficient in the longitudinal planes	0.35	-
μ_{23}: Poison's coefficient in the transversal plane	0.4	-

Tab. 3.7.: Fracture properties of the interface used in the simulation study of the moment-loaded DCB specimen.

Interface properties		
$\mathcal{G}_{Ic}$: Mode I fracture toughness	0.3	N/mm
$\mathcal{G}_{IIc} = \mathcal{G}_{IIIc}$: Modes II and III fracture toughness	3	N/mm
τ_{Ic}: Mode I interlaminar strength	10	MPa
$\tau_{IIc} = \tau_{IIIc}$: Modes II and III interlaminar strengths [168]	31.62	MPa
η: Benzeggagh-Kenane's interpolation parameter [29]	2	-
K: penalty stiffness	10^5	N/mm^3

In the FE analysis using the VCCT, the energy release rate is evaluated locally at every node forming the delamination front. A local crack coordinate system defines the mode-components, such that mode II and mode III are normal and tangential to the delamination front, respectively, and mode I is normal to mode II and III directions. For a straight front, like the one in study, the orientation of this local coordinate system is constant along the front and aligned with the mesh [85].

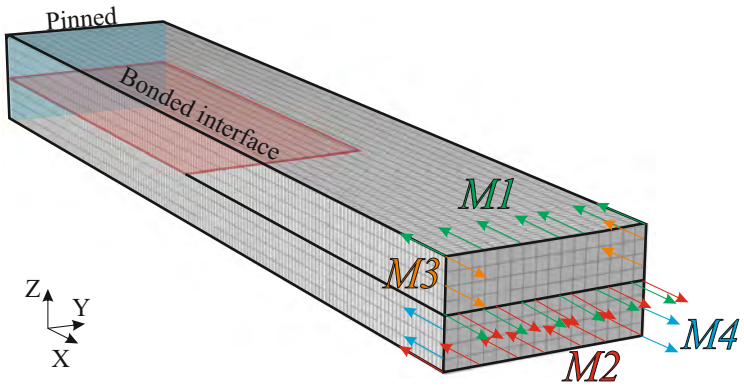

Fig. 3.23.: DCB specimen dimensions with four force couples: $M1$ and $M2$ generate uneven opening Y-moments, while $M3$ and $M4$ generate even tearing Z-moments.

Tab. 3.8.: Bending moment resultants from the application of the four force couples to the double-cantilevered-beam model.

Bending moment	[Nmm]
$M1$	270
$M2$	135
$M3$	960
$M4$	960

For the evaluation of the J-values, the interface undergoing delamination has been modeled using user-defined cohesive elements. To this end, the method presented in [167, 168] has been enhanced with the formulation for the numerical evaluation of the mode-decomposed CZ J-integral presented in Section 3.2.2. For comparison purposes with VCCT, a fixed GDD is defined normal to the straight delamination front.

The mode-decomposed energy release rate distributions along the width of the specimen, from both the VCCT and the CZ J-integral extraction methods, are plotted in Figure 3.24.

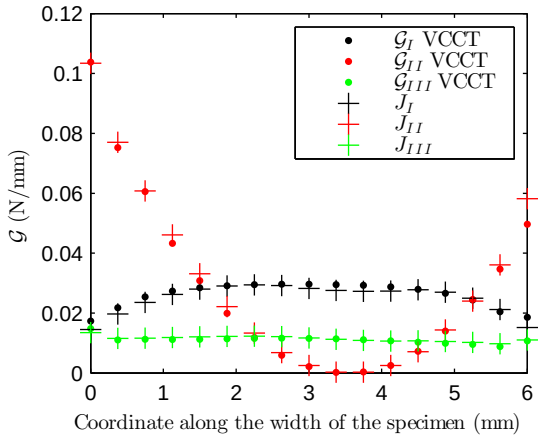

Fig. 3.24.: Comparison of the mode-components of strain energy release rate between VCCT and CZ J-integral extraction methods.

3.2.4 Application to a partially reinforced ELS specimen

In the ELS specimen presented in Section 3.1.3, the reinforcements do not span the entire width of the specimen in order to promote a curved delamination. Moreover, the specimen bends due to application of the end loading, resulting in a curved delamination front in a non-planar interface. Therefore, the partially reinforced ELS specimen is considered to be suitable to exemplify the applicability of the generalized CZ J-integral methodology for 3D curved and non-planar delamination fronts.

The mid-surface is modeled using user-defined cohesive elements which incorporate the formulation presented in [167, 168], enhanced with Criterion 2 for GDD presented in Section 3.1 and the CZ J-integral formulation described in Section 3.2.2. The undeformed cohesive elements are 0.27 mm wide, 0.23 mm long and have zero thickness. Only one half of the specimen is modeled exploiting X_2-symmetry to reduce the required computational resources. The elastic properties of the laminate and the fracture properties of the interface are listed in Tables 3.6 and 3.9, respectively. Note that, as a simple way to check the CZ J-integral implementation, the fracture toughness is set to be mode independent ($\mathcal{G}_c = \mathcal{G}_{Ic} = \mathcal{G}_{IIc} = \mathcal{G}_{IIIc} = 2$ N/mm), in order to ensure a constant J-value ($J = \mathcal{G}_c$) during static crack propagation. Thus,

Tab. 3.9.: Fracture properties of the interface used in the simulation study of the ELS specimen.

Interface properties		
$\mathcal{G}_{Ic} = \mathcal{G}_{IIc} = \mathcal{G}_{IIIc}$: Mode-independent fracture toughness	2	N/mm
$\tau_{Ic} = \tau_{IIc} = \tau_{IIIc}$: Mode-independent interlaminar strength	35	MPa
K: penalty stiffness	10^5	N/mm^3

the sum of the three mode-decomposed CZ J-integrals in Equation (3.39) must be constant and equal to 2 N/mm at every slice, regardless of the loading mode. In the following figures, only the blue-shadowed area of the mid-surface in Figure 3.9 is represented.

The historical evolution of the 0.5-valued energy-based damage isoline is plotted in Figure 3.25.a. The energy-based damage, $\mathcal{D}^e$, distribution is projected on the deformed mid-surface, in Figure 3.25.c, for a prescribed end displacement of 27.7 mm. The GDD distribution within the CZ is represented in Figure 3.26. As mentioned in Section 3.2.2, the CZ J-integral can be evaluated at any point within the CZ and, therefore, infinite integration paths can be tracked. For illustrative purposes, only a few selected integration paths are plotted on top of the GDD distribution. Note that the trajectory of the integration paths is established according to the GDD. Thus, since the $\frac{\omega_{tot}}{\mathcal{G}_c}$ isolines are not parallel, the integration paths are curved lines throughout the CZ.

The total J-value is evaluated at each of the 30,000 integration points forming the CZ. The result is represented in Figure 3.27.a. The step length ${}^*h^k$ used is 0.3 mm. Note that the J-distribution is constant and equal to the fracture toughness, which, during static propagation and for any mode mixity, amounts 2 N/mm. The decomposition of the CZ J-integral into modes, computed according to Equation (3.39), is also represented in Figure 3.27.

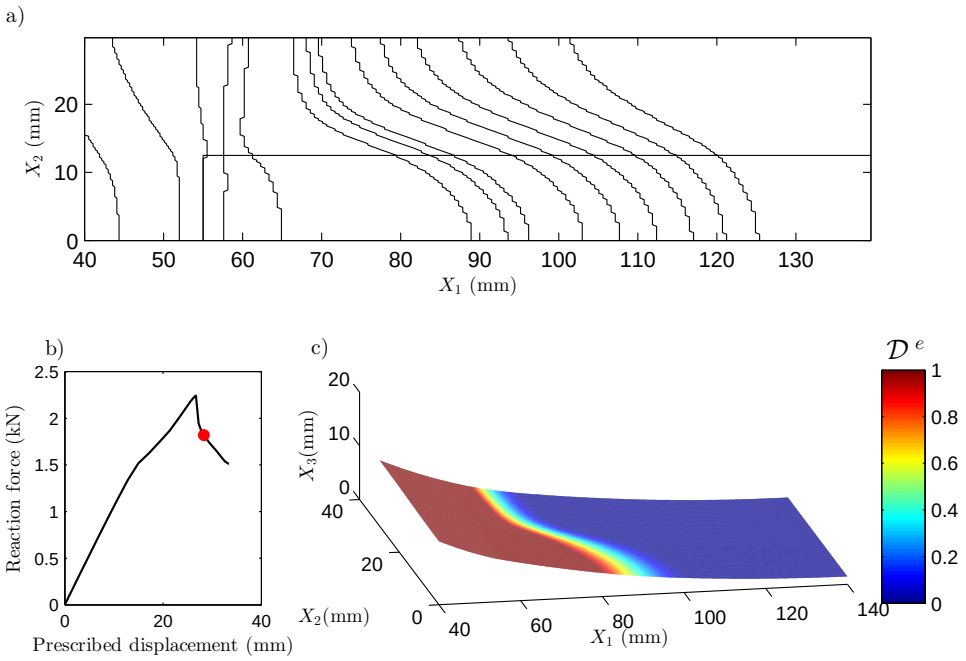

Fig. 3.25.: a) Historical evolution of the 0.5-valued energy-based damage isoline extracted at the integration points. b) Reaction force vs prescribed displacement curve with the current loading state highlighted in red. c) Energy-damage projected on the deformed mid-surface at the current loading stated marked in (b).

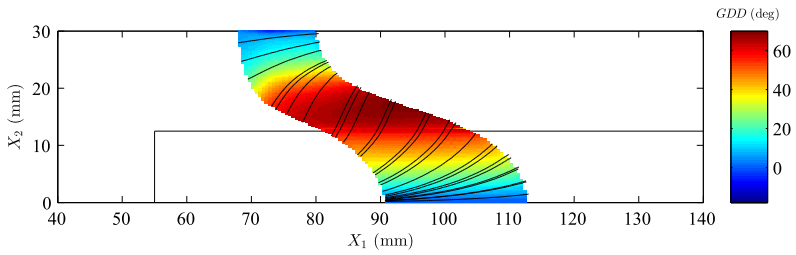

Fig. 3.26.: Growth driving direction (GDD) distribution along the cohesive zone and a few selected integration paths (black solid lines) plotted on top of it.The current loading state is marked in Figure 3.25.b.

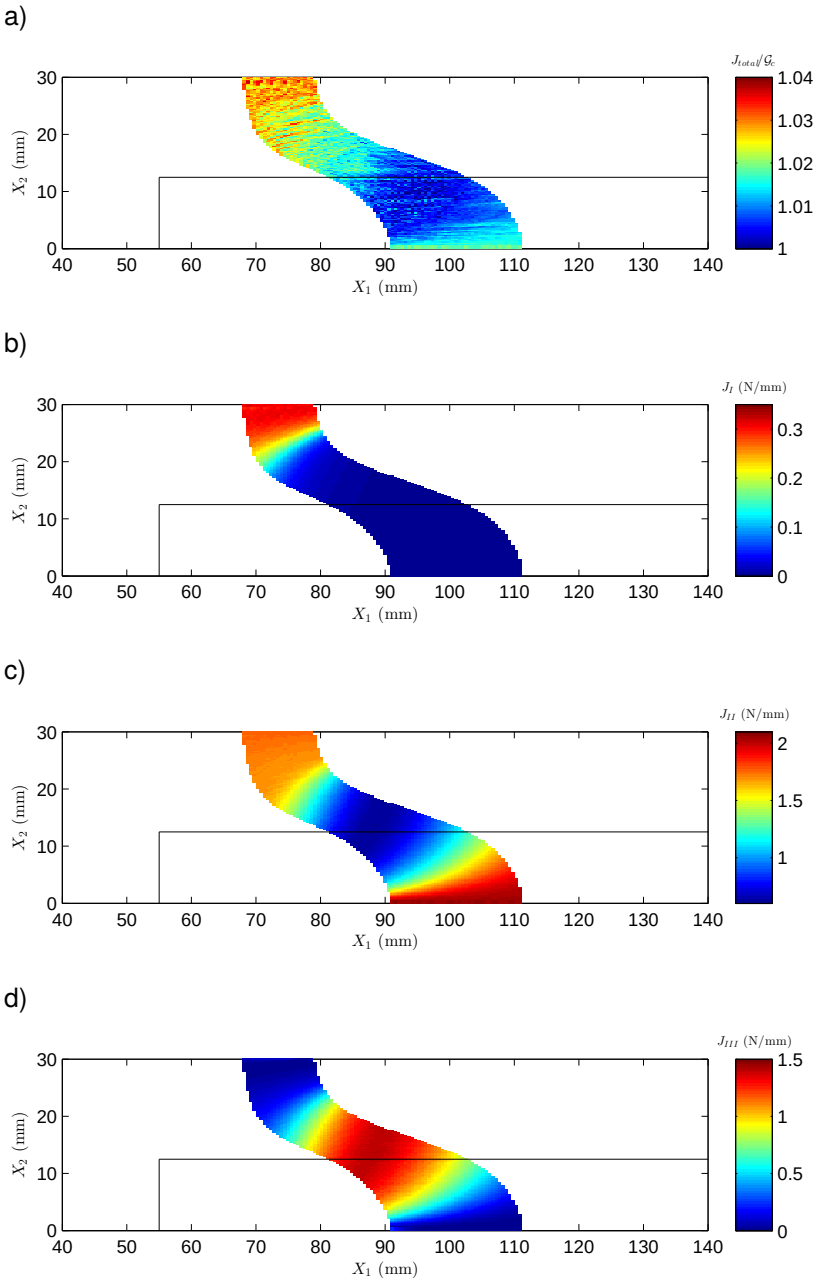

Fig. 3.27.: Distribution of a) $J_{total}/\mathcal{G}_c$ (where $J_{total} = J_I + J_{II} + J_{III}$ and $\mathcal{G}_c$=2 N/mm), b) J_I , c) J_{II} and d) J_{III} within the cohesive zone at current loading state marked in Figure 3.25.b.

3.2.5 Discussion

A comparison of the mode-components of the CZ J-integral with the energy release rates extracted from VCCT is done in Section 3.2.3. To make both decomposition schemes comparable, the GDD, which dictates the mode II direction in the CZ J-integral formulation, is forced normal to the initial crack front. Although both results are in good agreement (c.f. Figure 3.24), there are small differences which are caused by a slight difference in compliance between the two models. When using cohesive elements to simulate the delamination fracture behavior, some separation between crack faces occur before complete decohesion. This is not the case of the VCCT, where no relative displacements between crack faces occur until the condition for crack propagation ($\mathcal{G} \geq \mathcal{G}_c$) is fulfilled. The difference in compliance between the two models has an influence on the computed energy release rate. Another source of discrepancy is the nonlinearity introduced by the cohesive behavior. Using the CZM approach, the stiffness of the interface is reduced as it gets damaged. Conversely to VCCT, the existence of a damage process zone implies that the behavior of the material ahead of the crack front is nonlinear.

Furthermore, the standard formulations for VCCT require to have orthogonality of the mesh with the delamination front in order to obtain accurate energy release rate components [154]. Therefore, its application to three-dimensional FE models requires the option of moving meshes that conform according to the delamination front, which is not available in commercial finite element codes [86]. Alternative solutions that enable the use of stationary meshes are presented in [178, 98]. The basic assumption of these formulations is that the nodes at the delamination front will propagate along a normal vector to the current front. However, when the delamination originates from an artificial initial defect, e.g. caused by a Teflon insert, or when the loading conditions change, there is a transient stage during which the shape of the crack front changes according to the current propagation conditions. The formulation for the evaluation of the GDD does not depend on the geometry of the crack front (which is historical information), but on the current displacement field. Thus, any variation in the displacements due to a change in the loading scenario is captured by the GDD criterion at the current time. Therefore, the mode-decomposition scheme according to the GDD can be applied during transient propagation.

In Section 3.2.4, the presented mode-decomposed CZ J-integral formulation is applied to a real three-dimensional structure with a large fracture process zone (the maximum length of the CZ is approximately 20 mm). Due to the ELS test configuration, the structure is subjected to large deflections. Moreover, it is partially reinforced so that the stiffness along the specimen width is not constant. As a consequence, during propagation, both the delaminated surfaces and the CZ are curved. Due to a change in the GDD orientation across the CZ, the integration paths result in curved lines. The same $\mathcal{G}_{Ic}$, $\mathcal{G}_{IIc}$ and $\mathcal{G}_{IIIc}$ have been introduced as inputs to the CZM (see Table 3.9) in order to make the equivalent one-dimensional fracture toughness independent on the mode mixity. In this way, under static propagation conditions, the accurate computation of the total J-value can be easily assessed by direct comparison with a constant mode-independent fracture toughness. The total computed J-value is equal to the fracture toughness at all the integration points within the cohesive zone with a maximum error of 3.7% (c.f. Figure 3.27.a). The integration step, ${}^{*}h^{k}$, used in the computation of the J-value is 1.3 times the shortest element length. By reducing ${}^{*}h^{k}$, more accurate results may be obtained. However, for such a large CZ, the computational cost increases significantly with the number of segments in which the integration paths are discretized.

Moreover, the mode-decomposition of the CZ J-integral accounting for large CZ is also addressed. The mode II and III components of the CZ J-integral are predominant, while mode I slightly appears at a small region close to the specimen's edge (c.f. Figure 3.27.b). The contribution to the J-value of the tangent quantities to the mid-surface is decomposed into modes II and III according to the GDD. The bonded reinforcements cause the loading state to be uneven throughout the specimen's width, leading to a curved crack, so that the GDD amounts up to 60° with respect to the X_1 at the zones with highest delamination front curvature. Due to the test configuration, the loading is applied in the global X_1 direction. For straight cracks where the GDD is aligned with the X_1-direction, the shear component would be pure mode II. However, in the studied case with a curved delamination front, the maximum contribution of the external loading to the mode III CZ J-integral is at that zone were the GDD differs most from the X_1-direction (c.f. Figures 3.27.c and 3.27.d).

3.3 Extension of the fatigue damage rate model for 3D applications

The fatigue energy-based damage rate, $\frac{\mathrm{d}\mathcal{D}^e}{\mathrm{d}N}$, is a field variable, computed at integration point level. Following the model developed for 2D applications [23] summarized in Section 2.4, $\frac{\mathrm{d}\mathcal{D}^e}{\mathrm{d}N}$ is related to the crack growth rate, $\frac{\mathrm{d}a}{\mathrm{d}N}$, by:

$$\frac{\mathrm{d}\mathcal{D}^e}{\mathrm{d}N} = \frac{\partial \mathcal{D}^e\left(B,\lambda\right)}{\partial a}\frac{\mathrm{d}a}{\mathrm{d}N} \tag{3.40}$$

The term $\frac{\partial \mathcal{D}^e(B,\lambda)}{\partial a}$ depends on the static cohesive law and the current displacement jump field. Thus, $\frac{\partial \mathcal{D}^e(B,\lambda)}{\partial a}$ is also a field variable. Conversely, the crack growth rate, $\frac{\mathrm{d}a}{\mathrm{d}N}$, is evaluated non-locally using a modified Paris' law expressed in terms of the maximum cyclic energy release rate, $\mathcal{G}_{max}$ (c.f. Equation (2.55)). In this work, the 3D CZ J-integral formulation developed in Section 3.2 is used to compute the mode-decomposed $\mathcal{G}_{max}$. Following the argumentation given in Section 3.2, the three-dimensional cohesive interface can be understood as the aggregation of infinitesimal thickness slices, such that the J-value of each slice (and, consequently, $\frac{\mathrm{d}a}{\mathrm{d}N}$) is unique. Each point within the cohesive zone, belongs to a slice; and each of the slices contains a crack propagating in the GDD at a velocity of $\frac{\mathrm{d}a}{\mathrm{d}N}$.

The evaluation of each of the terms in Equation (3.40) is detailed in the following. The term $\frac{\partial \mathcal{D}^e(B,\lambda)}{\partial a}$ is derived as:

$$\frac{\partial \mathcal{D}^e\left(B,\lambda\right)}{\partial a} = \left(\frac{\partial \mathcal{D}^e}{\partial B}\frac{\partial B}{\partial a} + \frac{\partial \mathcal{D}^e}{\partial \lambda}\frac{\partial \lambda}{\partial a}\right) \tag{3.41}$$

The derivative of the energy-based damage with respect to the mode mixity, $\frac{\partial \mathcal{D}^e}{\partial B}$, and the derivative of the energy-based damage with respect to the mixed-mode displacement jump, $\frac{\partial \mathcal{D}^e}{\partial \lambda}$, depend only on the quasi-static cohesive law. Therefore, its derivation for 2D applications is still valid in the 3D model. Equations (2.41) and (2.42) are the resultant expressions for $\frac{\partial \mathcal{D}^e}{\partial B}$ and $\frac{\partial \mathcal{D}^e}{\partial \lambda}$ after the particular application of the quasi-static CZM from [167, 168].

According to the assumption done in Equation (2.53), the rates $\frac{\partial B}{\partial a}$ and $\frac{\partial \lambda}{\partial a}$ in Equation (3.41) can be computed as the slopes of the local mode-mixity and the mixed-mode displacement jump along the direction of crack propagation, $\frac{\partial B}{\partial x_1}$ and $\frac{\partial \lambda}{\partial x_1}$. To do so, the local Cartesian coordinates tangential to the cohesive element mid-surface, $\overline{S}_{coh}$, (c.f. Figure 2.9) can be oriented, using Equation (3.25), in such a way that x_1 is the tangential coordinate to the GDD. Then, by application of the chain rule, $\frac{\partial B}{\partial x_1}$ reads:

$$\frac{\partial B}{\partial x_1} = \frac{\partial B}{\partial \delta_j} \frac{\partial \delta_j}{\partial x_1} \tag{3.42}$$

where the term $\frac{\partial B}{\partial \delta_j}$ is solved in Equation (3.18), and the term $\frac{\partial \delta_j}{\partial x_1}$ derived in Equation (3.36). Similarly, $\frac{\partial \lambda}{\partial x_1}$ reads:

$$\frac{\partial \lambda}{\partial x_1} = \frac{\partial \lambda}{\partial \delta_j} \frac{\partial \delta_j}{\partial x_1} \tag{3.43}$$

and the term $\frac{\partial \lambda}{\partial \delta_j}$ is solved in Equation (3.8).

On the other hand, the crack growth rate, $\frac{\mathrm{d}a}{\mathrm{d}N}$, is computed for a given load ratio, R, by means of Equation (2.55), where the exponent, $p(\Phi)$, and coefficient, $A(\Phi)$, are mode-dependent parameters determined by Equation (2.56). The mode mixity, Φ, is computed, using the components of the CZ J-integral (c.f. Equation (3.39)), as:

$$\Phi = \frac{J_{II} + J_{III}}{J_I + J_{II} + J_{III}} \tag{3.44}$$

and the maximum cyclic energy release rate, $\mathcal{G}_{max}$, is computed as the sum of the J-terms:

$$\mathcal{G}_{max} = J_I + J_{II} + J_{III} \tag{3.45}$$

Finally, for the cycle jump strategy, at the end of a converged substep, the increment in cycles is determined using a target increment in crack length, Δa_t, and the maximum crack growth rate of the structure, $\left(\frac{\mathrm{d}a}{\mathrm{d}N}\right)_{max}$:

$$\Delta N = \frac{\Delta a_t}{\left(\frac{\mathrm{d}a}{\mathrm{d}N}\right)_{max}} \tag{3.46}$$

No interface properties are added at the material card for the extension of the 2D model for its applicability to 3D structures. Thus, the interface properties needed for feeding the 3D fatigue damage rate model are summarized in Table 2.3.

4

An efficient methodology for the experimental characterization of mode II delamination growth under fatigue loading

The fatigue characterization of interface properties is very time consuming and requires a lot of human and equipment resources, especially in the case of mode II and mixed-mode tests. Therefore, efficient test methods are needed in order to reduce the testing time and human intervention. To this end, a new testing methodology for mode II delamination growth characterization is developed in this thesis, which is extended for mixed-mode testing in [73].

A methodology to measure, in a single test, a larger region of the crack growth rate curve than that achieved in a constant cyclic displacement test is presented in the following. The procedure consists of varying the cyclic applied displacement, U_{min} and U_{max}, while keeping the displacement ratio, R, constant (c.f. Figure 4.1). Moreover, the displacement variation is calculated a priori, so that it can be implemented in the control software of the testing machine. Thus, the control loop does not make use of parameters related to the behavior of the specimen, which could lead to unpredictable responses from the test machine. This method requires neither human intervention during the test nor processing the data in real time. The chapter includes a test campaign carried out on carbon fiber reinforced composites which exemplifies the advantages of the proposed procedure: the crack growth rate curve can be characterized in, at most, 1/80 of the time required for a constant cyclic displacement test.

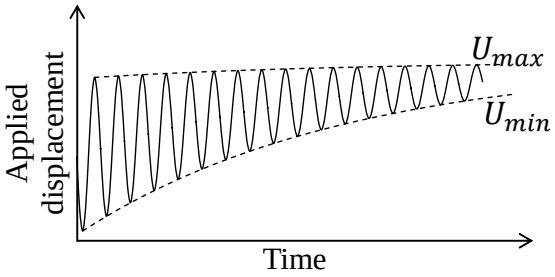

Fig. 4.1.: Variable cyclic displacement vs. time.

4.1 Methodology

Due to the geometry of the test, the maximum energy release rate during one load cycle, $\mathcal{G}_{max}$, corresponds to the minimum displacement, U_{min}. The aim of the proposed methodology is to define the evolution of U_{min} with the number of cycles, N, so that the severity of the load sweeps a predefined range, from $\mathcal{G}_{max,0}/\mathcal{G}_c$ to $\mathcal{G}_{max,f}/\mathcal{G}_c$, while the crack grows from the initial crack, a_0, to the maximum allowed crack length, a_f, (when the crack tip approaches a distance $2h$ from the load introduction point). U_{max} is established so that the R-ratio is constant throughout the fatigue test ($R = U_{min}/U_{max}$, for small deflections). The following paragraphs describe how the function $U_{min}(N)$ has been deduced. Note that the sign convention used in this work is negative for displacements which result in compressive reaction forces.

The function $U_{min}(N)$ depends on the chosen dependence between the severity of the load, $\mathcal{G}_{max}$ normalized to $\mathcal{G}_c$, and the crack length. A linear decreasing dependence, from the normalized $\mathcal{G}_{max,0}$ at a_0 to $\mathcal{G}_{max,f}$ at a_f, the end of the test (Figure 4.2) is chosen; however, other alternative monotonic dependence could be selected. Therefore, the gradient of the energy release rate, $\frac{\mathrm{d}\mathcal{G}_{max}}{\mathrm{d}a}$, is constant and negative. Thus, the load severity vs. the crack length, a, reads:

$$\frac{\mathcal{G}_{max}}{\mathcal{G}_c}(a) = m_{\mathcal{G}}\, a + n, \tag{4.1}$$

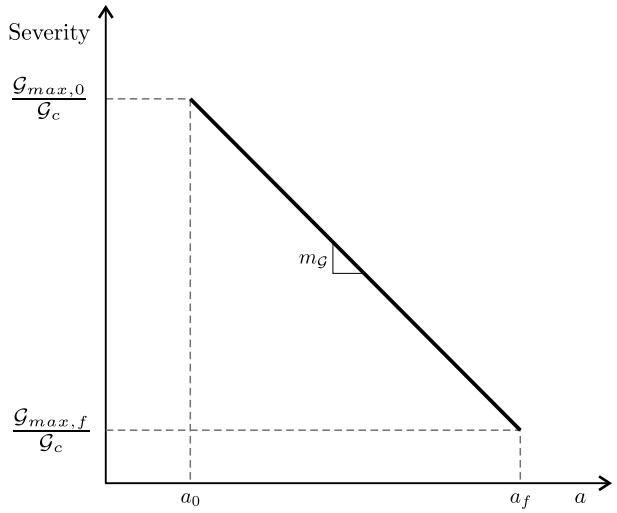

Fig. 4.2.: Chosen relation between the maximum cyclic energy release rate, $\mathcal{G}_{max}$, normalized to the quasi-static fracture toughness, $\mathcal{G}_c$, and the crack length. $\mathcal{G}_{max,0}$ and a_0 are the initital energy release rate and crack length, while $\mathcal{G}_{max,f}$ and a_f are the energy release rate and crack length at the end of the test.

where $m_{\mathcal{G}}$ and n are the slope and the y-intercept, respectively:

$$m_{\mathcal{G}} = \frac{\mathcal{G}_{max,f} - \mathcal{G}_{max,0}}{\mathcal{G}_c(a_f - a_0)}, \tag{4.2}$$

$$n = \frac{\mathcal{G}_{max,0}}{\mathcal{G}_c} - m_{\mathcal{G}}\, a_0, \tag{4.3}$$

Assuming a linear elastic behavior of the specimen, the energy release rate reads [16]:

$$\mathcal{G} = \frac{P^2}{2\,b}\frac{\mathrm{d}C}{\mathrm{d}a}, \tag{4.4}$$

thus, the minimum cyclic displacement, U_{min}, is related to $\mathcal{G}_{max}$ by :

$$U_{min} = -\sqrt{\frac{2\ b\ \mathcal{G}_{max}\ C^2}{\mathrm{d}C/\mathrm{d}a}}, \tag{4.5}$$

where b is the width of the specimen and C is the specimen's compliance (U/P, where P is the load). The compliance of the specimen increases as the crack length grows. The dependence $C(a)$ is experimentally determined by a series of static tests at different crack lengths (compliance calibration)[66, 67]:

$$C(a) = m_{cc}\ a^3 + C_0, \tag{4.6}$$

where m_{cc} and C_0 are fitting parameters.

Equations (4.1) to (4.6) can be used to write the dependence of U_{min} with the specimen compliance measured in real time:

$$U_{min}(C) = -\sqrt{\frac{2\ b\ \mathcal{G}_c \left[m_{\mathcal{G}} \left(\frac{C-C_0}{m_{cc}} \right)^{1/3} + n \right]}{3\ m_{cc} \left(\frac{C-C_0}{m_{cc}} \right)^{2/3}}}, \tag{4.7}$$

Following this equation, the load severity would sweep the desired range (Figure 4.2). The compliance can be easily measured in real time with current computerized testing systems, [134]. However, the control of the displacement based on the measurement of the compliance and Equation (4.7) is problematic because of the inherent scatter of the experimental measurement, C, and the lack of data at the initiation of the test. It is thus preferable to base the control of the test on a certainly well-behaved variable, as the number of cycles, N, is.

To deduce the $U_{min}(N)$ function, a relation between the crack length (or, equivalently, the compliance, Equation (4.6)) and the number of cycles is necessary. Here, it is assumed that the crack growth rate follows the Paris' law based expression [125]:

$$\frac{\mathrm{d}a}{\mathrm{d}N} = A\left(\frac{\mathcal{G}_{max}}{\mathcal{G}_c}\right)^p, \tag{4.8}$$

Although the simplest expression of the Paris like power law has been used to relate crack growth to the energy release rate, it is worth noting that the methodology described here can also be used with other fatigue data representations based on the existing formulation for metals, such as the NASGRO equation [53] or its adaptation for composite materials [74].

The pre-exponential factor, A, and the exponent, p, in Equation (4.8) are not yet known (in fact, the ultimate objective of the experimental characterization is to find them). Therefore, the parameters A and p, should be estimated before the test. The consequence of making use of erroneous parameters is that the load severity range explored would not be the one expected (Figure 4.2). In any case, a reasonable assumption would allow a much larger domain, with respect to the one achieved by means of a constant cyclic displacement experiment, to be explored. Parameters A and p can be taken from specimens of similar fibre and reinforcement or from preliminary experiments performed at constant displacement over the system studied.

The estimated A and p parameters are used to find the expression that relates the crack length to the number of cycles, by integrating Equation (4.8):

$$a(N) = \frac{\left(\alpha\, N + \beta\right)^\gamma - n}{m_{\mathcal{G}}}, \tag{4.9}$$

where:

$$\alpha = A\, m_{\mathcal{G}}(1-p), \tag{4.10}$$

$$\beta = \left(m_{\mathcal{G}}\ a_0 + n\right)^{1-p}, \tag{4.11}$$

and

$$\gamma = \frac{1}{1-p}. \tag{4.12}$$

Finally, by substituting equations (4.1), (4.9), and (4.6) and its derivative, into Equation (4.5), the functions of the minimum cyclic displacement with the number of cycles reads:

$$U_{min}(N) = -\sqrt{\frac{2\ b\ \mathcal{G}_c\ \left(\alpha\ N+\beta\right)^{\gamma}\ \left(m_{cc}\left(\frac{\left(\alpha\ N+\beta\right)^{\gamma}-n}{m_{\mathcal{G}}}\right)^{3}+C_0\right)^{2}}{3\ m_{cc}\left(\frac{\left(\alpha\ N+\beta\right)^{\gamma}-n}{m_{\mathcal{G}}}\right)^{2}}}. \tag{4.13}$$

Hence, the minimum cyclic displacement is a function of the number of cycles, N, the specimen width, b, the initial conditions, a_0 and $\mathcal{G}_{max,0}/\mathcal{G}_c$, the user-defined gradient of energy release rate, $m_{\mathcal{G}}$, the static compliance calibration parameters obtained prior to the fatigue test, m_{cc} and C_0, and, finally, the Paris' law parameters, A and p. In all events, $U_{min}(N)$ is calculated previous to the fatigue test, so that the displacement can be automatically shed in a continuous manner by implementing Equation (4.13) in the control software of the testing machine.

In this work, it is assumed that the fatigue delamination growth, under pure mode II loading conditions, depends only on the peak energy release rate, $\mathcal{G}_{max}$, and the load ratio (equivalent to the minimum to maximum cyclic displacement ratio, $R = U_{min}/U_{max}$, for small deflections). That is, it is assumed that the crack growth rate is neither history dependent nor dependent on the crack length, which is in agreement with other experimental evidence obtained from $\mathcal{G}_{max}$-constant tests with carbon/epoxy composites [18, 67, 161].

4.2 Experimental

The validity of the test method to characterize mode II delamination growth was evaluated by comparing the crack growth rate curves obtained in variable (described in Section 4.1) and constant cyclic displacement tests. As the range of crack growth was very narrow in the latter case, a multiplicity of constant cyclic displacement tests were performed. The Paris' law parameters were determined by both methods. In addition, this exemplification allowed for a detailed comparison to be made of the effort saved by following the new experimental methodology proposed in this chapter.

The laminates were 16 unidirectional carbon fiber/epoxy prepreg plies of 0.184 mm of nominal thickness stacked with the same fiber orientation (0^o). Panels were cured in an autoclave, following the supplier's recommendations, at AERNNOVA Engineering facilities. Before cutting the specimens, the panels were ultrasonically C-scanned. 3-ENF test specimens cut from these laminates were 25 mm wide, 3 mm thick and 200 mm long. A 30 μm thick and 60 mm length Teflon insert was introduced in the mid plane to create an artificial delamination. This teflon film was thicker than that usually recommended for static testing [45]; however, pre-cracking was expected to avoid any possible negative effect resulting from the insert [162, 76]. Precracks were performed under mode I quasi-static loading conditions until the increment in crack length was between 3 mm and 5 mm. The teflon film was removed from the crack after the pre-cracking procedure.

All the tests were carried out in a servohydraulic MTS Bionix® testing machine (25 kN of load capacity) under displacement control. The total force carried by the test specimen was measured with a 5kN MTS load cell. The three-point bending rig used to perform the tests met the specifications described in the ASTM standard for static testing [45]. The support rollers were 5 mm in radius, each with a span length between them of 100 mm. Some tests under constant cyclic displacement conditions were performed with a span length between supports of 120 mm (longer than the standard), to enlarge the range for crack extension (see Table 4.1). Tests were performed at AMADE Research lab, the mechanical testing laboratory of the University of Girona.

The fatigue tests were performed under displacement control, by applying a sinusoidal waveform at a frequency of 5 Hz and setting the ratio of minimum to maximum displacement per cycle, R, to $-10/(-3)$. The desired severity at the beginning of the test was defined by the ratio of the initial maximum cyclic energy release rate, $\mathcal{G}_{max,0}$, to the mean value of critical energy release rate, $\mathcal{G}_c$, measured by quasi-static tests carried out prior to the fatigue test on identical test specimens. Assuming that the behavior of the specimen was linear elastic, the selection of the initial minimum displacement, $U_{min,0}$, was related to $\mathcal{G}_{max,0}$ using equations (4.5), and (4.6) and its derivative, and the initial crack length, a_0,:

$$U_{min,0} = -\frac{\left(m_{cc}(a_0)^3 + C_0\right)}{a_0}\sqrt{\frac{2\ b\ \mathcal{G}_{max,0}}{3\ m_{cc}}} \tag{4.14}$$

A maximum initial severity, $\mathcal{G}_{max,0}/\mathcal{G}_c$, of 0.55 is established to avoid the horizontal movement of the sample occurring for displacements below -3.5 mm. Other authors use mechanical restraints to avoid this [34] although this could affect the results.

The TestStar v3.5C control software for the MTS servohydraulic testing machine includes a "Calculated Channels" option that allows for internal variables, either external inputs or calculated through simple arithmetic operations, to be generated. It was used to compute the dynamic compliance, C^*, by processing the instantaneous signals of load and displacement in line with the methodology described in [134]. Next, the crack length was derived from the dynamic compliance using Equation (4.6):

$$a = \sqrt[3]{\frac{C^* - C_0}{m_{cc}}} \tag{4.15}$$

One set of data (the dynamic compliance, C^*, the minimum cyclic load, P_{min}, and the number of cycles, N) was recorded every cycle and, as such, the crack length was calculated at the same monitoring frequency leading to a continuous $a(N)$ curve. Subsequently, the crack growth rate, $\frac{\mathrm{d}a}{\mathrm{d}N}$, was obtained from the numerical derivative of the $a(N)$ curve. The recommended data reduction techniques for the ASTM standard [20] are the secant and the incremental polynomial methods. However, when these methodologies are applied to high frequency data acquisition

curves, errors can occur because the dynamic compliance scatter might be too large compared to the increment in number of cycles between two successive data. For this reason, in this work the derivative was performed by linear regression of wider data sets, grouped so that the total increment of crack extension of each set was 0.1 mm [158].

Finally, $\frac{\mathrm{d}a}{\mathrm{d}N}$ was referred to the maximum energy release rate of the cycle normalized to the quasi-static critical value, $\mathcal{G}_{max}/\mathcal{G}_c$, or load severity. Taking Equation (4.4) and the derivative of the compliance calibration (4.6), $\mathcal{G}_{max}$ reads:

$$\mathcal{G}_{max} = \frac{3\, m_{cc}\, P_{min}^2\, a^2}{2\, b}, \tag{4.16}$$

where the crack length, a, is taken at the midpoint of the cycle.

Constant displacement tests were performed using eight different initial severities in order to cover a wider portion of the $\frac{\mathrm{d}a}{\mathrm{d}N}$ curve and the results were fitted together using the modified Paris' law from Equation (4.8).

The energy release rate does not evolve monotonically with the crack extension, but rather increases and then decreases under constant cyclic displacement, and with the maximum point (point 2 in Figure 2.14.a always being located at a=0.7L. Therefore, constant cyclic displacement tests were performed with initial crack length higher than 0.7L, in order to avoid sweeping the same part of the crack growth rate curve twice (c.f. Figure 2.14.b). In contrast, in variable cyclic displacement tests the initial crack length is not a limiting parameter because the dependence between the load severity and the crack length is monotonic. In this specific case, different crack lengths were chosen in order to analyze the influence of the initial conditions on the resultant crack growth rate curve.

Table 4.1 indicates the initial conditions for each propagation test. The specimens labeled "V" were tested by applying the variable cyclic displacement methodology presented in this work and the specimens labeled "C" were tested under constant cyclic displacement conditions.

Tab. 4.1.: Initial conditions for the propagation tests. In the specimen identification, "V" stands for variable displacement tests and "C" stands for constant displacement tests.

Specimen ID	Initial load severity $\mathcal{G}_{max,0}/\mathcal{G}_c$ [-]	Initial crack length a_0 [mm]	Mid-span length L [mm]	Initial minimum displacement $U_{min,0}$ [mm]
01_V	0.50	30.0	50.00	-3.108
02_V	0.50	35.0	50.00	-3.075
03_V	0.50	38.0	50.00	-3.071
04_C	0.55	38.0	50.00	-3.356
05_C	0.40	38.0	50.00	-2.770
06_C	0.30	38.0	50.00	-2.543
07_C	0.25	45.0	60.00	-3.096
08_C	0.20	38.0	50.00	-2.104
09_C	0.18	45.0	60.00	-2.743
10_C	0.14	45.0	60.00	-2.347
11_C	0.12	45.0	60.00	-2.223

For the variable cyclic displacement tests, the "Calculated Channels" from the MTS TestStar v3.5C software allowed an internal variable to be calculated (in accordance with Equation (4.13)) in real time. This variable was established as the continuous displacement setpoint, U_{min}.

Table 4.2 lists the parameters used for calculating of $U_{min}(N)$ (Equation (4.13)). The Paris' law parameters, A and p, obtained in the $\frac{\mathrm{d}a}{\mathrm{d}N}$ data fitting resulting from tests 07_C, 09_C, 10_C and 11_C, were used to estimate the curve $U_{min}(N)$ for test 01_V. The results from tests 06_C and 08_C were added to the previous data to obtain A and p for tests 02_V and 03_V.

Constant cyclic displacement tests were performed on specimens with a mode I pre-crack, whereas the variable cyclic displacement tests were performed on specimens already tested under constant cyclic displacement (thus having a mode II fatigue pre-crack). The reason for this was to avoid the transient behavior observed at the onset of delamination for specimens with a mode I pre-crack, as described further in sections 4.3 and 4.4.

Tab. 4.2.: Parameters used in the minimum variable displacement calculation, U_{min}, using Equation (4.13).

Specimen ID	Specimen width	Initial crack length	Estimated fatigue life constants (eq. 4.8), $\frac{\mathrm{d}a}{\mathrm{d}N}$ evaluated in mm/cycle		Compliance calibration parameters (eq. 4.6)		Energy release rate - crack length relation constants (eq. 4.1)	
	b [mm]	a_0 [mm]	A	p	m_{cc} [$N^{-1}mm^{-2}$]	C_0 [mm N^{-1}]	$m_{\mathcal{G}}$ [mm^{-1}]	n (-)
01_V	25.00	30.0	$6.192\ 10^{-2}$	3.674	$3.193\ 10^{-8}$	$2.608\ 10^{-3}$	-0.030	1.400
02_V	25.00	35.0	$5.595\ 10^{-2}$	3.695	$3.131\ 10^{-8}$	$2.626\ 10^{-3}$	-0.090	3.650
03_V	25.00	38.0	$5.595\ 10^{-2}$	3.695	$3.188\ 10^{-8}$	$2.594\ 10^{-3}$	-0.225	9.050

4.3 Results

A typical crack growth rate curve ($\frac{\mathrm{d}a}{\mathrm{d}N}$ vs severity) in a specimen pre-cracked under mode I and loaded under constant displacement amplitude exhibits three distinct stages (c.f. Figure 4.3). As the severity decreases from the onset of the test, the curve sweeps from right to left. The first region is characterized by a growing crack growth rate as the severity decreases. Then, the largest region (i.e. the second region), consists of a smooth direct dependence between $\frac{\mathrm{d}a}{\mathrm{d}N}$ and severity. Finally, in the third region the crack tends to arrest with a higher slope than that seen in the second region. For these reasons discussed in the next section, the curve was truncated, neglecting the first and third regions. Only the mid-region was considered in the modified Paris' law calculation.

As variable displacement tests were performed on specimens already tested under mode II, their crack growth rate curves did not show the first region of Figure 4.3. Figure 4.4 compares the preselected and the experimental dependence between the severity and the crack length increment, confirming the new experimental methodology as being suitable to enlarge the range of severities explored in a single test.

The crack growth rate curve in Figure 4.5 condensates the results obtained from the eleven tests performed in this study. All the tests were performed for the same load ratio, $R = -10/(-3)$, either under constant cyclic displacement or variable cyclic displacement control. The plot also includes the fitting of all the data from

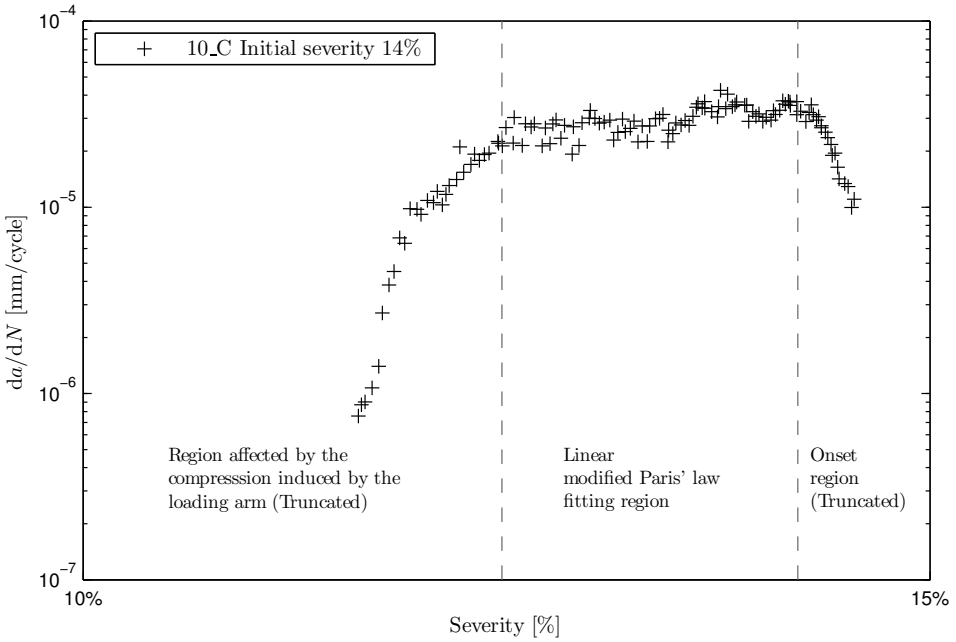

Fig. 4.3.: Reduced fatigue crack growth rate data with the truncated regions in the modified Paris' law fitting from the constant cyclic displacement tests.

the constant cyclic displacement tests in accordance with the modified Paris' law (Equation (4.8)).

The parameters of the modified Paris' law (Equation (4.8)), the exponent, p, and the coefficient, A, are obtained from the linear fitting of the data plotted on log-log scales (Table 4.3).

The duration of each variable cyclic displacement test depends on the slope of the relation between the energy release rate and crack length, $m_{\mathcal{G}}$ (Figure 4.4). Higher slopes tend to minimize the testing time. The total time employed in all tests (constant displacement and variable displacement) is specified in Table 4.4.

Tab. 4.3.: Fatigue life constants obtained from both variable displacement and constant displacement tests.

Specimen ID	Energy release rate slope - crack length relation (eq. 4.1)	Obtained fatigue life constants (eq. 4.8), $\frac{\mathrm{d}a}{\mathrm{d}N}$ evaluated in mm/cycle	
	$m_{\mathcal{G}}$ [mm^{-1}]	A	p
01_V	-0.030	$1.975 \cdot 10^{-1}$	4.326
02_V	-0.090	$1.677 \cdot 10^{-1}$	4.168
03_V	-0.225	$7.342 \cdot 10^{-2}$	3.786
Modified Paris' law (Eq. 4.8) fitting of the constant displacement tests' results		$7.636 \cdot 10^{-2}$	3.882

Tab. 4.4.: Time employed in obtaining the crack growth rate curve for both variable and constant minimum displacement methodologies.

	Specimen ID	Total time (hours)	Time 10-45% severity (hours)
Variable displacement tests	01_V Severity from 50% to 10%	42.0	4.3
	02_V Severity from 50% to 10%	18.0	1.9
	03_V Severity from 50% to 10%	7.0	0.4
Constant displacement tests	04_C Initial severity 55%	0.2	
	05_C Initial severity 40%	1.3	
	06_C Initial severity 30%	2.6	
	07_C Initial severity 25%	4.0	
	08_C Initial severity 20%	8.8	
	09_C Initial severity 18%	15.5	
	10_C Initial severity 14%	48.1	
	11_C Initial severity 12%	89.1	
Total time employed in constant displacement testing		169.6	

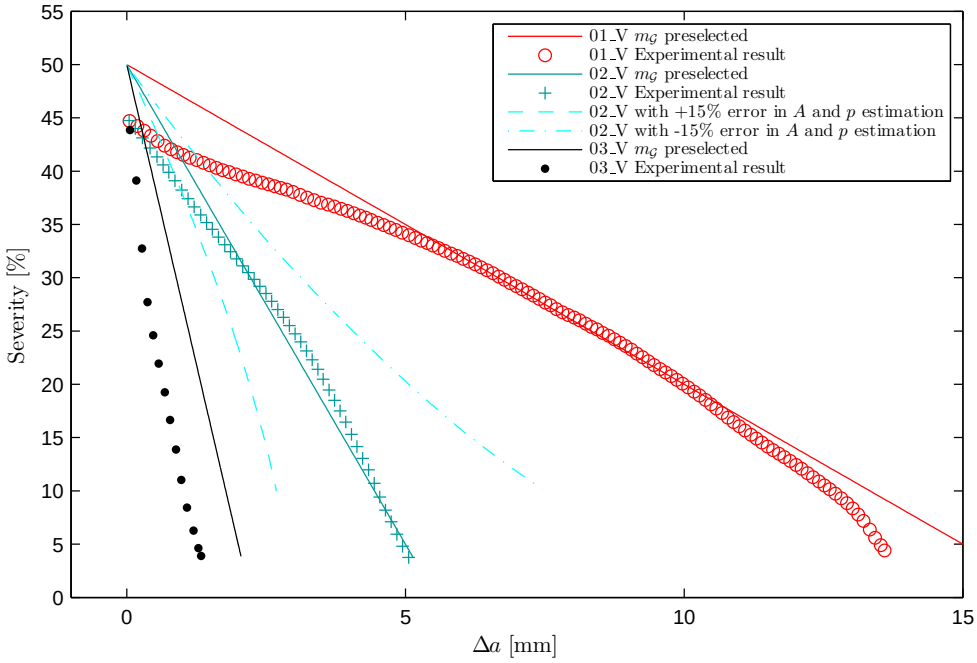

Fig. 4.4.: Comparison between the preselected slope, $m_{\mathcal{G}}$, from the energy release rate versus the crack length curve and the experimental relationship $\frac{\mathcal{G}_{max}}{\mathcal{G}_c} - \Delta a$ obtained from the variable displacement tests. Dashed lines illustrate the $\frac{\mathcal{G}_{max}}{\mathcal{G}_c} - \Delta a$ relation obtained if the Paris' law parameters, A and p, used in the calculation of $U_{min}(N)$ in test 02_V, were predicted with an error of $\pm 15\%$.

4.4 Discussion

The proposed experimental methodology for mode II testing in the 3-ENF configuration enables a chosen range of load severities to be swept while the crack grows in a predefined crack length increment. This is accomplished by varying the applied cyclic displacement as the number of cycles evolves. The $U_{min}(N)$ function depends on estimated Paris' law parameters, A and p, derived from the constant cyclic displacement tests. In spite of being just a rough estimation, the range of severities swept is close to the desired one and, in any case, much larger than what could be obtained from a constant displacement test. The consequence of using erroneous parameters is illustrated in Figure 4.4 for the specimen 02_V. An error in A and p of $\pm 15\%$ leads to changes in the crack length increment needed to sweep the desired

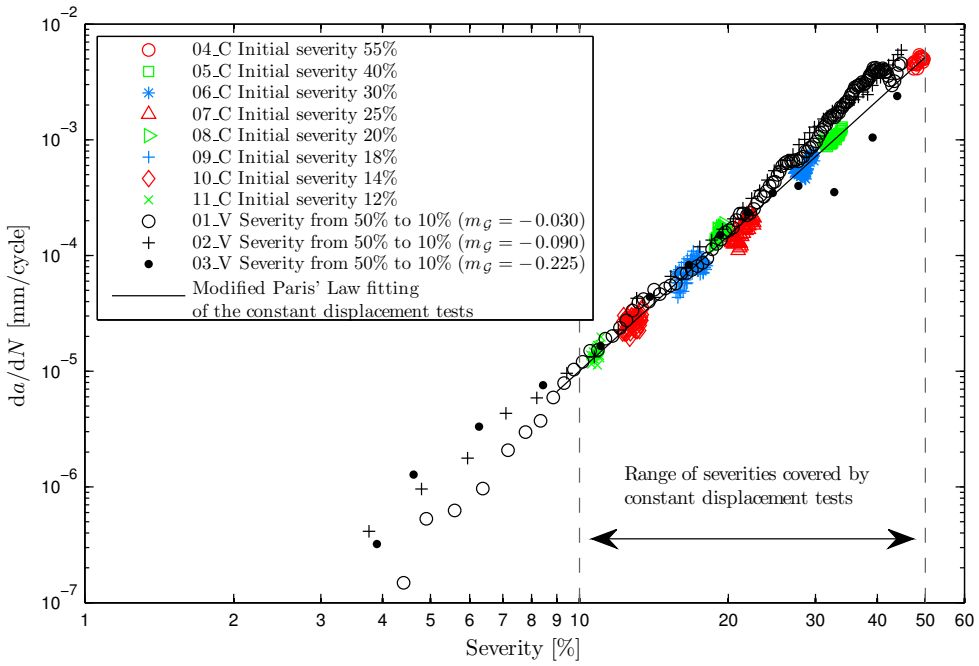

Fig. 4.5.: Relation between crack propagation rate and peak energy release rate for R=0.3. The results from both variable displacement ("V" labelled) and constant displacement ("C" labelled) tests are presented for comparison proposes.

severity range. In any event, the severity range achieved would be much larger than that attained using a constant displacement test.

The variable cyclic displacement method leads to crack growth rate data practically indistinguishable from that resulting from the complete set of eight constant displacement tests. In particular, the Paris' exponent, p, obtained from variable cyclic displacement tests under steady growth conditions (severities from 10 to 30%), deviated from the log-linear fitting of the constant cyclic displacement tests results by +11.4%, +7.4% and -2.5% (specimens 01_V, 02_V and 03_V, respectively). No experimental data for severities higher than 45% could be obtained because of specimen horizontal movement. The agreement between the results from both methods, however, is expected to persist if this issue could be solved practically.

One of the main advantages of the new experimental methodology is the reduction of the time duration of the fatigue mode II test. The selection of the shedding rate,

$m_{\mathcal{G}}$, determines the duration of the test. Table 4.4 exemplifies the time saved with this method. One single test performed with variable displacement to build the crack growth rate curve for a severity range between 10% and 45% is performed in 1.9 hours (specimen 02_V), while the 8 constant displacement tests needed to sweep the same severity range require 169.6 hours (80 times more if the times involved in setting up each of the tests is not considered).

The question arises of how fast the test can be carried out while still leading to the crack growth curve obtained in a constant displacement test. This question could be dealt with taking into account the formation of a failure process zone, FPZ, in front of the crack tip. While the FPZ for mode I delamination in CFRP is assumed to be so small as to be negligible in the data reduction of static interlaminar fracture toughness tests, the same does not apply for the FPZ in mode II tests [146]. Under mode II loading and for a given load severity, the crack growth rate would not reach its steady level until the FPZ is fully formed. In a variable displacement test, if the severity varies before the FPZ is fully formed, the crack growth rate would deviate from the steady crack growth rate for the actual severity being applied. This is more likely to happen as the shedding rate increases and that deviation would also be more important the stronger the variation of the FPZ with the load severity is.

Figure 4.5 illustrates the crack growth rate curves obtained from the variable cyclic displacement tests for the three shedding rates, $m_{\mathcal{G}}$, explored in this study. The tests performed at low $m_{\mathcal{G}}$ lie close to the Paris' curve of constant cyclic displacement tests from the very first stages of the crack growth curve (higher severities), whereas the test performed at high $m_{\mathcal{G}}$ (03_V) tends to deviate from these curves in the region of high (30-45%) and low ($< 10\%$) severities, while in the region in between the agreement is complete. The deviation of specimen 03_V at the beginning of the test (high severities) corresponds to the transient stage from the FPZ of the pre-crack to the steady FPZ. On the contrary, at lower severities, below 10%, the deviation is attributed to a shedding rate too fast to permit the stabilization of the FPZ, leading to a faster crack growth than observed in constant cyclic displacement tests. The confirmation of these hypothesis and the study of the FPZ zone in fatigue tests as a function of the load severity deserves further investigation.

These facts highlight the impact the pre-cracking stage has on the initial measurements of the crack growth rate curves. In the first stage of the crack growth curve for constant displacement tests in Figure 4.3 there is a clear evidence of the transient

region between the FPZ of the pre-crack and the steady FPZ. Indeed, due to the fact that the constant displacement tests start from a mode I pre-crack (short FPZ), the crack grows more slowly than the steady rate until the mode II FPZ is fully formed.

In view of the foregoing, the variable cyclic displacement tests were performed on specimens tested under mode II cyclic loading, where the crack grew until the tip reached the zone affected by loading arm compression (“Region affected by the compression induced by the loading arm" in Figure 4.3). In this region, the crack propagation tends to arrest, misrepresenting an artificial threshold. The FPZ formed in this situation (low severity), however, is different from the one expected at the beginning of the variable displacement tests (high severity). For that reason, a transient region in the variable displacement tests is expected. While this is not noticeable in specimens with low $m_{\mathcal{G}}$, it does span over several points for specimen 03_V.

The fact that the three crack growth curves obtained under variable cylic displacement amplitude with different $m_{\mathcal{G}}$ coincide in the severity range between 30% and 10% indicates that the shedding rate is slow enough to lead to a fully developed FPZ, even with the highest $m_{\mathcal{G}}$ selected (c.f. Figure 4.5). The prospect is that for a large enough $m_{\mathcal{G}}$, the crack growth curve would deviate from that of the constant displacement test. Following an equivalent rationale, the crack length increment can not be decreased arbitrarily if representative results are to be obtained. Figure 4.4 shows that the same Paris' law curve is obtained for crack increments of 2 mm (specimen 03_V) or 14 mm (specimen 01_V). These constraints should be specifically considered when testing materials with expected large FPZ, as the case of adhesive joints is. The larger the expected FPZ, the slower the shedding rate should be and, likewise, the larger the crack increment to be traveled.

The comparison of the results from constant cyclic displacement tests reveals that the propagation rate does not depend on the span length (e.g. specimens 07_C and 08_C, with span lengths of 60 and 50 mm respectively, have similar da/dN at 20% severity). Thus, the same results are obtained with different crack lengths. This is an indication that, for the material studied, the crack growth rate is history independent under mode II test conditions when a steady crack growth is achieved (initial transient curves must be truncated, Figure 4.3). This assertion is corroborated by the overlap among the crack growth rate curves obtained with the three variable displacement tests performed with different preselected gradients of energy release rate, $m_{\mathcal{G}}$

(see Table 4.3), again, once the FPZ is fully developed. Under this condition, the maximum difference in $\frac{\mathrm{d}a}{\mathrm{d}N}$, for a given severity, between the data obtained from variable displacement tests and the fitting of all the data from constant displacement tests, amounts 0.3 decades. This is comparable to the scatter of the raw data from a single constant displacement test.

In addition, the methodology derived in this chapter has been extended for MMB fatigue tests in [73]. The contribution of [73] relies in the compliance calibration to obtain a continuous crack length curve, $a(N)$. This compliance calibration is carried out by relating the dynamic compliance recorded in real time during the fatigue test [134] to the crack length extracted from photos that are taken while the fatigue test is running. In this way, the measurment of the crack length during the fatigue test is avoided and a continuous crack growth rate curve is obtained.

Material card definition

5

This chapter presents the experimental determination of all the parameters needed to feed the three-dimensional computational method developed.

The procedures followed for the characterization of the interlaminar properties are listed in Table 5.1. All the tests were conducted at AMADE Research lab, the mechanical testing laboratory of the University of Girona, which is Nadcap [6] (Non-metallic materials testing laboratory) and ISO 17025 [72] accredited. Since the quasi-static properties $\mathcal{G}_{Ic}$, $\mathcal{G}_{IIc}$, $\mathcal{G}_{50\%c}$, $\mathcal{G}_{75\%c}$ and τ_{IIo}, were obtained following standard procedures, special attention is given to the characterization of the fatigue properties under mode I (p_I, A_I, $\mathcal{G}_{Ith}$), mode II(p_{II}, A_{II}, $\mathcal{G}_{IIth}$), 50% mixed-mode ($p_{50\%}$, $A_{50\%}$) and 75% mixed-mode ($p_{75\%}$, $A_{75\%}$).

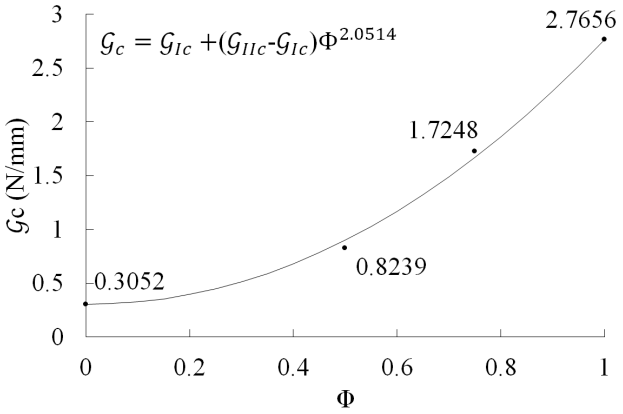

Fig. 5.1.: Mode interpolation of the fracture toughness [29].

The interlaminar fracture toughness were measured under 4 different mode mixity conditions: 0% ($\mathcal{G}_{Ic}$), 50%, 75% and 100% ($\mathcal{G}_{IIc}$). Following the standards recommendations, a batch of five different specimens were tested for each property. The nominal values are represented in Figure 5.1. The Benzeggagh-Kenane [29] mode interpolation parameter, η, in Equation 2.27 has been fitted to the results. It is worth mentioning that the mode II fracture toguhness, $\mathcal{G}_{IIc}$, was obtained from the maximum force (MAX point in Figure 5.2), as recommended in the ASTM D7905

Tab. 5.1.: Testing procedures followed to obtain the material card.

Property	Procedure
$\mathcal{G}_{Ic}$	ASTM D5528
$\mathcal{G}_{IIc}$	ASTM D7905
$\mathcal{G}_{50\%c}$	ASTM D6671
$\mathcal{G}_{75\%c}$	ASTM D6671
τ_{IIo}	ASTM D2344
p_I, A_I	Multi-fatigue testing rig [135]
p_{II}, A_{II}	Rapid testing procedure (Section 4)
$p_{50\%}$, $A_{50\%}$	Rapid testing procedure [73]
$p_{75\%}$, $A_{75\%}$	Rapid testing procedure [73]
$\mathcal{G}_{Ith}, \mathcal{G}_{IIth}$	Modified ASTM D6115

standard procedure for mode II fracture toughness [45]. However, other criteria that are described in the ASTM D5528 standard [41] for mode I may be adopted. These are: the deviation from linearity (NL point in Figure 5.2) and visual observation of delamination growth (VIS point in Figure 5.2). If these criteria are applied, the mode II fracture toughness, $\mathcal{G}_{IIc}$, results in significantly lower nominal values (0.472 N/mm for the NL criterion and 0.535 N/mm for VIS criterion). The reason for such a difference on $\mathcal{G}_{IIc}$ depending on the criterion used is attributed to the formation of a large fracture process zone ahead of the crack tip when mode II loading conditions are applied. The formation of micro cracks reduces the compliance and thus, the force vs displacement relation becomes nonlinear, but the force keeps increasing. The sudden drop in the measured force, immediately after the MAX point, evidences unstable crack propagation. Thus, propagation values could not be obtained. It is worth mentioning that, under mode II loading conditions and for certain material systems, initiation values of the mode II fracture toughness, $\mathcal{G}_{IIc}$, are significantly lower than propagation values [145]. Nevertheless, the MAX point gives the most similar result to propagation values and, indeed, it is the only covered by the ASTM D7905 standard [45].

Moreover, the interfacial shear strength, τ_{IIo}, was measured following the ASTMD2344 standard. The nominal value is 98 MPa. Then, the interfacial tensile strength, τ_{Io}, is expressed as a function of τ_{IIo}, $\mathcal{G}_{Ic}$ and $\mathcal{G}_{IIc}$ as [168]:

$$\tau_{Io} = \tau_{IIo}\sqrt{\frac{\mathcal{G}_{Ic}}{\mathcal{G}_{IIc}}} \tag{5.1}$$

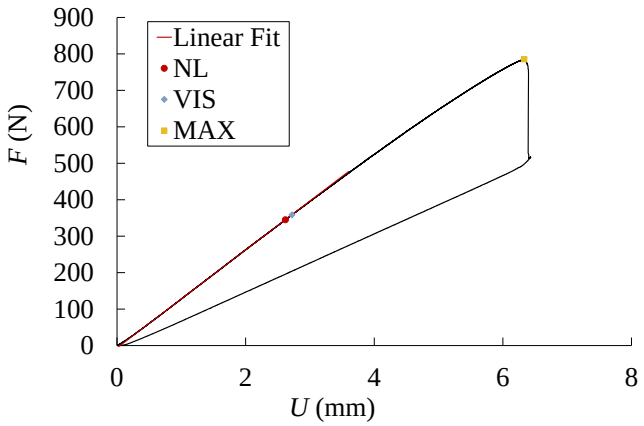

Fig. 5.2.: Load vs displacement curve from a quasi-static mode II ENF test.

Regarding fatigue characterization, parameters of the Paris' law-based expression of equations (2.55) and (2.56) were obtained from fatigue crack propagation tests for different mode mixities: p_I, A_I (mode I), p_{II}, A_{II} (mode II), $p_{50\%}$, $A_{50\%}$ (50% mixed mode), $p_{75\%}$ and $A_{75\%}$ (75% mixed mode).

Crack growth rate curves under mode I loading conditions were obtained using the multi-specimen testing methodology described in [135]. Two batches, of 6 specimens each, were tested under constant cyclic displacement with a load ratio of R=0.1. A third batch was tested with R=0.5 to investigate the effect of the load ratio in mode I fatigue properties. The crack growth rate curves of one of the batches tested with R=0.1 are represented in a single plot in Figure 5.3. Six different initial severities were applied by using different initial crack lengths. The overlapping of the curves is clearly observed, independently of the severity applied. The dispersion of the results is less than 1 decade, similar to what is obtained in other studies such as in [158].

Tests performed with a load ratio of R=0.1 and R=0.5 are compared in Figure 5.4. Moreover, the fatigue characterization campaign performed to obtain the material card was numerically simulated. Thus, 2D simulations of the fatigue DCB tests under different load ratios are compared to experimental data. Simulations were carried out by modeling the central slice of the specimen, with only one element in the width direction, and by applying plain strain conditions. The elastic properties of the unidirectional laminate, listed in Table 5.2, were provided by AERNNOVA

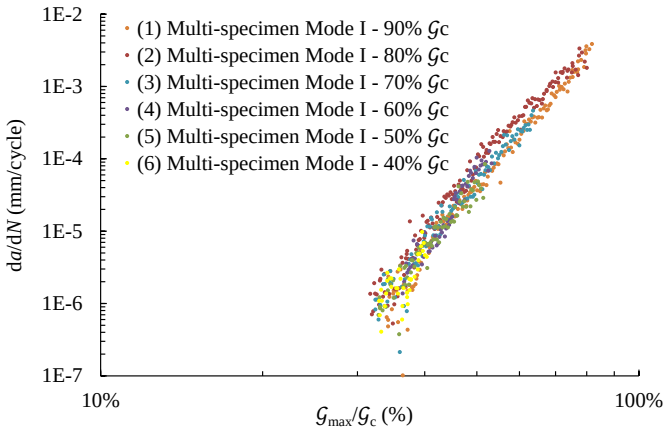

Fig. 5.3.: Crack growth rate, $\frac{\mathrm{d}a}{\mathrm{d}N}$, versus severity, $\mathcal{G}_{max}/\mathcal{G}_c$, of a batch of 6 specimens tested simultaneously using the multi-specimen testing devise presented in [135] with a load ratio R=0.1 and 6 initial different severities.

Engineering, the company supplying the CFRP composite material. The simulation input values for the crack growth rate exponent, p, and coefficient, A, were obtained from the Paris' law-like fitting of experimental fatigue propagation data.

Tab. 5.2.: Laminate elastic properties of the validator material.

Laminate properties		
E_{11}: Longitudinal Young's modulus	154	GPa
$E_{22} = E_{33}$: Transversal Young's modulus	8.5	GPa
$G_{12} = G_{13}$: Shear modulus in the longitudinal planes	4.2	GPa
G_{23}: Shear modulus in the transversal plane	3.036	GPa
$\mu_{12} = \mu_{13}$: Poison's coefficient in the longitudinal planes	0.35	-
μ_{23}: Poison's coefficient in the transversal plane	0.4	-

Regarding mode II fatigue loading conditions, the crack growth rate curve in Figure 5.5.a presents the results obtained from eight fatigue ENF tests performed under constant cyclic displacement with a load ratio of R=0.3. Figure 5.5.b condensates the eight constant cyclic displacement tests and two tests performed applying the efficient testing methodology presented in Section 4. In comparison, the 8 constant displacement tests needed to sweep the same severity range require 169.6 h (80 times more without considering the time involved in setting up each of the tests).

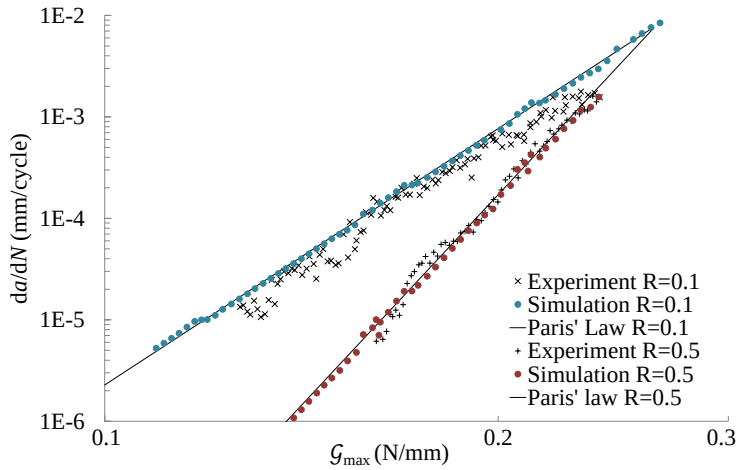

Fig. 5.4.: Comparison between the experimentally obtained mode I crack growth rate curves and the results form the 2D simulations using the method presented in [23]. The input parameters p_I and A_I are obtained from the Paris' law-based fitting of the experimental data.

The effect of load ratio was also analyzed under mode II fatigue loading conditions, and compared with simulation results. Figure 5.6 shows the results obtained for R=0.1 and R=0.3 (Note that the sign convention for negative for displacements which result in compressive reaction forces is no longer used. From now on, the absolute value of the prescribed cyclic displacements is used to calculate the load ratio, R).

Similarly to ENF tests, the results from three fatigue MMB tests with a mode mixity of 50%, performed under constant cyclic displacement and with a load ratio of R=0.1, are plotted in Figure 5.7.a. In Figure 5.7.b., a range spanning from from 80% to 20% of severity was covered with one single variable displacement test. The fatigue testing time was less for the variable cyclic displacement test by -80% in comparison with the constant displacement tests. Also, the results obtained from 4 fatigue MMB tests with a mode mixity of 75%, performed under constant cyclic displacement with a load ratio of R=0.1, are plotted in Figure 5.7.a and compared with the results obtained from variable cyclic displacement tests in Figure 5.7.b. Again, the range of severity covered by a variable cyclic displacement test equaled the range covered by a series of 4 constant displacement tests. The wider the range of explored severity is, the more preparation and testing time can be saved using the variable

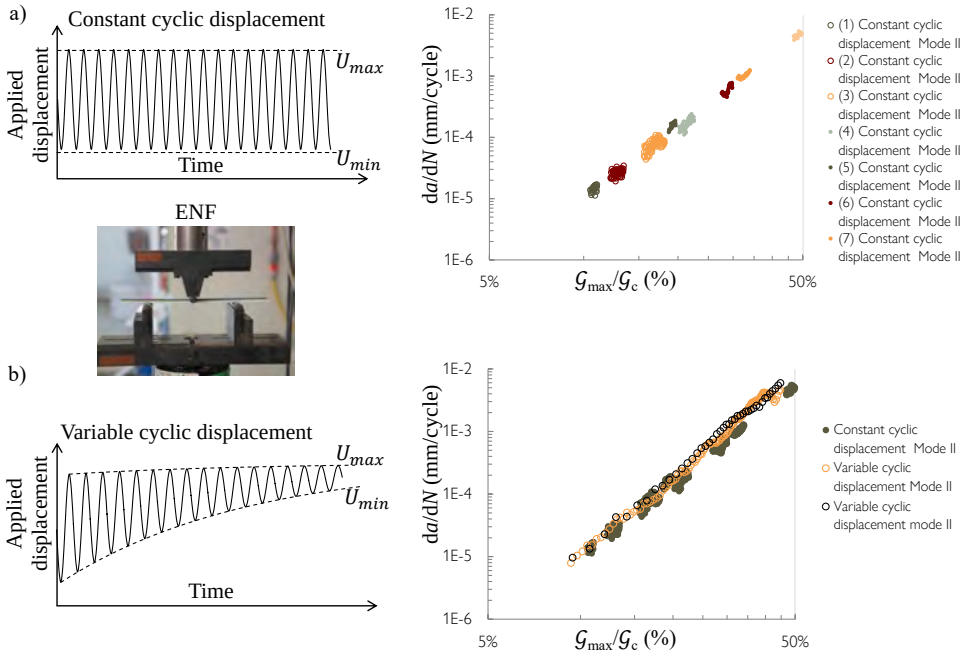

Fig. 5.5.: Crack growth rate, $\frac{\mathrm{d}a}{\mathrm{d}N}$, versus severity, $\mathcal{G}_{max}/\mathcal{G}_c$, under mode II loading conditions. Variable displacement tests are performed using the efficient testing methodology presented in Section 4 with a load ratio R=0.3.

cyclic displacement methodology in comparison with the traditional constant cyclic displacement test. For further information on the testing methodology and results, the reader is referred to [73]. Moreover, the experimental results are compared to numerical simulations in Figure 5.8.

In summary, the observed effect of the mode mixity, Φ, and the load ratio, R, on the crack growth rate curve in figures 5.4, 5.6 and 5.8 are in agreement with other experimental evidences published in the literature [25] and summarized in Section 2.3.2. Moreover, the simulation method is capable to reproduce with great accuracy the crack growth rate curve in all the analyzed loading conditions.

On the other hand, the mode I and mode II energy release rate threshold values, $\mathcal{G}_{Ith}$ and $\mathcal{G}_{IIth}$, have been obtained from fitting onset tests results performed under constant cyclic displacement. Experimental data has been fitted using Equation (2.4). The energy release threshold is set as the onset point for 2 million cycles.

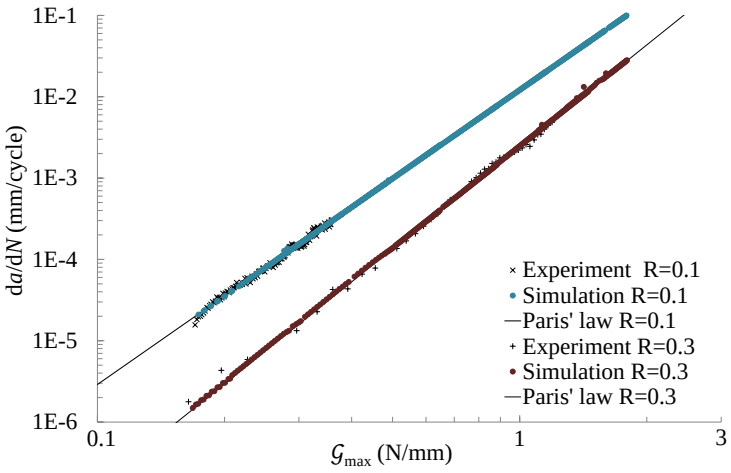

Fig. 5.6.: Comparison between the experimentally obtained mode II crack growth rate curves and the results form the 2D simulations using the method presented in [23]. The input parameters p_{II} and A_{II} are obtained from the Paris' law-based fitting of the experimental data.

For mode I, the multi-specimen testing rig was used. Thus, the onset point for 12 different severities (two batches, of 6 specimens each, tested with R=0.1) has been determined and plotted in Figure 5.9. Both criteria, a 1% and a 5% increase of the specimen's compliance relative to the initial value, are represented. From this data, the threshold value, $\mathcal{G}_{Ith}$, has been estimated to be at 24% $\mathcal{G}_{Ic}$ and 28% $\mathcal{G}_{Ic}$ using the criteria for 1% and 5% increase of the specimen's compliance, respectively. Moreover, in the specimens tested at 20% and 10% $\mathcal{G}_c$, propagation did not occur after 3 million cycles. Therefore, it is considered that under the extrapolated $\mathcal{G}_{Ith}$ value, no propagation occurs.

For mode II, 4 independent constant cyclic displacement tests with R=0.1 were performed near the energy release rate threshold region. The results are shown in Figure 5.10. Both criteria, a 1% and a 5% increase of the specimen's compliance relative to the initial value, are represented. From the fitting of this data using Equation (2.4), the onset value for 2 million cycles has been estimated to be at 2% $\mathcal{G}_{IIc}$ and 3% $\mathcal{G}_{IIc}$ using the criteria for 1% and 5% increase of the specimen's compliance, respectively. An experimental checking performed with a specimen tested at 3% $\mathcal{G}_c$ reveals that propagation did not occur even after 3 million cycles.

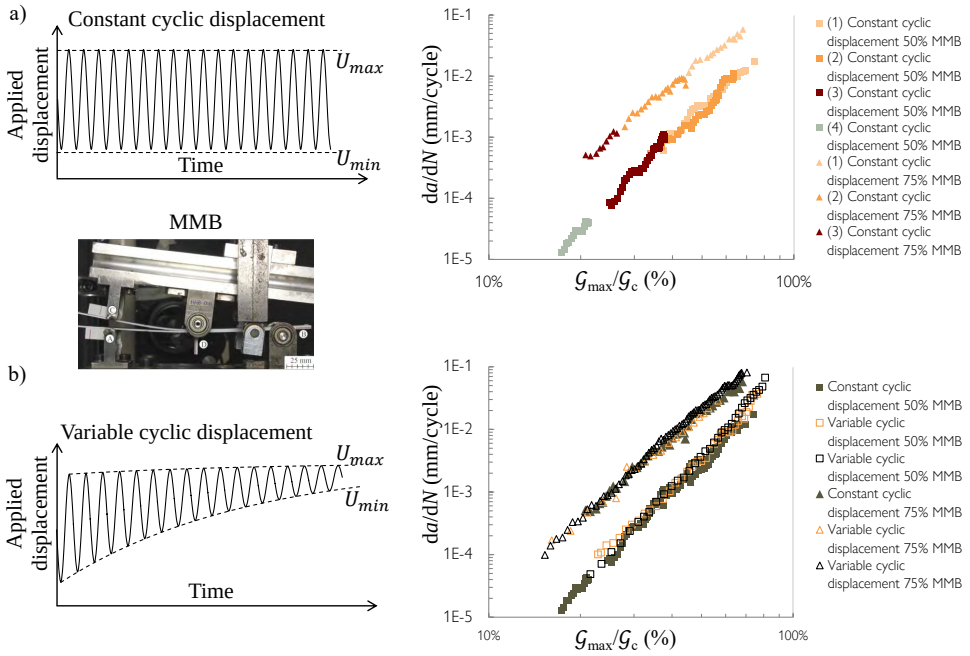

Fig. 5.7.: Crack growth rate, $\frac{\mathrm{d}a}{\mathrm{d}N}$, versus severity, $\mathcal{G}_{max}/\mathcal{G}_c$, under mixed mode loading conditions. Variable displacement tests are performed using the efficient testing methodology presented in [73] with a load ratio R=0.1.

It is worth mentioning that the absolute values for energy release rate thresholds for mode I and mode II with R=0.1 are very similar: using the criterion for 5% increase of the specimen's compliance, $\mathcal{G}_{Ith}$ = 28% $\mathcal{G}_{Ic}$ = 0.085 N/mm and $\mathcal{G}_{IIth}$ = 3% $\mathcal{G}_{IIc}$ = 0.083 N/mm. This is in agreement with the experimental works of [119, 19], which showed that, in the absence of fiber bridging, the fatigue threshold, $\mathcal{G}_{Ith}$, is independent of the mode mixity.

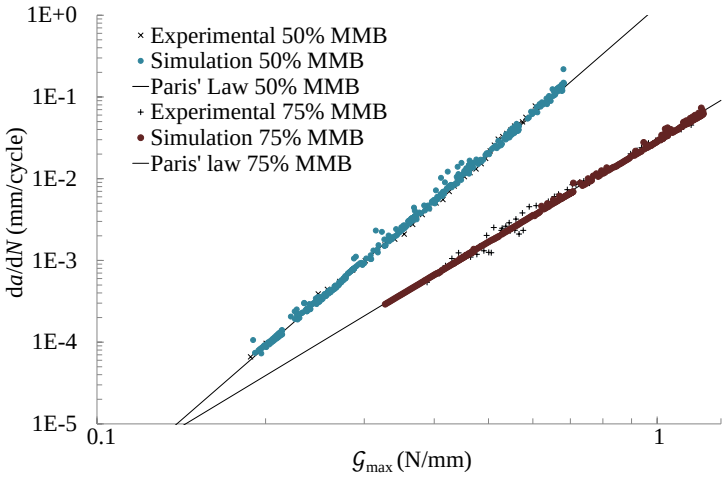

Fig. 5.8.: Comparison between the experimentally obtained 50% and 75% mixed-mode crack growth rate curves and the results form the 2D simulations using the method presented in [23]. The input parameters $p_{50\%}$, $A_{50\%}$, $p_{75\%}$ and $A_{75\%}$ are obtained from the Paris' law-based fitting of the experimental data.

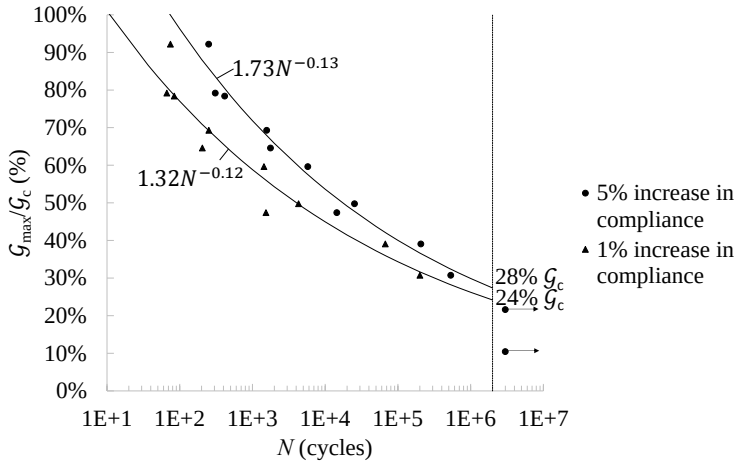

Fig. 5.9.: Onset curve obtained from 12 specimens tested under mode I loading conditions using the multi-specimen testing rig presented in [135]. The energy release rate threshold, $\mathcal{G}_{Ith}$, is extrapolated at 2 million cycles using the fitting of the onset values. The points with an arrow indicate that the run-out has been achieved without crack propagation.

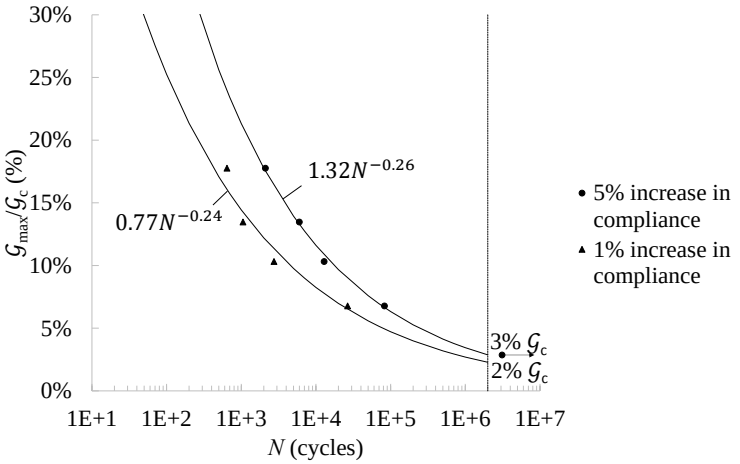

Fig. 5.10.: Onset curve obtained from 4 specimens tested under mode II loading conditions. The energy release rate threshold, $\mathcal{G}_{IIth}$, is extrapolated at 2 million cycles using the fitting of the onset values. The point with an arrow indicates that the run-out has been achieved without crack propagation.

6 Validation of the three-dimensional fatigue method

In order to evaluate the predictive capabilities of the simulation method developed in this Ph.D. thesis, a three-dimensional composite structure, representative of arbitrarily shaped delamination growth in a real structural component, has been designed and tested. Both quasi-static and fatigue tests were performed. Afterwards, the experimental results have been compared to the results predicted by the simulation tool.

6.1 Design of the demonstrator specimen

The design requirements for the demonstrator test are listed in the following:

- The shape of the delamination front must be curved and change during the test, since the simulation method must be applicable to arbitrarily shaped delamination fronts.
- The location and shape of the delamination front must be possible to monitor at selected testing times by means of non-destructive techniques in order to obtain data for comparison with numerical results from the simulations.
- The area of delamination must be confined between two subsequent layers. Thus, crack migration must be avoided.
- The geometry of the specimen must be simple, so it can be easily manufactured and tested.

The solution for test configuration adopted in this work, which fulfills the mentioned requirements, is a double cantilever beam (DCB) test on a symmetric run-out specimen

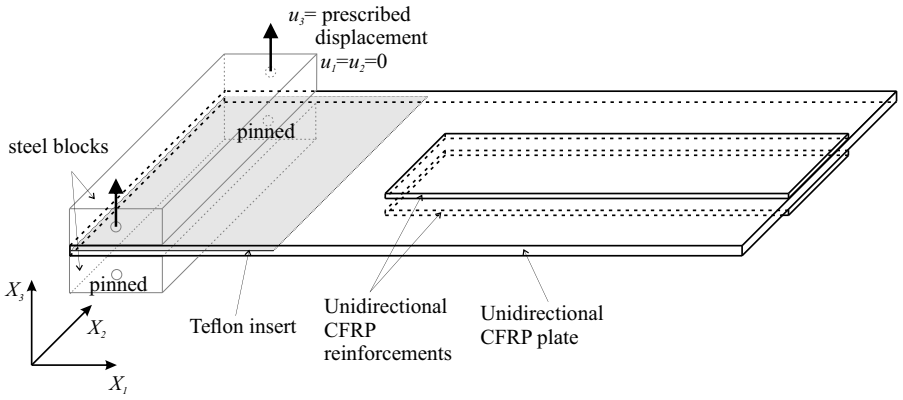

Fig. 6.1.: Sketch of the partially reinforced DCB specimen. The grey-shadowed area represents the Teflon insert.

with a midplane initial defect. A Teflon insert acts as an initial straight delamination (see Figure 6.1). Moreover, the middle width of the specimen is stiffened by bonding carbon fiber reinforced polymer (CFRP) reinforcements on the upper and lower faces. In this way, the stiffness along the specimen width is not constant. Consequently, during propagation, the crack front shape changes when it approaches the reinforced region. The dimensions of the DCB specimen are given in Figure 6.2.

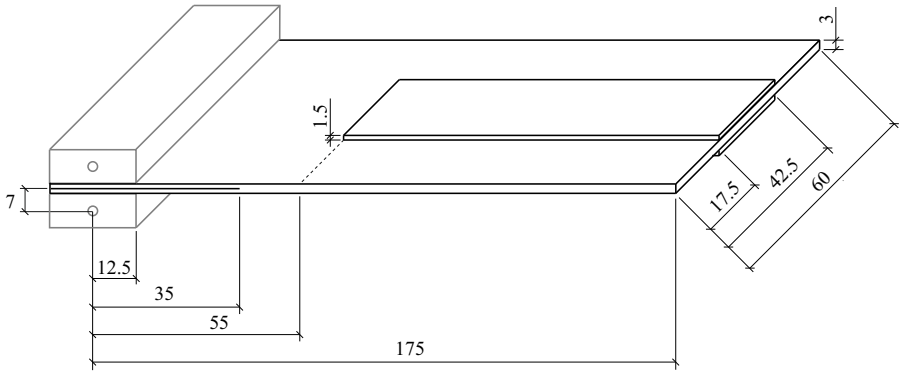

Fig. 6.2.: Dimensions of the partially reinforced DCB specimen (units in mm).

The specimens were made of unidirectional carbon fiber/epoxy prepreg plies of 0.184 mm of nominal thickness stacked with the same fiber orientation (0°). Panels were cured in an autoclave, following the supplier's recommendations, at AERNNOVA Engineering facilities. Before cutting the specimens, the panels were ultrasonically

C-scanned. The reinforcements were joined to the DCB plate using ARALDITE 2015 epoxy adhesive cured at room temperature. A picture of the partially reinforced DCB specimen is shown in Figure 6.3.

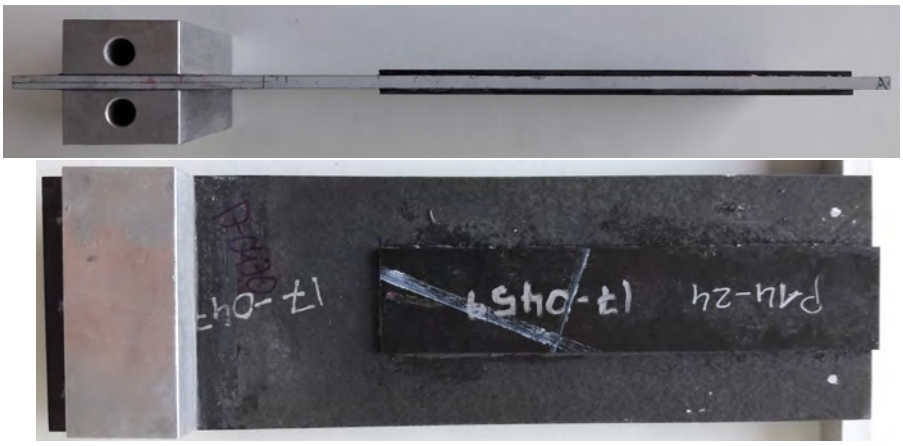

Fig. 6.3.: Partially reinforced DCB specimen.

6.2 Test methodology and post-processing of the results

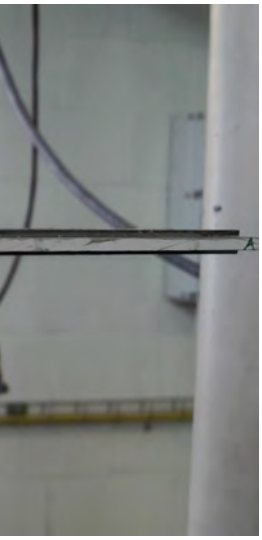

The tests were carried out in a MTS 858 servo-hydraulic Bionix testing machine in a controlled environment (23 $\pm$ 3°C and 50 $\pm$ 5% RH). The maximum load capacity of the testing machine was 25kN. The tests were performed under displacement control. The total force carried by the test specimen was measured with a 5 kN MTS load cell calibrated at 10% of the full range. The test rig is shown in Figure 6.4. Two different tests were performed: under quasi-static loading and under fatigue loading.

Following ASTM D5528 [41] standard recommendations, quasi-static tests were performed with a constant displacement rate of 1 mm/min. Three different specimens were tested stopping every 1 mm of accumulated opening displacement. In these stops, the specimen was removed from the test rig and mounted on an X-ray radiography equipment to monitor the delamination front location. In addition,

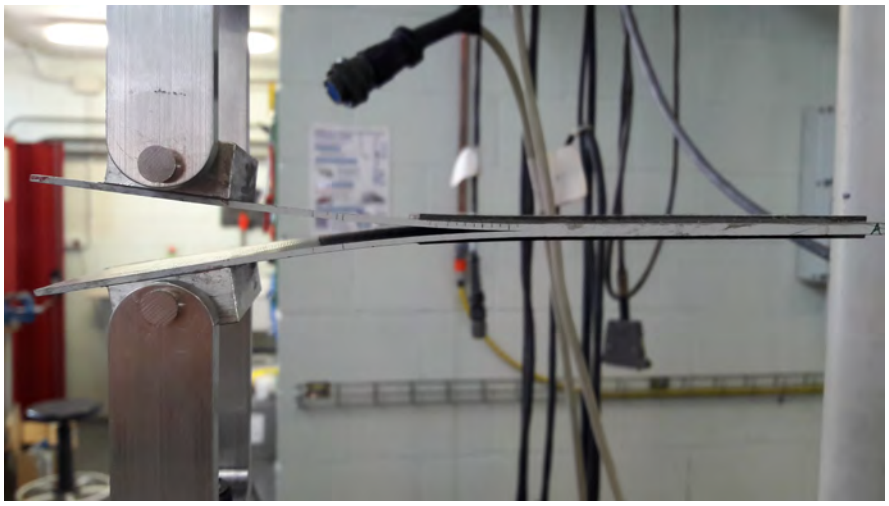

Fig. 6.4.: DCB test on partially reinforced specimen.

a fourth specimen was tested in a continuous manner and the delamination front location was inspected only at the end of the quasi-static test (15 mm of applied displacement).

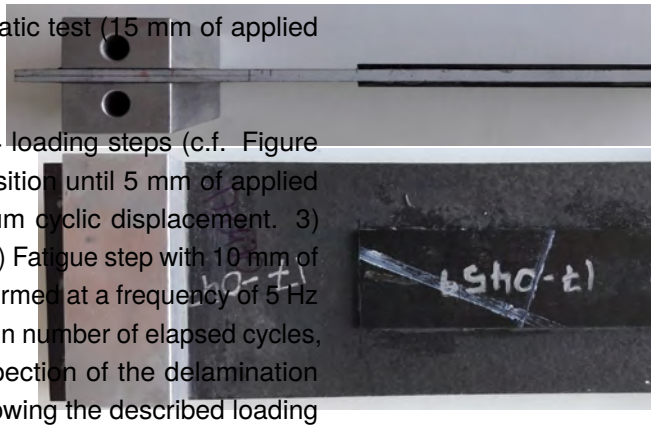

On the other hand, fatigue tests were comprised of 4 loading steps (c.f. Figure 6.5): 1) Quasi-static step from the initial unloaded position until 5 mm of applied displacement. 2) Fatigue step with 5 mm of maximum cyclic displacement. 3) Quasi-static step until 10 mm of applied displacement. 4) Fatigue step with 10 mm of maximum cyclic displacement. Fatigue steps were performed at a frequency of 5 Hz and a load ratio of R=0.1, and were stopped every certain number of elapsed cycles, as listed in Table 6.1, to perform non-destructive inspection of the delamination front location. A batch of 3 specimens were tested following the described loading sequence.

The shape and location of the delamination front was monitored using a Hamamatsu X-ray unit (c.f. Figure 6.6). X-ray pictures were made using the following settings: 35kV, 120 μA and analogue integration of 5 images with an exposure time of 3 s. To enhance X-ray contrast, a solution comprised of 520 g of zinc iodide, 86.5 mL of distilled water, 86.5 mL of alcohol and 26 mL Kodak Photo-Flo 200 was used. The liquid was introduced inside the delamination using a pipette. A vacuum chamber

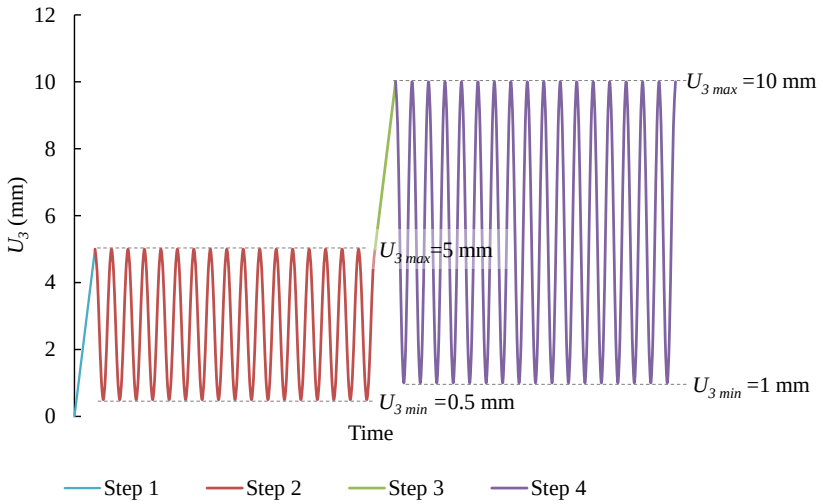

Fig. 6.5.: Loading steps of the fatigue tests.

was used to make the contrast solution penetrate to the tip of the delamination. This operation was repeated in every measurement.

Before starting the test, a reference X-ray picture of the specimen was taken. Then, the front location was evaluated at the programmed stops by subtracting the reference X-ray picture to the X-ray picture at the current time of the stop. The difference in intensity between both pictures was significant only at the delaminated area, which was filled with the contrast solution. Figure 6.7.a shows the X-ray picture obtained at the end of Step 1 of a fatigue test, just after the quasi-static opening. In Figure 6.7.b the picture has been binarized so the opened interface is shown in black and the closed interface is shown in white. In Figure 6.7.c the normalized absolute difference between Figure 6.7.a and the reference picture is shown along the X_2 coordinate for constant X_1=36 mm. Since, when taking the X-ray picture, the specimen arms were opened using a wedge, the accumulation of liquid at the delamination tip makes the difference in intensity change linearly with the height. Note, in Figure 6.6, that the specimen was standing such that the liquid remains inside the delamination cavity during the acquisition. In order to assess the crack front location for a given X_1, two linear functions of the intensity along the X_2-coordinate are intersect: the linear fitting of the base line region and the linear fitting of the increase in intensity. The crack front location is set as the intersection point (marked in red in Figure

Tab. 6.1.: Programed stops during the fatigue tests.

Maximum cyclic displacement (mm)	Number of cycles
5	1,500
5	3,000
5	5,000
5	10,000
5	25,000
5	80,000
5	420,000
10	1,500
10	3,000
10	5,000
10	10,000

6.7.c) between the two linear fittings. The data represented in gray in Figure 6.7.c is disregarded.

The X-ray picture shown in Figure 6.8.a was taken after 310,000 cycles of fatigue loading. Note, that, in this case, the delamination front was placed under the reinforcement. X-ray pictures were made by transmission, i.e. the specimen was located in between the X-ray transmitter and the detector. The detector counts the accumulated intensity of X-rays that cross the specimen. Thus, the intensity at the reinforced region was higher due to higher thickness of the specimen (higher absorption). Therefore, this region looks darker in the X-ray picture (c.f. Figure 6.8.a). Consequently, it is harder to visually inspect the location of the delamination front when it is located under the reinforcement, even if the picture is binarized (c.f. Figure 6.8.c). Nevertheless, the intersection of the linear fittings of the basline and the normalized absolute difference in intensity is a suitable means of localizing the crack front also under the reinforced region, as shown in Figure 6.8.b.

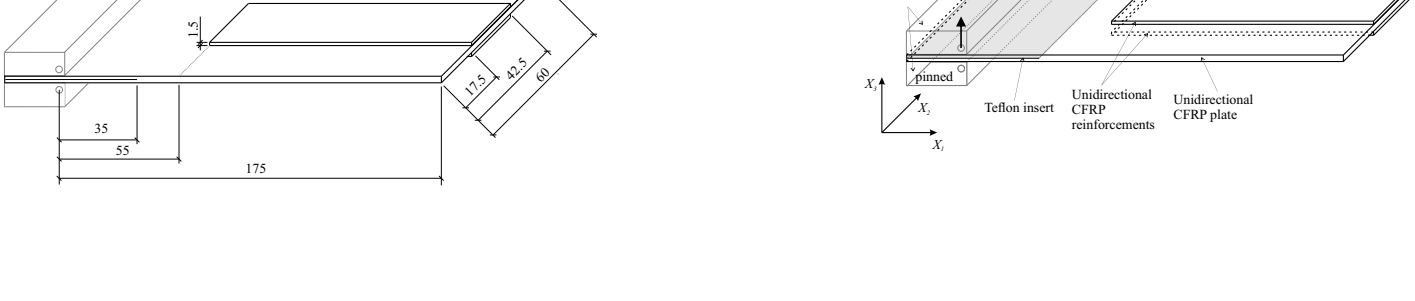

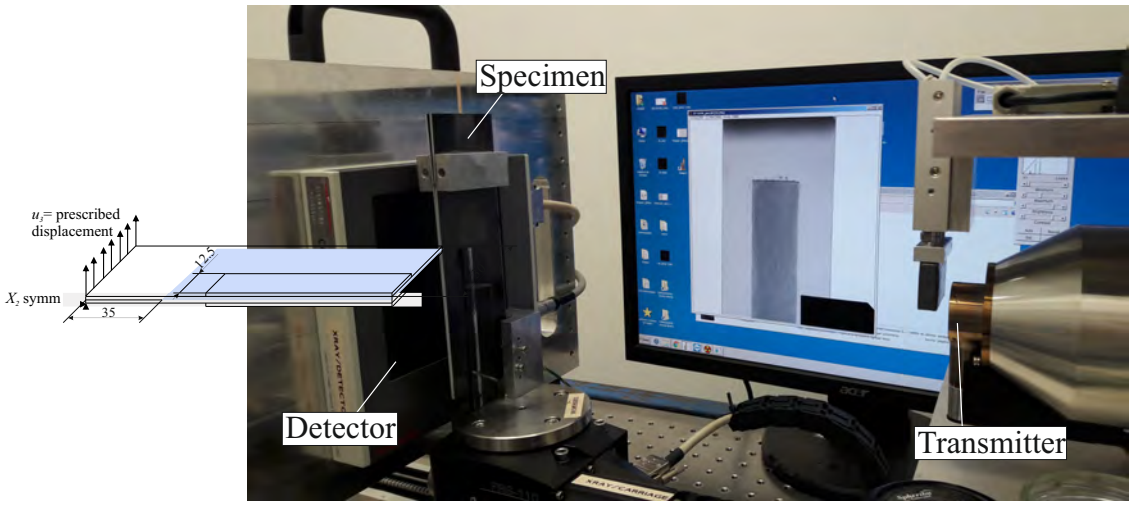

Fig. 6.6.: X-Ray unit.

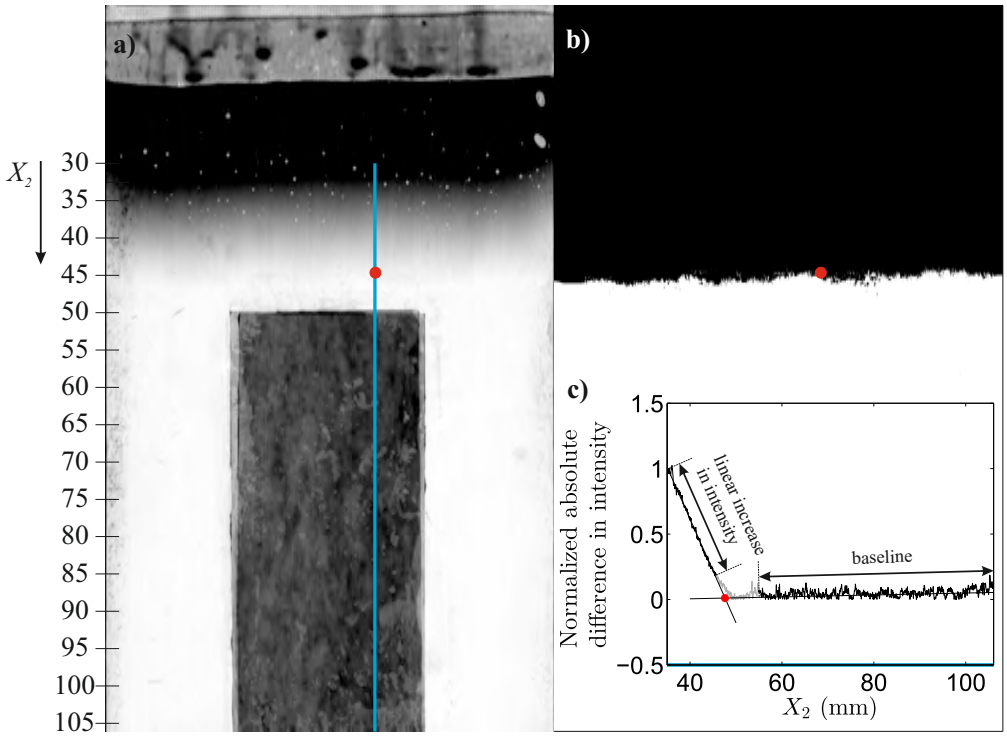

Fig. 6.7.: Determination of the delamination front location after quasi-static opening until 5 mm of applied displacement.

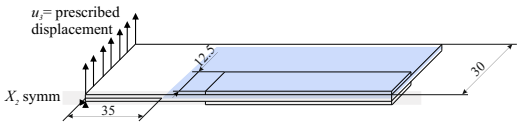

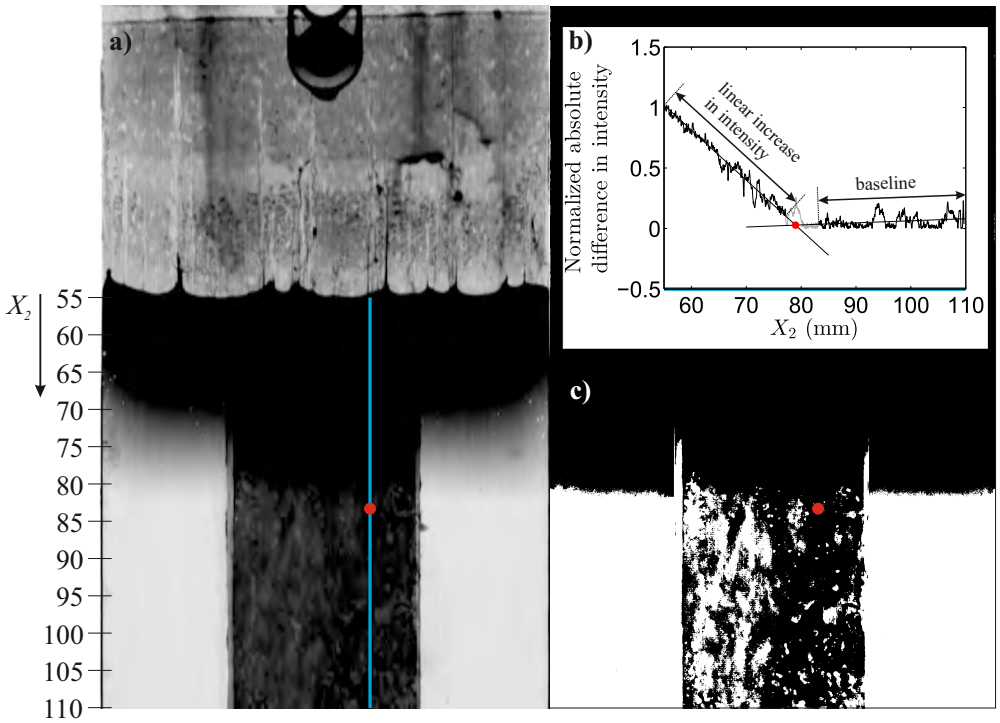

Fig. 6.8.: Determination of the delamination front location after 310,000 cycles of fatigue loading with 10 mm of maximum cyclic displacement.

6.3 Delamination in a 3D composite structure: Numerical prediction and comparison with experimental results

In the following, the results of the tests done with the partially reinforced DCB specimen introduced in Section 6.1 are presented. Tests were performed under quasi-static and fatigue loading according to the methodology described in Section 6.2.

Firstly, quasi-static tests were performed in order to analyze the crack front evolution. Four specimens were tested (c.f. Figure 6.9). Tests on specimens A, B, and C were stopped every 1 mm of applied displacement in order to perform X-ray inspection of the delamination front position. On the other hand, the test on Specimen D was conducted continuously and the X-ray inspection was only done at the end of the test. This was done to rule out any possible effect of the contrast solution on the interface. The repeatability in the force-displacement relationship of the 4 tests can be appreciated in Figure 6.9.

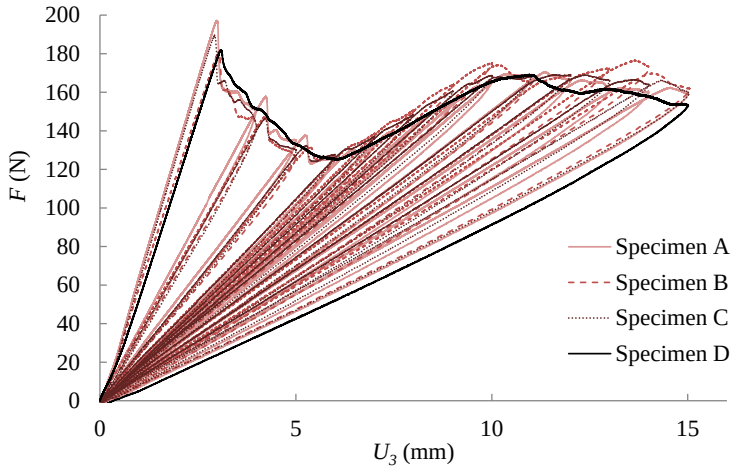

Fig. 6.9.: Comparison of numerical and experimental results for force versus displacement from quasi-static testing on the demonstrator specimen.

Moreover, the methodology to extract the delamination front position from X-ray pictures described in Section 6.2 was applied. Figure 6.10 represents the plane of delamination, spanned by coordinates X_1 and X_2 (c.f. Figure 6.1). The thick black solid straight lines mark the reinforcements borders. The delamination front position of specimens A, B and C is plotted for 5 different levels of applied displacement. Note that curved delamination was promoted by the reinforcements. The delamination front position of Specimen D at the end of the test (15 mm of applied displacement) is plotted for comparison purposes. The maximum difference between the delamination front of Specimen D and the front that has the most advanced position among specimens A, B and C is 4 mm. In view of the results, it cannot be concluded if the observed difference is due to an effect of the contrast solution on the constitutive behavior of the interface or due to structural differences between the specimens caused in the manufacturing process. Nevertheless, X-ray inspection is considered to be a suitable means of monitoring the delamination front position.

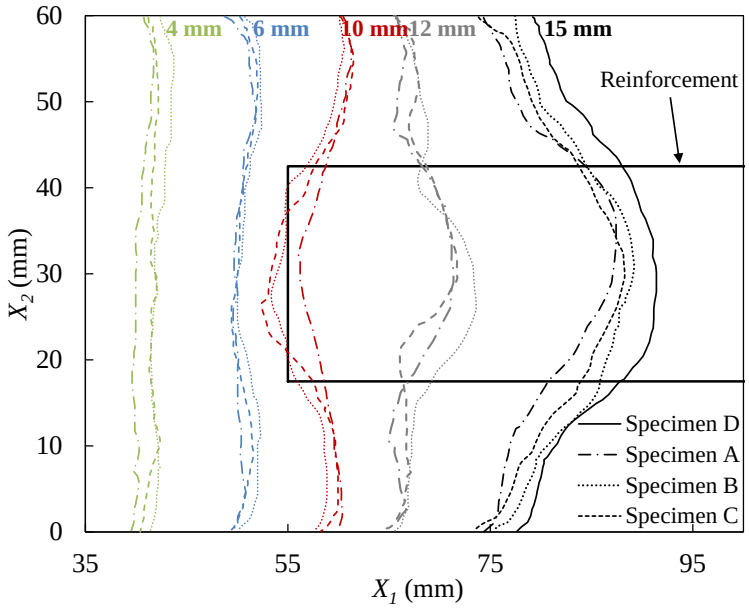

Fig. 6.10.: Delamination front position from quasi-static testing on the demonstrator specimen.

Combining figures 6.9 and 6.10, the response of the structure is analyzed. The maximum reaction force point occurred during elastic opening of the specimens arms, just before crack propagation (U_3= 3 mm). From this point, crack propagation caused a decrease in reaction force as the applied displacement was increased.

Tab. 6.2.: Input values for the simulation model.

Property	Value	Units
$\mathcal{G}_{Ic}$	0.3052	N/mm
$\mathcal{G}_{IIc}$	2.7656	N/mm
η	2.0514	-
τ_{Io}:	32.555	MPa
K:	10^5	N/mm^3
p_I	8.3936	-
A_I	564.39	mm/cycle
p_{II}	3.6204	-
A_{II}	0.0121	mm/cycle
p_m	-4.991	-
A_m	1.1975E-6	mm/cycle
$\mathcal{G}_{Ith}$	0.0854	N/mm
$\mathcal{G}_{IIth}$	0.0829	N/mm
η_2	-	-
R	0.1	-

When the delamination front approached the reinforced region, the force increased again (U_3= 6 mm) due to the stiffness supplied by the reinforcements. The turning point, from which the force again decreased, was the instant when the delamination front overcame the reinforcement edge (U_3= 10 mm).

On the other hand, the partially reinforced DCB fatigue test (see the loading sequence represented in Figure 6.5) has been used to validate the simulation method. The undeformed cohesive elements were 0.47 mm wide, 0.34 mm long and have zero thickness. Only one half of the specimen was modeled exploiting X_2-symmetry to reduce the required computational resources. The input parameters for the user-defined cohesive elements were obtained from the material card (c.f. Chapter 5) and are listed in Table 6.2. The elastic properties of the laminate are listed in Table 5.2.

The historical evolution of the growth driving direction (GDD) angle with respect to X_1 and the mode I J-integral within the cohesive zone are plotted in Figure 6.11. The mode II and III J-integrals are not plotted since they are negligible for this loading conditions. In Figure 6.11.a, it can be observed that the computed J-integral during quasi-static propagation (Step 1) is equal to the mode I fracture toughness, $\mathcal{G}_{Ic}$. Then, during Step 2 (fatigue loading with constant maximum cyclic displacement),

the computed J-integral decreases with crack propagation (c.f. figures 6.11.b and 6.11.c). The same is repeated for steps 3 and 4. In Figure 6.11.d, the J-integral during quasi-static propagation again equals the mode I fracture toughness, $\mathcal{G}_{Ic}$, whereas, in figures 6.11.e and 6.11.f, the J-integral decreases with crack propagation under constant maximum cyclic displacement conditions.

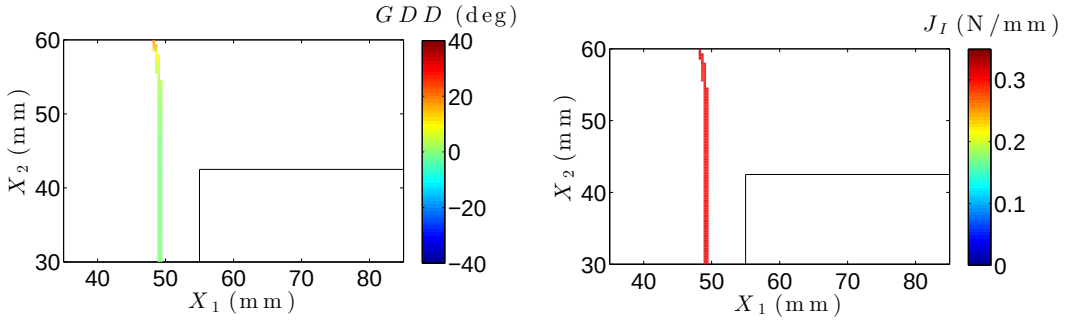

a) Step 1. Static loading U_3= 5 mm

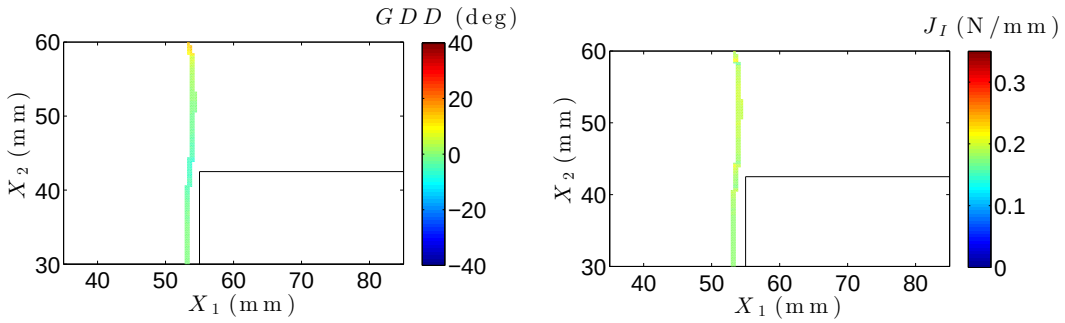

b) Step 2. Fatigue loading $U_{3\ max}$= 5 mm N= 3,000 cycles

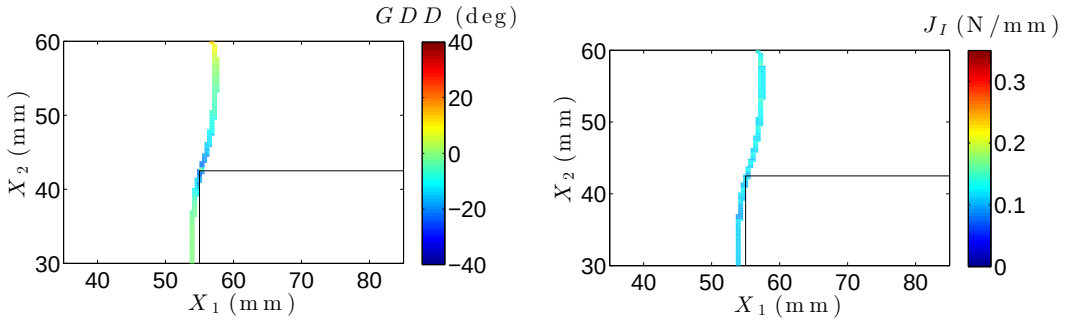

c) Step 2. Fatigue loading $U_{3\ max}$= 5 mm N= 410,000 cycles

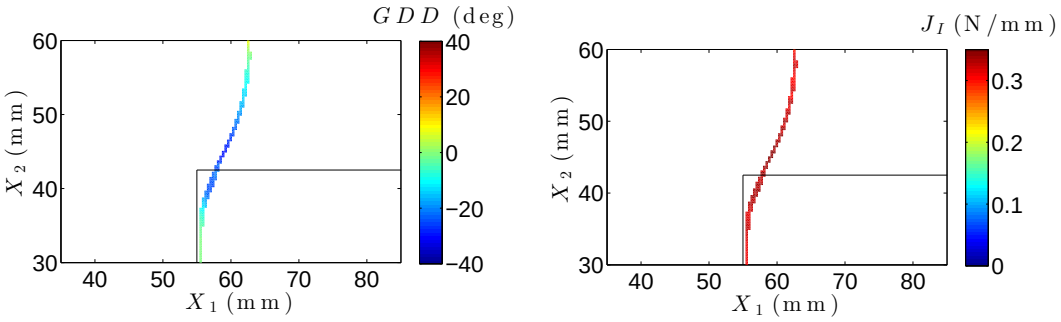

d) Step 3. Static loading U_3= 10 mm

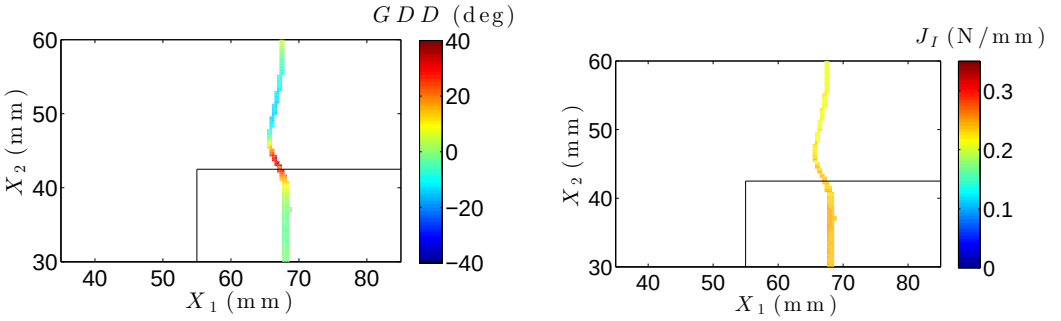

e) Step 4. Fatigue loading $U_{3\ max}$= 10 mm N= 3,000 cycles

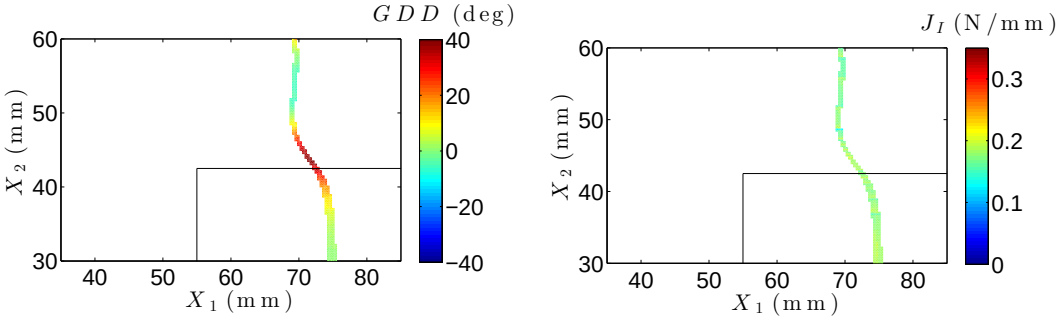

f) Step 4. Fatigue loading $U_{3\ max}$= 10 mm N= 10,000 cycles

Fig. 6.11.: Historical evolution of the growth driving direction (GDD) and the mode I J-integral within the cohesive zone. The mode II and III J-integral are negligible for this loading conditions.

For comparison purposes with numerical predictions, 3 partially reinforced DCB specimens were experimentally tested: Specimen 1, 2 and 3 using the loading sequence represented in Figure 6.5. The force-displacement relationship of the 3 specimens is plotted in Figure 6.12 (using different intensities of red color). The 3 tests present noticeable repeatability. Moreover, the simulation method (blue curve in Figure 6.12) is shown capable to reproduce with accuracy the mechanical response observed in the experiments. In Figure 6.13, the specimen's compliance is represented as a function of the number of elapsed cycles. The experimental and the numerical results are in good agreement. Indeed, the difference between both results is equal to the dispersion among specimens A, B and C.

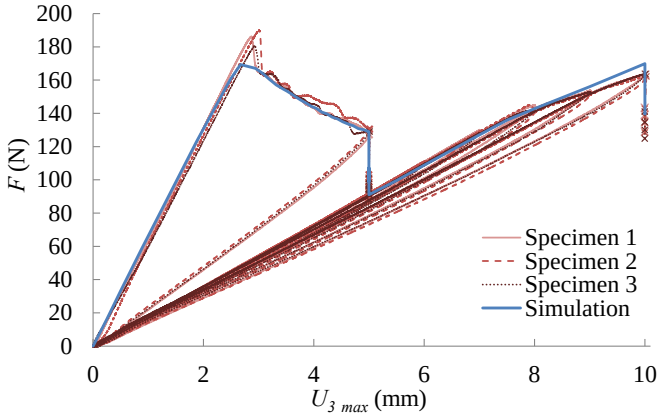

Fig. 6.12.: Comparison of numerical and experimental results for force versus displacement from fatigue testing on the demonstrator specimen.

Finally, the delamination front position was examined using the X-ray technique. In Figure 6.14 the binarized X-ray pictures of Specimen 1 are plotted in comparison with the numerical energy-based damage, $\mathcal{D}^e$, distribution at different instants during the test. It is believed that Figure 6.14 is useful for visual comparison of the experimental and numerical delamination fronts. However, this is not the case when the delamination front is placed under the reinforcements (c.f. figures 6.14.e and 6.14.f). The added CFRP material acting as reinforcements absorbed X-radiation so that the attenuation of the intensity captured by the detector at the delaminated region caused by the contrast solution is unnoticeable. This, difficulties the visual detection of the delamination front position. However, following the methodology described in Section 6.2, the delamination front has been accurately extracted from the X-ray pictures.

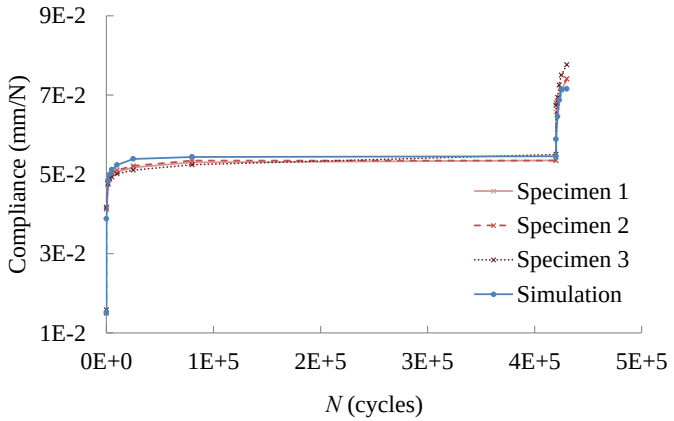

Fig. 6.13.: Comparison of numerical and experimental results for compliance versus number of cycles from fatigue testing on the demonstrator specimen.

In figure 6.15, the position of the delamination front of the tested specimens 1, 2 and 3 is plotted for every stop done during the test (using different intensities of red color). The programmed stops are listed in Table 6.1. Due to the presence of micro cracks, the fracture zone might contain some contrast liquid. Thus, it is hard to ensure whether the extracted delamination front location from the X-ray pictures corresponds to the beginning or the end of the fracture process zone. Consequently, for the comparison with the numerical results, both the 1 and 0-damage isolines limiting the cohesive zone are plotted.

It can be observed, in figures 6.15.a-6.15.h that the delamination front curved as it approached the stiffened region. Under fatigue loading, the reinforcement acted as a crack propagation preventer. Indeed, the front did not overcome the reinforcement edge during 410,000 cycles in any of the specimens tested. Then, during the quasi-static increment of displacement in Step 3, the delamination front overcame the reinforcement edge (c.f. Figure 6.15.i). During the fatigue Step 4, delamination propagation took place under the reinforcement, changing once more the delamination front curvature (c.f. figures 6.15.j-6.15.m).

The predictive capabilities of the simulation method have been proven. The most significant discrepancy is observed in Figure 6.15.i, during Step 3, when the load was increased to 10 mm of applied displacement in order to overcome the border of the reinforcement. This discrepancy is attributed to the fact that the transition to the

stiffened region in the finite element (FE) model was more abrupt than in the tested specimens. In the FE model, the reinforcements were placed at the exact equal position at both faces of the specimen. This is not the case of the tested specimens, where the reinforcements were manually bonded. In addition, some epoxy-based adhesive might exceed the boundaries of the reinforcements, creating a seam at the edges that smoothed the abrupt increment in stiffness supplied by the reinforcement. Nevertheless, beyond this small discrepancy, the evolution of the delamination front with the number of cycles has been captured with accuracy by the simulation tool.

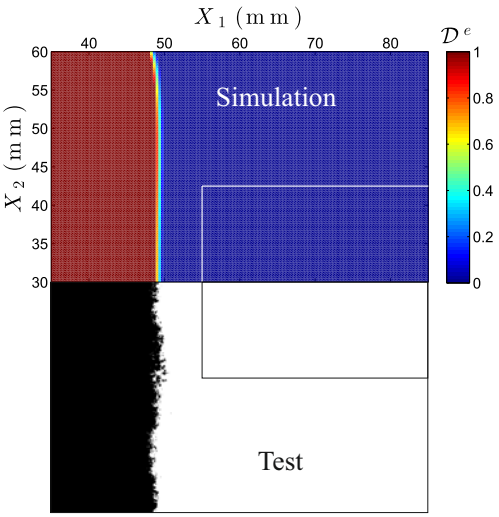

a) Step 1. Static loading U_3= 5 mm

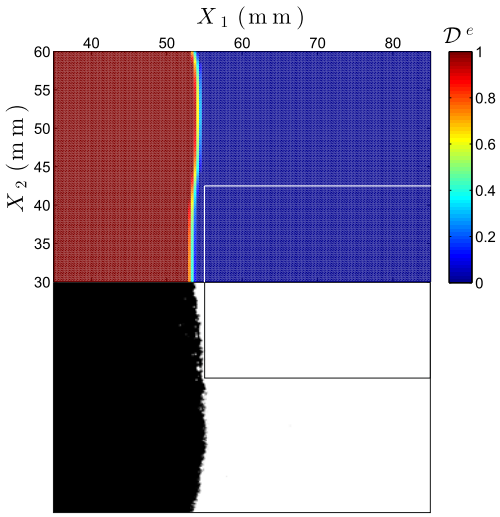

b) Step 2. Fatigue loading
$U_{3\ max}$= 5 mm N= 3,000 cycles

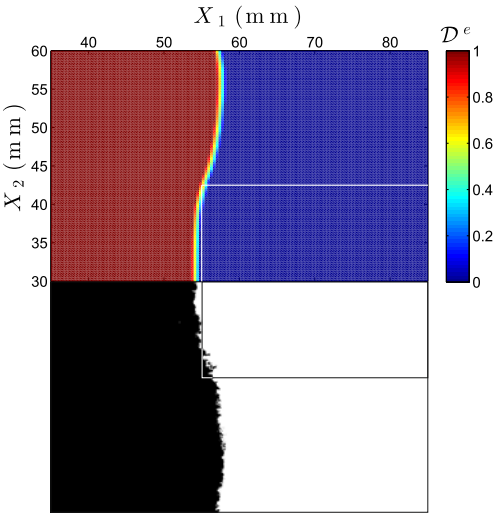

c) Step 2. Fatigue loading
$U_{3\ max}$= 5 mm N= 410,000 cycles

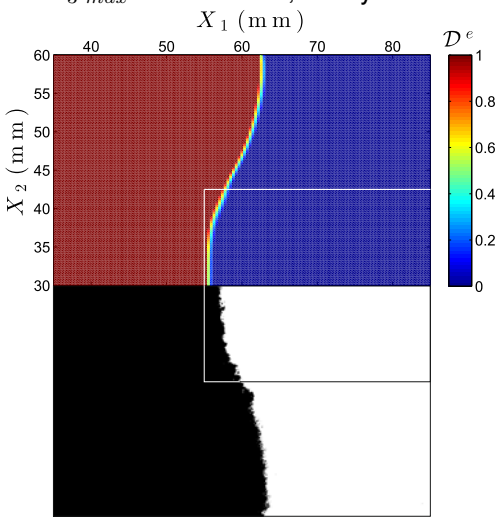

d) Step 3. Static loading U_3= 10 mm

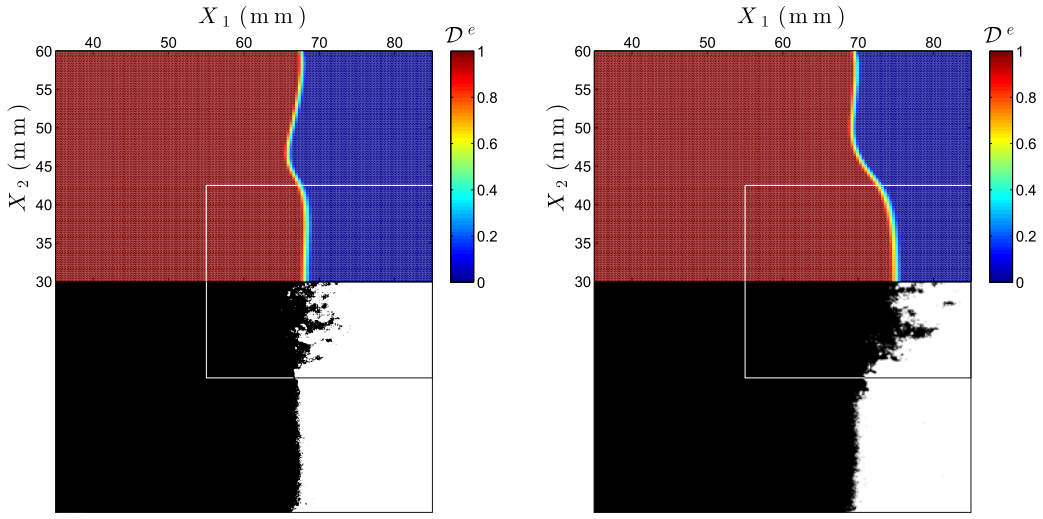

e) Step 4. Fatigue loading
$U_{3\ max}$= 10 mm N= 3,000 cycles

f) Step 4. Fatigue loading
$U_{3\ max}$= 10 mm N= 10,000 cycles

Fig. 6.14.: Comparison of numerical and experimental results for delamination front position from fatigue testing on Specimen 1.

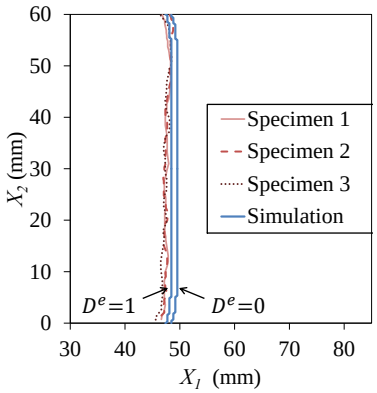

a) Step 1. Static loading
U_3= 5 mm

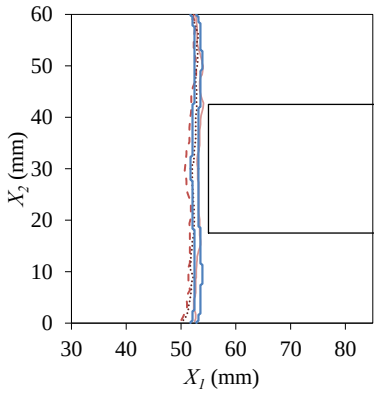

b) Step 2. Fatigue loading
$U_{3\ max}$= 5 mm N= 1,500 cycles

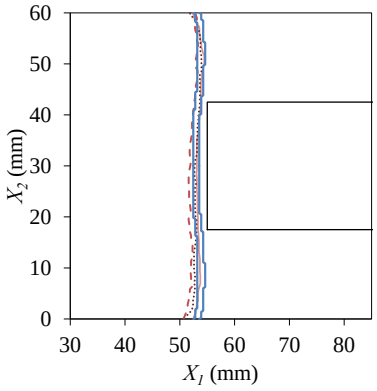

c) Step 2. Fatigue loading
$U_{3\ max}$= 5 mm N= 3,000 cycles

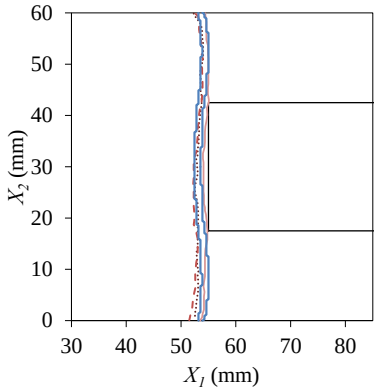

d) Step 2. Fatigue loading
$U_{3\ max}$= 5 mm N= 5,000 cycles

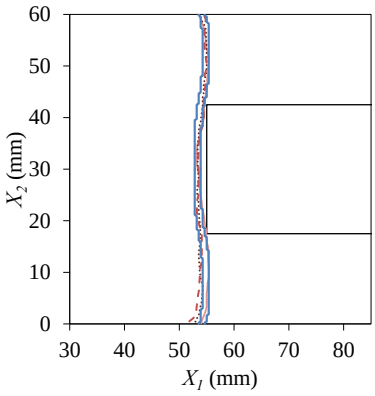

e) Step 2. Fatigue loading
$U_{3\ max}$= 5 mm N= 10,000 cycles

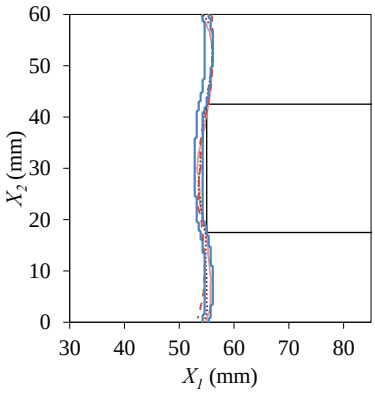

f) Step 2. Fatigue loading
$U_{3\ max}$= 5 mm N= 25,000 cycles

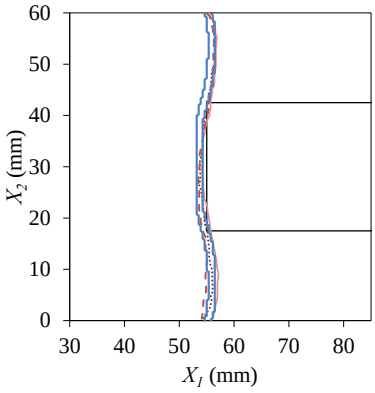

g) Step 2. Fatigue loading
$U_{3\ max}$= 5 mm N= 80,000 cycles

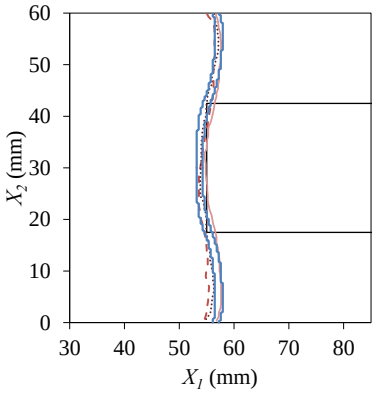

h) Step 2. Fatigue loading
$U_{3\ max}$= 5 mm N= 410,000 cycles

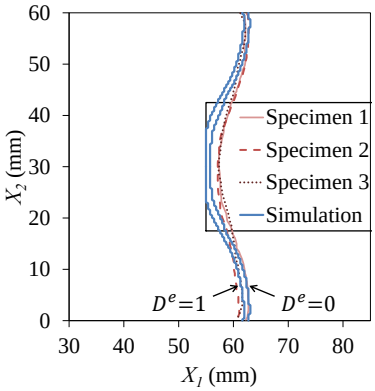

i) Step 3. Static loading
U_3= 10 mm

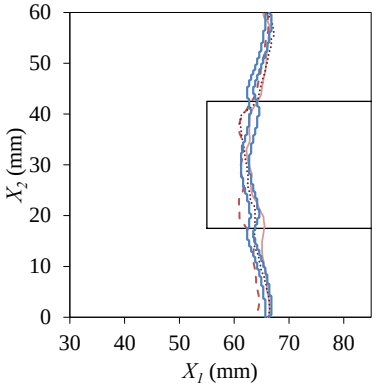

j) Step 4. Fatigue loading
$U_{3\ max}$= 10 mm N= 1,500 cycles

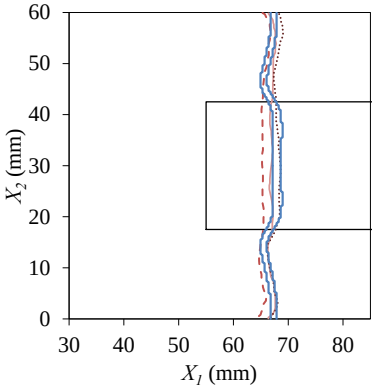

k) Step 4. Fatigue loading
$U_{3\ max}$= 10 mm N= 3,000 cycles

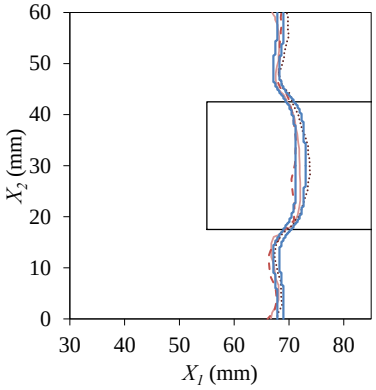

l) Step 4. Fatigue loading
$U_{3\ max}$= 10 mm N= 5,000 cycles

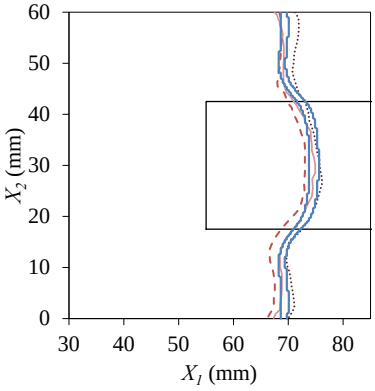

m) Step 4. Fatigue loading
$U_{3\ max}$= 10 mm N= 10,000 cycles

Fig. 6.15.: Comparison of numerical and experimental results for delamination front position from fatigue testing on the demonstrator specimens.

7 Conclusions

The work presented in this Ph.D. project constitutes a complete methodology for the reliable design of composite structures subjected to fatigue-driven delamination. The main contribution is the development of a cohesive zone model for the prediction of delamination growing in three-dimensional laminated structures.

Firstly, the necessary tools for the formulation of the three-dimensional fatigue method have been developed. These include a method for determining the growth driving direction and a means of evaluating the mode-decomposed energy releases in arbitrarily shaped delamination fronts.

Then, all the mentioned contributions are assembled together to conduct the analysis of fatigue-driven delamination in a three-dimensional structure.

Point-wise evaluation of the growth driving direction for arbitrarily shaped delamination fronts using cohesive elements

The formulation for the determination of the growth driving direction for cohesive zone models is evaluated point-wise. Therefore, it can be implemented as a part of a user-defined cohesive element subroutine and evaluated during simulation without the need of any extra loop, post-processing or global information.

The growth driving direction is defined as the negative gradient of the energy-based damage variable. However, other quantities can be used for the sake of simplicity. In this work, three different criteria are proposed. The implementation of the formulation for the proposed criteria applied to the CZM presented in [167, 168] is derived and validated by using one-element analysis under different loading conditions.

Furthermore, the usefulness of the method has been demonstrated via the analysis of delamination propagation in a three-dimensional structure with a complex shaped crack front. The results using the proposed point-wise formulation for the evaluation

of the growth driving direction are in agreement with the results from a global approximation of the normal direction to different damage isolines. Apart from being a low computational time-consuming task, the proposed formulation has the advantage that it can be evaluated at any point within the cohesive zone.

Evaluation of the mode-decomposed energy release rates for arbitrarily shaped delamination fronts using cohesive elements

A novel methodology for the calculation of the mode-decomposed J-integral in three-dimensional delamination simulation using a cohesive zone model approach is presented. The methodology incorporates the growth driving direction criterion to track the integration paths and determine the local directions of mode I, II and III components. The generality of the formulation makes it applicable to curved fronts with non-planar delamination interfaces and large fracture process zones. The application of the described methodology results in curved integration paths.

The calculation of the J-integral is based on dividing the delamination interface into elemental thickness slices, so that the J-value of each slice is unique. The definition of the curvature of such slices is done according to the growth driving direction. Since the growth driving direction is mesh independent, the definition of the slices is not affected by the mesh size.

By application of the presented formulation, a global measure of the energy release rate in three-dimensional structures modeled using a cohesive zone model approach can be obtained. Also, the energy release rate can be decomposed into mode I, II and III components. The decomposition of the shear component of the energy release rate into mode II and III, to date, has only been addressed under the assumption of elastic fracture mechanics. In addition, the new formulation enables to obtain a global measure of the mode mixity, overcoming the limitation of the current 3D cohesive zone model formulations, where the mode mixity is only obtained at integration point level in terms of opening displacements.

Besides the immediate applications of the formulation as just described, more applications will be uncovered in future research. The presented CZ J-integral is a decisive contribution on using fracture mechanics-based procedures in a cohesive

zone model framework, which will allow the design of lighter and more reliable structures. In addition, a direct application of the CZ J-integral formulation is its implementation in combination with existing fatigue simulation methods formulated in a CZM approach, which rely on mode-dependent Paris law' like expressions. Thus, the developed mode-decomposed CZ J-integral formulation becomes a new solution for extracting mode-decomposed energy release rates of real complex three-dimensional structures.

An efficient methodology for the experimental characterization of mode II delamination growth under fatigue loading

An automated procedure to obtain the log-linear region of a crack growth rate curve has been developed for an 3-ENF test for mode II fatigue delamination growth. The applied displacement, $U(N)$, is calculated prior to initiating the fatigue test in order to achieve a constant negative energy release rate gradient throughout crack propagation. The continuous displacement shedding is conducted by implementing the calculated $U(N)$ curve in a computer-controlled testing system. This, in combination with the automated and continuous estimation of the crack length by means of the real time monitoring of the specimen's compliance, avoids the need of human intervention during the test.

The usefulness of this methodology has been exemplified with an experimental testing campaign in which the crack growth rate curve obtained is compared with the modified Paris' law fitting data from a batch of constant cyclic displacement tests.

The range of severities covered by a single test using the developed methodology spans from 0.45 to 0.1. Due to the specimen movement, the initial severity could not be higher than 0.50.

The time saved employing the methodology developed has been demonstrated (the example performed shows a reduction of 1/80) and how the duration of the test, which is determined by the shedding rate and the range of severities explored, is limited by the requirement of forming the complete failure process zone corresponding to the actual load severity is discussed.

Moreover, the methodology is also applicable to mixed-mode bending fatigue tests.

Extension and validation of the 3D fatigue damage rate method

The tools developed in the framework of this project have been integrated into a numerical tool for the simulation of fatigue-driven delamination in three-dimensional structures.

A demonstrator specimen has been designed so that it provides experimental data for the validation of the simulation method. The test consists of a DCB specimen with a middle width reinforcement that causes the crack front to curve.

The demonstrator specimens have been manufactured and the fatigue properties of the material have been characterized to obtain the parameters that feed the numerical tool.

Tests on the demonstrator specimen have been done under quasi-static and fatigue loads. Quasi-static tests revealed that, as expected, the shape of the delamination front evolves during propagation. The repeatability of the test has been demonstrated by comparison of the results from three different specimens. The crack front location during propagation has been assessed using X-radiography. The methodology for extracting the delamination front shape and location from X-ray pictures has been defined. Moreover, a forth specimen has been tested continuously to exclude any effect of the contrast liquid to the interface properties. In view of the results, it is assumed X-ray to be a non-destructive technique which does not affect the behavior of specimen.

Fatigue tests have been conducted on three different specimens, presenting, again, good repeatability. The tests have been simulated using the numerical tool developed in the project. The results from the numerical simulations present excellent agreement with the experimental results in terms of evolution of the location and shape of the delamination front according to the number of cycles.

8 Contributions and impact

This chapter highlights the main contributions and the impact that the work done in this Ph.D. project may have in the scientific and industrial communities.

The general contribution of this work is focused on providing an integral method for the analysis of fatigue-driven delamination in 3D structures. In this regard, the following achievements have been pursued:

- The state-of-the-art models have been reviewed identifying unsolved areas, such as the accurate computation of the energy release rate in 3D models or the applicability of the existing models to three-dimensional structures.

- The concept of growth driving direction has been defined for CZM as the analogous to crack propagation direction. An efficient algorithm to identify it has been developed.

- An accurate means of calculating the mode-decomposed energy release rates in three-dimensional structures modeled using a cohesive zone approach has been proposed for the first time.

- A 3D fatigue model applicable to any structural component has been formulated and implemented in a commercial finite element code.

- An efficient testing methodology for the characterization of mode II crack growth rates curves has been developed. The method has been extended for mixed-mode loading conditions.

- The interlaminar properties of a material used in the aircraft industry has been fully characterized under static and fatigue loading.

- A 3D fatigue benchmark under mode I opening has been designed and tested. Information of delamination front shape and location is provided as a function of the number of cycles.

The impact of the methods developed can be evaluated at two scales, industrial and scientific. At an industrial level, the presented methodology is one of the few existing numerical tools that can be directly incorporated in the analysis and design of complex composite structures subjected to fatigue loading. From the scientific point of view, new concepts are provided which may inspire new developments and applications beside the objective of this thesis.

Perspectives and future Work

9

The contribution of this Ph.D. project represents a significant step forward for the analysis of fatigue-driven delamination in layered structures. Nevertheless, during its preparation, several shortcomings have been revealed which are listed in the following as suggestions for future work.

- Extend the analysis of fatigue-driven delamination to multi-directional laminates. There are experimental evidences that static delamination behavior is affected by the fibers orientation. However, this analysis has not been yet addressed under fatigue loading. In this regard, the growth driving direction becomes an essential tool.

- Formulate a mode II and mode III decomposed cohesive zone model for quasi-static and fatigue loading. The growth driving direction is needed to disregard the shear component of the tangential displacement jump into mode II and mode III directions.

- Develop efficient methods for the characterization of interlaminar properties under mode III loading conditions.

- Address damage accumulation under random amplitude fatigue loading. Real applications of the simulation tool demand the capability of modeling representative loading spectra. This may require the formulation of a low-cycle fatigue strategy.

- Develop experimental approaches to characterize the fatigue cohesive law. Due to the lack of characterization methods, the damage rate model is currently based on the link between the macroscopic description of the fatigue crack growth and the local point-wise evaluation of the damage in the cohesive zone model. It is assumed that the quasi-static cohesive traction-displacement jump relation is maintained during fatigue loading. However, there are no experimental evidences in this regard.

- Perform fatigue testing on the partially reinforced ELS specimen to obtain experimental results for the validation of the simulation methods under mixed-mode conditions. The characterization of mode III interlaminar properties (static and fatigue) are indispensable to address this point.

Bibliography

[1]ISO 15024. „Fibre-reinforced plastic composites - determination of mode I interlaminar fracture toughness, GIC, for unidirectionally reinforced“. In: *International Organisation for Standardisation* (2001) (cit. on p. 46).

[2]ISO 15114. „Fibre-reinforced plastic composites - Determination of the mode II fracture resistance for unidirectionally reinforced materials using the calibrated end-loaded split (C-ELS) test and an effective crack length approach“. In: *International Organisation for Standardisation* (2014) (cit. on p. 47).

[3]EN 6033. „Aerospace series - Carbon fibre reinforced plastics - Test method - Determination of interlaminar fracture toughness energy - Mode I - GIc“. In: *European Committee for Standardization* (2015) (cit. on p. 47).

[4]EN 6034. „Aerospace series - Carbon fibre reinforced plastics - Test method - Determination of interlaminar fracture toughness energy - Mode II - GIIc“. In: *European Committee for Standardization* (2015) (cit. on p. 47).

[5]A. Abdul-Baqi, P. J. G. Schreurs, and M. G. D. Geers. „Fatigue damage modeling in solder interconnects using a cohesive zone approach“. In: *International Journal of Solids and Structures* 42.3-4 (2005), pp. 927–942 (cit. on p. 22).

[6]AC7122/1 Rev B. *Nadcap Audit Criteria for Non Metallic Materials Testing - Mechanical Testing* (cit. on p. 127).

[7]D. F. Adams, R. S. Zimmermann, and E. M. Odem. „Frequency and Load Ratio Effects on Critical Strain Energy Release Rate and Thresholds of Graphite Epoxy Composites“. In: *Toughened Composites, ASTM. American Society for Testing and Materials, New York* (1987) (cit. on pp. 16, 19).

[8]H. Albersten, J. Ivens, P. Peters, M. Wevers, and I. Verpoest. „Interlaminar fracture toughness of CFRP influenced by fibre surface treatment: Part 1. Experimental results“. In: *Composites Science and Technology* 54.2 (1995), pp. 133–145 (cit. on p. 10).

[9]G. Alfano. „On the influence of the shape of the interface law on the application of cohesive-zone models“. In: *Composites Science and Technology* 66.6 (2006), pp. 723–730 (cit. on p. 11).

[10]G. Alfano and M. A. Crisÿeld. „Finite element interface models for the delamination analysis of laminated composites: mechanical and computational issues“. In: *International Journal for Numerical Methods in Engineering* 50 (2001), pp. 1701–1736 (cit. on p. 11).

[11]G. Allegri, M. R. Wisnom, and S. R. Hallett. „A new semi-empirical law for variable stress-ratio and mixed-mode fatigue delamination growth“. In: *Composites Part A: Applied Science and Manufacturing* 48.1 (2013), pp. 192–200 (cit. on pp. 16, 20).

[12]G. Allegri, M. I. Jones, M. R. Wisnom, and S. R. Hallet. „A New Semi-Empirical Model for Stress Ratio Effect on Mode II Fatigue Delamination Growth“. In: *Composites Part A* 42.7 (2011), pp. 733–740 (cit. on pp. 16, 20).

[13]M. Amestoy, H. D. Bui, and R. Labbens. „On the Definition of Local Path Independent Integrals in Three-Dimensional Crack Problems“. In: *Mechanic Research Communications* 8.4 (1981), pp. 231–236 (cit. on p. 15).

[14]A. Amiri-Rad and M. Mashayekhi. „A Cohesive Zone Approach for Fatigue-Driven Delamination Analysis in Composite Materials“. In: *Applied Composite Materials* 24.4 (2017), pp. 751–769 (cit. on pp. 23, 29).

[15]A. Amiri-Rad, M. Mashayekhi, and F. P. van der Meer. „Cohesive zone and level set method for simulation of high cycle fatigue delamination in composite materials“. In: *Composite Structures* 160 (2017), pp. 61–69 (cit. on p. 24).

[16]T. L. Anderson. „Fracture Mechanics: Fundamentals and Applications, 3rd Edition“. In: *CRC Press* (2005) (cit. on p. 111).

[17]J. Andersons, M. Hojo, and S. Ochiai. „Empirical model for stress ratio effect on fatigue delamination growth rate in composite laminates“. In: *International Journal of Fatigue* 26 (2004), pp. 597–604 (cit. on p. 20).

[18]A. Argüelles, J. Viña, A. F. Canteli, and J. Bonhomme. „Fatigue Delamination, Initiation, and Growth, Under Mode I and II of Fracture in a Carbon-Fiber Epoxy Composite“. In: *Polymer Composites* 31.4 (2010), pp. 700–706 (cit. on pp. 16, 17, 114).

[19]L. E. Asp, A. Sjören, and E. S. Greenhalgh. „Delamination growth and thresholds in a carbon/epoxy composite under fatigue loading“. In: *Journal of Composites Technology and Research* 23 (2001), pp. 55–68 (cit. on pp. 16, 18, 134).

[20]ASTM E647-13. „Standard Test Method for Measurement of Fatigue Crack Growth Rates“. In: *American Society for Testing and Materials (ASTM)* (2013), pp. 1–49 (cit. on pp. 51, 116).

[21]O. Bacarreza and M. H. Aliabadi. „A novel methodology for fatigue delamination growth analysis of composites“. In: *Key Engineering Materials*. Vol. 488. 2012, pp. 763–766 (cit. on p. 21).

[22]B. L. V. Bak, A. Turon, E. Lindgaard, and E. Lund. „A benchmark study of simulation methods for high-cycle fatigue-driven delamination based on cohesive zone models“. In: *Composite Structures* 164 (2017), pp. 198–206 (cit. on pp. 19, 29).

[23]B. L. V. Bak, A. Turon, E. Lindgaard, and E. Lund. „A Simulation Method for High-Cycle Fatigue-Driven Delamination Using a Cohesive Zone Model“. In: *International Journal for Numerical Methods in Engineering* 106 (2016), pp. 163–191 (cit. on pp. 23, 27–30, 35–38, 41, 45, 53, 105, 131, 133, 135).

[24]B. L. V. Bak, E. Lindgaard, and E. Lund. „Analysis of the integration of cohesive elements in regard to utilization of coarse mesh in laminated composite materials“. In: *International Journal for Numerical Methods in Engineering* 99.8 (2014), pp. 566–586 (cit. on pp. 14, 86).

[25]B. L. V. Bak, C. Sarrado, A. Turon, and J. Costa. „Delamination Under Fatigue Loads in Composite Laminates: A Review on the Observed Phenomenology and Computational Methods“. In: *Applied Mechanics Reviews* 66.6 (2014), pp. 1–24 (cit. on pp. 13, 16, 18–21, 27, 132).

[26]E. J. Barbero. „Introduction to Composite Materials Design, Third Edition“. In: *Boca Raton: CRC Press* (2017) (cit. on p. 1).

[27]G. I. Barenblatt. „The Mathematical Theory of Equilibrium Cracks in Brittle Fracture“. In: *Advances in Applied Mechanics* 7 (1962), pp. 55–129 (cit. on pp. 8, 10).

[28]M. Beghini, L. Bertini, and P. Forte. „Experimental Investigation on the Influence of Crack Front to Fiber Orientation on Fatigue Delamination Growth Rate Under Mode II“. In: *Composite Science and Technology* 66.2 (2006), pp. 597–605 (cit. on p. 16).

[29]M. L. Benzeggagh and M. Kenane. „Measurement of Mixed-Mode Delamination Fracture Toughness of Unidirectional Glass/ Epoxy Composites with Mixed-ModeE Bending Apparatus“. In: *Composite Science and Technology* 56 (1996), pp. 439–449 (cit. on pp. 34, 41, 46, 55, 66, 74, 97, 127).

[30]S. Bhattacharya, I. V. Singh, B. K. Mishra, and T. Q. Bui. „Fatigue crack growth simulations of interfacial cracks in bi-layered FGMs using XFEM“. In: *Computational Mechanics* 52.4 (2013), pp. 799–814 (cit. on p. 21).

[31]N. Blanco, E. K. Gamstedt, L. E. Asp, and J. Costa. „Mixed-mode delamination growth in carbon fiber composite laminates under cyclic loading“. In: *International Journal of Solids and Structures* 41 (2004), pp. 4219–4235 (cit. on pp. 20, 40).

[32]A. J. Brunner, B. R. K. Blackman, and P. Davies. „A status report on delamination resistance testing of polymer-matrix composites“. In: *Engineering Fracture Mechanics* 75 (2008), pp. 2779–2794 (cit. on p. 46).

[33]A. J. Brunner, N. Murphy, and G. Pinter. „Development of a standardized procedure for the characterization of interlaminar delamination propagation in advanced composites under fatigue mode I loading conditions“. In: *Engineering Fracture Mechanics* 76 (2009), pp. 2678–2689 (cit. on pp. 18, 48).

[34]S. Brunner A. J. Stelzer, G. Pinter, and G .P. Terrassi. „Mode II fatigue delamination resistance of advanced fiber-reinforced polymer-matrix laminates: Towards the development of a standardized test procedure“. In: *International Journal of Fatigue* 50 (2013), pp. 57–62 (cit. on pp. 48, 116).

[35]Pradhan S. C. and T. E. Tay. „Three-dimensional finite element modelling of delamination growth in notched composite laminates under compression loading“. In: *Engineering Fracture Mechanics* 60.2 (1998), pp. 157–171 (cit. on pp. 20, 21).

[36]P. P. Camanho, C. G. Dávila, and M. F. de Moura. „Numerical simulation of mixed-mode progressive delamination in composite materials“. In: *Journal of Composite Materials* 37.16 (2003), pp. 1415–1438 (cit. on p. 11).

[37]R. D. S .G. Campilho, M. D. Banea, F. J. P. Chaves, and L. F. M. Da Silva. „eXtended Finite Element Method for fracture characterization of adhesive joints in pure mode I“. In: *Computational Materials Science* 50.4 (2011), pp. 1543–1549 (cit. on p. 21).

[38]M. Chiarelli and A. Frediani. „A Computation of the Three-Dimensional J-Integral for Elastic Materials with a View to Applications in Fracture Mechanics“. In: *Engineering Fracture Mechanics* 44.5 (1993), pp. 763–788 (cit. on p. 15).

[39]A. C. Chisholm, A. C. Rufin, B. D. Chapman, and Q. J. Benson. „Forty Years of Structural Durability and Damage Tolerance at Boeing Commercial Airplanes“. In: *Boeing Technical Journal. Innovation quarterly* May (2017) (cit. on pp. 2, 3).

[40]ASTM D2344/D2344M. „Standard Test Method for Short-Beam Strength of Polymer Matrix Composite Materials an Their Laminates“. In: *American Society for Testing and Materials International* (2016) (cit. on p. 47).

[41]ASTM D5528. „Standard Test Method for Mode I Interlaminar Fracture Toughness of Unidirectional Fiber-Reinforced Polymer Matrix Composites“. In: *American Society for Testing and Materials International* (2013) (cit. on pp. 46, 47, 128, 139).

[42]ASTM D6115. „Standard Test Method for Mode I Fatigue Delamination Growth Onset of Unidirectional Fiber-Reinforced Polymer Matrix Composites“. In: *International Organisation for Standardisation* (1997) (cit. on pp. 17, 48, 51).

[43]ASTM D6415/D6415M. „Standard Test Method for Measuring the Curved Beam Strength of a Fiber-Reinforced Polymer-Matrix Composite“. In: *American Society for Testing and Materials International* (2013) (cit. on p. 47).

[44]ASTM D7291/D7291M. „Standard Test Method for Through-Thickness "Flatwise" Tensile Strength and Elastic Modulus of a Fiber-Reinforced Polymer Matrix Composite Material“. In: *American Society for Testing and Materials International* (2015) (cit. on p. 47).

[45]ASTM D7905/7905M. „Standard Test Method for Determination of the Mode II Interlaminar Fracture Toughness of Unidirectional Fiber-Reinforced Polymer“. In: *American Society for Testing and Materials International* (2014) (cit. on pp. 47, 115, 128).

[46]C. Dahlen and G. S. Springer. „Delamination Growth in Composites under Cyclic Loads“. In: *Journal of Composite Materials* 28.8 (1994), pp. 732–781 (cit. on pp. 16, 17, 20).

[47]P. Davies, B. R. K. Blackman, and A. J. Brunner. „Standard Test Methods for Delamination Resistance of Composite Materials: Current Status“. In: *Applied Composite Materials* 5 (1998), pp. 345–364 (cit. on p. 46).

[48]H. G. deLorenzi. „On the Energy Release Rate and the J-Integral for 3-D Crack Configurations“. In: *International Journal of Fracture* 19 (1982), pp. 183–193 (cit. on p. 15).

[49]D. S. Dugdale. „Yielding of Steel Sheets Containing Slits“. In: *Journal of the Mechanics and Physics of Solids* 8.2 (1960), pp. 100–104 (cit. on pp. 8, 10).

[50]K. Eriksson. „A Domain Independent Integral Expression for the Crack Extension Force of a Curved Crack in Three Dimensions“. In: *Journal of the Mechanics and Physics of Solids* 50 (2002), pp. 381–403 (cit. on p. 15).

[51]K. Eriksson. „Decomposition of Eshelby's Energy Momentum Tensor and Application to Path and Domain Independent Integrals for the Crack Extension Force of a Plane Circular Crack in Mode III Loading“. In: *International Journal of Fracture* 144 (2007), pp. 215–225 (cit. on p. 93).

[52]G. Fernlund, D. McCammond, and J. K. Spelt. „A Curvilinear Formulation of the 3-D J integral: Application to Delamination Cracking of Curved Laminates“. In: *Composite Structures* 28 (1994), pp. 123–130 (cit. on pp. 15, 87–89).

[53]F. G. Forman, V. Shivakumar, J. W. Cardinal, L. C. Williams, and P. C. McKeighan. „Fatigue Crack Growth Database for Damage Tolerance Analysis“. In: *DOT/FAA/AR-05/15. US Department of Transportation, Federal Aviation Administration (2005)* (1992) (cit. on p. 113).

[54]FRANC3D. „FRANC3D Concepts and User Guide - Version 2.6“. In: *Cornell Fracture Group, Ithaca, New York* (2003) (cit. on p. 14).

[55]M. Gosz, J. Doldow, and B. Moran. „Domain Integral Formulation for Stress Intensity Factor Computation along Curved Three-Dimensional Interface Cracks“. In: *International Journal of Solid Structures* 35.15 (1998), pp. 1763–1783 (cit. on p. 15).

[56]V. K. Goyal. „Analytical modeling of the mechanics of nucleation and growth of cracks“. In: *PhD Thesis, Faculty of Virginia Polytechnic Institute and State University* USA (2002) (cit. on p. 44).

[57]V. K. Goyal, E. R. Johnson, and C. G. Dávila. „Irreversible constitutive law for modeling the delamination process using interfacial surface discontinuities“. In: *Composite Structures* 65 (2004), pp. 289–305 (cit. on p. 11).

[58]A. A. Griffith. „The Phenomena of Rupture and Flow in Solids“. In: *Philosophical Transactions of the Royal Society A: Mathematical, Physical and Engineering Sciences* 221 (1921), pp. 582–593 (cit. on p. 9).

[59]C-G. Gustafson and Hojo M. „Delamination fatigue crack growth in unidirectional graphite/epoxy laminates“. In: *Journal of Reinforced Plastic Composites* 6.1 (1987), 36–52 (cit. on p. 20).

[60]P. W. Harper and S. R. Hallett. „A fatigue degradation law for cohesive interface elements - Development and application to composite materials“. In: *International Journal of Fatigue* 32 (2010), pp. 1774–1787 (cit. on pp. 23, 26, 28, 29, 37).

[61]S. Hashemi, A. J. Kinloch, and J. G. Williams. „The Analysis of Interlaminar Fracture in Uniaxial Fibre-Polymer Composites“. In: *Proceedings of the Royal Society of London. A. Mathematical and Physical Sciences* 427.1872 (1990), pp. 173–199 (cit. on p. 10).

[62]Moéer M. Hillerborg A. and Petersson P. E. „Analysis of crack formation and crack growth in concrete by means of fracture mechanics and finite elements“. In: *Cement and Concrete Research* 6.6 (1976), pp. 773–781 (cit. on p. 10).

[63]H. Hojo, K. Tsuda, and K. Ogasawara. „Form and rate of corrosion of corrosion-resistant FRP resins“. In: *Advanced Composite Materials* 1.1 (1991), pp. 55–67 (cit. on p. 16).

[64]M. Hojo, S. Ochiai, C. G. Gustafson, and K. Tanaka. „Effect of Matrix Resin on Delamination Fatigue Crack Growth in CFRP Laminates“. In: *Engineering Fracture Mechanics* 49.1 (1987), pp. 35–47 (cit. on pp. 16, 19).

[65]M. Hojo, K. Tanaka, C. G. Gustafson, and R. Hayashi. „Effect of Stress Ratio on Near-Threshold Propagation of Delamination Fatigue Cracks in Unidirectional CFRP“. In: *Composite Science and Technology* 29 (1987), pp. 273–292 (cit. on pp. 16, 19, 20, 50, 51).

[66]M. Hojo, S. Matsuda, B. Fiedler, et al. „Mode I and II delamination fatigue crack growth behavior of alumina fiber/epoxy laminates in liquid nitrogen“. In: *International Journal of Fatigue* 24.2-4 (2002), pp. 109–118 (cit. on pp. 16, 18, 112).

[67]M. Hojo, T. Ando, M. Tanaka, et al. „Modes I and II interlaminar fracture toughness and fatigue delamination of CF/epoxy laminates with self-same epoxy interleaf“. In: *International Journal of Fatigue* 28.10 (2006), pp. 1154–1165 (cit. on pp. 50, 51, 112, 114).

[68]O. Huber, J. Nickel, and G. Kuhn. „On the Decomposition of the J-Integral for 3D Crack Problems“. In: *International Journal of Fracture* 64 (1993), pp. 339–348 (cit. on p. 15).

[69]W. Hwang and K. S. Han. „Interlaminar Fracture Behavior and Fiber Bridging of Glass-Epoxy Composite Under Mode I Static and Cyclic Loadings“. In: *Journal of Composite Materials* 23 (1989), pp. 396–430 (cit. on p. 16).

[70]E. Iesulauro. „FRANC2D/L: A Crack Propagation Simulator for Plane Layered Structures - Version 1.5 User's Guide.“ In: *Cornell Fracture Group, Ithaca, New York* (2009) (cit. on p. 14).

[71]G. R. Irwin. „Analysis of Stress and Strains Near the End of a Crack Transversing a Plate“. In: *Journal of Applied Mechanics* 24 (1957), pp. 361–364 (cit. on pp. 8, 10).

[72]ISO/IEC 17025. *General requirements for the competence of testing and calibration laboratories*. 2014 (cit. on p. 127).

[73]I. Jaeck, L. Carreras, J. Renart, et al. „Experimental methodology for obtaining fatigue crack growth rate curves in mixed-mode I-II by means of variable cyclic displacement tests“. In: *International Journal of Fatigue* 110 (2018), pp. 63–70 (cit. on pp. 109, 126, 128, 132, 134).

[74]R. Jones, S. Stelzer, and A. J. Brunner. „Mode I, II and Mixed Mode I/II delamination growth in composites“. In: *Composite Structures* 110 (2014), pp. 317–324 (cit. on p. 113).

[75]O'Brien T. K. „Composite interlaminar shear fracture toughness, GIIC: shear measurement or sheer myth?“ In: *Composite materials: fatigue and fracture, vol. 7. ASTM STP 1330* (1998), pp. 3–18 (cit. on p. 18).

[76]JIS K7086. „Testing methods for interlaminar fracture toughness of carbon fibre reinforced plastics“. In: *Japanese Standards Association* (1993) (cit. on pp. 46, 47, 115).

[77]L. M. Kachanov. „Time of the rupture process under creep conditions“. In: *IVZ Akad Nauk - S.S.R. Otd Tech Nauk* 8 (1958) (cit. on p. 11).

[78]G. A. Kardomateas, A. A. Pelegri, and B. Malik. „Growth of internal delaminations under cyclic compression in composite plates“. In: *Journal of the Mechanics and Physics of Solids* 43.6 (1995), pp. 847–868 (cit. on p. 20).

[79]L. F. Kawashita and S. R. Hallett. „A crack tip tracking algorithm for cohesive interface element analysis of fatigue delamination propagation in composite materials“. In: *International Journal of Solids and Structures* 49 (2012), pp. 2898–2913 (cit. on pp. 23, 27, 29, 37).

[80]M. Kenane and M. L. Benzeggagh. „Mixed-Mode Delamination Fracture Toughness of Unidirectional Glass/Epoxy Composites Under Fatigue Loading“. In: *Composite Science and Technology* 57 (1997), pp. 597–605 (cit. on pp. 16, 20).

[81]H. Khoramishad, A. D. Crocombe, K. B. Katnam, and I. A. Ashcroft. „Predicting fatigue damage in adhesively bonded joints using a cohesive zone model“. In: *International Journal of fatigue* 32.7 (2010), pp. 1146–1158 (cit. on pp. 23, 25).

[82]D. Krajcinovic. „Damage mechanics“. In: *Mechanics of Materials* 8.2-3 (1989), pp. 117–197 (cit. on p. 11).

[83]R. Krueger. „Development and Application of Benchmark Examples for Mode II Static Delamination Propagation and Fatigue Growth Predictions“. In: *Langley Research Center, Technical Report No. NASA/CR-2011-217305* (2011) (cit. on p. 21).

[84]R. Krueger. „Development of a Benchmarck Example for Delamination Fatigue Growth Prediction“. In: *Technical Report No. NASA/CR-2010-216723* (2010) (cit. on p. 17).

[85]R. Krueger. „Influence of Finite Element Software on Energy Release Rates Computed Using the Virtual Crack Closure Technique“. In: *NIA Report No. 2006-06, NASA/CR-214523,* (2006) (cit. on p. 97).

[86]R. Krueger. „The virtual crack closure technique for modeling interlaminar failure and delamination in advanced composite materials“. In: *Numerical Modelling of Failure in Advanced Composite Materials*. Woodhead Publishing Series in Composites Science and Engineering, 2015, pp. 3–53 (cit. on pp. 14, 21, 103).

[87]R. Krueger. „The virtual crack closure technique: history, approach and applications“. In: *Tech Rep NASA/CR-2002-211628* NASA (2002) (cit. on p. 21).

[88]R. Krueger. „Virtual Crack Closure Technique: History, Approach and Applications“. In: *Applied Mechanics Reviews* 57 (2004), pp. 109–143 (cit. on pp. 14, 21).

[89]B. G. Kumar, R. P. Singh, and T. Nakamura. „Degradation of carbon fibre reincorced epoxy composites by ultraviolet radiation and condensation“. In: *Journal of Composite Materials* 36.4 (2002), pp. 2713–2733 (cit. on p. 16).

[90]B. Landry and G. LaPlante. „Modeling delamination growth in composites under fatigue loadings of varying amplitudes“. In: *Composites Part B: Engineering* 43.2 (2012), pp. 533–541 (cit. on pp. 16, 23).

[91]M. Latifi, F. P. van der Meer, and L. J. Sluys. „A level set model for simulating fatigue-driven delamination in composites“. In: *International Journal of Fatigue* 80 (2015), pp. 434–442 (cit. on p. 23).

[92]M. Latifi, F. P. van der Meer, and L. J. Sluys. „An interface thick level set model for simulating delamination in composites“. In: *International Journal for Numerical Methods in Engineering* 111.4 (2017), pp. 303–324 (cit. on p. 16).

[93]M. Latifi, F. P. van der Meer, and L. J. Sluys. „Fatigue modeling in composites with the thick level set interface method“. In: *Composites Part A: Applied Science and Manufacturing* 101 (2017), pp. 72–80 (cit. on p. 23).

[94]F. A. Leone Jr., D. Girolamo, and C. G. Dávila. „Progressive damage analysis of bonded composite joints“. In: *NASA/TM2012-217790* (2012) (cit. on p. 11).

[95]F. Z. Li, C. F. Shih, and A. Needleman. „A Comparison of Methods for Calculating Energy Release Rates“. In: *Engineering Fracture Mechanics* 21.2 (1985), pp. 405–421 (cit. on p. 15).

[96]F. Z. Li, C. F. Shih, and A. Needleman. „On the Path Independence of the Point-Wise J Integral in Three Dimensions“. In: *International Journal of Fracture* 136 (2005), pp. 1–36 (cit. on p. 15).

[97]X. Li, C. Ferrie, E. Nottorf, and M. Portanova. „Virtual crack closure technique on stepped crack front (VCCT-S)“. In: *Annual Forum Proceedings - American Helicopter Society* 64.2 (2008) (cit. on p. 15).

[98]Y. P. Liu, C. Y. Chen, and G. Q. Li. „A modified zigzag approach to approximate moving crack front with arbitrary shape“. In: *Engineering Fracture Mechanics* 78.2 (2011), pp. 234–251 (cit. on pp. 15, 103).

[99]C. A. Lopez-Armas. „Evaluation of Constitutive Laws for the Computer Simulation of Fatigue Driven Delamination in Composite Materials“. In: (2008) (cit. on p. 12).

[100]S. Maiti and P. H. Geubelle. „A cohesive model for fatigue failure of polymers“. In: *Engineering Fracture Mechanics* 72.5 (2005), pp. 691–708 (cit. on p. 22).

[101]J. C. Mankins. „Technology readiness assessments: A retrospective“. In: *Acta Astronautica* 65 (2009), pp. 1216–1223 (cit. on p. 2).

[102]J. C. Mankins. „Technology readiness level“. In: *A White Paper (NASA)* (1995) (cit. on p. 2).

[103]R. H. Martin. „Evaluation of the Split Cantilever Beam for Mode III Delamination Testing“. In: *Technical Report No. NASA/TM 101562.* (1989) (cit. on pp. 18, 34).

[104]R. H. Martin and G. B. Murri. „Characterization of Mode I and Mode II Delamination Growth and Thresholds in AS4/PEEK Composites“. In: *Composite Materials: Testing and Design, Vol. 9, ASTM. American Society for Testing and Materials, Philadelphia* (1990), pp. 251–270 (cit. on pp. 16, 18–20).

[105]G. Matsubara, H. Ono, and K. Tanaka. „Mode II fatigue crack growth from delamination in unidirectional tape and satin-woven fabric laminates of high strength GFRP“. In: *International Journal of Fatigue* 28.10 (2006), pp. 1177–1186 (cit. on pp. 16, 50).

[106]S. Matsuda, M. Hojo, and S. Ochiai. „Mesoscopic Fracture Mechanism of Mode II Delamination Fatigue Crack Propagation in Interlayer-Toughened CFRP“. In: *JSME International Journal* 40 (1997), pp. 423–429 (cit. on pp. 16, 19).

[107]M. Matsuishi and T. Endo. „Fatigue of metals subjected to varying stress“. In: *The Japan Society of Mechanical Engineers* (1968) (cit. on p. 13).

[108]M. May and S. R. Hallett. „A combined model for initiation and propagation of damage under fatigue loading for cohesive interface elements“. In: *Composites Part A: Applied Science and Manufacturing* 41.12 (2010), pp. 1787–1796 (cit. on p. 23).

[109]M. May and S .R. Hallett. „An advanced model for initiation and propagation of damage under fatigue loading-part I: Model formulation“. In: *Composite Structures* 93.9 (2011), pp. 2340–2349 (cit. on p. 23).

[110]H. Mivehchi and A. Varvani-Farahani. „The effect of temperature on fatigue strength and cumulative fatigue damage of FRP composites“. In: *Procedia Engineering 2.1* (2010), pp. 2011–2020 (cit. on p. 16).

[111]N. Moës and T. Belytschko. „Extended finite element method for cohesive crack growth“. In: *Engineering fracture mechanics* 69.7 (2002), pp. 813–833 (cit. on p. 21).

[112]F. Moroni and A. Pirondi. „A procedure for the simulation of fatigue crack growth in adhesively bonded joints based on the cohesive zone model and different mixed-mode propagation criteria“. In: *Engineering Fracture Mechanics* 78.8 (2011), pp. 1808–1816 (cit. on pp. 23, 26).

[113]T. Murakami and T. Sato. „Three-Dimensional J-Integral Calculations of Part-Through Surface Crack Problems“. In: *Computers ans Structures* 17.5-6 (1983), pp. 731–736 (cit. on p. 15).

[114]P. Naghipour, M. Bartsch, and H. Voggenreiter. „Simulation and experimental validation of mixed mode delamination in multidirectional CF/PEEK laminates under fatigue loading“. In: *International Journal of Solids and Structures* 48.6 (2011), pp. 1070–1081 (cit. on p. 23).

[115]Y. Nakai and C. Hiwa. „Effects of Loading Frequency and Environment on Delamination Fatigue Crack Growth of CFRP“. In: *International Journal of Fatigue* 24.2-4 (2002), pp. 161–170 (cit. on p. 16).

[116]O. Nguyen, E. A. Repetto, M. Ortiz, and R. A. Radovitzky. „A cohesive model of fatigue crack growth“. In: *International Journal of Fracture* 110.4 (2001), pp. 351–369 (cit. on p. 22).

[117]T. K. O'Brien. „Fatigue Delamination Behavior of PEEK Thermoplastic Composite Laminates“. In: *Journal of Reinforced Plastic Composites* 7 (1988), pp. 341–359 (cit. on p. 16).

[118]T. K. O'Brien. „Mixed-Mode Strain Energy Release Rate Effects on Edge Delamination of Composites“. In: *ASTM. American Society for Testing and Materials, West Conshohocken* (1984), pp. 125–142 (cit. on p. 16).

[119]T. K. O'Brien, G. B. Murri, and S. A. Salpekar. „Interlaminar shear fracture toughness and fatigue thresholds for composite materials“. In: *Composite Materials: Fatigue and Fracture (2nd Vol.)* ASTM STP 1012 (1989), pp. 222–250 (cit. on pp. 16, 18, 134).

[120]A. Ortega. „Characterization of the translaminar cohesive law“. In: *Ph.D. dissertation. Universitat de Girona* (2017) (cit. on p. 11).

[121]M. Ortiz and A. Pandolfi. „Finite-Deformation Irreversible Cohesive Elements for Three-Dimensional Crack-Propagation Analysis“. In: *International Journal for Numerical Methods in Engineering I* 44 (1999), pp. 1267–1282 (cit. on p. 11).

[122]van der Meer F. P., L. J. Sluys, and N. Möes. „Toward efficient and robust computation of energy release rate and mode mix for delamination“. In: *Composites Part A: Applied Science and Manufacturing* 43.7 (2012), pp. 1101–1112 (cit. on pp. 15, 23).

[123]N. J. Pagano and G. A. Schoeppner. „Delamination of polymer matrix composites: problems and assessment“. In: *Comprehensive Composite Materials* (2000) (cit. on p. 1).

[124]P. Paris and F. Erdogan. „A Critical Analysis of Crack Propagation Laws“. In: *ASME Journal of Basic Engineering* 85.4 (1963), pp. 528–533 (cit. on pp. 14, 20).

[125]P. C. Paris. „A Rational Analytic Theory of Fatigue“. In: *The Trend in Engineering* 13 (1961), pp. 9–14 (cit. on pp. 14, 20, 38, 40, 113).

[126]J. A. Pascoe, R. C. Alderliesten, and R. Benedictus. „Methods for the prediction of fatigue delamination growth in composites and adhesive bonds - A critical review“. In: *Engineering Fracture Mechanics* 112-113 (2013), pp. 72–96 (cit. on pp. 13, 14, 21).

[127]R. H. J. Peerlings, W. A. M. Brekelmans, R. de Borst, and M. G. D. Geers. „Gradient-enhanced damage modelling of high-cycle fatigue“. In: *International Journal for Numerical Methods in Engineering* 49.12 (2000), pp. 1547–1569 (cit. on pp. 24, 25).

[128]L. Peng, J. Zhang, L. Zhao, et al. „Mode I Delamination Growth of Multidirectional Composite Laminates Under Fatigue Loading“. In: *Journal of Composite Materials* 45.10 (2011), pp. 1077–1090 (cit. on p. 16).

[129]A. Pirondi and F. Moroni. „A Progressive Damage Model for the Prediction of Fatigue Crack Growth in Bonded Joints“. In: *The Journal of Adhesion* 86.5-6 (2010), pp. 501–521 (cit. on pp. 23, 26).

[130]A. Pirondi and F. Moroni. „Simulation of Mixed-Mode I/II Fatigue Crack Propagation in Adhesive Joints with a Modified Cohesive Zone Model“. In: *Journal of Adhesion Science and Technology* 25 (2011), pp. 2483–2499 (cit. on pp. 29, 37).

[131]A. Poursartip and N. Chinatambi. „Fatigue Damage Development in Notched (0 2/$\pm$45) s Laminates“. In: *Composite Materials: Fatigue and Fracture. ASTM STP 1012 Philadelphia. American Society for Testing and Materials*. Vol. 2. 1989, pp. 45–65 (cit. on p. 21).

[132]R. L. Ramkumar and J. D. Whitcomb. „Characterization of mode I and mixed-mode delamination growth in T300/5208 graphite/ epoxy“. In: *Delamination and Debonding of Materials ASTM STP 876. American Society for Testing and Materials, Philadelphia* (1985), pp. 315–335 (cit. on p. 20).

[133]M. M. Ratwani and H. P. Kan. „Compression fatigue analysis of fiber composites“. In: *Journal of Aircraft* 18.6 (1981), pp. 458–462 (cit. on p. 21).

[134]J. Renart, J. Vicens, Budhe S., et al. „ An automated methodology for mode II delamination tests under fatigue loading basedon the real time monitoring of the specimen's compliance“. In: *International Journal of Fatigue* 82 (2016), pp. 634–642 (cit. on pp. 48, 51, 52, 112, 116, 126).

[135]J. Renart, S. Budhe, L. Carreras, J.A. Mayugo, and J. Costa. „A new testing device to simultaneously measure the fatigue delamination behaviour of a batch of specimens“. In: *Submitted to International Journal of Fatigue* () (cit. on pp. 48, 128–130, 135).

[136]J. R. Rice. „A Path Independent Integral and the Approximate Analysis of Strain Concentration by Notches and Cracks“. In: *Journal of Applied Mechanics* 35 (1968), pp. 379–386 (cit. on pp. 14, 22, 41, 89).

[137]J. R. Rice. *The mechanics of earthquake rupture*. Division of Engineering, Brown University, 1979 (cit. on p. 25).

[138]R. H. Rigby and M. H. Aliabadi. „Decomposition of the Mixed-Mode J-Integral - Revisited“. In: *International Journal of Solid Structures* 35.17 (1998), pp. 2073–2099 (cit. on pp. 15, 93).

[139]R. H. Rigby and M. H. Aliabadi. „Mixed-Mode J-Integral Method for Analysis of 3D Fracture Problems using BEM“. In: *Engineering Analysis with Boundary Elements* 11 (1993), pp. 239–256 (cit. on p. 15).

[140]P. Robinson, U. Galvanetto, D. Tumino, G. Bellucci, and D. Violeau. „Numerical simulation of fatigue-driven delamination using interface elements“. In: *International Journal for Numerical Methods in Engineering* 63.13 (2005), pp. 1824–1848 (cit. on pp. 22–24, 29).

[141]K. L. Roe and T. Siegmund. „An irreversible cohesive zone model for interface fatigue crack growth simulation“. In: *Engineering fracture mechanics* 70.2 (2003), pp. 209–232 (cit. on p. 22).

[142]A. J. Russell and K. N. Street. „Predicting interlaminar fatigue crack growth rates in compressively loaded laminates“. In: *Delamination and Debonding of Materials ASTM STP 1012. American Society for Testing and Materials, Philadelphia* (1989), pp. 162–178 (cit. on p. 20).

[143]R. Sachse, A. K. Pickett, W. Essig, and P. Middendorf. „Experimental and numerical investigation of the influence of rivetless nut plate joints on fatigue crack growth in adhesively bonded composite joints“. In: *International Journal of Fatigue* 105 (2017), pp. 262–275 (cit. on p. 20).

[144]SAE International. „Polymer Matrix Composites: Materials Usage, Design and Analysis“. In: *Composite Materials Handbook Series* 3 (2013), pp. 686–794 (cit. on p. 2).

[145]C. Sarrado, A. Turon, J. Costa, and J. Renart. „An experimental analysis of the fracture behavior of composite bonded joints in terms of cohesive laws“. In: *Composites Part A: Applied Science and Manufacturing* 90 (2016), pp. 234–242 (cit. on pp. 11, 128).

[146]C. Sarrado, A. Turon, J. Renart, and I. Urresti. „Assessment of energy dissipation during mixed-mode delamination growth using cohesive zone models“. In: *Composites Part A* 43.11 (2012), pp. 2128–2136 (cit. on p. 124).

[147]D. W. Saxena A.and Schmidt, J. K. Donald, and S. J. Hudak. „Computer-controlled decreasing stress intensity technique for low rate fatigue crack growth testing“. In: *Journal of Testing and Evaluation* 6.3 (1978), pp. 167–174 (cit. on p. 51).

[148]D. W. Schmidt and J. K. Donald. „Computer-controlled stress intensity gradient technique for high rate fatigue crack growth testing“. In: *Journal of Testing and Evaluation* 8.1 (1980), pp. 19–24 (cit. on p. 51).

[149]M. Schollmann, M. Fulland, and H. Richard. „Development of a new software for adaptive crack growth simulations in 3D structures“. In: *Engineering Fracture Mechanics* 70 (2003), pp. 249–268 (cit. on p. 14).

[150]C. F. Shih, B. Moran, and T. Nakamura. „Energy Release Rate Along a Three-Dimensional Crack Front in a Thermally Stressed Body“. In: *International Journal of Fracture* 30 (1986), pp. 79–102 (cit. on p. 15).

[151]Y. Shindo, A. Inamoto, F. Narita, and K. Horiguchi. „Mode I Fatigue Delamination Growth in GFRP Woven Laminates at Low Temperatures“. In: *Engineering Fracture Mechanics* 73.14 (2006), pp. 2080–2090 (cit. on p. 16).

[152]K. Shivakumar, H. Chen, F. Abali, D. Le, and C. Davis. „A total fatigue life model for mode I delaminated composite laminates“. In: *International Journal of Fatigue* 28.1 (2006), pp. 33–42 (cit. on p. 20).

[153]A. Sjögren and L. E. Asp. „Effects of Temperature on Delamination Growth in a Carbon/Epoxy Composite Under Fatigue Loading“. In: *International Journal of Fatigue* 24 (2002), pp. 179–184 (cit. on pp. 16, 18).

[154]S. A. Smith and I. S. Raju. „Evaluation of Stress-Intensity Factors Using General Finite-Element Models“. In: *Fatigue and Fracture Mechanics. ASTM STP 1321. American Society for Testing and Materials* 29 (1998) (1998) (cit. on p. 103).

[155]B. F. Sørensen and P. Kirkegaard. „Determination of mixed mode cohesive laws“. In: *Engineering fracture mechanics* 73.17 (2006), pp. 2642–2661 (cit. on pp. 10, 11).

[156]S. M. Spearing and A. G. Evans. „The role of fiber bridging in the delamination resistance of fiber-reinforced composites“. In: *Acta Metallurgica et Materialia* 40.9 (1992), pp. 2191–2199 (cit. on p. 10).

[157]M. Springer. „Modeling and Simulation of Fatigue Dmage in Power Semiconductors“. In: *Ph.D. dissertation. Technical University of Wien* (2017) (cit. on p. 22).

[158]S. Stelzer, A. Brunner, A. Arguelles, N. Murphy, and G. Cano. „Mode I delamination fatigue crack growth in unidirectional fiber reinforced composites: Results from ESIS TC4 round-robins“. In: *Engineering Fracture Mechanics* 116 (2014), pp. 92–107 (cit. on pp. 117, 129).

[159]U. Stigh, K. S. Alfredsson, and A. Biel. „Measurement of cohesive laws and related problems“. In: *ASME 2009 international mechanical engineering congress and exposition. American Society of Mechanical Engineers* (2009), pp. 293–298 (cit. on p. 11).

[160]Dassault Systémes. „Abaqus manual 6.12“. In: (2012) (cit. on pp. 41, 74, 97).

[161]K. Tanaka and H. Tanaka. „Stress-ratio effect on mode II propagation of interlaminar fatigue cracks in graphite/epoxy composites“. In: *Composite Materials: Fatigue and Fracture,Vol. 6, ASTM International. American Society for Testing and Materials* (1997) (cit. on pp. 16, 18, 19, 50, 114).

[162]K. Tanaka, K. Kageyama, and M. Hojo. „Prestandardization study on mode II interlaminar fracture toughness test for CFRP in japan“. In: *Composites* 26.4 (1995), pp. 257–267 (cit. on p. 115).

[163]C. Tao, J. Qiu, W. Yao, and H. Ji. „A novel method for fatigue delamination simulation in composite laminates“. In: *Composites Science and Technology* 128 (2016), pp. 104–115 (cit. on pp. 23, 27–29, 37).

[164]C. Tao, S. Mukhopadhyay, B. Zhang, et al. „An improved delamination fatigue cohesive interface model for complex three-dimensional multi-interface cases“. In: *Composites Part A: Applied Science and Manufacturing* 107 (2018), pp. 633–646 (cit. on pp. 23, 27, 29).

[165]T. E. Tay. „Characterization and analysis of delamination fracture in composites: An overview of developments from 1990 to 2001“. In: *Applied Mechanical Reviews* 56.1 (2003), pp. 1–23 (cit. on p. 46).

[166]D. Tumino and F. Cappello. „Simulation of fatigue delamination growth in composites with different mode mixtures“. In: *Journal of Composite Materials* 41.20 (2007), pp. 2415–2441 (cit. on pp. 22–24).

[167]A. Turon, P. P. Camanho, J. Costa, and C. G. Dávila. „A Damage Model for the Simulation of Delamination in Advanced Composites Under Variable-Mode Loading“. In: *Mechanics of Materials* 38 (2006), pp. 1072–1089 (cit. on pp. 11, 30, 33, 38–41, 44, 54, 65, 74, 98, 99, 105, 159).

[168]A. Turon, P. P. Camanho, J. Costa, and J. Renart. „Accurate Simulation of Delamination Growth Under Mixed-Mode Loading Using Cohesive Elements: Definition of Interlaminar Strengths and Elastic Stiffness“. In: *Composite Structures* 92.8 (2010), pp. 1857–1864 (cit. on pp. 11, 30, 33–35, 38–41, 47, 54, 65, 74, 92, 97–99, 105, 128, 159).

[169]A. Turon, E. V. Gonzalez, C. Sarrado, G. Guillamet, and P. Maimi. „Accurate simulation of delamination under mixed-mode loading using a cohesive model with a mode-dependent penalty stiffness“. In: *Composite Structures* 184 (2018), pp. 506–511 (cit. on p. 59).

[170]A. Turon, P. P. Camanho, E. V. González, and A. Soto. „Analysis of delamination damage in composite structures using cohesive elements“. In: *Comprehensive Composite Materials II* (2017) (cit. on pp. 11, 13).

[171]A. Turon, J. Costa, P. P. Camanho, and P. Maimí. „Analytical and numerical investigation of the length of the cohesive zone in delaminated composite materials“. In: *Mechanical response of composites*. Springer, 2008, pp. 77–97 (cit. on p. 25).

[172]A. Turon, J. Costa, and P. P. Camanho. „Simulation of delamination in composites under high-cycle fatigue“. In: *Composites: Part A* 38 (2007), pp. 2270–2282 (cit. on pp. 23, 25, 26, 28, 29, 37, 41, 46).

[173]F. P. van der Meer and L. J. Sluys. „The Thick Level Set method: Sliding deformations and damage initiation“. In: *Comput. Methods Appl. Mech. Engrg.* 285 (2015), pp. 64–82 (cit. on p. 9).

[174]F. P. van der Meer, N. Moës, and L. J. Sluys. „A level set model for delamination – Modeling crack growth without cohesive zone or stress singularity“. In: *Engineering Fracture Mechanics* 79 (2012), pp. 191–212 (cit. on pp. 9, 15, 23).

[175]J. G. M. Van Mier. „Mode I fracture of concrete: discontinuous crack growth and crack interface grain bridging“. In: *Cement and Concrete Research* 21.1 (1991), pp. 1–15 (cit. on p. 10).

[176]W. Van Paepegem and J. Degrieck. „Effects of Load Sequence and Block Loading on the Fatigue Response of Fiber Reinforced Composites“. In: *Mechanics of Advanced Materials and Structures* 9.1 (2002), pp. 19–35 (cit. on p. 16).

[177]Z. C. Xia and J. W. Hutchinson. „Mode II fracture toughness of a brittle adhesive layer“. In: *International Journal of Solids and Structures* 31.8 (1994), pp. 1133–1148 (cit. on p. 10).

[178]D. Xie and Sherrill B. Biggers Jr. „Strain energy release rate calculation for a moving delamination front of arbitrary shape based on the virtual crack closure technique . Part I : Formulation and validation“. In: *Engineering Fracture Mechanics* 73 (2006), pp. 771–785 (cit. on pp. 15, 103).

[179]B. Yang, S. Mall, and K. Ravi-Chandar. „A cohesive zone model for fatigue crack growth in quasibrittle materials“. In: *International Journal of Solids and Structures* 38.22-23 (2001), pp. 3927–3944 (cit. on p. 22).

[180]J. Zhang, L. Peng, L. Zhao, and B. Fei. „Fatigue Delamination Growth Rates and Thresholds of Composite Laminates Under Mixed Mode Loading“. In: *International Journal of Fatigue* 40 (2012), pp. 7–15 (cit. on pp. 16, 18).

[181]Z. Zou, S. R. Reid, and P. D. Soden. „Application of a delamination model to laminated composite structures“. In: *Composite Structures* 56 (2002), pp. 375–389 (cit. on p. 15).

[182]Z. Zou, S. R. Reid, P. D. Soden, and S. Li. „Mode separation of energy release rate for delamination in composite laminates using sublaminates“. In: *International Journal of Solids and Structures* 38 (2001), pp. 2597–2613 (cit. on p. 15).

Generated papers

PAPER A

A

PAPER A

Point-wise evaluation of the growth driving direction for arbitrarily shaped delamination fronts using cohesive elements

L. Carreras [a], B.L.V. Bak [b], A. Turon [a], J. Renart [a], E. Lindgaard [b]

[a] AMADE, Mechanical Engineering and Industrial Construction Department, Universitat de Girona, Carrer Universitat de Girona 4, 17003 Girona, Spain

[b] Department of Materials and Production, Aalborg University, Fibigerstraede 16, DK-9220 Aalborg East, Denmark

The paper has been published in *European Journal of Mechanics / A Solids* (In press).

ACCEPTED MANUSCRIPT

Point-wise evaluation of the growth driving direction for arbitrarily shaped delamination fronts using cohesive elements

L. Carreras[a,*], B.L.V. Bak[b], A. Turon[a], J. Renart[a], E. Lindgaard[b]

[a] *AMADE, Polytechnic School, University of Girona, Campus Montilivi s/n, E-17003 Girona, Spain*
[b] *Dept. of Materials and Production, Aalborg University, Fibigerstraede 16, DK-9220 Aalborg East, Denmark*

Abstract

The identification of the delamination propagation direction in three-dimensional structures with arbitrarily shaped fronts is needed in many applications. In the cohesive element framework, the propagation direction may be computed as the normal direction to a numerical damage isoline. The damage isoline tracking requires to exchange information between neighboring elements, thus post-processing global data, which is computationally expensive. This work presents a novel approach for the evaluation of the growth driving direction, only using local element information. The method can be directly implemented in a user-defined element subroutine and be evaluated at the execution time of the analysis. The presented formulation and its implementation in the commercial Finite Element code Abaqus is validated by comparison to the damage isoline shape rendering using global information.

Keywords:

Delamination growth, Cohesive zone model, Finite element analysis

1. Introduction

Long fiber-reinforced polymers are layered materials produced by stacking plies which contain continuous fibers in different orientations. Fibers supply stiffness and strength to the material in the laminate plane. Although laminated composite structures are designed so that the highest stresses are in the fiber directions, out-of-plane stresses may also occur at many types of geometric discontinuities

*Corresponding author. Tel.: +34 972 418 817
Email addresses: laura.carreras@udg.edu (L. Carreras), brianbak@mp.aau.dk (B.L.V. Bak), albert.turon@udg.edu (A. Turon), jordi.renart@udg.edu (J. Renart), elo@mp.aau.dk (E. Lindgaard)

ACCEPTED MANUSCRIPT

such as ply drops, skin-stiffener terminations, intersections, sandwich panels, free edges, holes, cut-outs, flanges, bonded and bolted joints or impacted zones. These load cases may damage the interface between plies, causing the failure mechanism called delamination. Delamination is considered the most detrimental failure mechanism in laminated composite structures because it occurs at relatively low load levels but still entails significant reduction of the structure's load carrying capacity. To address this problem without recoursing to impractical safe-life designs, damage-tolerant approaches are used. In that event, Finite Element (FE) analysis is an indispensable tool to predict delamination growth in complex laminated structures subjected to both static and fatigue loading.

The virtual crack closure technique (VCCT) is one of the most widely used FE techniques [1]. However, its application to realistic three-dimensional geometries with arbitrarily shaped crack front requires a continuous adaptive meshing technique in order to get a smooth front that fits with the instantaneous crack front curvature [2–4]. Alternative methods, that allow the use of stationary meshes, consist of tracing a smooth virtual front around the stepped front [5–7]. These techniques require the use of algorithms to determine the normal direction to the virtual delamination front using global information (or 18-noded elements as in [5]). This direction is used to compute the virtually closed area and to define a local coordinate system that enables to calculate the energy release rate components according to it.

An alternative to VCCT, is the cohesive zone model (CZM), firstly developed by Dugdale [8] and Barrenblatt [9]. In contrast with the VCCT approach, the application of the CZM is not limited to Linear Elastic Fracture Mechanics (LEFM). Indeed, it accounts for a large fracture process zone ahead of the crack tip where the material undergoes stiffness degradation until complete decohesion. This nonlinear material behavior is lumped into a surface, the cohesive zone, modeled by cohesive elements. Under static loading conditions, no crack tip tracking algorithm is required as long as the assumptions of identical fracture toughnesses for shear mode openings and independence of fracture toughness with propagation direction with respect to fiber orientation are made [10–17]. However, some of the existing methods for the simulation of fatigue-driven delamination using the CZM approach do require

ACCEPTED MANUSCRIPT

the identification of the propagation direction for its three-dimensional implementation [18–22], even making the same assumptions as in the static formulation. To the authors knowledge, the existing formulations to estimate the direction of crack propagation using CZM are nonlocal and, thus, require additional post-processing. In practice, these algorithms are computationally inefficient for the analysis of large structures.

Another and more recent approach presented by Van der Meer et al. [23] uses the level set method to describe the crack front location. Like the VCCT, it is a fracture mechanics approach. Furthermore, its variant for large process zone simulation [24] makes use of a stiffness degrading damage variable that allows a band of damaged material with predefined width. Conversely to most of the existing CZM formulations, the damage variable is not a function of the local properties but it is defined by the distance to the crack front, where the crack front is defined as the line that separates the damage process zone and the completely damaged interface.

In this work, a local algorithm to determine the growth driving direction in CZM is presented. It can be evaluated at any point within the cohesive zone at the same time the damage state is being computed. Therefore, it can be used to enhance the cohesive element formulation under static loading, preserving the local nature of the formulation. Moreover, it is an efficient alternative to the existing nonlocal propagation direction algorithms used in the methods for fatigue simulation.

The concept of growth driving direction applied to cohesive elements is presented in 2.1. Three different criteria for the growth driving direction identification are defined in Section 2.2. The formulation according to the first criterion is developed in Section 2.3. The formulation for the other two criteria is given in Appendix B. The three growth driving direction criteria are implemented for the particular case of the CZM presented in [15, 17], which is summarized in Appendix A. However, it is worth to mention that the same criteria could be applied to any other CZM formulation. Sections 3 and 4 present the results from the application of the formulation to three one-element case studies under different loading conditions and a real three-dimensional composite structure, respectively. The work closes by discussing the obtained results and with the conclusions.

ACCEPTED MANUSCRIPT

2. Determination of the growth driving direction

In the framework of LEFM, the propagation direction is assumed to be the normal direction to the crack front, where the crack front is the line separating the uncracked and cracked parts (see Figure 1.a). In contrast to LEFM, the CZM technique accounts for a band of damaged interface of variable length, called the fracture process zone, FPZ (light grey band in Figure 1.b). Therefore, the propagation direction, understood as the normal to the crack front line, can not be defined in the CZM framework. In this work, the concept of "growth driving direction"is introduced for CZM as the analogous to the propagation direction. It is assumed to be normal to a given damage isoline and can be calculated at any point within the FPZ. This definition follows naturally from the LEFM definition and provides the exact same result in the limiting case where the length of the fracture process zone goes to zero.

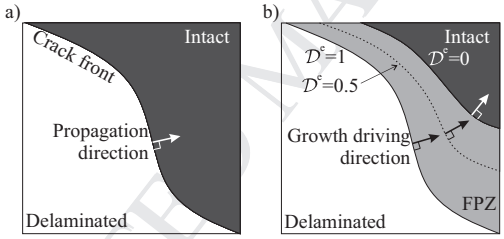

Figure 1: a) The propagation direction is assumed to be the normal direction to the crack front in the LEFM framework. b) The growth driving direction is assumed to be the normal direction to a damage isoline in the CZM framework. The energy-based damage variable, $\mathcal{D}^e$, is defined in Appendix A.

2.1. Growth driving direction using cohesive elements

Consider a laminated structure undergoing a delamination crack restricted to propagate in the interface between two adjacent plies. The degradation process of the material ahead of the crack tip is modeled in this work using the bilinear CZM formulation developed by Turon et al. in [15, 17]. As detailed in Appendix A, the process of the degradation of the interface properties is governed by an energy-based damage variable, $\mathcal{D}^e$, defined in Equation (A.16) as the ratio between the specific dissipated energy, ω_d, and the fracture toughness, $\mathcal{G}_c$. Thus, $\mathcal{D}^e$ is a scalar quantity that measures the

ACCEPTED MANUSCRIPT

degree of crack development: when $\mathcal{D}^e$ equals 0, the degradation process is yet to start, while, when $\mathcal{D}^e$ equals 1, the crack is completely developed. The total specific work, ω_{tot}, corresponding to a given state of damage is the sum of the specific dissipated energy, ω_d, and the specific elastic energy, ω_e.

To ensure the proper energy dissipation under mixed-mode conditions, a one-dimensional cohesive law relates the equivalent mixed-mode traction, μ, to the equivalent mixed-mode displacement jump, λ. Such constitutive law is formed by an initial elastic region, before damage initiation, and a softening region. When the area under the one-dimensional traction-displacement jump curve is equal to the fracture toughness, $\mathcal{G}_c$, a new crack surface is formed. The Benzeggagh-Kenane criterion [25] is used to define the mixed-mode displacement jumps at which the onset of damage, λ_o, and propagation, λ_c, occur. A sketch of the equivalent one dimensional bilinear law is represented in Figure 2 for a given mode-mixity, B.

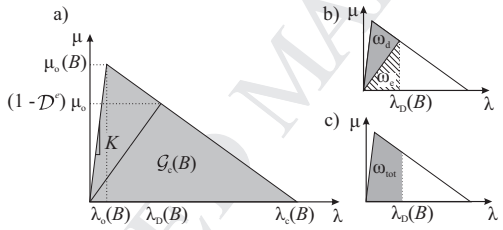

Figure 2: Equivalent one-dimensional cohesive law for a given mode-mixity, B. The shadowed area in a) represents the fracture toughness, $\mathcal{G}_c$, in b), the specific dissipated energy, ω_d, and the specific elastic energy, ω_e, and in c), the total specific work, ω_{tot}, for a given state of damage.

Complying with the cohesive element definition, the interfacial tractions and displacement jumps are evaluated at the interfacial deformed midsurface, $\overline{S}$, and determined by its local orientation. Thus, the normal and tangential traction components, acting on a unit deformed interfacial midsurface area, are conjugated to the normal and tangential displacement jumps across the material discontinuity. For the analysis of delamination propagation in three-dimensional structures, the interfacial midsurface is defined by the Cartesian coordinates $\overline{x}_i$, with $i = 1, 2, 3$. The local Cartesian coordinate system located on the deformed midsurface is defined by two tangential unit vectors, $\hat{\boldsymbol{e}}_1$ and $\hat{\boldsymbol{e}}_2$, and a normal unit vector, $\hat{\boldsymbol{e}}_3$. Assuming that the crack propagation is confined to the interface, the vector defining

ACCEPTED MANUSCRIPT

the growth driving direction must belong to the plane spanned by the tangential vectors $\hat{\boldsymbol{e}}_1$ and $\hat{\boldsymbol{e}}_2$ at the point $\overline{p}_i$ where the direction is evaluated. Thus, the three-dimensional problem, can be solved in a two-dimensional space defined by the local Cartesian coordinates (e_1, e_2), where e_l, with $l = 1, 2$, are the coordinates spanned by the unit vectors $\hat{\boldsymbol{e}}_l$.

Then, for any given distribution of $\mathcal{D}^e(e_1, e_2)$, the growth driving direction at any point on the midsurface is assumed normal to the damage isolines, following the discussion related to Figure 1, i.e. is given by the negative of the gradient vector:

$$-\nabla \mathcal{D}^e(e_1, e_2) \tag{1}$$

2.2. Growth driving direction criteria

The growth driving direction at any point $\overline{p}_i$, contained in $\overline{S}$, is defined in this work as the one that provides the largest rate of decrease of $\mathcal{D}^e$. This is the direction of the negative gradient of $\mathcal{D}^e$, defined in the local Cartesian coordinate system (e_1, e_2) with origin at $\overline{p}_i$ (see Equation (1)). However, polar coordinates are most appropriate when looking for a direction from a pole (See Figure 3). Thus, the growth driving direction can be found by identifying the angle φ that minimizes the slope of $\mathcal{D}^e$ with respect to the radial coordinate, ρ:

$$\min_{\varphi} \frac{\partial \mathcal{D}^e}{\partial \rho} \tag{2}$$

Considering the energy-based damage, $\mathcal{D}^e$, dependent on both the mode mixity, B, and the mixed-mode displacement jump, λ, and by application of the chain rule, the angle φ that minimizes Equation (2) can be found by solving:

$$\frac{\partial}{\partial \varphi} \frac{\partial \mathcal{D}^e(B, \lambda)}{\partial \rho} = \frac{\partial}{\partial \varphi} \left(\frac{\partial \mathcal{D}^e}{\partial B} \frac{\partial B}{\partial \rho} + \frac{\partial \mathcal{D}^e}{\partial \lambda} \frac{\partial \lambda}{\partial \rho} \right) = 0 \tag{3}$$

and by checking its convexity:

ACCEPTED MANUSCRIPT

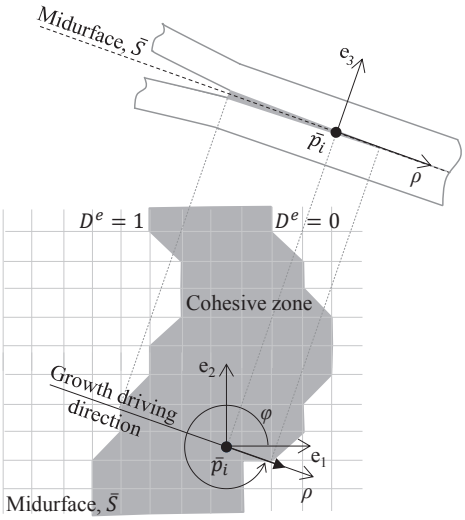

Figure 3: The growth driving direction evaluated at point $\overline{p}_i$ is embedded in the tangential plane spanned by the local Cartesian coordinates e_1 and e_2.

$$\frac{\partial^2}{\partial\varphi^2}\frac{\partial\mathcal{D}^e\left(B,\lambda\right)}{\partial\rho} = \frac{\partial^2}{\partial\varphi^2}\left(\frac{\partial\mathcal{D}^e}{\partial B}\frac{\partial B}{\partial\rho} + \frac{\partial\mathcal{D}^e}{\partial\lambda}\frac{\partial\lambda}{\partial\rho}\right) > 0 \tag{4}$$

However, equations (3) and (4) are equal to zero in the elastic regime ($\lambda \in [0, \lambda_o]$), since the energy based damage variable, $\mathcal{D}^e$, is also equal to zero (see Equation (A.16). In order to compute the growth driving direction before the initiation of the degradation process, another criterion, based on the ratio between the total specific work, ω_{tot} and the fracture toughness, $\mathcal{G}_c$, can be formulated such that the growth driving direction can be found by solving:

$$\min_{\varphi} \frac{\partial\left(\frac{\omega_{tot}}{\mathcal{G}_c}\left(B,\lambda\right)\right)}{\partial\rho} \tag{5}$$

Note that, similarly to the energy-based damage, $\mathcal{D}^e$, the ratio between the total specific work and the fracture toughness, $\frac{\omega_{tot}}{\mathcal{G}_c}$, is dependent on both the mode mixity, B, and the mixed-mode displacement jump, λ.

Finally, for the sake of simplicity, a third criterion, which is also active before damage initiation,

ACCEPTED MANUSCRIPT

can be formulated only taking into account the mixed-mode displacement jump field, λ:

$$\min_{\varphi} \frac{\partial \lambda}{\partial \rho} \tag{6}$$

The general expressions to solve for each of the criteria are listed in Table B.5.

In summary, three different criteria are presented depending on the quantity being analyzed: the energy-based damage, $\mathcal{D}^e$, (Criterion 1), the total specific work over the fracture toughness, $\frac{\omega_{tot}}{\mathcal{G}_c}$ (Criterion 2), and the mixed-mode displacement jump, λ, (Criterion 3). The evolution of these quantities along the growth driving direction are sketched in Figure 4 for an interface opened under pure mode I conditions. The three criteria are listed in Table 1 and presented in the following.

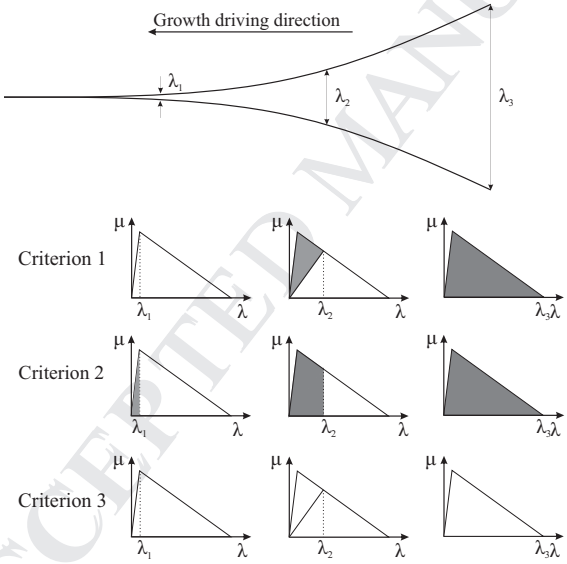

Figure 4: Quantities being minimized in each criterion for a pure mode I opened interface.

Criterion 1. The growth driving direction is defined by the negative gradient of the energy-based damage variable, $\mathcal{D}^e$. This is equivalent to computing the negative gradient of the ratio between the specific dissipated energy, ω_d (see Figure 2.b), and the fracture toughness, $\mathcal{G}_c$. Since Criterion 1 is based on the energy-based damage distribution, $\mathcal{D}^e$, it is only active once the degradation process is

ACCEPTED MANUSCRIPT

Criterion ID	Function to solve	Nomenclature	Approach	Limitations
1	$-\nabla\mathcal{D}^e$	$\mathcal{D}^e$: Energy-based damage	Energy-based	Not active in elastic regime
2	$-\nabla\frac{\omega_{tot}}{\mathcal{G}_c}$	ω_{tot}:total specific work $\mathcal{G}_c$: fracture toughness	Energy-based	May depend on the specific elastic energy in CZM
3	$-\nabla\lambda$	λ: mixed-mode opening displacement	Geometrical	Independent of interface properties

Table 1: Summary of the criteria to determine the growth driving direction.

already initiated. Moreover, Criterion 1 is an energy-based approach that depends on the kinematics and the constitutive law of the cohesive element. Since the cohesive law is usually mode-dependent, an uneven distribution of mode-mixity, B, can affect the gradient vector.

Criterion 2. The growth driving direction is defined by the negative gradient of the ratio between the total specific work, ω_{tot} (see Figure 2.c), and the fracture toughness, $\mathcal{G}_c$. Thus, both the specific dissipated energy, ω_d and the specific elastic energy, ω_e, are included in the computation of Criterion 2. Since, as soon as two initially coinciding points separate from each other some elastic energy is stored, Criterion 2 is active before any energy dissipation due to fracture takes place. Moreover, this approach depends on both the kinematics and the constitutive law of the cohesive element and, therefore, can be affected by the variation in mode-mixity, B, with the direction.

It is worth to mention that, with the constitutive model used in this work, presented in Appendix A.2, criteria 1 and 2 lead to the same growth driving direction results. However, since both the conservative and non-conservative work are computed in Criterion 2, in contrast to Criterion 1, in which only the non-conservative work is quantified, both criteria might provide different results when using other CZ formulations that allow the definition of mode-dependent penalty stiffness, K [26].

Criterion 3. The growth driving direction is defined by the negative gradient of the mixed-mode displacement jump, λ. This is a pure geometrical approach, since the only governing parameter is the mixed-mode displacement jump. Thus, the solution only depends on the kinematics of the cohesive element. Indeed, changes in the cohesive law due to variation in mode-mixity, B, with direction are

ACCEPTED MANUSCRIPT

not affecting Criterion 3.

2.3. Formulation of Criterion 1 for the identification of the growth driving direction

A complete description of the derivation of Criterion 1 is presented in this section. Moreover, the formulation for the evaluation of the growth driving direction using criteria 2 and 3 is given in Appendix B.

It can be seen, from equations (3) and (4), that, in order to find the growth driving direction using Criterion 1, the radial slope of the energy-based damage, $\frac{\partial \mathcal{D}^e}{\partial \rho}$, must be minimized as a function of the angle φ. Each of the terms in equations (3) and (4) are derived in the following.

The derivative of the energy-based damage with respect to the mode mixity, $\frac{\partial \mathcal{D}^e}{\partial B}$, and the derivative of the energy-based damage with respect to the mixed-mode displacement jump, $\frac{\partial \mathcal{D}^e}{\partial \lambda}$, are scalar factors that depend on the parameters defining the CZM. The expression for $\frac{\partial \mathcal{D}^e}{\partial B}$ obtained after the particular application to the CZM from [15, 17] is:

$$\frac{\partial \mathcal{D}^e}{\partial B} = \frac{\eta \left(\mathcal{G}_{IIc} - \mathcal{G}_{Ic}\right) B^{(\eta-1)} \lambda}{K \lambda_c \lambda_o \left(\lambda_o - \lambda_c\right)} = F_B \tag{7}$$

and the expression for $\frac{\partial \mathcal{D}^e}{\partial \lambda}$ reads:

$$\frac{\partial \mathcal{D}^e}{\partial \lambda} = \frac{1}{\lambda_c - \lambda_o} = F_\lambda \tag{8}$$

Furthermore, the radial slope of the mixed-mode displacement jump, $\frac{\partial \lambda}{\partial \rho}$, in equations (3) and (4) is addressed in the following. Taking into account the dependency of the mixed-mode displacement jump, λ (Equation (A.7)), on the normal and tangential displacement jumps, arranged in vector δ_i, and by application of the chain rule, the following expression is obtained:

$$\frac{\partial \lambda}{\partial \rho} = \frac{\partial \lambda}{\partial \delta_j} \frac{\partial \delta_j}{\partial \rho} \tag{9}$$

The first term in the right hand side of Equation (9) reads:

ACCEPTED MANUSCRIPT

$$\frac{\partial \lambda}{\partial \delta_j} = \left\{ \frac{\delta_1}{\lambda}, \ \frac{\delta_2}{\lambda}, \ \frac{\langle \delta_3 \rangle}{\lambda} \right\}^T = A_j \tag{10}$$

and the second term in the right hand side of Equation (9) is the derivative of the displacement jumps, δ_j, with respect to the radial coordinate, ρ, which is obtained as follows:

$$\frac{\partial \delta_j}{\partial \rho} = \frac{\partial \Theta_{ji}}{\partial \rho} M_{im} Q_m + \Theta_{ji} \frac{\partial M_{im}}{\partial \rho} Q_m \tag{11}$$

where Θ_{ji} is the rotation matrix that relates the global to the local Cartesian coordinate system and M_{im} is the transformation matrix that relates the global displacement jump with the nodal global displacement, Q_m (see Appendix A).

The derivative of the rotation matrix, Θ_{ji}, with respect to the radial coordinate, ρ, can be approximated to zero, by assuming that the curvature of the interface within the element domain is small. Moreover, its derivation leads to a complex expression that would increase the difficulty of the formulation and its further implementation into FE without a substantial improvement in the accuracy of the solution. For the sake of simplicity, in the following it is assumed that $\frac{\partial \Theta_{ji}}{\partial \rho} = 0$. Therefore, only the second summand in the right hand side of Equation (11) is addressed.

The derivative of the transformation matrix, M_{im}, with respect to the local polar coordinate, ρ, is obtained by successive application of the chain rule:

$$\frac{\partial M_{im}}{\partial \rho} = \frac{\partial M_{im}}{\partial \eta_\alpha} \frac{\partial \eta_\alpha}{\partial e_l} \frac{\partial e_l}{\partial \rho} \tag{12}$$

The first partial derivative in the right hand side of Equation (12) is the variation of the transformation matrix, M_{im}, with the isoparametric coordinates of the cohesive element formulation, η_α (see Appendix A):

$$\frac{\partial M_{im}}{\partial \eta_\alpha} = \left[-\frac{\partial N_{ik}}{\partial \eta_\alpha}, \ \frac{\partial N_{ik}}{\partial \eta_\alpha} \right] = E_{im\alpha} \tag{13}$$

ACCEPTED MANUSCRIPT

where N_{ik} is the shape function matrix and the subscript k runs from 1 to the number of degrees of freedom of each of top and bottom surface of the cohesive element. In case of an eight-noded element, $k = 1...12$.

The derivative $\frac{\partial \eta_\alpha}{\partial e_l}$ is the inverse matrix of the two vectors tangential to the deformed midsurface, described in Equation (A.2) and expressed in local tangential coordinates, these being:

$$\frac{\partial e_l}{\partial \eta_\alpha} = \Theta_{li} \frac{1}{2} \frac{\partial N_{ik}}{\partial \eta_\alpha} \left(C_k^+ + C_k^- + Q_k^+ + Q_k^- \right) = \Theta_{li} J_{i\alpha} \tag{14}$$

where $J_{i\alpha}$ is the Jacobian matrix defined in Equation (A.26). Thus, let matrix $G_{\alpha l}$ be defined as:

$$G_{\alpha l} = (\Theta_{li} J_{i\alpha})^{-1} = \begin{bmatrix} \frac{\partial \eta_1}{\partial e_1} & \frac{\partial \eta_2}{\partial e_1} \\ \frac{\partial \eta_1}{\partial e_2} & \frac{\partial \eta_2}{\partial e_2} \end{bmatrix} \tag{15}$$

Using the following transformation relation:

$$\begin{bmatrix} e_1 \\ e_2 \end{bmatrix} = \begin{bmatrix} \rho \ \cos(\varphi) \\ \rho \ \sin(\varphi) \end{bmatrix} \tag{16}$$

the derivative of the local Cartesian coordinates, e_l, with respect to the radial coordinate, ρ, reads:

$$\frac{\partial e_l}{\partial \rho} = \begin{bmatrix} \cos(\varphi) \\ \sin(\varphi) \end{bmatrix} \tag{17}$$

Then, the slope of the mixed-mode displacement jump, λ, with respect to the radial coordinate, ρ, is obtained using equations (10)-(17) in Equation (9):

$$\frac{\partial \lambda}{\partial \rho} = A_j \Theta_{ji} E_{im\alpha} \left(G_{\alpha 1} \left(\cos \varphi \right) + G_{\alpha 2} \left(\sin \varphi \right) \right) Q_m \tag{18}$$

The same procedure can be applied to find the radial slope of the mode mixity, $\frac{\partial B}{\partial \rho}$, in equations (3) and (4). Taking into account the dependency of the mode mixity, B, defined in Equation (A.10),

ACCEPTED MANUSCRIPT

on the displacement jumps, δ_j, the radial slope $\frac{\partial B}{\partial \rho}$ is obtained by applying the chain rule as:

$$\frac{\partial B}{\partial \rho} = \frac{\partial B}{\partial \delta_j} \frac{\partial \delta_j}{\partial \rho} \tag{19}$$

where the derivative of the mode mixity, B, with respect to the displacement jumps, δ_j, reads:

$$\frac{\partial B}{\partial \delta_j} = \left\{ \frac{2\delta_1 \langle \delta_3 \rangle^2}{\lambda^4}, \ \frac{2\delta_2 \langle \delta_3 \rangle^2}{\lambda^4}, \ -\frac{2\delta_s^2 \langle \delta_3 \rangle}{\lambda^4} \right\}^T = O_j \tag{20}$$

and $\frac{\partial \delta_j}{\partial \rho}$ is developed through equations (11)-(17). Hence, the radial slope $\frac{\partial B}{\partial \rho}$ is given by:

$$\frac{\partial B}{\partial \rho} = O_j \Theta_{ji} E_{im\alpha} \left(G_{\alpha 1} \left(\cos \varphi \right) + G_{\alpha 2} \left(\sin \varphi \right) \right) Q_m \tag{21}$$

Finally, let matrix V_α be:

$$V_\alpha = F_B O_j \Theta_{ji} E_{im\alpha} Q_m \tag{22}$$

and matrix W_α be:

$$W_\alpha = F_\lambda A_j \Theta_{ji} E_{im\alpha} Q_m \tag{23}$$

then, the growth driving direction according to Criterion 1 is found using equations (18) and (21)-(23) in Equation (3), solving for the angular coordinate, φ:

$$\varphi = \operatorname{atan} \left(- \frac{\left(V_1 + W_1 \right) G_{11} + \left(V_2 + W_2 \right) G_{21}}{\left(V_1 + W_1 \right) G_{12} + \left(V_2 + W_2 \right) G_{22}} \right) \tag{24}$$

and fulfilling the condition for convexity (Equation (4)):

$$\left(V_\alpha + W_\alpha \right) \left(G_{\alpha 1} \left(- \cos \varphi \right) + G_{\alpha 2} \left(- \sin \varphi \right) \right) > 0 \tag{25}$$

Once φ is identified, the transformation of the global Cartesian coordinates, X_i, into the local

ACCEPTED MANUSCRIPT

Cartesian coordinates that are located on the midsurface and oriented according to the growth driving direction is done by means of the following rotation matrix:

$$R_{ri} = T_{rj}\Theta_{ji} \tag{26}$$

where T_{rj} is:

$$T_{rj} = \begin{bmatrix} \cos\varphi & -\sin\varphi & 0 \\ \sin\varphi & \cos\varphi & 0 \\ 0 & 0 & 1 \end{bmatrix} \tag{27}$$

As shown, all the information necessary to evaluate Criterion 1 (and also criteria 2 and 3, as demonstrated in Appendix B) are the global nodal coordinates, C_m and displacements Q_m. Using the cohesive element formulation in [15, 17], this information is available at the element level and, thus, the presented growth driving direction algorithms can be implemented into a user-defined element subroutine and evaluated at any point in the cohesive zone without any additional post-processing or non-local information.

3. One-element validation examples

The following one-element studies serve to validate the formulation of the growth driving direction criteria presented in Section 2. The proposed method has been implemented in a MATLAB program. The eight-noded cohesive element used is illustrated in Figure 5. The kinematics and constitutive law associated to the element are detailed in Appendix A. Newton-Cotes integration scheme is used, with 2x2 integration points located at the midsurface vertexes. The undeformed element is 0.1 mm wide, 0.1 mm long and has zero thickness. The cohesive properties are listed in Table 2. Three different loading cases (A, B and C) have been analyzed. The applied nodal displacement is listed in Table 3 for each case. The growth driving direction is calculated at a point $\overline{\boldsymbol{p}}\,(\eta_1, \eta_2)$ located on the midsurface, with natural coordinates $(-0.5, -0.5)$. The results of the angle φ obtained in each case are listed in

ACCEPTED MANUSCRIPT

Interface properties		
$\mathcal{G}_{Ic}$	0.3	N/mm
$\mathcal{G}_{IIc}$	0.7	N/mm
τ_{Ic}	50	MPa
τ_{IIc}	76.4	MPa
η	2	-
K	1E5	N/mm^3

Table 2: Cohesive law properties used in the one-element case studies.

Case ID	Loading conditions	Nodal displacements (mm)	φ at point $\overline{\boldsymbol{p}}$ (deg) Criterion 1	Criterion 2	Criterion 3
A	Pure mode I B constant	$u_3^5 = 0.005$ $u_3^6 = 0.005$ $u_3^7 = 0.01$ $u_3^8 = 0.01$	270.0	270.0	270.0
B	Mixed mode I-shear B constant	$u_1^5 = u_2^5 = u_3^5 = 0.001$ $u_1^6 = u_2^6 = u_3^6 = 0.002$ $u_1^7 = u_2^7 = u_3^7 = 0.003$ $u_1^8 = u_2^8 = u_3^8 = 0.002$	225.3	225.3	225.3
C	Mixed mode I-shear same λ at nodes	$u_1^5 = \sqrt{2 \cdot 0.008}$ $u_1^6 = u_3^6 = 0.008$ $u_3^7 = \sqrt{2 \cdot 0.008}$ $u_1^8 = u_3^8 = 0.008$	225.0	225.0	45.0

Table 3: Loading conditions and growth driving direction results at point $\overline{\boldsymbol{p}}$ from the one-element case studies

Table 3 for the three criteria.

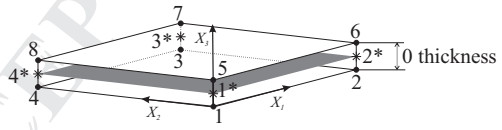

Figure 5: Sketch of the undeformed cohesive element. The nodes are represented as black dots and numbered from 1 to 8 and the integration points are represented as asterisks and numbered from 1* to 4*.

Case A is a pure mode I-opened element. The distribution of the mixed-mode displacement jump, λ, along the element midsurface is projected on the deformed element midsurface in Figure 6, where the point $\overline{\boldsymbol{p}}$ is highlighted in white. Integation points 1 and 2 have the lowest λ value, while points 3 and 4 are the most opened. As illustrated, the growth driving direction according to Criterion 3

is determined by the greatest rate of decrease of λ. The other quantities being analyzed in criteria 1 and 2, $\mathcal{D}^e$ and $\frac{\omega_{tot}}{\mathcal{G}_c}$ respectively, are represented in Figure 7, as well as the mode-mixity, B. Like the B-distribution along the element midsurface is constant, the growth driving direction is only defined by the direction that minimizes the slope of the mixed-mode displacement jump. Therefore, in Case A only, the kinematics of the element governs the growth driving direction, independently of which criteria is used.

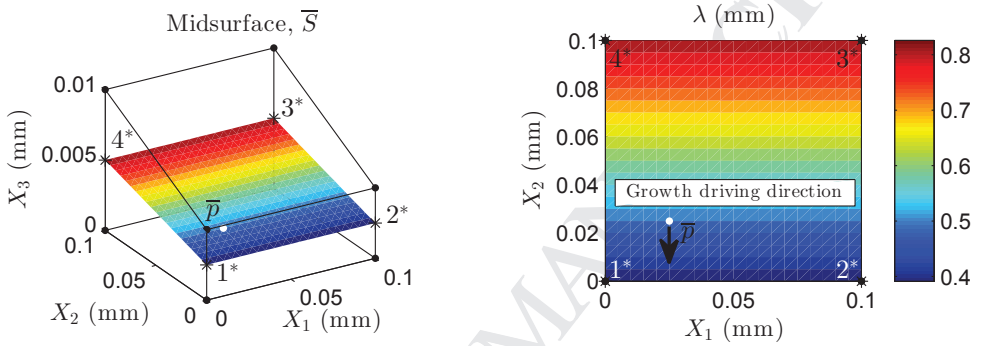

Figure 6: Mixed-mode displacement jump distribution at the element midsurface for Case A loading conditions. The growth driving direction is analyzed at point $\overline{\boldsymbol{p}}$, indicated with a white circle, and the result is listed in Table 3.

On the other hand, in Case B, the element is opened under constant mixed mode I-shear opening conditions (See Figure 8). In this case, λ linearly increases along the midsurface diagonal direction, from integration point 1 to integration point 3. However, B is constant and, thus, also the constitutive law associated to it. Again, in Case B, the growth driving direction is only defined by the direction that minimizes the slope of the mixed-mode displacement jump, λ. Therefore, it is governed by the kinematics of the cohesive element and there is agreement between the three criteria.

Finally, in Case C, all the integration points have the same λ-value, although the mode-mixity, B, changes from 0 to 1 along the midsurface diagonal direction (See Figure 9). At integration point 1, only shear sliding displacement is applied, while at the opposite corner, at integration point 3, there is only mode I opening. At the integration points 2 and 4, there is 50% mixed-mode opening. On the other

ACCEPTED MANUSCRIPT

hand, λ is lower at the center part of the element midsurface than at the corners and its distribution is determined by the interpolation functions. Criterion 3 is only affected by the λ-interpolation and results in the direction that points to the center of the element. Furthermore, due to the uneven B-distribution, the constitutive law is not constant. With the cohesive properties used in these studies, the direction of steepest negative slopes of $\mathcal{D}^e$ and $\frac{\omega_{tot}}{\mathcal{G}_c}$ coincides with the direction that maximizes the rate of increase of B. Note that, when evaluated at point $\overline{\boldsymbol{p}}$, this is the direction of largest slope of λ. Therefore, Criterion 3 and criteria 1 and 2 point to opposite directions.

In addition, the slopes $\frac{\Delta \mathcal{D}^e}{\Delta \rho}$, $\frac{\Delta(\omega_{tot}/\mathcal{G}_c)}{\Delta \rho}$ and $\frac{\Delta \lambda}{\Delta \rho}$ have been numerically evaluated using a central difference at every 1 degree at point $\overline{\boldsymbol{p}}$ under Case C loading conditions using a perturbation size for the radius of 0.001 mm. Thus, the slope of any quantity f has been calculated as:

$$\frac{\Delta f}{\Delta \rho} = \frac{f(0.001, \varphi) - f(-0.001, \varphi)}{2 \cdot 0.001} \tag{28}$$

The resulting slopes are represented in Figure 10. The disagreement between Criterion 3 and criteria 1 and 2 can be observed. For Criterion 3, the angle φ that minimizes $\frac{\Delta \lambda}{\Delta \rho}$ is 45 degrees, while for criteria 1 and 2, the angle that minimizes $\frac{\Delta \mathcal{D}^e}{\Delta \rho}$ and $\frac{\Delta(\omega_{tot}/\mathcal{G}_c)}{\Delta \rho}$, respectively, amounts 225 degrees. Note that these results are in agreement with the results obtained by implementing the formulation developed in Section 2.

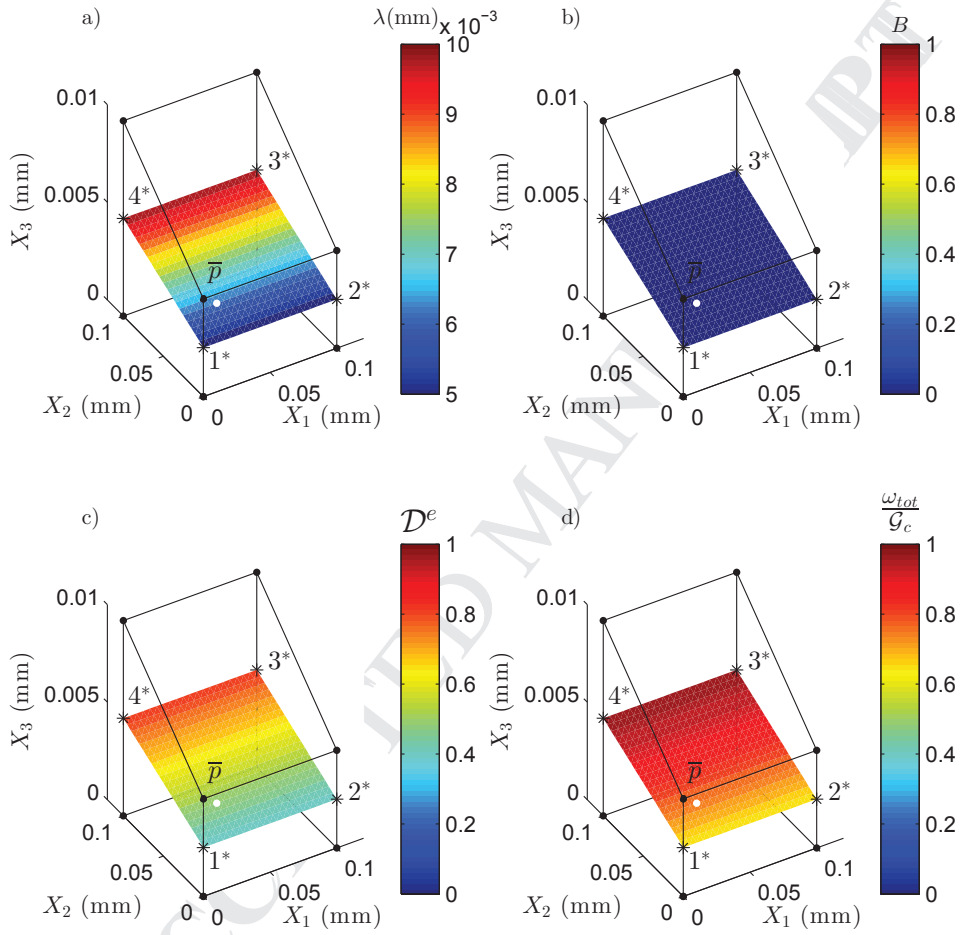

Figure 7: a) Mixed-mode displacement jump, λ, b) mode-mixity, B, c) energy-based damage, $\mathcal{D}^e$, and d) total specific work over the fracture toughness, $\frac{\omega_{tot}}{\mathcal{G}_c}$, distributions at the element midsurface for Case A loading conditions. The point $\overline{\boldsymbol{p}}$, where the growth driving direction is analyzed, is indicated with a white circle.

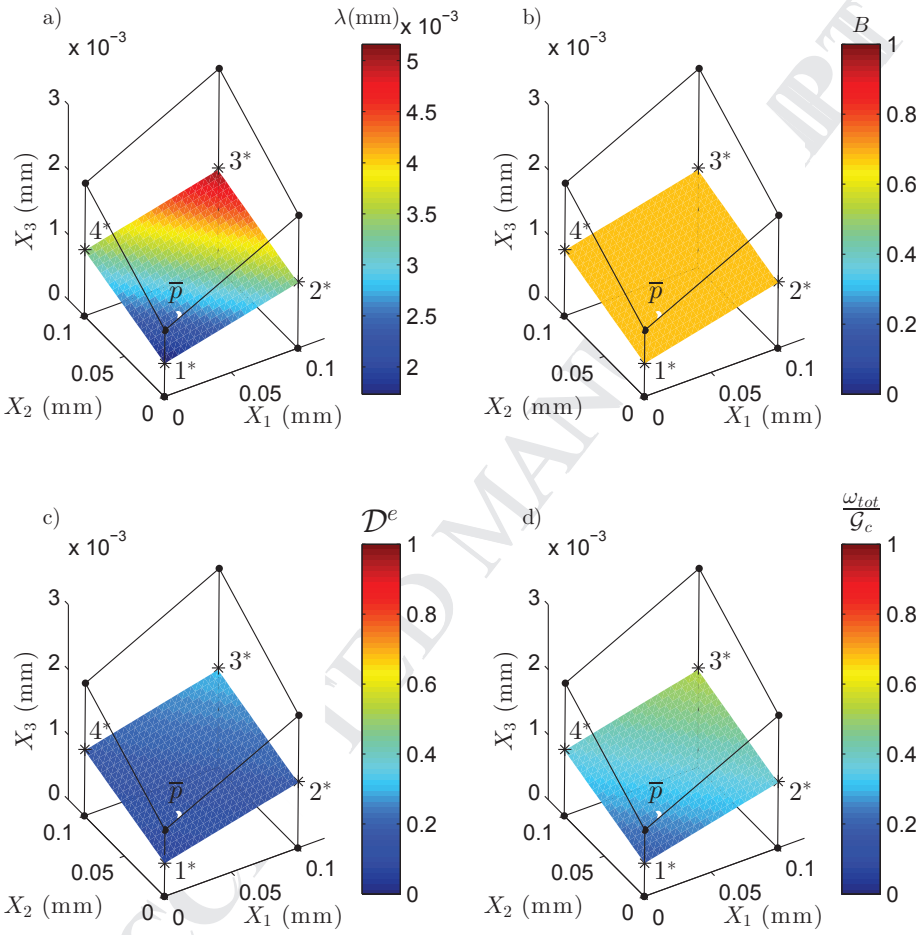

Figure 8: a) Mixed-mode displacement jump, λ, b) mode-mixity, B, c) energy-based damage, $\mathcal{D}^e$, and d) total specific work over the fracture toughness, $\frac{\omega_{tot}}{\mathcal{G}_c}$, distributions at the element midsurface for Case B loading conditions. The point $\overline{\boldsymbol{p}}$, where the growth driving direction is analyzed, is indicated with a white circle.

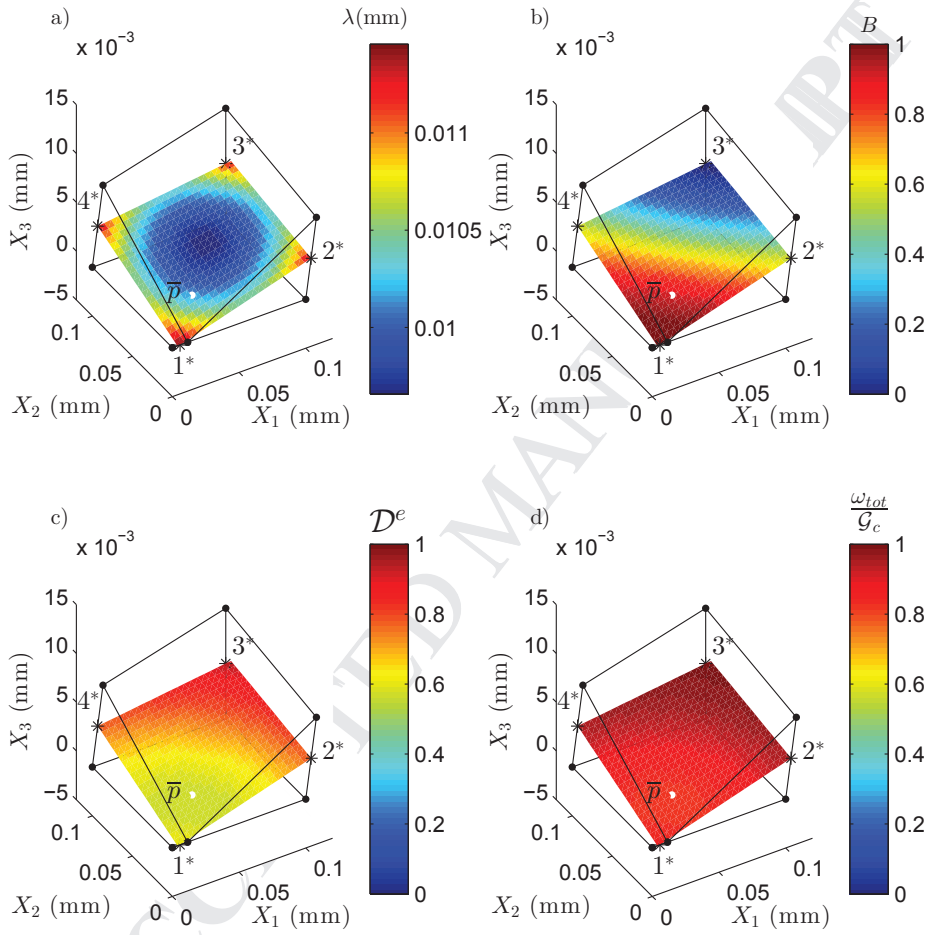

Figure 9: a) Mixed-mode displacement jump, λ, b) mode-mixity, B, c) energy-based damage, $\mathcal{D}^e$, and d) total specific work over the fracture toughness, $\frac{\omega_{tot}}{\mathcal{G}_c}$, distributions at the element midsurface for Case C loading conditions. The point $\overline{\boldsymbol{p}}$, where the growth driving direction is analyzed, is indicated with a white circle.

ACCEPTED MANUSCRIPT

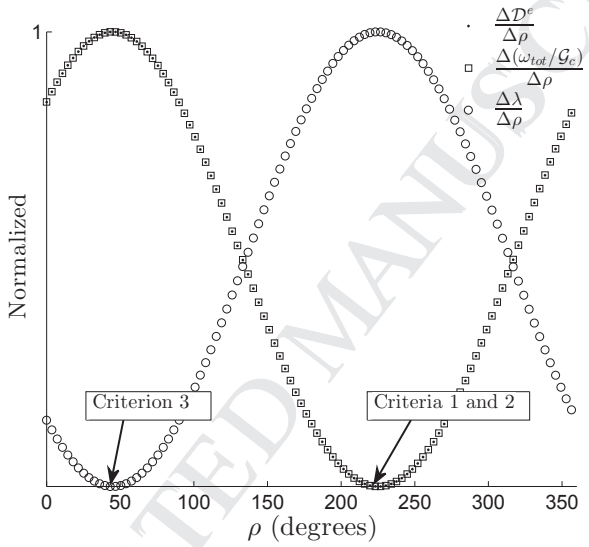

Figure 10: Slopes in the radial direction, ρ, of the energy-based damage, $\mathcal{D}^e$, the total specific work over the fracture toughness, $\frac{\omega_{tot}}{\mathcal{G}_c}$, and the mixed-mode displacement jump, λ, as a function of the angle φ evaluated at point $\overline{\boldsymbol{p}}$ for Case C loading conditions. The slopes have been calculated using a central difference with a perturbation for the radius of 0.001 mm. The values $\frac{\Delta \mathcal{D}^e}{\Delta \rho}$, $\frac{\Delta (\omega_{tot}/\mathcal{G}_c)}{\Delta \rho}$ and $\frac{\Delta \lambda}{\Delta \rho}$ have been normalized by their maximum value.

4. Three-Dimensional application

To exemplify the applicability of the presented formulation, a three-dimensional model with a non-straight crack front is used. The test configuration is a End-Loaded Split (ELS) test on a symmetric run-out specimen with a midplane initial defect. A Teflon insert acts as an initial straight delamination (see Figure 11). Moreover, the middle width of the specimen is stiffened by bonding CFRP reinforcements on the upper and lower faces. During propagation the crack front shape changes when it approaches the reinforced region. The formulation presented in Section 2 can be used to evaluate the growth driving criteria at any given loading state during the quasi-static simulation. To this end, the method in [15, 17] has been enhanced with the growth driving direction calculation and implemented in Abaqus [27] as a UEL subroutine. The user-defined cohesive elements that model the middle interface are 0.2 mm x 0.5 mm. The laminate and interface properties used in the simulation are listed in Table 4.

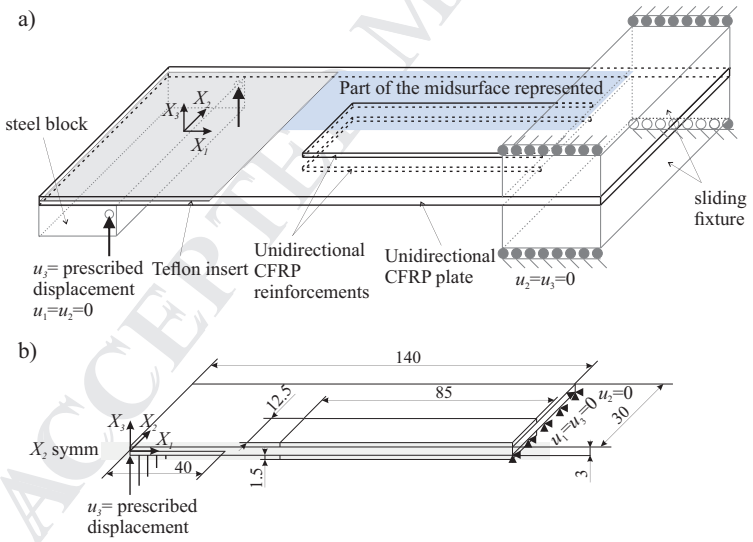

Figure 11: a) Sketch of the partially reinforced ELS specimen. The grey-shadowed area represents the Teflon insert. The blue-shadowed area is the area represented in figures 12.b, 13 and 18. b) Simplified model for FE simulation and dimensions (units in mm).

The historical evolution of the 0.5-valued damage isoline is plotted in Figure 12.a. The energy-

ACCEPTED MANUSCRIPT

Laminate properties			Interface properties		
E_{11}: Longitudinal Young's modulus	154	GPa	$\mathcal{G}_{Ic}$	0.3	N/mm
$E_{22} = E_{33}$: Transversal Young's modulus	8.5	GPa	$\mathcal{G}_{IIc}$	3	N/mm
$G_{12} = G_{13}$: Shear modulus in the longitudinal planes	4.2	GPa	τ_{Ic}	10	MPa
G_{23}: Shear modulus in the transversal plane	3.036	GPa	τ_{IIc}	31.62	MPa
$\mu_{12} = \mu_{13}$: Poison's coefficient in the longitudinal planes	0.35	-	η	2	-
μ_{23}: Poison's coefficient in the transversal plane	0.4	-	K	1E5	N/mm^3

Table 4: Laminate and interface properties used in the simulation study of Section 4. The nomenclature of the interface properties is defined in Appendix A.

based damage, $\mathcal{D}^e$, distribution is projected on the deformed midsurface, in Figure 12.c, for a prescribed displacement of 32.55 mm. Only the blue-shadowed area in Figure 11 is represented. The crack growth direction is evaluated at each integration point within the FPZ using criteria 1, 2 and 3, and represented in Figure 13. Note that criteria 1 (Figure 13.a) and 2 (Figure 13.b) are coincident except from at the elastic region, where no results from Criterion 1 can be obtained. By comparison of figures 13.b and 13.c, it can be observed that Criterion 3 only differs from criteria 1 and 2 at a region located at the upper left part of the cohesive zone ($X_1 < 85$ mm and $X_2 > 10$ mm). Indeed, the mode-mixity, B, is constant and equal to 1 in the entire cohesive zone, except for this region, where it locally decreases to 0.6 (see Figure 13.d). As demonstrated in Section 3, under constant B conditions, the growth driving direction is only governed by the kinematics of the cohesive elements. Therefore, evaluating any of the three criteria results in the same growth driving direction solution. On the other hand, only criteria 1 and 2 are affected by changes in the mode-dependent constitutive law, leading to different results, if compared to Criterion 3, at the region where the mode-mixity, B, varies.

In addition, four damage isolines have been traced. The damage isolines are constructed by connecting integration points with the same damage value. The first damage isoline, represented in Figure 14.a, is the line connecting the completely damaged integration points adjacent to the damage process zone. At each point on the damage isoline, the geometrical normal direction has been approximated by the normal to the slope of a second degree polynomial expression fitted to five consecutive points represented in white in Figure 14.a): the current point and the two preceding and the two succeeding points. Therefore, the approximated normal direction is computed by post-processing global informa-

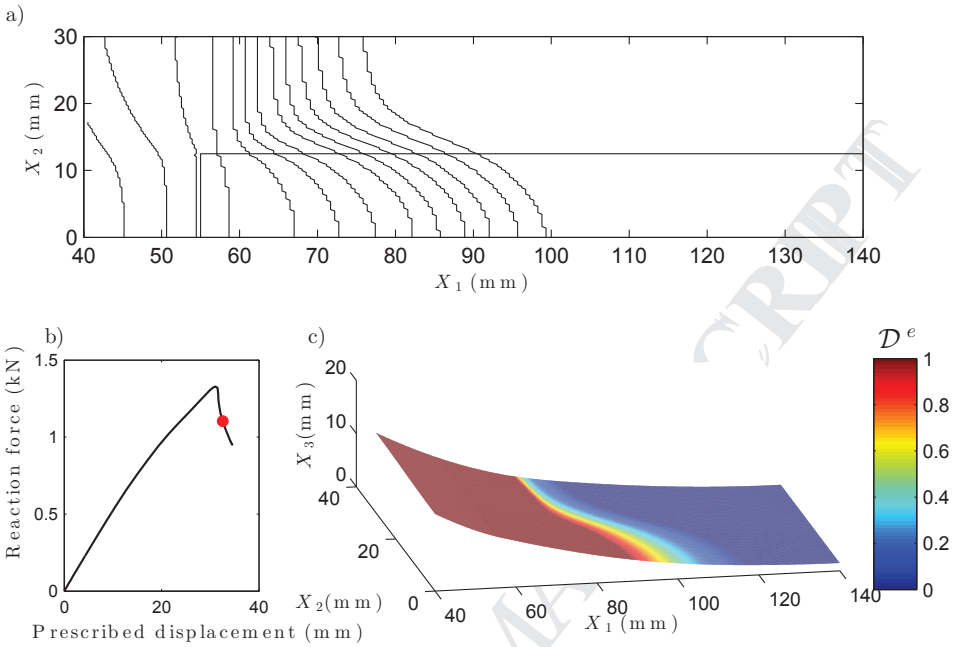

Figure 12: a) Historical evolution of the 0.5-valued damage isoline. b) Reaction force vs prescribed displacement curve with the current loading state highlighted in red. c) Energy-based damage projected on the deformed midsurface.

tion and it is heavily affected by the discretization and the choice of the fitting function. The results are compared to the local growth driving direction criteria developed in Section 2 in Figure 14.b. The same analysis is done with a 0.5-valued damage isoline (Figure 15), a 0.1-valued damage isoline (Figure 16) and the line connecting the undamaged integration points adjacent to the damage process zone (Figure 17). Note that, although for comparison purposes the growth driving direction is evaluated in a discrete manner at the same points where the approximated normal direction is computed, it is a continuous field that can be evaluated at any point, as shown in Figure 13.

Finally, three different FE models with element sizes 0.5 x 0.2 mm, 1 x 1.25 mm and 2.5 x 2.5 mm (see Figure 18) are used to compare the element size effect on both the approximated normal direction to the 1-valued damage isoline, evaluated by using global information, and the predicted growth driving direction using Criterion 1, evaluated point-wise at the element level. The results are

212

ACCEPTED MANUSCRIPT

obtained using the information of the points on the 1-valued damage isoline traced in Figure 19 for the three meshes. The direction obtained along the damage isoline using both methods is plotted in Figure 20.

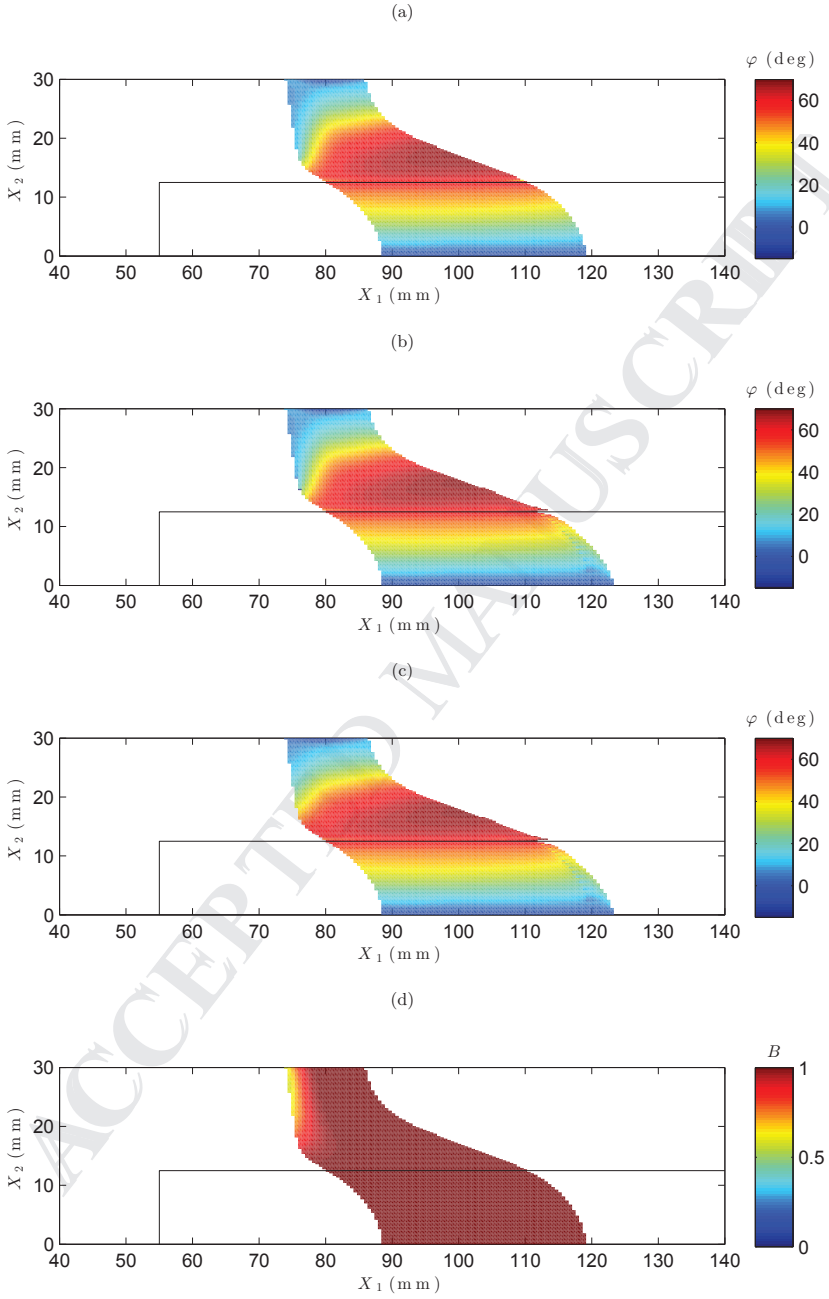

Figure 13: a) Growth driving direction resulting from the evaluation of Criterion 1. b) Growth driving direction resulting from the evaluation of Criterion 2. c) Growth driving direction resulting from the evaluation of Criterion 3. b) Mode mixity, B. The black line marks the reinforcements.

ACCEPTED MANUSCRIPT

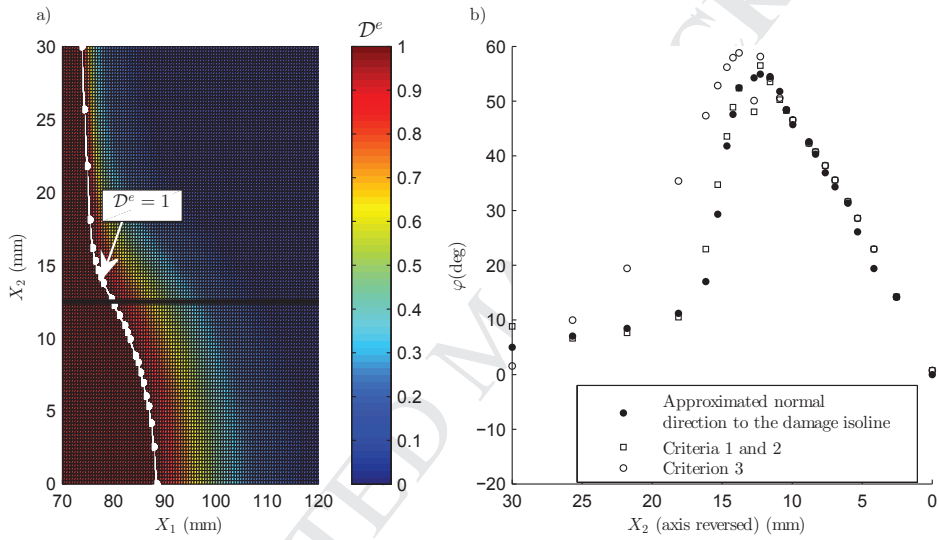

Figure 14: a) Energy-based damage, $\mathcal{D}^e$, distribution along the cohesive zone. The points forming the 1-valued damage isoline are highlighted in white. The thick black solid line marks the reinforcements border. b) Comparison of the angle φ obtained at the 1-valued damage front by computing the normal direction using global information and by locally evaluating the growth driving direction criteria. Criteria 1 and 2 are represented by the same marker because they lead to identical growth driving direction results.

ACCEPTED MANUSCRIPT

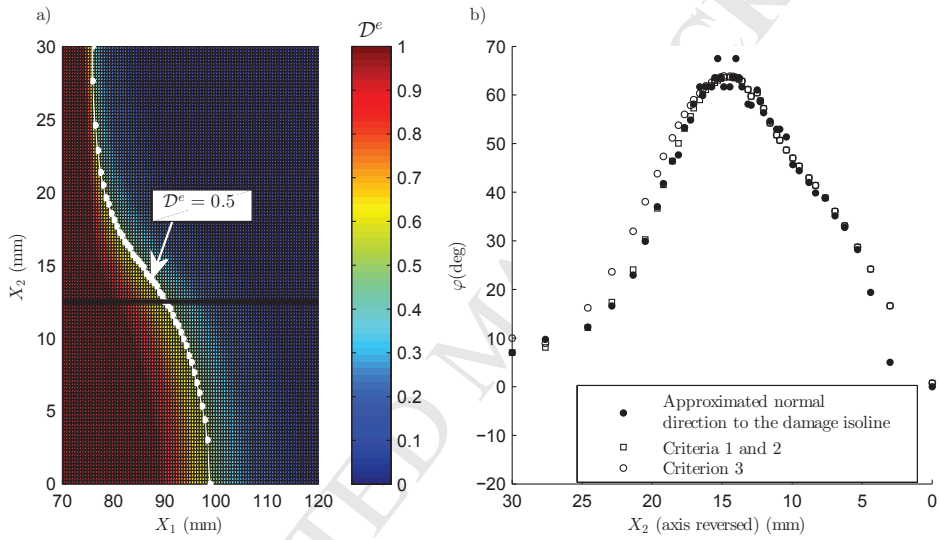

Figure 15: a) Energy-based damage, $\mathcal{D}^e$, distribution along the cohesive zone. The points forming the 0.5-valued damage isoline are highlighted in white. The thick black solid line marks the reinforcements border. b) Comparison of the angle φ obtained at the 0.5-valued damage front by computing the normal direction using global information and by locally evaluating the growth driving direction criteria. Criteria 1 and 2 are represented by the same marker because they lead to identical growth driving direction results.

ACCEPTED MANUSCRIPT

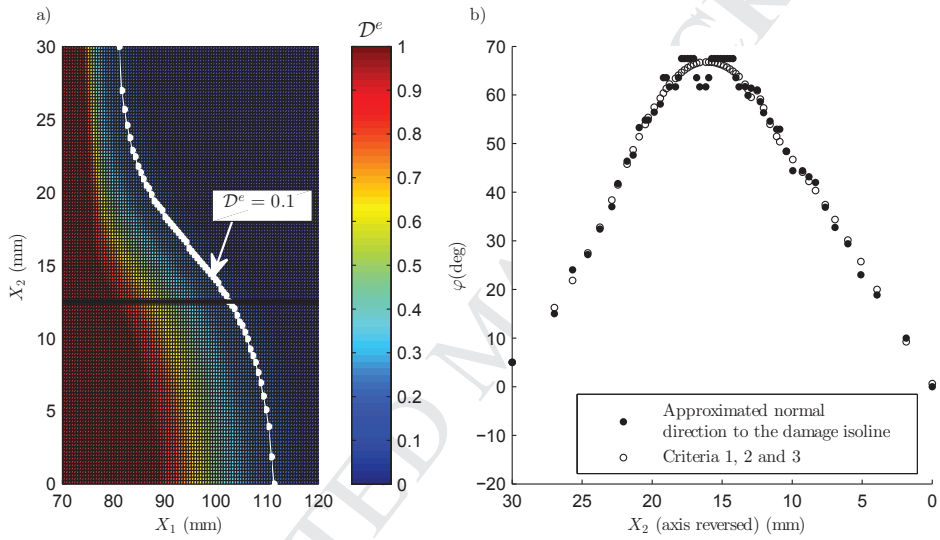

Figure 16: a) Energy-based damage, $\mathcal{D}^e$, distribution along the cohesive zone. The points forming the 0.1-valued damage isoline are highlighted in white. The thick black solid line marks the reinforcements border. b) Comparison of the angle φ obtained at the 0.1-valued damage front by computing the normal direction using global information and by locally evaluating the growth driving direction criteria. Criteria 1, 2 and 3 are represented by the same marker because they lead to identical growth driving direction results.

ACCEPTED MANUSCRIPT

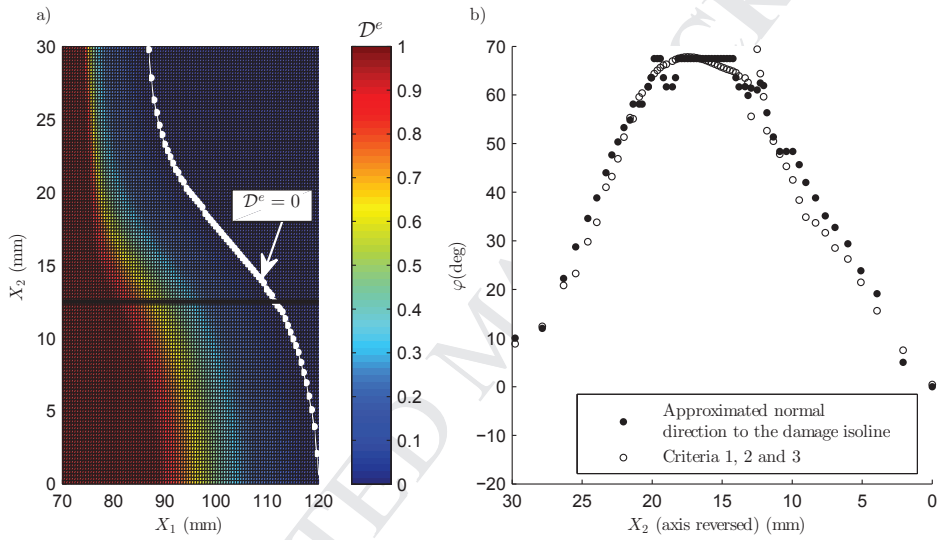

Figure 17: a) Energy-based damage, $\mathcal{D}^e$, distribution along the cohesive zone. The points forming the 0-valued damage isoline are highlighted in white. The thick black solid line marks the reinforcements border. b) Comparison of the angle φ obtained at the 0-valued damage front by computing the normal direction using global information and by locally evaluating the growth driving direction criteria. Criteria 1, 2 and 3 are represented by the same marker because they lead to identical growth driving direction results.

(a) Element size: 0.5 x 0.2 mmm

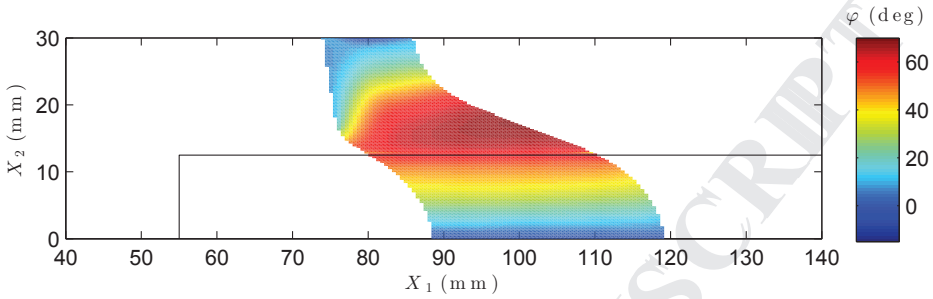

(b) Element size: 1 x 1.25 mmm

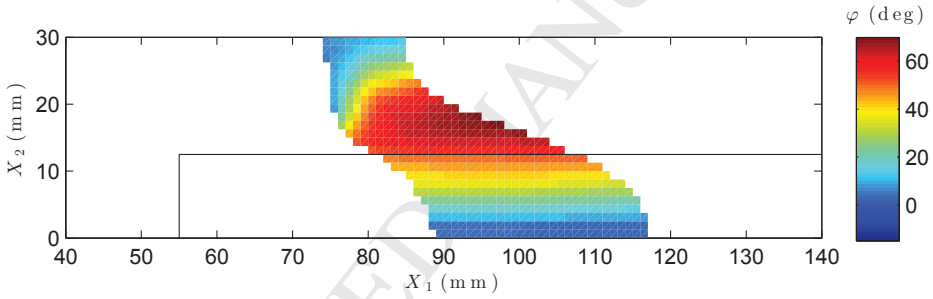

(c) Element size: 2.5 x 2.5 mmm

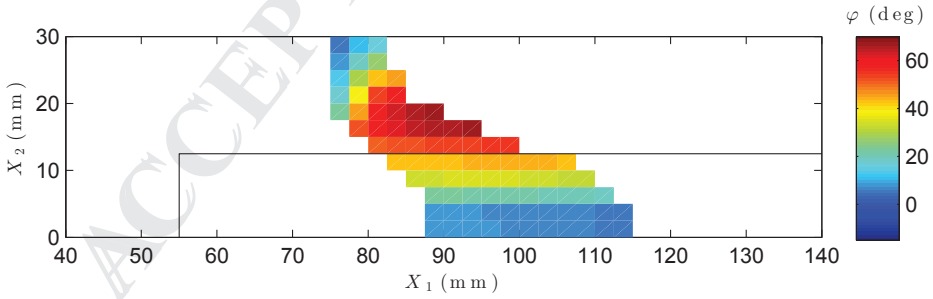

Figure 18: Growth driving direction resulting from the evaluation of Criterion 1 using three different element sizes.

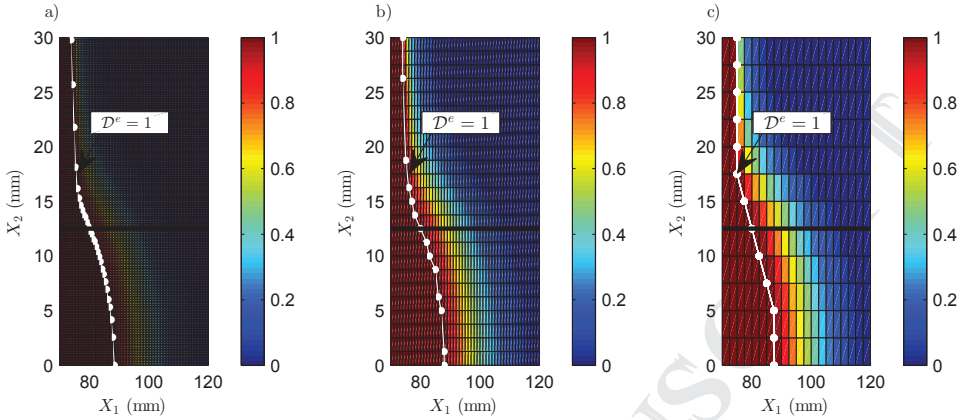

Figure 19: 1-valued damage fronts using different element sizes: a) 0.2 x 0.5 mm. b) 1 x 1.25 mm. c) 2.5 x 2.5 mm.

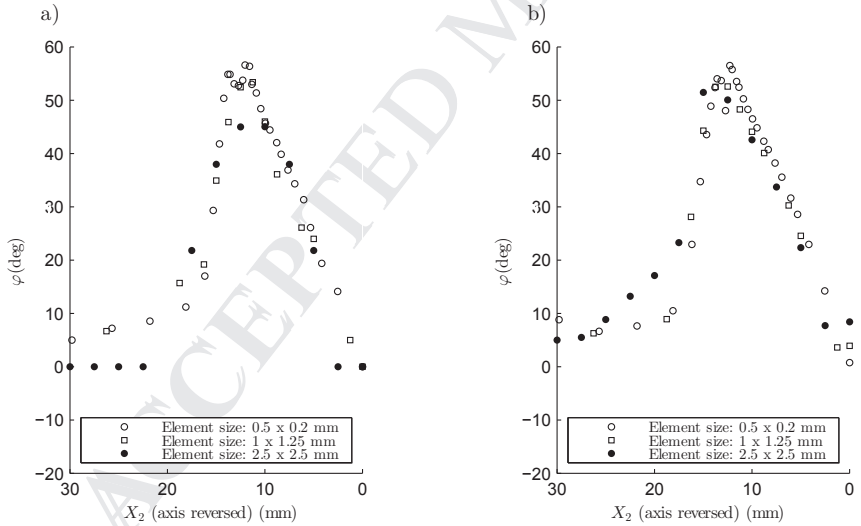

Figure 20: Comparison of the angle φ obtained at the 1-valued damage isoline using three different element sizes by a) computing the normal direction to the crack front using global information and b) evaluating Criterion 1.

220

ACCEPTED MANUSCRIPT

5. Discussion

Three different growth driving direction criteria have been proposed as element-level algorithms, that can be evaluated at any point within the cohesive zone. Criteria 1 and 2 are energetically-based formulations that account for both the kinematics and the constitutive law of the interface element. On the other hand, Criterion 3 is a geometrical approach, which only accounts for the kinematics of the interface element. Therefore, when the mode-mixity, B, is not constant, criteria 1 and 2 are the most appropriate. Moreover, Criterion 2 computes the rate of decrease of both the specific elastic energy, ω_e, and the dissipated energy, ω_d, normalized to the fracture toughness, $\mathcal{G}_c$. On the contrary, Criterion 1 only computes the rate of decrease of the dissipated energy, ω_d, normalized to the fracture toughness, $\mathcal{G}_c$, which is equivalent to computing the rate of decrease of the energy-based damage, $\mathcal{D}^e$. On this basis, Criterion 1 is not active before damage initiation, while Criterion 2 can be computed as soon as some separation between two initially coinciding points at the interface occurs. The three criteria have been presented for completeness, since they can be developed for other CZM formulations following the methodology described in Section 2.3. With the CZM used in this work, criteria 1 and 2 lead to the same growth driving direction solution at the damaged region. However, different results may be obtained if a mode-dependent penalty-stiffness is used, which could render the specific elastic energy of Crietion 2 dependent on growth driving direction.

The implementation of the formulation for the proposed growth driving direction criteria has been validated with one-element case studies in Section 3. The distribution of the quantities being analyzed have been projected on the element midsurface for visual verification (see figures 7-9 for different loading cases). In addition, the slopes of such quantities have been numerically evaluated at different orientations around a given evaluation point under Case C loading conditions (Figure 10). The orientation that results in lowest slopes coincides with the angle of growth driving direction predicted by each criteria, respectively.

Finally, the capabilities of the presented formulation are demonstrated in Section 4 using a three-dimensional run-out specimen loaded under ELS test conditions (Figure 11). The crack front propa-

ACCEPTED MANUSCRIPT

gates with non-straight shape due to the reinforcements bonded at the middle width of the specimen Figure 12. The growth driving direction criteria are evaluated at all the integration points within the cohesive zone for a given loading state with large deformations (Figure 13). The results from the three criteria differ only at those regions where the mode-mixity, B, is not constant, as already demonstrated in Section 3. Moreover, the resulting crack growth driving direction is compared with the geometrical normal direction of four different damage isolines computed by post-processing global information (figures 14-17). Both results are in good agreement, although the agreement is higher between the geometrical normal direction to the damage isolines derived from global information and the results from criteria 1 and 2, than from Criterion 3, specially at the non-constant mode-mixity, B, region. It is noteworthy that the global description of the damage isoline is highly dependent on the methodology used to compute it, mainly the number of points taken into account and its fitting. Therefore, in a FE framework, the computation of the approximated normal direction to the damage isoline using global information may, in some cases, misrepresent the actual normal direction. Indeed, the local computation of the negative gradient of the energy-based damage, $\mathcal{D}^e$, by means of Criterion 1 is the exact normal to the damage isolines. The fitting of the points forming the damage isoline, that leads to an approximate global description of it, is only used to validate the implementation of the formulation presented. To close, the effect of the mesh size on the determination of the normal direction to the 1-valued damage isoline is analyzed using both methods (Figure 20): the approximated normal direction using global information and the growth driving direction obtained by evaluating Criterion 1. The results show that the growth driving direction, evaluated locally, shows less sensitivity to the element size. Indeed, the growth driving direction is a continuum field which does not explicitly depend on the mesh size, but it implicitly does, due to discretization of the displacement field in the FEM [28].

ACCEPTED MANUSCRIPT

6. Conclusions

A novel method has been proposed for the determination of the growth driving direction for cohesive zone models. The presented formulation is evaluated point-wise. Therefore, it can be implemented as a part of a user-defined cohesive element subroutine and evaluated during simulation without the need of any extra loop, post-processing or global information.

The growth driving direction is defined as the negative gradient of the energy-based damage variable. However, other quantities can be used for the sake of simplicity. In this work, three different criteria are proposed. The implementation of the formulation for the proposed criteria applied to a particular CZM [15, 17] is derived and validated by using one-element analysis under different loading conditions.

Finally, the usefulness of the method has been demonstrated via the analysis of delamination propagation in a three-dimensional structure with a complex shaped crack front. The results using the proposed point-wise formulation for the evaluation of the growth driving direction are in agreement with the results from a global approximation of the normal direction to different damage isolines. Apart from being a low computational time-consuming task, the proposed formulation has the advantage that it can be evaluated at any point within the cohesive zone.

7. Acknowledgements

This work has been partially funded by the Spanish Government (Ministerio de Economia y Competitividad) under contract TRA2015-71491-R, cofinanced by the European Social Fund.

[1] R. Krueger, The virtual crack closure technique for modeling interlaminar failure and delamination in advanced composite materials, in: Numerical Modelling of Failure in Advanced Composite Materials, Woodhead Publishing Series in Composites Science and Engineering, 2015, pp. 3–53.

[2] FRANC3D, FRANC3D Concepts and User Guide - Version 2.6, Cornell Fracture Group, Ithaca, New York.

ACCEPTED MANUSCRIPT

[3] M. Schollmann, M. Fulland, H. Richard, Development of a new software for adaptive crack growth simulations in 3D structures, Engineering Fracture Mechanics 70 (2003) 249–268. doi:10.1016/S0013-7944(02)00028-0.

[4] E. Iesulauro, FRANC2D/L: A Crack Propagation Simulator for Plane Layered Structures - Version 1.5 User's Guide., Cornell Fracture Group, Ithaca, New York.

[5] D. Xie, S. B. Biggers Jr, Strain energy release rate calculation for a moving delamination front of arbitrary shape based on the virtual crack closure technique . Part I : Formulation and validation, Engineering Fracture Mechanics 73 (2006) 771–785. doi:10.1016/j.engfracmech.2005.07.013.

[6] X. Li, C. Ferrie, E. Nottorf, M. Portanova, Virtual crack closure technique on stepped crack front (VCCT-S), Annual Forum Proceedings - American Helicopter Society 64 (2).

[7] Y.-P. Liu, C.-Y. Chen, G.-Q. Li, A modified zigzag approach to approximate moving crack front with arbitrary shape, Engineering Fracture Mechanics 78 (2) (2011) 234–251. doi:10.1016/j.engfracmech.2010.08.007.

[8] D. Dugdale, Yielding of steel sheets containing slits, Journal of the Mechanics and Physics of Solids 8 (2) (1960) 100–104. doi:10.1016/0022-5096(60)90013-2.

[9] G. Barenblatt, The Mathematical Theory of Equilibrium Cracks in Brittle Fracture, Advances in Applied Mechanics 7 (1962) 55–129. doi:10.1016/S0065-2156(08)70121-2.

[10] J. L. Chaboche, R. Girard, A. Schaff, Numerical analysis of composite systems by using interphase / interface models, Computational Mechanics 20 (1-2). doi:10.1007/s004660050209.

[11] M. Ortiz, A. Pandolfi, Finite-Deformation Irreversible Cohesive Elements for Three-Dimensional Crack-Propagation Analysis, International Journal for Numerical Methods in EngineeringI 44 (1999) 1267–1282. doi:10.1002/(SICI)1097-0207(19990330)44:9¡1267::AID-NME486¿3.0.CO;2-7.

ACCEPTED MANUSCRIPT

[12] G. Alfano, M. A. Crisÿeld, Finite element interface models for the delamination analysis of laminated composites: mechanical and computational issues, International Journal for Numerical Methods in Engineering 50 (2001) 1701–1736. doi:10.1002/nme.93.

[13] P. P. Camanho, C. Davila, M. de Moura, Numerical simulation of mixed-mode progressive delamination in composite materials, Journal of Composite Materials 37 (16) (2003) 1415–1438. doi:10.1177/0021998303034505.

[14] V. K. Goyal, E. R. Johnson, G. D. Carlos, Irreversible constitutive law for modeling the delamination process using interfacial surface discontinuities, Composite Structures 65 (2004) 289–305. doi:10.1016/j.compstruct.2003.11.005.

[15] A. Turon, P. P. Camanho, J. Costa, C. G. Da, A damage model for the simulation of delamination in advanced composites under variable-mode loading, Mechanics of Materials 38 (2006) 1072–1089. doi:10.1016/j.mechmat.2005.10.003.

[16] W.-G. Jiang, S. R. Hallett, B. G. Green, M. R. Wisnom, A concise interface constitutive law for analysis of delamination and splitting in composite materials and its application to scaled notched tensile specimens, International Journal for Numerical Methods in Engineering 69 (2007) 1982–1995. doi:10.1002/nme.

[17] A. Turon, P. P. Camanho, J. Costa, J. Renart, Accurate simulation of delamination growth under mixed-mode loading using cohesive elements: Definition of interlaminar strengths and elastic stiffness, Composite Structures 92 (8) (2010) 1857–1864. doi:10.1016/j.compstruct.2010.01.012.

[18] B. L. V. Bak, C. Sarrado, A. Turon, J. Costa, Delamination Under Fatigue Loads in Composite Laminates: A Review on the Observed Phenomenology and Computational Methods, Applied Mechanics Reviews 66 (6).

[19] L. F. Kawashita, S. R. Hallett, A crack tip tracking algorithm for cohesive interface element

ACCEPTED MANUSCRIPT

analysis of fatigue delamination propagation in composite materials, International Journal of Solids and Structures 49 (21) (2012) 2898–2913. doi:10.1016/j.ijsolstr.2012.03.034.

[20] C. Wang, X. Xu, Cohesive element analysis of fatigue delamination propagation in composite materials with improved crack tip tracking algorism, Composite Structures 134 (2015) 176–184. doi:10.1016/j.compstruct.2015.07.118.

[21] B. L. V. Bak, A. Turon, E. Lindgaard, E. Lund, A simulation method for high-cycle fatigue-driven delamination using a cohesive zone model, International Journal for Numerical Methods in Engineering 106 (2016) 163–191. doi:10.1002/nme.5117.

[22] B. L. V. Bak, A. Turon, E. Lindgaard, E. Lund, A benchmark study of simulation methods for high-cycle fatigue-driven delamination based on cohesive zone models, Composite structures 164 (2017) 198–206.

[23] F. P. van Der Meer, N. Moës, L. J. Sluys, A level set model for delamination Modeling crack growth without cohesive zone or stress singularity, Engineering Fracture Mechanics 79 (2012) 191–212. doi:10.1016/j.engfracmech.2011.10.013.

[24] F. P. van der Meer, L. J. Sluys, The Thick Level Set method : Sliding deformations and damage initiation, Comput. Methods Appl. Mech. Engrg. 285 (2015) 64–82. doi:10.1016/j.cma.2014.10.020.

[25] M. L. Benzeggagh, M. Kenane, Measurement of Mixed-Mode Delamination Fracture Toughness of Unidirectional Glass/ Epoxy Composites with Mixed-ModeE Bending Apparatus, Composite Science and Technology 56 (1996) 439–449. doi:10.1016/S0266-3538(97)00021-3.

[26] A. Turon, E. Gonzalez, C. Sarrado, G. Guillamet, P. Maimi, Accurate simulation of delamination under mixed-mode loading using a cohesive model with a mode-dependent penalty stiffness, Composite Structures 184 (2018) 506–511.

[27] D. Systémes, Abaqus manual 6.12.

[28] B. L. V. Bak, E. Lindgaard, E. Lund, International Journal for Numerical Methods in Engineering.

ACCEPTED MANUSCRIPT

Appendix A. The cohesive element formulation

The cohesive zone model from the original work of Turon et al. [15, 17] and its finite element implementation are outlined in the following.

Appendix A.1. Kinematics

Let the delamination be understood as a strong discontinuous singular surface, S, that crosses a volume of material, Ω, and divides it into two subdomains, Ω^+ and Ω^-, as shown in Figure A.21. There are two surfaces that bound into S: the upper surface, S^+, associated with Ω^+, and the lower surface, S^-, associated with Ω^-. These two surfaces, which are initially coincident with the reference surface, S^0, in the undeformed configuration, represent the crack faces. They independently translate, rotate and stretch, though their motion is constrained by the constitutive law used to describe the interface.

The reference surface, S^0, is defined in a the three-dimensional space, as shown in Figure A.22, by the global Cartesian coordinates X_i, where $i = 1, 2, 3$. Conveniently, the internal deformed middle surface, $\overline{S}$, can be defined, through the history of deformations, as the average distance between two initially coinciding points,

$$\overline{x}_i = X_i + \frac{1}{2}\left(u_i^+ + u_i^-\right) \tag{A.1}$$

where $u_i^{\pm}$ are the displacements of the two material points on $S^{\pm}$ that are related to the point X_i, contained in S^0. Hence, defining a local Cartesian coordinate system $(\hat{\boldsymbol{e}}_1, \hat{\boldsymbol{e}}_2, \hat{\boldsymbol{e}}_3)$ on $\overline{S}$, the normal and tangential components of the displacement jump across the material discontinuity can be expressed according to the local orientation of the midsurface.

Let η_1 and η_2 be curvilinear coordinates located on $\overline{S}$, as represented in Figure A.22 (Note that the isoparametric representation of the physical space is reduced to the interfacial element midsurface). Then, two vectors tangential to the deformed midsurface are established as:

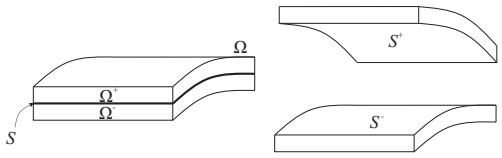

Figure A.21: Interfacial surface, S, traversing a body, Ω, and diving it into Ω^+ and Ω^- subdomains. The exploded view shows the upper S^+ and lower S^- surfaces that bound into S.

$$\boldsymbol{e'_1} = \frac{\partial \overline{x}_i}{\partial \eta_1} \qquad \boldsymbol{e'_2} = \frac{\partial \overline{x}_i}{\partial \eta_2} \tag{A.2}$$

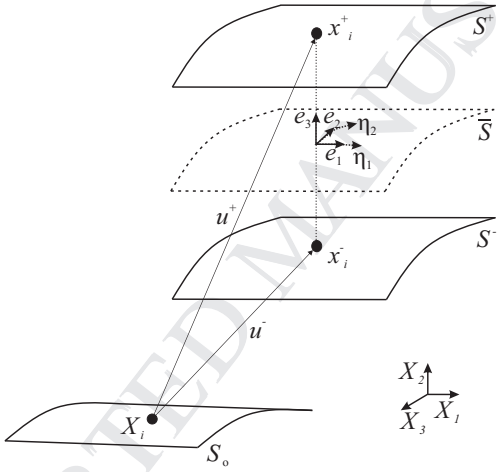

Figure A.22: Description of the deformed element midsurface, $\overline{S}$.

The direction cosines of the local Cartesian coordinate system, are the normal, $\hat{\boldsymbol{e}}_3$, and tangential, $\hat{\boldsymbol{e}}_1$ and $\hat{\boldsymbol{e}}_2$, unit vectors to $\overline{S}$, and can be derived from the Equation (A.2) as follows:

$$\hat{\boldsymbol{e}}_1 = \frac{\boldsymbol{e'_1}}{|\boldsymbol{e'_1}|} \qquad \hat{\boldsymbol{e}}_3 = \frac{\boldsymbol{e'_1} \times \boldsymbol{e'_2}}{|\boldsymbol{e'_1} \times \boldsymbol{e'_2}|} \qquad \hat{\boldsymbol{e}}_2 = \hat{\boldsymbol{e}}_3 \times \hat{\boldsymbol{e}}_1 \tag{A.3}$$

Finally, the displacement jump in local coordinates can be expressed in terms of the displacement field:

ACCEPTED MANUSCRIPT

$$\delta_j = \Theta_{ji}\left(u_i^+ - u_i^-\right), \qquad i,j = 1,2,3 \tag{A.4}$$

where $\left(u_i^+ - u_i^-\right)$ is the separation of two initially coinciding points at the interface in the global Cartesian coordinate system, and Θ_{ji} is the transformation tensor that relates the global to the local coordinate system,

$$\boldsymbol{\Theta} = [\hat{\boldsymbol{e}}_1, \hat{\boldsymbol{e}}_2, \hat{\boldsymbol{e}}_3]^T \tag{A.5}$$

Appendix A.2. Constitutive model

The constitutive relation between the displacement jumps, δ_j, and the tractions between crack faces, τ_j, is defined as

$$\begin{aligned} \tau_j &= \left(1 - \mathcal{D}^K\right) K \delta_j \qquad \text{for} \qquad j = 1,2 \\ \tau_3 &= \left(1 - \mathcal{D}^K\right) K \delta_3 - \mathcal{D}^K K \langle -\delta_3 \rangle \end{aligned} \tag{A.6}$$

where $\mathcal{D}^K \in [0,1]$ is a scalar damage parameter reducing the initial constitutive tangent stiffness, K and $\langle\ \rangle$ are the Macaulay brackets defined as $\langle x \rangle = (x + |x|)$. Note that, as interpenetration of crack faces is physically prevented by contact, negative normal opening values are avoided.

The evolution of the stiffness degrading damage variable, $\mathcal{D}^K$ is governed by an equivalent one-dimensional cohesive law and a damage criterion. For the formulation of this equivalent one-dimensional cohesive law, and so that different stages of the degrading process can be compared under changing mixed-mode loading conditions, a non-negative scalar displacement jump is defined:

$$\lambda = \sqrt{(\delta_I)^2 + (\delta_s)^2} \tag{A.7}$$

where δ_I is the mode I opening, associated to the displacement jump in the normal direction to the

ACCEPTED MANUSCRIPT

midsurface, and δ_s is the shear sliding resulting of the displacement jumps in the tangential directions to the midsurface.

$$\delta_I = \langle \delta_3 \rangle, \qquad \delta_s = \sqrt{(\delta_1)^2 + (\delta_2)^2} \tag{A.8}$$

Note that the two tangential (orthogonal among each other) displacement jumps, δ_1 and δ_2, are reduced to an equivalent shear displacement jump, δ_s. It is worth to mention that this is due to the incapability of the original formulation [15, 17] to distinguish into modes II and III, mainly attributed to the hitherto lack of computationally-efficient crack front tracking algorithms, and not supported by any physical evidence. In any event, shear opening mode is, conservatively, treated as mode II in the present constitutive model.

The equivalent one-dimensional interface traction is related to the equivalent one-dimensional displacement jump with

$$\mu = \left(1 - \mathcal{D}^K\right) K \lambda \tag{A.9}$$

With increasing displacement jump, the traction increases to a peak value, μ_o, corresponding to the interfacial strength, and then decreases until complete decohesion. To ensure the correct energy dissipation during the process of fracture, the total area under the traction-displacement jump curve is set equal to the fracture toughness, $\mathcal{G}_c$. Both the interfacial strength and the fracture toughness are material parameters that depend on the opening mode-mixity, and, together with the penalty stiffness, K, define the shape of the constitutive law.

The local mode-mixity, B, is defined in terms of the displacement jump as:

$$B = \frac{\delta_s^2}{\delta_I^2 + \delta_s^2} \tag{A.10}$$

and it is equivalent to the amount of total specific work related to shear mode over the entire total

ACCEPTED MANUSCRIPT

specific work (the reader is referred to Figure 2 for an schematic representation of the total specific work of the interface).

The critical energy release rate, $\mathcal{G}_c$, for a given mode-mixity is determined using the expression proposed in [25],

$$\mathcal{G}_c = \mathcal{G}_{Ic} + (\mathcal{G}_{IIc} - \mathcal{G}_{Ic})\, B^{\eta} \tag{A.11}$$

where subscripts I and II denote the pure modes I and II values, respectively, and η is an experimentally determined mode interaction parameter. Similarly, the interfacial strength, μ_o, for a given mode-mixity is defined as

$$\mu_o = \sqrt{(\tau_{Io})^2 + [(\tau_{IIo} - \tau_{Io})]\, B^{\eta}} \tag{A.12}$$

In terms of the displacement jump, the onset, λ_o, and propagation, λ_c, of delamination are related to the parameters of the cohesive law:

$$\lambda_o = \frac{\mu_o}{K}, \qquad \lambda_c = \frac{2\mathcal{G}_c}{\mu_o} \tag{A.13}$$

The damage criterion is formulated ensuring damage irreversibility, such that the damage variable at the current time t_c determined as

$$\mathcal{D}^K = \min\left(\max\left(0, \frac{\lambda_c^t\,(\lambda^t - \lambda_o^t)}{\lambda^t\,(\lambda_c^t - \lambda_o^t)}\right), 1\right) \qquad \forall\ t \in [0, t_c] \tag{A.14}$$

Thus, the mixed-mode displacement jump associated to the current damage state is

$$\lambda_{\mathcal{D}} = \frac{\lambda_o \lambda_c}{\lambda_c - \mathcal{D}^K\,(\lambda_c - \lambda_o)} \tag{A.15}$$

The stiffness degrading damage variable, $\mathcal{D}^K$, is strongly nonlinear in terms of $\lambda_{\mathcal{D}}$. This might hinder the performance of the numerical method [21]. Conversely, an energy-based damage variable,

ACCEPTED MANUSCRIPT

which exhibits linear dependency with $\lambda_{\mathcal{D}}$, is defined in [17] and [21] as the specific dissipated energy due to fracture over the fracture toughness during degradation ($\lambda_o < \lambda_{\mathcal{D}} < \lambda_c$):

$$\begin{cases} \mathcal{D}^e = 0 & \text{for} \quad \lambda_{\mathcal{D}} \leq \lambda_o \\ \mathcal{D}^e = \dfrac{\omega_d}{\mathcal{G}_c} & \text{for} \quad \lambda_o \leq \lambda_{\mathcal{D}} \leq \lambda_c \\ \mathcal{D}^e = 1 & \text{for} \quad \lambda_{\mathcal{D}} \geq \lambda_c \end{cases} \tag{A.16}$$

where ω_d is, in terms of the displacement jump is given as:

$$\omega_d = \max\left\{0, \frac{1}{2} K \lambda_o \lambda_c \frac{\lambda_o - \lambda_{\mathcal{D}}}{\lambda_o - \lambda_c}\right\} \tag{A.17}$$

Finally, the total specific work associated to the current damage state can also be determined in terms of the displacement jump:

$$\omega_{tot} = \frac{1}{2} K \lambda_o \left(\lambda_c - \frac{(\lambda_c - \lambda_{\mathcal{D}})^2}{\lambda_c - \lambda_o}\right) \tag{A.18}$$

Note that, during crack propagation, the μ-λ relation follows the equivalent one-dimensional cohesive law, i.e.:

$$\lambda_{\mathcal{D}} = \lambda \tag{A.19}$$

and that before damage initiation, the no energy is dissipated yet and the total specific work corresponds to the specific elastic energy:

$$\omega_{tot} = \frac{1}{2} K \lambda^2 \tag{A.20}$$

Appendix A.3. Finite element implementation

The three dimensional crack propagation problem is discretized here using the FE method. The cohesive interface is implemented into an eight-noded zero-thickness element. This interface element

232

ACCEPTED MANUSCRIPT

is compatible with three dimensional continuum elements that may form the upper and lower part of the body containing the singularity.

The nodal coordinates of the undeformed interface element are arranged in vector $\boldsymbol{C}$ in such a way that:

$$\boldsymbol{C} = \left\{\boldsymbol{C}^{-}, \boldsymbol{C}^{+}\right\} \tag{A.21}$$

being $C_k^- = \left\{X_1^1, X_2^1, X_3^1, ..., X_1^4, X_2^4, X_3^4\right\}^T$ and $C_k^+ = \left\{X_1^5, X_2^5, X_3^5, ..., X_1^8, X_2^8, X_3^8\right\}^T$ the global coordinates of the nodes at the lower and upper interfaces, respectively, where X_i^n is the i-th coordinate of the n-th node.

The nodal displacements, relative to the global coordinates, are arranged in vector $\boldsymbol{Q}$ similarly to the nodal coordinates, i.e. the nodal displacements of the lower interface, $Q_k^- = \left\{u_1^1, u_2^1, u_3^1, ..., u_1^4, u_2^4, u_3^4\right\}^T$, are numbered first, and the nodal displacements of the upper interface, $Q_k^+ = \left\{u_1^5, u_2^5, u_3^5, ..., u_1^8, u_2^8, u_3^8\right\}^T$, are numbered second,

$$\boldsymbol{Q} = \left\{\boldsymbol{Q}^{-}, \boldsymbol{Q}^{+}\right\} \tag{A.22}$$

The material coordinates and the displacement field are interpolated within the domain of the surface element using isoparametric bilinear shape functions,

$$\begin{aligned} L_1 &= \frac{1}{2}\left(1-\eta_1\right)\left(1-\eta_2\right); \qquad L_2 = \frac{1}{2}\left(1+\eta_1\right)\left(1-\eta_2\right) \\ L_3 &= \frac{1}{2}\left(1+\eta_1\right)\left(1+\eta_2\right); \qquad L_4 = \frac{1}{2}\left(1-\eta_1\right)\left(1+\eta_2\right) \end{aligned} \tag{A.23}$$

organized in matrix the shape function matrix, N_{ik}, as follows:

ACCEPTED MANUSCRIPT

$$N_{ik} = \begin{bmatrix} L_1 & 0 & 0 & L_2 & 0 & 0 & L_3 & 0 & 0 & L_4 & 0 & 0 \\ 0 & L_1 & 0 & 0 & L_2 & 0 & 0 & L_3 & 0 & 0 & L_4 & 0 \\ 0 & 0 & L_1 & 0 & 0 & L_2 & 0 & 0 & L_3 & 0 & 0 & L_4 \end{bmatrix} \tag{A.24}$$

According to Equation (A.1) and making use of equations (A.21)-(A.24), the coordinates of the interfacial deformed midsurface are:

$$\overline{x}_i = \frac{1}{2} N_{ik} \left(C_k^+ + C_k^- + Q_k^+ + Q_k^- \right) \tag{A.25}$$

The tangential vectors to the interfacial midsurface at (η_1, η_2), defined in Equation (A.2), are now arranged in the Jacobian matrix,

$$\boldsymbol{J} = [\boldsymbol{e}_1', \boldsymbol{e}_2'] \qquad \text{where} \qquad J_{i\alpha} = \frac{1}{2} \frac{\partial N_{ik}}{\partial \eta_\alpha} \left(C_k^+ + C_k^- + Q_k^+ + Q_k^- \right) \tag{A.26}$$

where the subscript $\alpha = 1, 2$.

Hence, the unit vectors, $\hat{\boldsymbol{e}}_1$, $\hat{\boldsymbol{e}}_2$, $\hat{\boldsymbol{e}}_3$, corresponding to the direction cosines of the local Cartesian coordinate system, can be derived from $J_{i\alpha}$ following equation (A.3).

Finally, the transformation matrix, M_{im}, computes the displacement jump in global coordinates of two initially coinciding points from the nodal global displacement vector:

$$u_i^+ - u_i^- = M_{im} Q_m \tag{A.27}$$

where subscript m runs form 1 to the number of degrees of freedom of the element ($m = 1...24$) and M_{im} is defined as:

$$M_{im} = [-N_{ik} \; N_{ik}] \tag{A.28}$$

Thus, from Equation (A.4), the displacement jump in local coordinates reads:

ACCEPTED MANUSCRIPT

$$\delta_j = \Theta_{ji} M_{im} Q_m \tag{A.29}$$

For the sake of simplicity, only the derivation of the displacement jump field is depicted above, as the only field needed for the resolution of the criteria presented in section 2.2. See [15] for the derivation of the interface element tangent stiffness matrix, $\boldsymbol{K}$, and internal force vector, ${}^{int}\boldsymbol{f}$ required in the nonlinear solution procedure.

Appendix B. Development of the criteria to determine the growth driving direction

The formulation of the three proposed criteria in section 2.2 to determine the growth driving direction is synthesized in Table B.5. The equations to solve for Criterion 1 are found by introducing equations (B.2) and (B.3) in equations (B.1) and (B.4) and computing the radial slopes of the mixed-mode displacement jump, $\frac{\partial \lambda}{\partial \rho}$, and mode-mixity, $\frac{\partial B}{\partial \rho}$. On the ohter hand, the equations for Criterion 2 are found by introducing equations (B.6) and (B.7) in equations (B.5) and (B.8). Also the radial slopes of the mixed-mode displacement jump, $\frac{\partial \lambda}{\partial \rho}$, and mode-mixity, $\frac{\partial B}{\partial \rho}$, are required. Finally, for the evaluation of Criterion 3 only the slope of the mixed-mode displacement jump in the radial direction, $\frac{\partial \lambda}{\partial \rho}$, is needed (see equations (B.9) and (B.10)).

Moreover, in this work, the criteria are applied to the CZM presented in [15, 17] to exemplify their capabilities. In this particular case, the factors F_B and F_λ are reduced to equations (B.11) and (B.12), for Criterion 1, and reduced to equations (B.13) and (B.14), for Criterion 2. Equations (B.11) and (B.12) are obtained by introducing equations (B.15)-(B.24) into equations (B.2) and (B.3). Equations (B.13) and (B.14) are obtained by introducing equations (B.15)-(B.19) and (B.25)-(B.29) into equations (B.6) and (B.7). Also, the derivation of the radial slopes of the mixed-mode displacement jump and mode-mixity, $\frac{\partial \lambda}{\partial \rho}$ and $\frac{\partial B}{\partial \rho}$, after the particular application to the CZM from [15, 17] is detailed in section 2.3.

Criterion ID	Functions to solve		F_B		F_λ	
1	$\frac{\partial}{\partial\varphi}\frac{\partial\mathcal{D}^e}{\partial\rho} = \frac{\partial}{\partial\varphi}\left(F_B\frac{\partial B}{\partial\rho} + F_\lambda\frac{\partial\lambda}{\partial\rho}\right) = 0$	(B.1)	$\frac{\partial\left(\frac{\omega_d}{\mathcal{G}_c}\right)}{\partial\omega_d}\left(\frac{\partial\omega_d}{\partial\lambda_o}\frac{\partial\lambda_o}{\partial\mu_o} + \frac{\partial\omega_d}{\partial\lambda_c}\frac{\partial\lambda_c}{\partial\mu_o}\right)\frac{\partial\mu_o}{\partial B} +$	(B.2)	$\frac{\partial\left(\frac{\omega_d}{\mathcal{G}_c}\right)}{\partial\omega_d}\frac{\partial\omega_d}{\partial\lambda}$	(B.3)
	$\frac{\partial^2}{\partial\varphi^2}\frac{\partial\mathcal{D}^e}{\partial\rho} = \frac{\partial^2}{\partial\varphi^2}\left(F_B\frac{\partial B}{\partial\rho} + F_\lambda\frac{\partial\lambda}{\partial\rho}\right) > 0$	(B.4)	$+\left(\frac{\partial\left(\frac{\omega_d}{\mathcal{G}_c}\right)}{\partial\omega_d}\frac{\partial\omega_d}{\partial\lambda_c}\frac{\partial\lambda_c}{\partial\mathcal{G}_c} + \frac{\partial\left(\frac{\omega_d}{\mathcal{G}_c}\right)}{\partial\mathcal{G}_c}\right)\frac{\partial\mathcal{G}_c}{\partial B}$			
2	$\frac{\partial}{\partial\varphi}\frac{\partial\left(\frac{\omega_{tot}}{\mathcal{G}_c}\right)}{\partial\rho} = \frac{\partial}{\partial\varphi}\left(F_B\frac{\partial B}{\partial\rho} + F_\lambda\frac{\partial\lambda}{\partial\rho}\right) = 0$	(B.5)	$\frac{\partial\left(\frac{\omega_{tot}}{\mathcal{G}_c}\right)}{\partial\omega_{tot}}\left(\frac{\partial\omega_{tot}}{\partial\lambda_o}\frac{\partial\lambda_o}{\partial\mu_o} + \frac{\partial\omega_{tot}}{\partial\lambda_c}\frac{\partial\lambda_c}{\partial\mu_o}\right)\frac{\partial\mu_o}{\partial B} +$	(B.6)	$\frac{\partial\left(\frac{\omega_{tot}}{\mathcal{G}_c}\right)}{\partial\omega_{tot}}\frac{\partial\omega_{tot}}{\partial\lambda}$	(B.7)
	$\frac{\partial^2}{\partial\varphi^2}\frac{\partial\left(\frac{\omega_{tot}}{\mathcal{G}_c}\right)}{\partial\rho} = \frac{\partial^2}{\partial\varphi^2}\left(F_B\frac{\partial B}{\partial\rho} + F_\lambda\frac{\partial\lambda}{\partial\rho}\right) > 0$	(B.8)	$+\left(\frac{\partial\left(\frac{\omega_{tot}}{\mathcal{G}_c}\right)}{\partial\omega_{tot}}\frac{\partial\omega_{tot}}{\partial\lambda_c}\frac{\partial\lambda_c}{\partial\mathcal{G}_c} + \frac{\partial\left(\frac{\omega_{tot}}{\mathcal{G}_c}\right)}{\partial\mathcal{G}_c}\right)\frac{\partial\mathcal{G}_c}{\partial B}$			
3	$\frac{\partial}{\partial\varphi}\frac{\partial\lambda}{\partial\rho} = 0$	(B.9)	—		—	
	$\frac{\partial^2}{\partial\varphi^2}\frac{\partial\lambda}{\partial\rho} > 0$	(B.10)				

Table B.5: Equations to solve for each criteria to determine the growth driving direction, φ.

ACCEPTED MANUSCRIPT

Criterion ID	F_B		F_λ	
1	$\dfrac{\eta\left(\mathcal{G}_{IIc}-\mathcal{G}_{Ic}\right)B^{(\eta-1)}\lambda}{K\lambda_c\lambda_o\left(\lambda_o-\lambda_c\right)}$	(B.11)	$\dfrac{1}{\lambda_c-\lambda_o}$	(B.12)
2	$\dfrac{2\eta\left(\mathcal{G}_{IIc}-\mathcal{G}_{Ic}\right)B^{(\eta-1)}\lambda\left(\lambda_c-\lambda\right)}{K\lambda_c^2\lambda_o\left(\lambda_o-\lambda_c\right)}$	(B.13)	$\dfrac{2\left(\lambda_c-\lambda\right)}{\lambda_c\left(\lambda_c-\lambda_o\right)}$	(B.14)

Table B.6: Expressions for the factors F_B and F_λ after application of the CZM formulation presented in [15, 17].

ACCEPTED MANUSCRIPT

Dependencies	Partial derivatives	
$\lambda_o(\mu_o)$	$\frac{\partial \lambda_o}{\partial \mu_o} = \frac{1}{K}$	(B.15)
$\lambda_c(\mu_o, \mathcal{G}_c)$	$\frac{\partial \lambda_c}{\partial \mu_o} = -\frac{2\mathcal{G}_c}{\mu_o^2}$	(B.16)
	$\frac{\partial \lambda_c}{\partial \mathcal{G}_c} = \frac{2}{\mu_o}$	(B.17)
$\mu_o(B)$	$\frac{\partial \mu_o}{\partial B} = \frac{\eta\left(\tau_{IIo}^2 - \tau_{Io}^2\right) B^{\eta-1}}{2\mu_o}$	(B.18)
$\mathcal{G}_c(B)$	$\frac{\partial \mathcal{G}_c}{\partial B} = \eta\left(\mathcal{G}_{IIc} - \mathcal{G}_{Ic}\right) B^{\eta-1}$	(B.19)
$\omega_d(\lambda_o, \lambda_c, \lambda)$	$\frac{\partial \omega_d}{\partial \lambda_o} = \frac{1}{2} K \lambda_c \frac{\lambda_o^2 - 2\lambda_c\lambda_o + \lambda_c\lambda}{(\lambda_o - \lambda_c)^2}$	(B.20)
	$\frac{\partial \omega_d}{\partial \lambda_c} = \frac{1}{2} K \lambda_o^2 \frac{\lambda_o - \lambda}{(\lambda_o - \lambda_c)^2}$	(B.21)
	$\frac{\partial \omega_d}{\partial \lambda} = \frac{1}{2} K \lambda_o \lambda_c \frac{1}{(\lambda_c - \lambda_o)}$	(B.22)
$\mathcal{D}^e(\omega_d, \mathcal{G}_c)$	$\frac{\partial\left(\frac{\omega_d}{\mathcal{G}_c}\right)}{\partial \omega_d} = \frac{1}{\mathcal{G}_c}$	(B.23)
	$\frac{\partial\left(\frac{\omega_d}{\mathcal{G}_c}\right)}{\partial \mathcal{G}_c} = \frac{-\omega_d}{\mathcal{G}_c^2}$	(B.24)
$\omega_{tot}(\lambda_o, \lambda_c, \lambda)$	$\frac{\partial \omega_{tot}}{\partial \lambda_o} = \frac{1}{2} K \lambda_c (\lambda_o - \lambda) \frac{\lambda - 2\lambda_c + \lambda_o}{(\lambda_o - \lambda_c)^2}$	(B.25)
	$\frac{\partial \omega_{tot}}{\partial \lambda_c} = \frac{1}{2} K \lambda_o \frac{(\lambda_o - \lambda)^2}{(\lambda_o - \lambda_c)^2}$	(B.26)
	$\frac{\partial \omega_{tot}}{\partial \lambda} = K \lambda_o \frac{\lambda_c - \lambda}{\lambda_c - \lambda_o}$	(B.27)
$\frac{\omega_{tot}}{\mathcal{G}_c}(\omega_{tot}, \mathcal{G}_c)$	$\frac{\partial\left(\frac{\omega_{tot}}{\mathcal{G}_c}\right)}{\partial \omega_{tot}} = \frac{1}{\mathcal{G}_c}$	(B.28)
	$\frac{\partial\left(\frac{\omega_{tot}}{\mathcal{G}_c}\right)}{\partial \mathcal{G}_c} = \frac{-\omega_{tot}}{\mathcal{G}_c^2}$	(B.29)

Table B.7: Dependencies and partial derivatives of the variables in the system using the CZM presented in [15, 17].

PAPER B

B

PAPER B

Evaluation of the mode-decomposed energy release rates for arbitrarily shaped delamination fronts using cohesive elements

L. Carreras [a], E. Lindgaard [b], J. Renart [a], B.L.V. Bak [b], A. Turon [a]

[a] AMADE, Mechanical Engineering and Industrial Construction Department, Universitat de Girona, Carrer Universitat de Girona 4, 17003 Girona, Spain

[b] Department of Materials and Production, Aalborg University, Fibigerstraede 16, DK-9220 Aalborg East, Denmark

The paper has been submitted for publication in *Journal of the Mechanics and Physics of Solids*, 2018

Evaluation of the mode-decomposed energy release rates for arbitrarily shaped delamination fronts using cohesive elements

L. Carreras[a,*], E. Lindgaard[b], J. Renart[a], B.L.V. Bak[b], A. Turon[a]

[a] *AMADE, Polytechnic School, University of Girona, Campus Montilivi s/n, E-17003 Girona, Spain*
[b] *Dept. of Materials and Production, Aalborg University, Fibigerstraede 16, DK-9220 Aalborg East, Denmark*

Abstract

The computation of the mode-decomposed energy release rates in three-dimensional problems involving delaminations, modeled using a cohesive zone model approach, has not been previously investigated. The J-integral is a suitable method for calculating it, since its domain-independence can be employed to shrink the integration domain to the cohesive interface, and reduce it to a line integral. In this work, a numerical procedure to evaluate the mode-decomposed J-integral in curved delamination fronts is presented. A growth driving direction criterion, previously developed by the authors, is used to track the integration path along the cohesive zone and decompose the energy release rate. The formulation is implemented in a finite element framework and validated by comparison with VCCT results. The significance and generality of the formulation are demonstrated on crack propagation in a three-dimensional composite structure.

Keywords:

Delamination growth, Cohesive zone model, Finite element analysis, Energy Release Rate, Mode-decomposed J-Integral

1. Introduction

Delamination is a common cause of failure in layered materials and, therefore, the analysis of delamination onset and growth is essential for any mechanical application. In this regard, the finite

*Corresponding author. Tel.: +34 972 418 817
Email addresses: laura.carreras@udg.edu (L. Carreras), elo@mp.aau.dk (E. Lindgaard), jordi.renart@udg.edu (J. Renart), brianbak@mp.aau.dk (B.L.V. Bak), albert.turon@udg.edu (A. Turon)

element (FE) method has become an indispensable tool in the design of laminated composite structures and in the prediction of their service life.

The most common methods for the prediction of interlaminar failure can be divided in two main approaches: Methods purely based on fracture mechanics and methods based on the cohesive zone model (CZM) concept [1, 2], the latter combining the framework of fracture mechanics and damage mechanics.

In the fracture mechanics approach, usually a local Griffith's criterion [3] is used to predict delamination growth: the energy release rate, $\mathcal{G}$, is compared to the interlaminar fracture toughness, $\mathcal{G}_c$. Two of the most common extraction methods for the energy release rate (also called the crack extension force) rely either on the virtual crack closure technique (VCCT) [4] or the J-integral [5]. Then, applying Griffith's criterion, crack propagation occurs at the points where $\mathcal{G} \geq \mathcal{G}_c$. This local energy balance criterion implies negligible fracture process zone. Conversely, CZMs can capture fracture energy dissipation mechanisms of quasi-brittle materials, such as the formation of micro cracks ahead of the crack tip before complete separation of the crack faces. Therefore, the CZM approach is a suitable means of predicting crack propagation when a nonnegligible fracture process zone is present. The strain singularity at the tip of a sharp crack is removed by accounting for a cohesive zone (CZ), where the material undergoes degradation until complete decohesion. The mechanical behavior of the interface is modeled by means of a damage variable, which is a measure of the degradation of the mechanical properties of the material ahead of the crack tip. When the damage variable reaches its maximum value, new crack surface is created. Moreover, CZMs are specially suited for simulating interlaminar cracks in laminated structures, as the delamination is confined to propagate between two adjacent plies. Thus, when a progressive delamination simulation is solved using a FE analysis, the potential failure surfaces are known in advance, and the cohesive elements can be efficiently located.

Under static loading conditions, existing CZMs [6–12] do not require the computation of the energy release rate in order to simulate crack growth. However, some of the recently published methods for the simulation of fatigue-driven delamination based on CZM [13–18] link the rate of the local fatigue

damage with any variant of the Paris' law [19]. The Paris' law-like expressions relate the crack growth rate with a power law function of the loading level in terms of a fracture mechanics parameter [13, 20], usually the stress intensity factor, K, or the energy release rate, $\mathcal{G}$, where only the latter is relevant for a CZM. Therefore, the computation of the energy release rate is required in order to integrate the rate of the local fatigue damage. In this regard, the J-integral directly equates to $\mathcal{G}$ [21]. Indeed, the benchmark study of the simulation methods for fatigue-driven delamination using a CZM approach presented in [18] showed a better performance for the methods using the J-integral as means of extracting the energy release rate.

The path-independence of the two-dimensional J-integral makes it very attractive in practice, since it avoids the need of accurate computations on the stress field at the crack tip, which is hard to deal with in a FE framework. For this reason, much effort has been devoted to extend the applicability of the J-integral to three-dimensional domains [22–32]. The published extensions of the J-integral for its evaluation in three-dimensional problems, where the crack extension force may change along the crack front, is commonly done by means of two approaches. The first is a point-wise evaluation of the J-integral on a cross-section of the crack surface, resulting in a combination of a contour integral and a surface integral defined over the area enclosed by the contour. See [30] for a detailed description. The computation of the surface integral requires accurate calculation of the field quantities at the crack tip. For this reason, it is commonly treated with the boundary element method [27, 30]. The second approach is the equivalent domain integral over a finite volume surrounding the crack front [25, 26]. With this method, it is not required to capture the singular field near the crack tip and, hence, it is usually applied in a FEM framework. Regardless, the applicability of most of these J-integral extensions to three-dimensional domains is restricted to certain assumptions such as plane-strain/stress, i.e. at the vicinity of the crack tip, or planar cracks. By employing curvilinear coordinates, Eriksson [33] and Fernlund et al. [34] obtained generalized expressions applicable to curved cracks with non-planar crack surfaces. In [33], a volume-independent integral expression for the evaluation of the crack extension force is derived from the principle of virtual work. In [34],

the decrease of the potential energy with crack extension is employed to obtain a general path-area independent J-integral expression for non-planar cracks with curved crack fronts. In both cases, the fracture process zone is considered negligible and the mode-decomposition is not addressed.

Delamination propagation may be described through a combination of the three basic fracture modes, Mode I, II and III [35], and the fracture resistance of the interface, under both static and fatigue loading, highly depends on the mode mixity conditions. Consequently, the delamination models available in the literature [13, 20, 36] are based on a mode-decomposed definition of the load, expressed in terms of the energy release rate ($\mathcal{G}_I$, $\mathcal{G}_{II}$ and $\mathcal{G}_{III}$). In this regard, the decomposition of the J-integral into fracture modes, as a tool for extracting energy release rates, becomes necessary.

In this work, a procedure to numerically evaluate the mode-decomposed J-integral in a three-dimensional body undergoing a delamination, modeled using cohesive elements, is presented. The formulation is derived from the general expression of the J-integral for 3D curved delaminations with non-planar surfaces expressed in terms of curvilinear coordinates [34]. Its application to cohesive interfaces is addressed in Section 2, while its implementation in a FE framework is presented in Section 3. In Section 4, the formulation is applied to a moment-loaded double-cantilevered-beam (DCB) specimen, and the mixed-mode J-components are compared to the mode-decomposed energy release rates obtained from VCCT. In section 5, the formulation is used to compute the J-integral components of a partially reinforced end-loaded split (ELS) specimen with non-straight crack front. The work finishes with the discussion of the obtained results and conclusions.

2. Formulation of the mode-decomposed energy release rates

In this section, the formulation of the mode-decomposed energy release rates in three-dimensional delaminations, modeled using a cohesive zone model approach, is presented. The point of departure is the generalized J-integral for non-planar curved cracks obtained by Fernlund et al. [34].

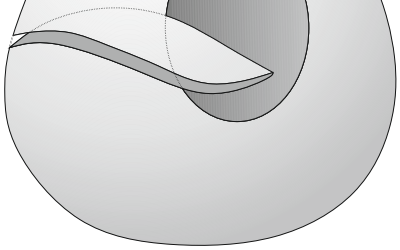

2.1. Assessment of the energy release rate by means of the J-integral formulation in curvilinear coordinates

Consider an elastic body (c.f. Figure 1), with a crack, subjected to prescribed tractions, T, and displacements, u, along parts of its boundary surface (Note that T and u are physical entities which are not yet described in any particular coordinate basis). In a general three dimensional domain, both the crack surfaces and the crack front may be curved. Let θ^i, $i = 1, 2, 3$, be an orthogonal curvilinear coordinate system with origin at a given point P along the crack front. This local coordinate system is oriented such that, at point P, θ^3 is normal to the crack surface in the undeformed configuration where the crack surfaces are coinciding, θ^2 is the coordinate along the crack front and θ^1 is the direction of crack propagation, which is always tangent to the crack surface and perpendicular to θ^2 and θ^3.

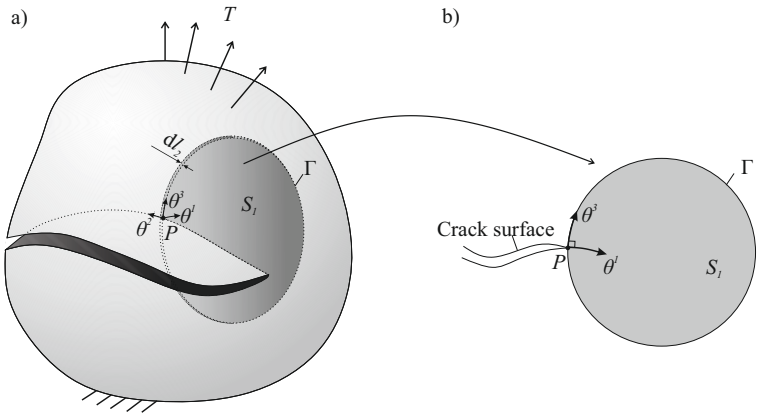

Figure 1: a) Three-dimensional body undergoing a delamination with curved front and non-planar crack surfaces. b) The integration domain is a slice of infinitesimal thickness, $\mathrm{d}l_2$.

Let us focus on a thin slice of elemental thickness, $\mathrm{d}l_2$, of the cracked body, which contains P (c.f. Figure 1). Note that an infinitesimal length segment, $\mathrm{d}l_i$ along a curvilinear axis, θ^i is given by:

$$\mathrm{d}l_i = \sqrt{g_{ii}}\mathrm{d}\theta^i \tag{1}$$

where g_{ij} is the covariant metric tensor. In the absence of body forces, the change in potential energy,

Π, per unit of newly created crack area is [34]:

$$-\frac{\mathrm{d}\Pi}{\mathrm{d}A} = -\int_V \frac{\mathrm{d}W}{\mathrm{d}A}\mathrm{d}V + \int_S T^i \frac{\mathrm{d}u_i}{\mathrm{d}A}\mathrm{d}S \tag{2}$$

where $\mathrm{d}A$ is the elemental crack area extension, V the volume of the slice, S is the surface surrounding V, W is the strain energy density, T^i are the contravariant components of the traction vector and u_i are the covariant components of the displacement vector.

The infinitesimal thickness of the slice, allows to lump the three-dimensional slice into a surface S_1, defined by $\theta^2 = 0$ ($\mathrm{d}l_2 \to 0$). Then, by application of Green's theorem, and under the assumption of small deformations, elastic material behavior, symmetry of the stress tensor and equilibrium conditions, the decrease in potential energy per unit area extension is expressed, in [34], as a contour integral and an area integral on the surface S_1:

$$J = -\frac{\mathrm{d}\Pi}{\mathrm{d}A} = \frac{1}{\sqrt{g_{11}}}\oint_\Gamma \left(W n_1 - T^i \frac{\partial u_i}{\partial \theta^1}\right)\mathrm{d}\Gamma - \frac{1}{\sqrt{g_{11}g_{22}}}\int_{S_1} \frac{\partial}{\partial \theta^2}\left(\sigma^{i2}\frac{\partial u_i}{\partial \theta^1}\right)\mathrm{d}S \tag{3}$$

where Γ is the contour enclosing S_1 in the clockwise direction and n_j is the outward unit normal vector on Γ. Note that in [34], the curvilinear coordinate system is rotated 90° around the θ^1-coordinate.

The J-integral is equivalent to the energy release rate, $\mathcal{G}$, for an elastic material response. In a three-dimensional body, the energy release rate may vary along the crack front. Therefore, in order to assess the delamination extension force in three-dimensional problems, it is customary to compute the point-wise value of J as a function of the crack front position, P.

2.2. Application to cohesive interfaces

Conversely to LEFM, the CZM relies on the existence of a band of material ahead of the crack tip, called the cohesive zone (CZ), where the material behaves nonlinearly [1, 2]. In the CZ, a cohesive traction distribution acts on the separating surfaces, thus avoiding stress singularities at the tip of sharp cracks. The constitutive law that relates the cohesive tractions, $T^i(\delta_i)$, to the displacement jumps at the interface, δ_i, is governed by a scalar damage variable. The damage variable evolves

monotonically with time to ensure irreversibility. To guarantee the proper energy dissipation under mixed-mode conditions, in [11], the cohesive law is formulated in a one-dimensional space, where the equivalent mixed-mode traction, μ, is related to the norm of the displacement jump, λ. A sketch of the bilinear cohesive law used in [11] is represented in Figure 2. An energy-based damage variable, $\mathcal{D}^e$, is introduced as the ratio of specific dissipated energy due to fracture, ω_d (Figure 2.b), and the fracture toughness, $\mathcal{G}_c$ (Figure 2.a). Thus, $\mathcal{D}^e$ ranges from 0 to 1, and it can be understood as the degree of crack development, taking a value of 0 if the degradation process is yet to start, and a value of 1 if the crack is completely developed.

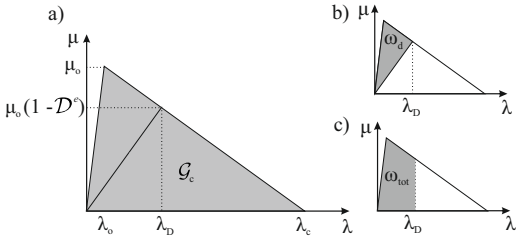

Figure 2: Equivalent one-dimensional cohesive law. The shadowed area in a) represents the fracture toughness, $\mathcal{G}_c$, in b), the specific dissipated energy, ω_d and in c), the total specific work, ω_{tot}, for a given state of damage.

The constitutive law is formed by an initial elastic region, before damage initiation, and a softening region. The onset and propagation of delamination are limited by the onset mixed-mode displacement jump, λ_o, and the critical mixed-mode displacement jump, λ_c, such that the applicability of the energy-based damage variable, $\mathcal{D}^e$, is restricted to:

$$\begin{cases} \mathcal{D}^e = 0 & \text{for} \quad \lambda_{\mathcal{D}} \leq \lambda_o \\ \mathcal{D}^e = \dfrac{\omega_d}{\mathcal{G}_c} & \text{for} \quad \lambda_o \leq \lambda_{\mathcal{D}} \leq \lambda_c \\ \mathcal{D}^e = 1 & \text{for} \quad \lambda_{\mathcal{D}} \geq \lambda_c \end{cases} \tag{4}$$

where $\lambda_{\mathcal{D}}$ is the mixed-mode displacement jump associated to the current damage state.

When applied to delamination modeling in laminated composite materials, the cohesive behavior is lumped into the interface between subsequent plies. In [34], it is demonstrated that the J-integral

of Equation (3), generalized in terms of curvilinear coordinates for cracks with curved front and non-planar crack surfaces, is path-area-independent. Then, for the measurement of the delamination extension force in 3D laminated structures modeled using a CZM approach, the path-area-independence of Equation (3) can be employed to shrink the contour Γ to the upper and lower crack surfaces (c.f. Figure 3), similarly to what is done with the two-dimensional form of the J-integral [5]. Therefore, the term related to the surface in Equation (3) vanishes due to the zero-thickness of the cohesive interface. Moreover, the contribution from the strain energy term within the cohesive interface also vanishes and Equation (3) is reduced to:

$$J = -\frac{1}{\sqrt{g_{11}}} \oint_{\Gamma} \left(T^i \frac{\partial u_i}{\partial \theta^1} \right) \mathrm{d}\Gamma \tag{5}$$

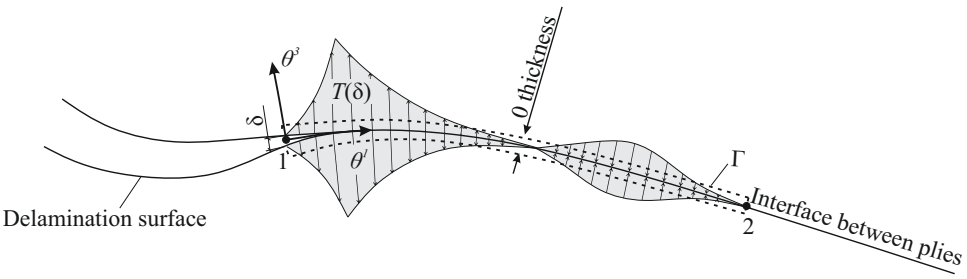

Figure 3: The integration path, Γ, is reduced to the cohesive interface.

Let σ^{ij} be the contravariant components of the cohesive stress tensor. Then, the contravariant traction vector at the crack faces is given by:

$$T^i = \sigma^{ij} n_j \tag{6}$$

being n_j is the outward unit normal vector on the contour Γ, i.e. on the crack surfaces. Thus, n_j vanishes for $j \neq 3$, and Equation (5) reads:

$$J = -\frac{1}{\sqrt{g_{11}}} \int_{\Gamma} \left(\sigma^{i3} \frac{\partial u_i^+}{\partial \theta^1} + \sigma^{i3} \frac{\partial u_i^-}{\partial \theta^1} \right) \mathrm{d}\theta^1 \tag{7}$$

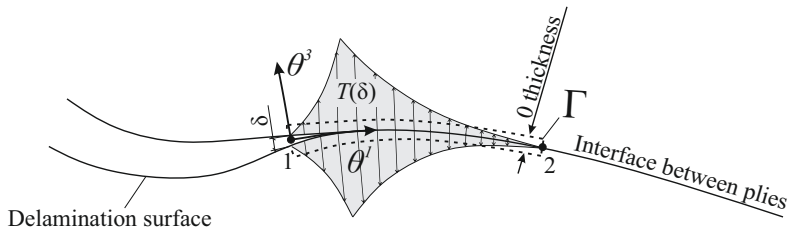

where u^+ and u^- are the displacements at the upper ($^+$) and lower ($^-$) crack surfaces, respectively. Finally, introducing the displacement jump as the separation of two initially coinciding points on the interface, defined as:

$$\delta_i = \left(u_i^+ - u_i^-\right) \tag{8}$$

the curvilinear CZ J-integral, when applied to cohesive interfaces, can be expressed as:

$$J = -\frac{1}{\sqrt{g_{11}}} \int_{CZ} \left(\sigma^{i3} \frac{\partial \delta_i}{\partial \theta^1}\right) \mathrm{d}\theta^1 \tag{9}$$

Observe, in Figure 3, that the integration path is the entire CZ so that all the cohesive stresses contribute to the CZ J-integral.

2.3. Integration paths

As demonstrated in Section 2.2, the integration domain of the curvilinear CZ J-integral applied to cohesive interfaces is a slice of infinitesimal thickness, $\mathrm{d}l_2$, lumped into the delamination interface. Thus, the integration domain is reduced to a path contained in the delamination interface which follows the direction of crack propagation, θ^1. In order to compute the J-distribution in three-dimensional structures, the interface can be divided into infinite slices. Obviously, the J-value of each slice is unique, and is obtained when the integration path is covered in its entirety, i.e. going through the entire cohesive zone, from the completely damaged zone (point 1 in Figure 3, with zero cohesive stress) until the end of the zone in elastic regime (point 2 in Figure 3, with zero cohesive stress).

In LEFM, the propagation direction, θ^1, is assumed to be the normal to the crack front at the point P, where the crack front is the line separating the damaged and undamaged parts (c.f. Figure 4.a). However, the definition of the propagation direction as the normal to the crack front does not apply for CZM, due to existence of a cohesive zone of variable length. The authors have recently introduced the concept of the growth driving direction (GDD) for CZM [37], as an analog to the crack propagation direction in LEFM. The GDD is defined as the gradient vector field of the scalar energy-based damage,

$\mathcal{D}^e$ with respect to the coordinates tangent to the cohesive interface mid-surface:

$$\text{GDD} = -\nabla \mathcal{D}^e \tag{10}$$

Thus, the GDD is normal to the energy-based damage, $\mathcal{D}^e$, isolines (c.f. Figure 4.a) and it converges with the normal to the crack front in LEFM (c.f. Figure 4.b) in the limiting case where the length of the CZ approaches zero. Therefore, making use of the criterion presented in [37], θ^1 can be defined according to the GDD. In this way, the integration paths, defined along the θ^1-coordinate, never cross and the three-dimensional structure can be understood as the aggregation of infinite individual slices of infinitesimal thickness which contain a crack propagating in the GDD. It is worth to mention that the damage isolines may not be parallel along the CZ, leading to slices with double curvature if, in addition, the cohesive interface mid-surface is non-planar.

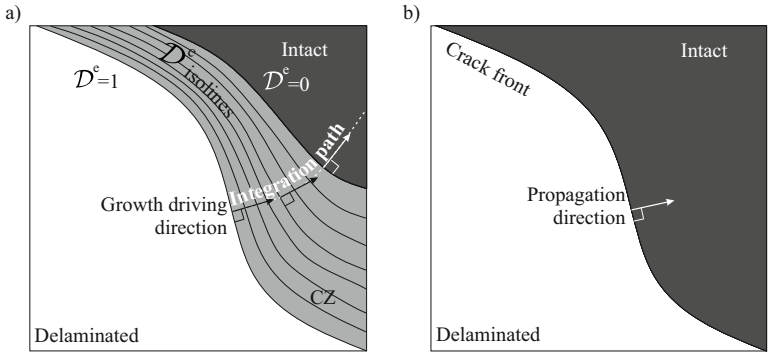

Figure 4: a) The growth driving direction is assumed to be the normal direction to the energy-based damage isolines in the CZM framework. The integration paths are tangent ot the local GDD direction. b) The propagation direction is assumed to be the normal direction to the crack front in the LEFM framework.

It is noted that, for the computation of the J-value in cohesive interfaces using Equation (9), the contribution of the stress, σ^{i3}, and displacement jump slope in the GDD direction, $\frac{\partial \delta_i}{\partial \theta^1}$, in the elastic regime is needed. However, the criterion in Equation (10) for the identification of the GDD, based on the negative gradient of the energy-based damage, $\mathcal{D}^e$, is only meaningful for $\mathcal{D}^e \in]0, 1[$ (see Equation (4)). Therefore, a new criterion for the identification of GDD in the elastic regime must be used. In

this regard, another criterion, which is also active in before the initiation of the degradation process, is purposed in [37]:

$$GDD = -\nabla \left(\frac{\omega_{tot}}{\mathcal{G}_c} \right) \tag{11}$$

where $\frac{\omega_{tot}}{\mathcal{G}_c}$ is the ratio between the total specific work (c.f. Figure 2.c) and the fracture toughness. Both the conservative and the non-conservative work are computed in this criterion. Thus, since, as soon as two initially coinciding points separate from each other some elastic energy is stored, this criterion is active before any energy dissipation due to fracture takes place. Moreover, using the CZM presented in [11] once the damage is initiated, both criteria lead to the same GDD solution.

2.4. Mode-decomposition of the CZ J-integral for its application to cohesive interfaces

A crack can grow under a combination of three loading modes [35]: the opening mode (mode I), the sliding mode (mode II) and the tearing mode (mode III). Mode I is defined normal to the cohesive interface mid-surface, mode II, tangent to the mid-surface in the propagation direction and mode III, tangent to the mid-surface and perpendicular to mode II. As already stated in Section 3.1, the GDD is defined as the direction equivalent to crack propagation direction when a CZM approach is used [37]. Thus, the mode II direction is defined coincident to the GDD, whereas the mode III direction is defined perpendicular to it. Indeed, since θ^i are orthogonal curvilinear coordinates, the local covariant and contravariant basis vectors are coincident. The local basis vectors are aligned with the three loading modes directions, since θ^1 is locally coincident with the GDD (i.e. tangent to the mid-surface), θ^3 is normal to the mid-surface, and θ^2 is normal to θ^1 and θ^3.

At an interface modeled using a CZM approach, only three uncoupled components of cohesive stresses (σ^{13}, σ^{23} and σ^{33}) result from the displacements jumps between crack faces (δ_1, δ_2, δ_3). Stresses are expressed in the local contravariant basis vectors and displacements jumps in the local covariant basis vectors of the curvilinear crack coordinate system, θ^i. Therefore, necessarily, the quantities σ^{13} and $\frac{\partial \delta_1}{\partial \theta_1}$ contribute to mode II, σ^{23} and $\frac{\partial \delta_2}{\partial \theta_1}$, to mode III, and σ^{33} and $\frac{\partial \delta_3}{\partial \theta_1}$, to mode

I crack loading. Hence, the mode-decomposed CZ J-integrals are defined according to the local θ^i coordinate system such that the terms with $i = 3$ are attributed to Mode I, the terms with $i = 1$, to Mode II and the terms with $i = 2$, to Mode III:

$$\begin{aligned} J_I &= -\frac{1}{\sqrt{g_{11}}} \int_{CZ} \left(\sigma^{33} \frac{\partial \delta_3}{\partial \theta^1} \right) \mathrm{d}\theta^1 \\ J_{II} &= -\frac{1}{\sqrt{g_{11}}} \int_{CZ} \left(\sigma^{13} \frac{\partial \delta_1}{\partial \theta^1} \right) \mathrm{d}\theta^1 \\ J_{III} &= -\frac{1}{\sqrt{g_{11}}} \int_{CZ} \left(\sigma^{23} \frac{\partial \delta_2}{\partial \theta^1} \right) \mathrm{d}\theta^1 \end{aligned} \tag{12}$$

For 3D planar cracks, described by a rectangular Cartesian coordinate system, the mode decomposed CZ J-integrals in Equation (12) evaluated at the cohesive interface, are in agreement with that in [30, 38].

3. Discretization with the Finite Element Method

In the following, the formulation presented in Section 2 is applied into a FE framework. The CZM used in this work, and its implementation to FE, was presented by Turon et al. in [10, 11]. Complying with the cohesive element definition, the interfacial tractions and displacement jumps are expressed in a local Cartesian coordinate system, x_i, located on the deformed mid-surface, $\overline{S}_{coh}$, defined as the average distance between two initially coinciding points, P^- and P^+ (c.f. Figure 5). The direction cosines of the local Cartesian coordinate system, are the normal, $\hat{e}_3$, and tangential, $\hat{e}_1$ and $\hat{e}_2$, unit vectors to $\overline{S}_{coh}$. Furthermore, employing the criterion developed in [37], the local tangential coordinates can be oriented in such a way that x_1 and x_2 are the tangential and normal coordinates to the GDD, respectively.

To numerically integrate Equation (12), trapezoidal integration is employed (although any other numerical integration method could be used). Thus, the curved integration pathline is discretized into small linear subintervals tangent to the curvilinear coordinate θ^1. The quantities in the integrand

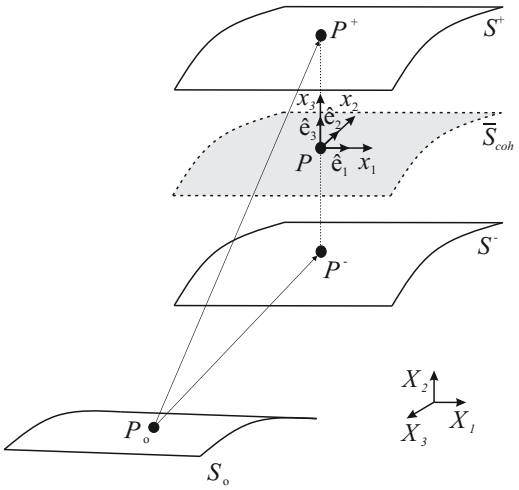

Figure 5: Description of the undeformed, S_o, and deformed, S^+ and S^-, configurations of the delamination interfaces. The quantities of the CZM are calculated at the deformed misurface, $\overline{S}_{coh}$, in terms of the local Cartesian coordinates x_i. P is a point located at the mid-surface in the deformed configuration, while points P^+ and P^- are points belonging to the upper and lower crack surfaces, respectively. P, P^+ and P^- coincide at P_o in the undeformed configuration.

of Equation (12) must, thereby, be defined according to the local Cartesian coordinate system, x_i, with locally coincident direction with the covariant and contravariant basis vectors of the orthogonal curvilinear coordinate system, θ^i. The tracking of the integration path, as well as its limits, are addressed in Section 3.1.

The derivative of the displacement jumps, δ_i, with respect to x_1, the local Cartesian coordinate aligned with the GDD, is addressed in the following. X_j is the Cartesian reference system, x_i is the local Cartesian coordinate system and R_{ij} is the transformation tensor which relates the global to the local coordinate system. By assuming that the derivative of R_{ij} with respect to x_1 can be omitted, the derivative $\frac{\partial \delta_i}{\partial x_1}$ reads:

$$\frac{\partial \delta_i}{\partial x_1} = R_{ij} \frac{\partial M_{jm}}{\partial x_1} Q_m \tag{13}$$

where M_{jm} is the transformation matrix that relates the global displacement jump with the nodal global displacement, Q_m. The size of Q_m is the number of degrees of freedom of the element (in the

case of 8-noded cohesive elements, $m = 1...24$). The derivative of the transformation matrix, M_{jm}, with respect to the local coordinate, x_1, is obtained by application of the chain rule:

$$\frac{\partial M_{jm}}{\partial x_1} = \frac{\partial M_{jm}}{\partial \eta_\alpha} \frac{\partial \eta_\alpha}{\partial x_1} \tag{14}$$

The first partial derivative in the right hand side of Equation (14) is the variation of the transformation matrix, M_{jm}, with the isoparametric coordinates of the cohesive element formulation, η_α (α=1,2):

$$\frac{\partial M_{jm}}{\partial \eta_\alpha} = \left[-\frac{\partial N_{jk}}{\partial \eta_\alpha},\ \frac{\partial N_{jk}}{\partial \eta_\alpha} \right] \tag{15}$$

where N_{jk} is the shape function matrix and the subscript k runs from 1 to the number of degrees of freedom of respectively the top and bottom surface of the cohesive element. In case of an 8-noded element, $k = 1...12$. In [10, 11], the material coordinates and the displacement fields are interpolated within the domain of the interface element using isoparametric bilinear shape functions:

$$\begin{aligned} L_1 &= \frac{1}{2}(1-\eta_1)(1-\eta_2); \qquad L_2 = \frac{1}{2}(1+\eta_1)(1-\eta_2) \\ L_3 &= \frac{1}{2}(1+\eta_1)(1+\eta_2); \qquad L_4 = \frac{1}{2}(1-\eta_1)(1+\eta_2) \end{aligned} \tag{16}$$

organized in N_{jk} as follows:

$$N_{jk} = \begin{bmatrix} L_1 & 0 & 0 & L_2 & 0 & 0 & L_3 & 0 & 0 & L_4 & 0 & 0 \\ 0 & L_1 & 0 & 0 & L_2 & 0 & 0 & L_3 & 0 & 0 & L_4 & 0 \\ 0 & 0 & L_1 & 0 & 0 & L_2 & 0 & 0 & L_3 & 0 & 0 & L_4 \end{bmatrix} \tag{17}$$

where the local isoparametric coordinates, η_1 and η_2, range from -1 to 1 over the element domain.

The derivatives $\frac{\partial \eta_\alpha}{\partial x_1}$ are the inverse of the derivatives of the local coordinate, x_1, with respect to the isoparametric coordinates, η_α, defined as:

$$\frac{\partial x_1}{\partial \eta_\alpha} = R_{1j}\frac{1}{2}\frac{\partial N_{jk}}{\partial \eta_\alpha}\left(C_k^+ + C_k^- + Q_k^+ + Q_k^-\right) \tag{18}$$

where C_k^- and C_k^+ are the global coordinates of the nodes at the lower and upper surfaces, and Q_k^- and Q_k^+ are the nodal displacements, relative to the global coordinates, of the lower and upper surfaces.

3.1. Tracking of the integration paths

Using the formulation described above, the delamination extension force, which may vary for every slice, can be evaluated everywhere within the CZ. Moreover, any point within the CZ belongs to a single slice, i.e. to a single integration path, which is defined according to the local GDD. Therefore, one can randomly select any location of the CZ and, by means of the GDD, identify the tangent to the integration pathline at that point in order to move, either forward or backward, along the integration path. The delamination extension force corresponding to such slice is obtained when the path is tracked in its entirety.

Consider a point, P^k, belonging to the CZ. In order to assess the delamination extension force at the slice which the point P^k belongs to, the numerical integration of Equation (12) is performed along the integration path, defined tangent to the local GDD direction and limited by vanishing stress conditions at both ends (c.f. Figure 3). In the general case, the initial point P^k is not located at one end of the integration path, i.e. point P^k is located in the middle of the CZ. In this case, the path will be tracked from P^k in the GDD and in the opposite direction to GDD: In the positive GDD until vanishing elastic stress is reached (point 2 in Figure 3); in the negative GDD until the intersection with the 1-valued energy-based damage isoline, where the cohesive stress also equals zero (point 1 in Figure 3).

In order to move along the integration path, the following procedure is applied. Starting from P^k, the next point along the integration path is established by moving in a straight line a ${}^*h^k$-length step further in the local GDD, which is tangent to the cohesive interface mid-surface, $\bar{S}_{coh}$, at P^k. Then, a new point, ${}^*P^{k+1}$, in the space is found. Nevertheless, ${}^*P^{k+1}$ is not necessarily placed on the

mid-surface, $\bar{S}_{coh}$. This becomes evident when $\bar{S}_{coh}$ is highly non-planar (c.f. Figure 6). Thus, the real next point constituting the integration path, P^{k+1}, is found by performing the projection of ${}^{*}P^{k+1}$ on $\bar{S}_{coh}$ in the normal x_3-direction of point P^k.

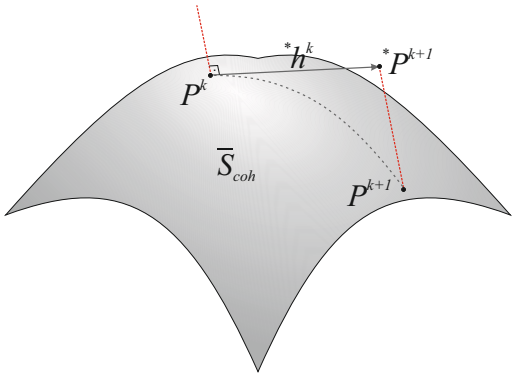

Figure 6: Point P^k is a point on the integration path of a curved cohesive interface, $\bar{S}_{coh}$. The following point on the integration path, P^{k+1}, is found by projecting point ${}^{*}P^{k+1}$ along the normal direction to the interface at point P^k. Point ${}^{*}P^{k+1}$ is at a ${}^{*}h$ distance from P^k in the tangential GDD.

3.2. FE-discretized mode-decomposed CZ J-integral

After discretization of the cohesive interface into FE, the numerical integration of Equation (12), performed by means of the trapezoidal rule, reads:

$$
\begin{aligned}
J_I &\backsimeq \sum_k \left[h^k \left(\frac{\sigma_{33}^k \frac{\partial \delta_3^k}{\partial x_1} + \sigma_{33}^{k+1} \frac{\partial \delta_3^{k+1}}{\partial x_1}}{2} \right) \right] \\
J_{II} &\backsimeq \sum_k \left[h^k \left(\frac{\sigma_{13}^k \frac{\partial \delta_1^k}{\partial x_1} + \sigma_{13}^{k+1} \frac{\partial \delta_1^{k+1}}{\partial x_1}}{2} \right) \right] \\
J_{III} &\backsimeq \sum_k \left[h^k \left(\frac{\sigma_{23}^k \frac{\partial \delta_2^k}{\partial x_1} + \sigma_{23}^{k+1} \frac{\partial \delta_2^{k+1}}{\partial x_1}}{2} \right) \right]
\end{aligned}
\tag{19}
$$

where h^k is the integration interval length, approximated to the Euclidean distance between two consecutive points along the integration path, P^k and P^{k+1}.

4. Comparison with mode-decomposed energy release rates extracted by VCCT

The capabilities of the presented CZ J-integral formulation are assessed by comparison with the energy release rate mode-components of a moment-loaded DCB model obtained by VCCT. The unidirectional composite specimen is 30 mm long, 6 mm wide and 3 mm thick (Figure 7). The elastic properties of the laminate and the fracture properties of the interface are listed in Tables 1 and 2, respectively. The specimen arms are modeled in the commercial FE code ABAQUS [39] using C3D8I hexahedral elements. The undeformed elements are 0.4 mm wide, 0.2 mm long and 0.5 mm thick. The delamination front is completely straight and located at the mid-surface at a distance of 15.1 mm from the loading application edges. A combined I, II and III fracture mode is created by application of four force couples (Figure 7). $M1$ and $M2$ generate uneven opening Y-moments at the upper and lower arms, respectively. $M3$ and $M4$ generate even tearing Z-moments at both arms. The resultant bending moments are listed in Table 3.

Laminate properties		
E_{11}: Longitudinal Young's modulus	154	GPa
$E_{22} = E_{33}$: transversal Young's modulus	8.5	GPa
$G_{12} = G_{13}$: Shear modulus in the longitudinal planes	4.2	GPa
G_{23}: Shear modulus in the transversal plane	3.0	GPa
$\mu_{12} = \mu_{13}$: Poison's coefficient in the longitudinal planes	0.35	-
μ_{23}: Poison's coefficient in the transversal plane	0.4	-

Table 1: Elastic properties of the laminate used in the simulation studies of the moment-loaded DCB and the ELS specimens.

Interface properties		
$\mathcal{G}_{Ic}$: Mode I fracture toughness	0.3	N/mm
$\mathcal{G}_{IIc} = \mathcal{G}_{IIIc}$: Modes II and III fracture toughness	3	N/mm
τ_{Ic}: Mode I interlaminar strength	10	MPa
$\tau_{IIc} = \tau_{IIIc}$: Modes II and III interlaminar strengths [11]	31.62	MPa
η: Benzeggagh-Kenane's interpolation parameter [40]	2	-
K: penalty stiffness	10^5	N/mm^3

Table 2: Fracture properties of the interface used in the simulation study of the moment-loaded DCB specimen.

In the FE analysis using the VCCT, the energy release rate is evaluated locally at every node forming the delamination front. A local crack coordinate system defines the mode-components, such

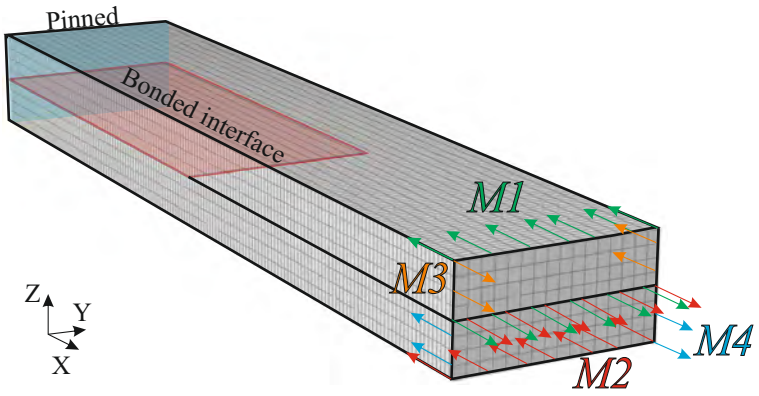

Figure 7: DCB specimen dimensions with four force couples: $M1$ and $M2$ generate uneven opening Y-moments, while $M3$ and $M4$ generate even tearing Z-moments.

Bending moment	[Nmm]
$M1$	270
$M2$	135
$M3$	960
$M4$	960

Table 3: Bending moment resultants from the application of the four force couples to the double-cantilevered-beam model.

that mode II and mode III are normal and tangential to the delamination front, respectively, and mode I is normal to mode II and III directions. For a straight front, like the one in study, the orientation of this local coordinate system is constant along the front and aligned with the mesh [41].

For the evaluation of the J-values, the interface undergoing delamination has been modeled using user-defined cohesive elements. To this end, the method presented in [10, 11] has been enhanced with the formulation for the numerical evaluation of the mode-decomposed CZ J-integral presented in Section 3. For comparison purposes with VCCT, a fixed GDD is defined normal to the straight delamination front.

The mode-decomposed energy release rate distributions along the width of the specimen, from both the VCCT and the CZ J-integral extraction methods, are plotted in Figure 8.

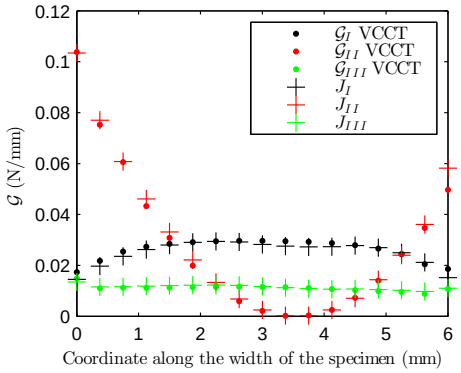

Figure 8: Comparison of the mode-components of strain energy release rate between VCCT and CZ J-integral extraction methods.

5. Application to a partially reinforced ELS specimen

In [37], an end-loaded split (ELS) test on a symmetric run-out specimen with a mid-plane initial defect was presented. The particularity of such test is that the delamination shape changes during propagation as it approaches the stiffened region made by bonded reinforcements on the upper and lower faces (c.f. Figure 9). The reinforcements do not span the entire width of the specimen in order to promote a curved delamination. Moreover, the specimen bends due to application of the end loading, resulting in a curved delamination front in a non-planar interface. Therefore, the partially reinforced ELS specimen is considered to be suitable to exemplify the applicability of the generalized CZ J-integral methodology for 3D curved and non-planar delamination fronts.

The mid-surface is modeled using user-defined cohesive elements which incorporate the formulation presented in [10, 11], enhanced with the GDD criterion presented in [37] and the CZ J-integral formulation described in Section 3. The undeformed cohesive elements are 0.27 mm wide, 0.23 mm long and have zero thickness. Only one half of the specimen is modeled exploiting X_2-symmetry to reduce the required computational resources. The elastic properties of the laminate and the fracture properties of the interface are listed in Tables 1 and 4, respectively. Note that, as a simple way to check the CZ J-integral implementation, the fracture toughness is set to be mode independent ($\mathcal{G}_c = \mathcal{G}_{Ic} = \mathcal{G}_{IIc} = \mathcal{G}_{IIIc} = 2$ N/mm), in order to ensure a constant J-value ($J = \mathcal{G}_c$) during static

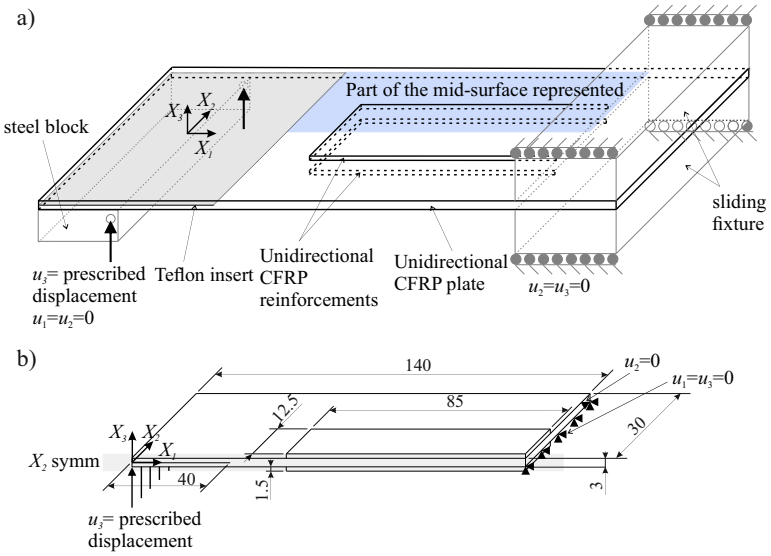

Figure 9: a) Sketch of the partially reinforced ELS specimen [37]. The grey-shadowed area represents the Teflon insert. The blue-shadowed area is the part of the mid-surface represented in figures 10, 11 and 12. b) Simplified model for FE simulation and dimensions (units in mm).

Interface properties		
$\mathcal{G}_{Ic} = \mathcal{G}_{IIc} = \mathcal{G}_{IIIc}$: Mode-independent fracture toughness	2	N/mm
$\tau_{Ic} = \tau_{IIc} = \tau_{IIIc}$: Mode-independent interlaminar strength	35	MPa
K: penalty stiffness	10^5	N/mm^3

Table 4: Fracture properties of the interface used in the simulation study of the ELS specimen.

crack propagation. Thus, the sum of the three mode-decomposed CZ J-integrals in Equation (19) must be constant and equal to 2 N/mm at every slice, regardless of the loading mode. In the following figures, only the blue-shadowed area of the mid-surface in Figure 9 is represented.

The historical evolution of the 0.5-valued energy-based damage isoline is plotted in Figure 10.a. The energy-based damage, $\mathcal{D}^e$, distribution is projected on the deformed mid-surface, in Figure 10.c, for a prescribed end displacement of 27.7 mm. The GDD distribution within the CZ is represented in Figure 11. As mentioned in Section 3.1, the CZ J-integral can be evaluated at any point within the CZ and, therefore, infinite integration paths can be tracked. For illustrative purposes, only a few selected integration paths are plotted on top of the GDD distribution. Note that the trajectory of the

integration paths is established according to the GDD. Thus, since the $\frac{\omega_{tot}}{\mathcal{G}_c}$ isolines are not parallel, the integration paths are curved lines throughout the CZ.

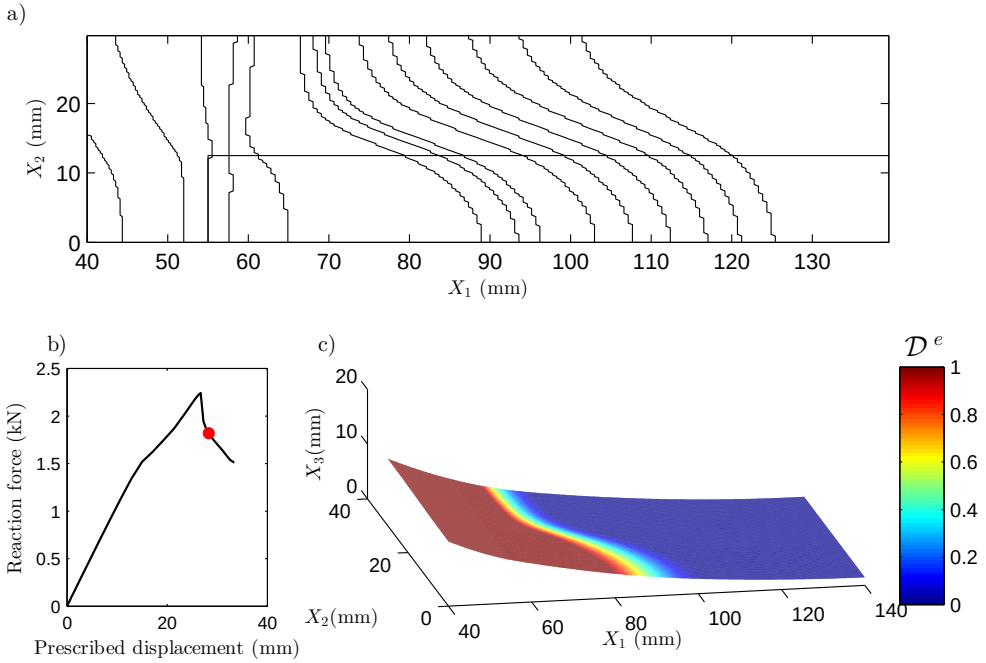

Figure 10: a) Historical evolution of the 0.5-valued energy-based damage isoline extracted at the integration points. b) Reaction force vs prescribed displacement curve with the current loading state highlighted in red. c) Energy-damage projected on the deformed mid-surface at the current loading stated marked in (b).

The total J-value is evaluated at each of the 30,000 integration points forming the CZ. The result is represented in Figure 12.a. The step length ${}^*h^k$ used is 0.3 mm. Note that the J-distribution is constant and equal to the fracture toughness, which, during static propagation and for any mode mixity, amounts 2 N/mm. The decomposition of the CZ J-integral into modes, computed according to Equation (19), is also represented in Figure 12.

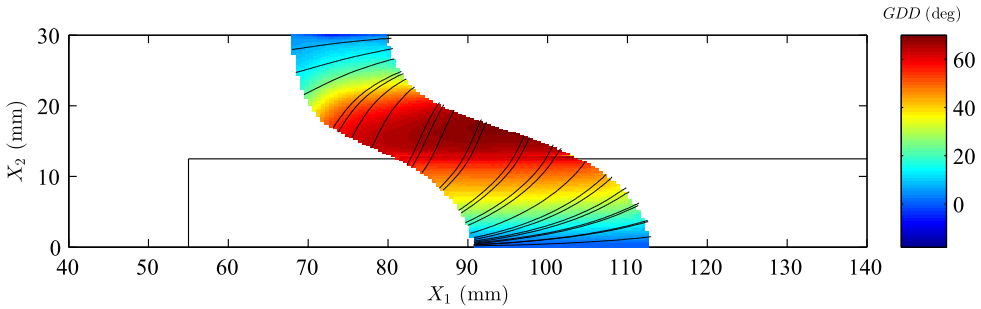

Figure 11: Growth driving direction (GDD) distribution along the cohesive zone and a few selected integration paths (black solid lines) plotted on top of it.The current loading state is marked in Figure 10.b.

(a)

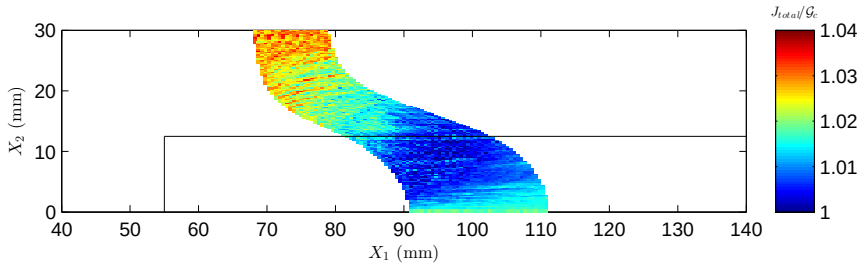

(b)

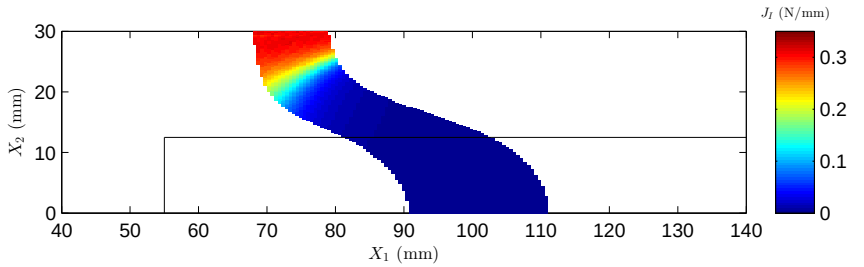

(c)

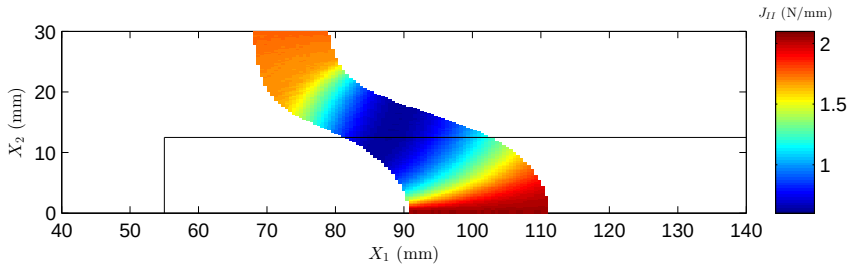

(d)

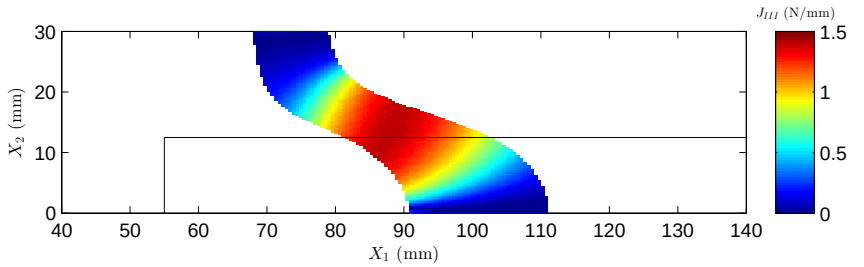

Figure 12: Distribution of a) $J_{total}/\mathcal{G}_c$ (where $J_{total} = J_I + J_{II} + J_{III}$ and $\mathcal{G}_c$=2 N/mm), b) J_I , c) J_{II} and d) J_{III} within the cohesive zone at current loading state marked in Figure 10.b.

6. Discussion

A comparison of the mode-components of the CZ J-integral with the energy release rates extracted from VCCT is done in Section 4. To make both decomposition schemes comparable, the GDD, which dictates the mode II direction in the CZ J-integral formulation, is forced normal to the initial crack front. Although both results are in good agreement (c.f. Figure 8), there are small differences which are caused by a slight difference in compliance between the two models. When using cohesive elements to simulate the delamination fracture behavior, some separation between crack faces occur before complete decohesion. This is not the case of the VCCT, where no relative displacements between crack faces occur until the condition for crack propagation ($\mathcal{G} \geq \mathcal{G}_c$) is fulfilled. The difference in compliance between the two models has an influence on the computed energy release rate. Another source of discrepancy is the nonlinearity introduced by the cohesive behavior. Using the CZM approach, the stiffness of the interface is reduced as it gets damaged. Conversely to VCCT, the existence of a damage process zone implies that the behavior of the material ahead of the crack front is nonlinear.

Furthermore, the standard formulations for VCCT require to have orthogonality of the mesh with the delamination front in order to obtain accurate energy release rate components [42]. Therefore, its application to three-dimensional FE models requires the option of moving meshes that conform according to the delamination front, which is not available in commercial finite element codes [43]. Alternative solutions that enable the use of stationary meshes are presented in [44, 45]. The basic assumption of these formulations is that the nodes at the delamination front will propagate along a normal vector to the current front. However, when the delamination originates from an artificial initial defect, e.g. caused by a Teflon insert, or when the loading conditions change, there is a transient stage during which the shape of the crack front changes according to the current propagation conditions. The formulation for the evaluation of the GDD does not depend on the geometry of the crack front (which is historical information), but on the current displacement field. Further details are given in [37]. Thus, any variation in the displacements due to a change in the loading scenario is captured by the GDD criterion at the current time. Therefore, the mode-decomposition scheme according to the

GDD can be applied during transient propagation.

In Section 5, the presented mode-decomposed CZ J-integral formulation is applied to a real three-dimensional structure with a large fracture process zone (the maximum length of the CZ is approximately 20 mm). Due to the ELS test configuration, the structure is subjected to large deflections. Moreover, it is partially reinforced so that the stiffness along the specimen width is not constant. As a consequence, during propagation, both the delaminated surfaces and the CZ are curved. Due to a change in the GDD orientation across the CZ, the integration paths result in curved lines. The same $\mathcal{G}_{Ic}$, $\mathcal{G}_{IIc}$ and $\mathcal{G}_{IIIc}$ have been introduced as inputs to the CZM (see Table 4) in order to make the equivalent one-dimensional fracture toughness independent on the mode mixity. In this way, under static propagation conditions, the accurate computation of the total J-value can be easily assessed by direct comparison with a constant mode-independent fracture toughness. The total computed J-value is equal to the fracture toughness at all the integration points within the cohesive zone with a maximum error of 3.7% (c.f. Figure 12.a). The integration step, ${}^{*}h^{k}$, used in the computation of the J-value is 1.3 times the shortest element length. By reducing ${}^{*}h^{k}$, more accurate results may be obtained. However, for such a large CZ, the computational cost increases significantly with the number of segments in which the integration paths are discretized.

Moreover, the mode-decomposition of the CZ J-integral accounting for large CZ is also addressed. The mode II and III components of the CZ J-integral are predominant, while mode I slightly appears at a small region close to the specimen's edge (c.f. Figure 12.b). The contribution to the J-value of the tangent quantities to the mid-surface is decomposed into modes II and III according to the GDD. The bonded reinforcements cause the loading state to be uneven throughout the specimen's width, leading to a curved crack, so that the GDD amounts up to 60° with respect to the X_1 at the zones with highest delamination front curvature. Due to the test configuration, the loading is applied in the global X_1 direction. For straight cracks where the GDD is aligned with the X_1-direction, the shear component would be pure mode II. However, in the studied case with a curved delamination front, the maximum contribution of the external loading to the mode III CZ J-integral is at that zone were the

GDD differs most from the X_1-direction (c.f. Figures 12.c and 12.d).

7. Conclusions

A novel methodology for the calculation of the mode-decomposed J-integral in three-dimensional delamination simulation using a cohesive zone model approach is presented. The methodology incorporates the growth driving direction criterion, recently developed by the authors, to track the integration paths and determine the local directions of mode I, II and III components. The generality of the formulation makes it applicable to curved fronts with non-planar delamination interfaces and large fracture process zones. The application of the described methodology results in curved integration paths.

The calculation of the J-integral is based on dividing the delamination interface into elemental thickness slices, so that the J-value of each slice is unique. The definition of the curvature of such slices is done according to the growth driving direction. Since the growth driving direction is mesh independent, the definition of the slices is not affected by the mesh size.

By application of the presented formulation, a global measure of the energy release rate in three-dimensional structures modeled using a cohesive zone model approach can be obtained. To the authors knowledge, this has not been previously addressed. Also, the energy release rate can be decomposed into mode I, II and III components. The decomposition of the shear component of the energy release rate into mode II and III, to date, has only been addressed under the assumption of elastic fracture mechanics. In addition, the new formulation enables to obtain a global measure of the mode mixity, overcoming the limitation of the current 3D cohesive zone model formulations, where the mode mixity is only obtained at integration point level in terms of opening displacements.

Besides the immediate applications of the formulation as just described, it is of the authors belief that more applications will be uncovered in future research. The presented CZ J-integral is a decisive contribution on using fracture mechanics-based procedures in a cohesive zone model framework, which will allow the design of lighter and more reliable structures. In addition, a direct application of the CZ

J-integral formulation is its implementation in combination with existing fatigue simulation methods formulated in a CZM approach, which rely on mode-dependent Paris law' like expressions. Thus, the developed mode-decomposed CZ J-integral formulation becomes a new solution for extracting mode-decomposed energy release rates of real complex three-dimensional structures.

8. Acknowledgements

This work has been partially funded by the Spanish Government (Ministerio de Economia y Competitividad) under contract TRA2015-71491-R, cofinanced by the European Social Fund.

References

[1] D. Dugdale, Yielding of Steel Sheets Containing Slits, Journal of the Mechanics and Physics of Solids 8 (2) (1960) 100–104. doi:10.1016/0022-5096(60)90013-2.

[2] G. Barenblatt, The Mathematical Theory of Equilibrium Cracks in Brittle Fracture, Advances in Applied Mechanics 7 (1962) 55–129. doi:10.1016/S0065-2156(08)70121-2.

[3] A. A. Griffith, The Phenomena of Rupture and Flow in Solids, Philosophical Transactions of the Royal Society A: Mathematical, Physical and Engineering Sciences 221 (1921) 582–593.

[4] R. Krueger, Virtual Crack Closure Technique: History, Approach and Applications, Applied Mechanics Reviews 57 (2004) 109–143.

[5] J. Rice, A Path Independent Integral and the Approximate Analysis of Strain Concentration by Notches and Cracks, Journal of Applied Mechanics 35 (1968) 379–386.

[6] M. Ortiz, A. Pandolfi, Finite-Deformation Irreversible Cohesive Elements for Three-Dimensional Crack-Propagation Analysis, International Journal for Numerical Methods in EngineeringI 44 (1999) 1267–1282.

[7] G. Alfano, M. A. Crisÿeld, Finite element interface models for the delamination analysis of laminated composites: mechanical and computational issues, International Journal for Numerical Methods in Engineering 50 (2001) 1701–1736.

[8] P. P. Camanho, C. Davila, M. de Moura, Numerical simulation of mixed-mode progressive delamination in composite materials, Journal of Composite Materials 37 (16) (2003) 1415–1438.

[9] V. K. Goyal, E. R. Johnson, G. D. Carlos, Irreversible constitutive law for modeling the delamination process using interfacial surface discontinuities, Composite Structures 65 (2004) 289–305.

[10] A. Turon, P. P. Camanho, J. Costa, C. G. Dávila, A Damage Model for the Simulation of Delamination in Advanced Composites Under Variable-Mode Loading, Mechanics of Materials 38 (2006) 1072–1089.

[11] A. Turon, P. P. Camanho, J. Costa, J. Renart, Accurate Simulation of Delamination Growth Under Mixed-Mode Loading Using Cohesive Elements: Definition of Interlaminar Strengths and Elastic Stiffness, Composite Structures 92 (8) (2010) 1857–1864.

[12] E. Lindgaard, B. Bak, J. Glud, J. Sjølund, E. Christensen, A user programmed cohesive zone finite element for ANSYS Mechanical, Engineering Fracture Mechanics 180 (2017) 229–239.

[13] B. L. V. Bak, C. Sarrado, A. Turon, J. Costa, Delamination Under Fatigue Loads in Composite Laminates: A Review on the Observed Phenomenology and Computational Methods, Applied Mechanics Reviews 66 (6) (2014) 1–24.

[14] A. Turon, J. Costa, P. Camanho, C. Dávila, A Simulation Method for High-Cycle Fatigue-Driven Delamination Using a Cohesive Zone Model, International Journal for Numerical Methods in Engineering 106 (2007) 163–191.

[15] A. Pirondi, F. Moroni, A Progressive Damage Model for the Prediction of Fatigue Crack Growth in Bonded Joints, The Journal of Adhesion 86 (5-6) (2010) 501–521.

[16] L. Kawashita, S. Hallett, A Crack Tip Tracking Algorithm for Cohesive Interface Element Analysis of Fatigue Delamination Propagation in Composite Materials, International Journal of Solids and Structures 49 (21) (2012) 2898–2913.

[17] B. L. V. Bak, A. Turon, E. Lindgaard, E. Lund, A Simulation Method for High-Cycle Fatigue-Driven Delamination Using a Cohesive Zone Model, International Journal for Numerical Methods in Engineering 106 (2016) 163–191.

[18] B. L. V. Bak, A. Turon, E. Lindgaard, E. Lund, A Benchmark Study of Simulation Methods for High-Cycle Fatigue-Driven Delamination Based on Cohesive Zone Models, Composite structures 164 (2017) 198–206.

[19] P. C. Paris, A Rational Analytic Theory of Fatigue, The Trend in Engineering 13 (1961) 9–14.

[20] J. Pascoe, R. Alderliesten, R. Benedictus, Methods for the prediction of fatigue delamination growth in composites and adhesive bonds - A critical review, Engineering Fracture Mechanics 112-113 (2013) 72–96.

[21] J. Eshelby, The Elastic Energy-Momentum Tensor, Journal of Elasticity 5 (1975) 321–335.

[22] M. Amestoy, H. Bui, R. Labbens, On the Definition of Local Path Independent Integrals in Three-Dimensional Crack Problems, Mechanic Research Communications 8 (4) (1981) 231–236.

[23] H. deLorenzi, On the Energy Release Rate and the J-Integral for 3-D Crack Configurations, International Journal of Fracture 19 (1982) 183–193.

[24] T. Murakami, T. Sato, Three-Dimensional J-Integral Calculations of Part-Through Surface Crack Problems, Computers ans Structures 17 (5-6) (1983) 731–736.

[25] F. Li, C. Shih, A. Needleman, A Comparison of Methods for Calculating Energy Release Rates, Engineering Fracture Mechanics 21 (2) (1985) 405–421.

[26] C. Shih, B. Moran, T. Nakamura, Energy Release Rate Along a Three-Dimensional Crack Front in a Thermally Stressed Body, International Journal of Fracture 30 (1986) 79–102.

[27] O. Huber, J. Nickel, G. Kuhn, On the Decomposition of the J-Integral for 3D Crack Problems, International Journal of Fracture 64 (1993) 339–348.

[28] M. Chiarelli, A. Frediani, A Computation of the Three-Dimensional J-Integral for Elastic Materials with a View to Applications in Fracture Mechanics, Engineering Fracture Mechanics 44 (5) (1993) 763–788.

[29] R. Rigby, M. Aliabadi, Mixed-Mode J-Integral Method for Analysis of 3D Fracture Problems using BEM, Engineering Analysis with Boundary Elements 11 (1993) 239–256.

[30] R. Rigby, M. Aliabadi, Decomposition of the Mixed-Mode J-Integral - Revisited, International Journal of Solid Structures 35 (17) (1998) 2073–2099.

[31] M. Gosz, J. Doldow, B. Moran, Domain Integral Formulation for Stress Intensity Factor Computation along Curved Three-Dimensional Interface Cracks, International Journal of Solid Structures 35 (15) (1998) 1763–1783.

[32] F. Li, C. Shih, A. Needleman, On the Path Independence of the Point-Wise J Integral in Three Dimensions, International Journal of Fracture 136 (2005) 1–36.

[33] K. Eriksson, A Domain Independent Integral Expression for the Crack Extension Force of a Curved Crack in Three Dimensions, Journal of the Mechanics and Physics of Solids 50 (2002) 381–403.

[34] G. Fernlund, D. McCammond, J. Spelt, A Curvilinear Formulation of the 3-D J integral: Application to Delamination Cracking of Curved Laminates, Composite Structures 28 (1994) 123–130.

[35] G. Irwin, Analysis of Stress and Strains Near the End of a Crack Transversing a Plate, Journal of Applied Mechanics 24 (1957) 361–364.

[36] A. Turon, B. Bak, E. Lindgaard, C. Sarrado, E. Lund, Interface elements for fatigue-driven delaminations in advanced composite materials, in: Numerical Modelling of Failure in Advanced Composite Materials, Woodhead Publishing Series in Composites Science and Engineering, 2015, pp. 73–91.

[37] L. Carreras, B. Bak, A. Turon, J. Renart, E. Lindgaard, Point-Wise Evaluation of the Growth Driving Direction for Arbitrarily Shaped Delamination Fronts Using Cohesive Elements, Submitted for Review.

[38] K. Eriksson, Decomposition of Eshelby's Energy Momentum Tensor and Application to Path and Domain Independent Integrals for the Crack Extension Force of a Plane Circular Crack in Mode III Loading, International Journal of Fracture 144 (2007) 215–225.

[39] D. Systémes, Abaqus manual 6.12.

[40] M. L. Benzeggagh, M. Kenane, Measurement of Mixed-Mode Delamination Fracture Toughness of Unidirectional Glass/Epoxy Composites with Mixed-Mode Bending Apparatus, Composite Science and Technology 56 (1996) 439–449.

[41] R. Krueger, Influence of Finite Element Software on Energy Release Rates Computed Using the Virtual Crack Closure Technique, NIA Report No. 2006-06, NASA/CR-214523,.

[42] S. Smith, I. Raju, Evaluation of Stress-Intensity Factors Using General Finite-Element Models, Fatigue and Fracture Mechanics. ASTM STP 1321. American Society for Testing and Materials 29 (1998).

[43] R. Krueger, The virtual crack closure technique for modeling interlaminar failure and delamination in advanced composite materials, in: Numerical Modeling of Failure in Advanced Composite Materials, Woodhead Publishing Series in Composites Science and Engineering, 2015, pp. 3–53.

[44] D. Xie, S. B. Biggers Jr, Strain Energy Release Rate Calculation for a Moving Delamination Front of Arbitrary Shape Based on the Virtual Crack Closure Technique. Part I : Formulation and Validation, Engineering Fracture Mechanics 73 (2006) 771–785.

[45] Y.-P. Liu, C.-Y. Chen, G.-Q. Li, A Modified Zigzag Approach to Approximate Moving Crack Front with Arbitrary Shape, Engineering Fracture Mechanics 78 (2) (2011) 234–251.

PAPER C

C

PAPER C

An efficient methodology for the experimental characterization of mode II delamination growth under fatigue loading

L. Carreras [a], J. Renart [a], A. Turon [a], J. Costa [a], Y. Essa [b], F. Martin de la Escalera [b]

[a] AMADE, Mechanical Engineering and Industrial Construction Department, Universitat de Girona, Carrer Universitat de Girona 4, 17003 Girona, Spain

[b] AERNNOVA Engineering Division SAU, Parque Tecnológico de Álava, Leonardo Da Vinci 13, E-01510 Álava, Spain

The paper has been published in *International Journal of Fatigue* Vol. 95 (2017) 185-193.

International Journal of Fatigue 95 (2017) 185–193

Contents lists available at ScienceDirect

International Journal of Fatigue

journal homepage: www.elsevier.com/locate/ijfatigue

An efficient methodology for the experimental characterization of mode II delamination growth under fatigue loading

L. Carreras [a,*], J. Renart [a], A. Turon [a], J. Costa [a], Y. Essa [b], F. Martin de la Escalera [b]

[a] AMADE, Polytechnic School, University of Girona, Campus Montilivi s/n, E-17003 Girona, Spain
[b] AERNNOVA Engineering Division SAU, Parque Tecnológico de Álava, Leonardo Da Vinci 13, E-01510 Álava, Spain

ARTICLE INFO

Article history:
Received 16 August 2016
Received in revised form 13 October 2016
Accepted 17 October 2016
Available online 18 October 2016

Keywords:
Mode II
Delamination
Testing method
Fatigue
3-ENF
Composites

ABSTRACT

Crack growth rate curves provide information about the delamination resistance of composite materials under cyclic loading. The existing methodologies for mode II fatigue testing using three-point bending end-notched flexure (3-ENF) under constant cyclic displacement conditions yield discontinuous delamination growth rate curves, therefore requiring a batch of several specimens to be tested under different severity conditions in order to fully characterize the crack growth. This work describes a variable cyclic displacement test procedure that, in combination with the real time monitoring of the specimen's compliance, allows the crack growth rate to be measured for the desired range of severities with a single specimen, thus avoiding any human intervention during the test.

1. Introduction

Emerging delaminations and their growth under repeated or cyclic loads can reduce the load carrying capacity of composite structures. In consequence, a reliable design should account for this damage mechanism. The experimental characterization of interlaminar fracture properties under fatigue loading assesses the damage tolerance of the composite materials in service.

The no-growth criterion and the damage tolerance approach are two alternatives to deal with interlaminar fatigue damage in aircraft design [1]. The first aims to ensure that no crack propagation will ever occur over the lifetime of the component. This approach relies on fatigue onset tests [2] which, for a given load intensity, determine the number of cycles required to make a crack grow perceptibly. Conversely, the damage tolerance approach is based on a structure's remaining capacity to safely sustain in-service loads, even with the presence of sub-critical sized delaminations. That is, crack growth is allowed provided that it does not reach an unsafe size during service. To this end, crack propagation tests evaluate the crack growth rate (da/dN) as a function of the severity of load. The severity of load is usually defined as the ratio of the maximum energy release rate of the cycle ($\mathcal{G}_{max}$) to the quasi-static fracture toughness $\mathcal{G}_c$ [3–7], although other expressions also exist in the literature.

The onset and propagation of interlaminar cracks are experimentally characterized for the different loading modes of propagation (I, II or III). Delamination growth under mode I loading is usually assessed with double cantilever beam (DCB) specimens, while for mode II the End Notched Flexure (3-ENF) test performed under displacement control with sinusoidal shaped loading cycles of constant displacement is the most widely employed (see Fig. 1a) [3,4,8–11]. Other mode II test set-ups include the calibrated end-loaded split (C-ELS) [12] and the four-point bending end-notched flexure (4-ENF). Either the C-ELS [10] and the 4-ENF [13] have been used for delamination resistance testing under fatigue. However, while the 4-ENF test is not preferable because of friction effects [14], only further research will show whether 3-ENF or C-ELS is better suited for cyclic mode II fatigue delamination characterization [10].

The selection of the testing parameters for mode I fatigue experiments is not critical. For a test conducted under displacement control and constant displacement amplitude, the energy release rate (the severity of the load) decreases as the crack grows. That is, the crack growth rate vs. load severity curve sweeps from left to right until the crack growth rate becomes unnoticeable (the threshold, the severity for which the crack growth rate tends to zero). Nevertheless, even in mode I, the determination of the threshold value

* Corresponding author.
E-mail addresses: laura.carreras@udg.edu (L. Carreras), jordi.renart@udg.edu (J. Renart), albert.turon@udg.edu (A. Turon), josep.costa@udg.edu (J. Costa), yasser.essa@aernnova.com (Y. Essa), federico.martindelaescalera@aernnova.com (F. Martin de la Escalera).

http://dx.doi.org/10.1016/j.ijfatigue.2016.10.017
0142-1123/

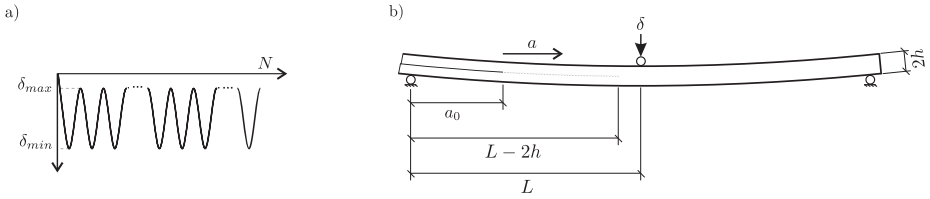

Fig. 1. (a) Sinusoidal shaped loading cycles with constant displacement. The sign convention used in this work is negative for displacements which result in compressive reaction forces. (b) 3-ENF test configuration, where L is the mid-span length, a is the crack length, a_0 is the initial crack length and $2h$ is the specimen's total thickness of the specimen.

remains elusive due to the need of high sensitivity measurement devices to capture the actual growth rates [15].

For mode II 3-ENF experiments the contrary applies as the range of the crack growth rate curve swept in a single test under constant cyclic displacement is very narrow. This results from the dependence of the energy release rate on the geometry of the specimen and the configuration of the test. Indeed, in 3-ENF tests the region available for crack propagation spans between the support and the vicinity of the loading roller, where the through-thickness compression arrests crack propagation. Previous studies [16] estimate that when the crack tip approaches the loading point by $2h$ the experiment is no longer valid; being $2h$ the laminate thickness (see Fig. 1b). The energy release rate does not evolve monotonically with the crack extension but, as the cracks extends, it increases and then decreases, as shown in Fig. 2a. Thus, only a small segment of the crack growth curve is covered by a single test. In fact, the same segment of the curve is tracked twice: first upward and then downward (Fig. 2b). In addition, detecting the threshold becomes practically unfeasible. Hence, to construct the entire crack growth curve requires various constant cyclic displacement tests at different load intensities [3,8–10]. The alternative to performing multiple tests is to implement a test with a proper variation of the displacement, which is what this manuscript focuses on.

Preceding the methodology presented in this work, only Tanaka and Tanaka [17], Matsubara et al. [18] and Hojo et al. [19,20] carried out 3-ENF fatigue tests with fiber reinforced polymer specimens by decreasing the applied peak load as the crack propagates. In [17] the authors conducted fatigue tests under either a constant or decreasing stress intensity range, ΔK, to graphite/epoxy composite specimens. The same data on crack growth rate, da/dN, with crack extension was obtained in the ΔK-constant tests. Tanaka and Tanaka determined that fiber bridging had no influence on Mode II crack propagation and concluded that crack growth is independent of crack extension history. Matsubara et al. [18] used a decreasing-load test procedure based on the ASTM standard for metals [21]. This methodology enables the crack growth rate for a broader range of the load intensity factor to be determined and also to approach the low-rate region, near the threshold, by decreasing the applied load. The load shedding can be done manually at selected crack size intervals or, alternatively, by continuously reducing the force to adjust the normalized K-gradient, $(1/K)\,dK/da$, to a fixed value. They conducted constant- and decreasing- load tests with glass fiber reinforced polymer specimens and obtained identical results, confirming that crack growth rate is independent of crack extension history. Similarly, Hojo et al. [19,20] carried out fatigue tests under constant normalized gradient of energy release rate, $(1/\mathcal{G})d\mathcal{G}/da$, by measuring the specimen's compliance and decreasing the peak load accordingly.

In practice, incrementally shedding the force with increasing crack size requires the continuous intervention of a technician. On the other hand, computer-controlled stress intensity or,

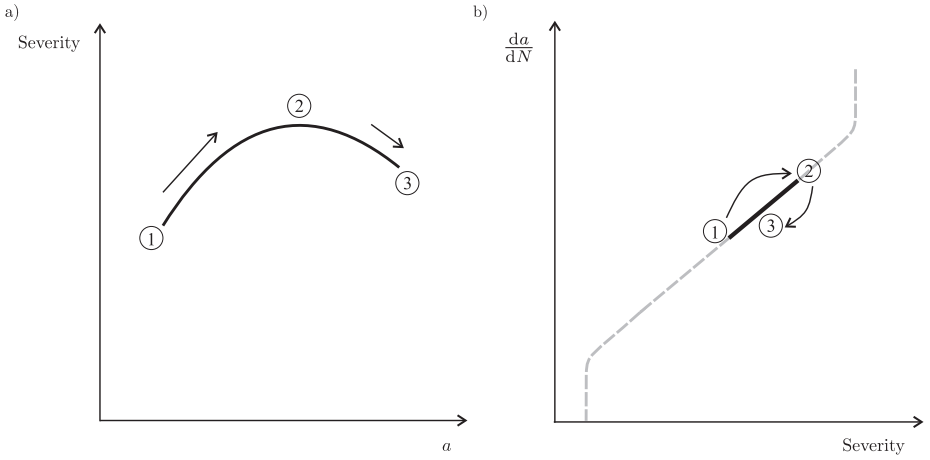

Fig. 2. (a) Maximum energy release rate applied to the 3-ENF test as a function of the crack length. (b) Crack growth rate curve segment analyzed in a single test with constant cyclic displacement.

equivalently, energy release rate gradient techniques [22,23], require the crack length to be monitored in real-time, usually by means of the specimen's compliance. Indeed, the use of the compliance to control the machine, or any other behavioral-based control technology, can lead to unexpected load setpoints.

This work presents a methodology to measure, in a single test, a larger region of the crack growth rate curve than that achieved in a constant cyclic displacement test. The procedure consists of varying the cyclic applied displacement, δ_{min} and δ_{max}, while keeping the displacement ratio, R, constant. Moreover, the displacement variation is calculated a priori, so that it can be implemented in the control software of the testing machine. Thus, the control loop does not make use of parameters related to the behavior of the specimen, which could lead to unpredictable responses from the test machine. This method requires neither human intervention during the test nor processing the data in real time. The manuscript includes a test campaign carried out on carbon fiber reinforced composites which exemplifies the advantages of the proposed procedure: the crack growth rate curve can be characterized in, at most, 1/80 of the time required for a constant cyclic displacement test.

2. Methodology

Due to the geometry of the test, the maximum energy release rate during one load cycle, $\mathcal{G}_{max}$, corresponds to the minimum displacement, δ_{min}. The aim of the proposed methodology is to define the evolution of δ_{min} with the number of cycles, N, so that the severity of the load sweeps a predefined range, from $\mathcal{G}_{max,0}/\mathcal{G}_c$ to $\mathcal{G}_{max,f}/\mathcal{G}_c$, while the crack grows from the initial crack, a_0, to the maximum allowed crack length, a_f, (when the crack tip approaches a distance $2h$ from the load introduction point). δ_{max} is established so that the R-ratio is constant throughout the fatigue test ($R = \delta_{min}/\delta_{max}$, for small deflections). The following paragraphs describe how the function $\delta_{min}(N)$ has been deduced.

The function $\delta_{min}(N)$ depends on the chosen dependence between the severity of the load, $\mathcal{G}_{max}$ normalized to $\mathcal{G}_c$, and the crack length. We have chosen a linear decreasing dependence, from the normalized $\mathcal{G}_{max,0}$ at a_0 to $\mathcal{G}_{max,f}$ at a_f, the end of the test (Fig. 3); however, other alternative monotonic dependence could be selected. Therefore, the gradient of the energy release rate, $d\mathcal{G}_{max}/da$, is constant and negative. Thus, the load severity vs. the crack length, a, reads:

$$\frac{\mathcal{G}_{max}}{\mathcal{G}_c}(a) = m_{\mathcal{G}}\, a + n, \tag{1}$$

where $m_{\mathcal{G}}$ and n are the slope and the y-intercept, respectively:

$$m_{\mathcal{G}} = \frac{\mathcal{G}_{max,f} - \mathcal{G}_{max,0}}{\mathcal{G}_c(a_f - a_0)}, \tag{2}$$

$$n = \frac{\mathcal{G}_{max,0}}{\mathcal{G}_c} - m_{\mathcal{G}}\, a_0, \tag{3}$$

Assuming a linear elastic behavior of the specimen, the energy release rate reads [24]:

$$\mathcal{G} = \frac{P^2}{2B}\frac{dC}{da}, \tag{4}$$

thus, the minimum cyclic displacement (δ_{min}) is related to $\mathcal{G}_{max}$ by:

$$\delta_{min} = -\sqrt{\frac{2B\mathcal{G}_{max}C^2}{dC/da}}, \tag{5}$$

where B is the width of the specimen and C is the specimen's compliance (δ/P, where P is the load). The compliance of the specimen increases as the crack length grows. The dependence $C(a)$ is experimentally determined by a series of static tests at different crack lengths (compliance calibration) [19,25]:

$$C(a) = m_{cc}a^3 + C_0, \tag{6}$$

where m_{cc} and C_0 are fitting parameters.

Eqs. (1)–(6) can be used to write the dependence of (δ_{min}) with the specimen compliance measured in real time:

$$\delta_{min}(C) = -\sqrt{\frac{2B\mathcal{G}_c\left[m_{\mathcal{G}}\left(\frac{C-C_0}{m_{cc}}\right)^{1/3} + n\right]}{3m_{cc}\left(\frac{C-C_0}{m_{cc}}\right)^{2/3}}}, \tag{7}$$

Following this equation, the load severity would sweep the desired range (Fig. 3). The compliance can be easily measured in real time with current computerized testing systems, [11]. However, the control of the displacement based on the measurement of the compliance and Eq. (7) is problematic because of the inherent scatter of the experimental measurement, C, and the lack of data at the initiation of the test. It is thus preferable to base the control of the test on a certainly well-behaved variable, as the number of cycles, N, is.

To deduce the $\delta_{min}(N)$ function, a relation between the crack length (or, equivalently, the compliance, Eq. (6)) and the number of cycles is necessary. Here, we assume that the crack growth rate follows the Paris' law based expression [26]:

$$\frac{da}{dN} = A\left(\frac{\mathcal{G}_{max}}{\mathcal{G}_c}\right)^p, \tag{8}$$

Although the simplest expression of the Paris like power law has been used to relate crack growth to the energy release rate, it is worth noting that the methodology described here can also be used with other fatigue data representations based on the existing formulation for metals, such as the NASGRO equation [27] or its adaptation for composite materials [28].

The pre-exponential factor, A, and the exponent, p, in Eq. (8) are not yet known (in fact, the ultimate objective of the experimental characterization is to find them). Therefore, the parameters A, and p, should be estimated before the test. The consequence of making use of erroneous parameters is that the load severity range explored would not be the one expected (Fig. 3). In any case, a

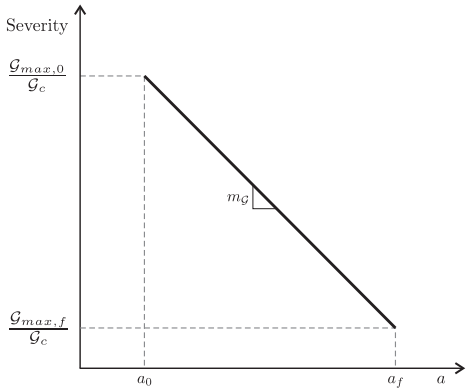

Fig. 3. Chosen relation between the maximum cyclic energy release rate, $\mathcal{G}_{max}$, normalized to the quasi-static fracture toughness, $\mathcal{G}_c$, and the crack length. $\mathcal{G}_{max,0}$ and a_0 are the initial energy release rate and crack length, while $\mathcal{G}_{max,f}$ and a_f are the energy release rate and crack length at the end of the test.

reasonable assumption would allow a much larger domain, with respect to the one achieved by means of a constant cyclic displacement experiment, to be explored. Parameters A and p can be taken from specimens of similar fiber and reinforcement or from preliminary experiments performed at constant displacement over the system studied.

The estimated A and p parameters are used to find the expression that relates the crack length to the number of cycles, by integrating Eq. (8):

$$a(N) = \frac{(\alpha\, N + \beta)^{\gamma} - n}{m_{\mathcal{G}}}, \tag{9}$$

where

$$\alpha = A m_{\mathcal{G}} (1 - p), \tag{10}$$

$$\beta = (m_{\mathcal{G}} a_0 + n)^{1-p}, \tag{11}$$

and

$$\gamma = \frac{1}{1-p}. \tag{12}$$

Finally, by substituting Eqs. (1), (9) and (6) and its derivative, into Eq. (5), the functions of the minimum cyclic displacement with the number of cycles reads:

$$\delta_{min}(N) = -\sqrt{\frac{2B\mathcal{G}_c(\alpha N + \beta)^{\gamma}\left(m_{cc}\left(\frac{(\alpha N+\beta)^{\gamma}-n}{m_{\mathcal{G}}}\right)^3 + C_0\right)^2}{3\; m_{cc}\left(\frac{(\alpha N+\beta)^{\gamma}-n}{m_{\mathcal{G}}}\right)^2}}. \tag{13}$$

Hence, the minimum cyclic displacement is a function of the number of cycles (N), the specimen width (B), the initial conditions ($a_0, \mathcal{G}_{max,0}/\mathcal{G}_c$), the user-defined gradient of energy release rate ($m_{\mathcal{G}}$), the static compliance calibration parameters obtained prior to the fatigue test (m_{cc}, C_0) and, finally, the Paris' law parameters (A, p). In all events, $\delta_{min}(N)$ is calculated previous to the fatigue test, so that the displacement can be automatically shed in a continuous manner by implementing Eq. (13) in the control software of the testing machine.

In this work it is assumed that the fatigue delamination growth, under pure mode II loading conditions, depends only on the peak energy release rate, $\mathcal{G}_{max}$, and the load ratio (equivalent to the minimum to maximum cyclic displacement ratio, $R = \delta_{min}/\delta_{max}$, for small deflections). That is, it is assumed that the crack growth rate is neither history dependent nor dependent on the crack length, which is in agreement with other experimental evidence obtained from $\mathcal{G}_{max}$-constant tests with carbon/epoxy composites [4,17,19].

3. Experimental

The validity of the test method to characterize mode II delamination growth was evaluated by comparing the crack growth rate curves obtained in variable (described in the previous section) and constant cyclic displacement tests. As the range of crack growth was very narrow in the latter case, a multiplicity of constant cyclic displacement tests were performed. The Paris' law parameters were determined by both methods. In addition, this exemplification allowed for a detailed comparison to be made of the effort saved by following the new experimental methodology proposed in this paper.

The laminates were 16 unidirectional carbon fiber/epoxy prepreg plies of 0.184 mm of nominal thickness stacked with the same fiber orientation [0°]. Panels were cured in an autoclave, following the supplier's recommendations, at AERNNOVA Engineering facilities. Before cutting the specimens, the panels were ultrasonically C-scanned. 3-ENF test specimens cut from these laminates were 25 mm wide, 3 mm thick and 200 mm long. A 30 μm thick and 60 mm length Teflon insert was introduced in the mid plane to create an artificial delamination. This Teflon film was thicker than that usually recommended for static testing [29]; however, precracking was expected to avoid any possible negative effect resulting from the insert [30,31]. Precracks were performed under mode I quasi-static loading conditions until the increment in crack length was between 3 mm and 5 mm. The Teflon film was removed from the crack after the precracking procedure.

All the tests were carried out in a servohydraulic MTS Bionix® testing machine (25 kN of load capacity) under displacement control. The total force carried by the test specimen was measured with a 5 kN MTS load cell. The three-point bending rig used to perform the tests met the specifications described in the ASTM standard for static testing [29]. The support rollers were 5 mm in radius, each with a span length between them of 100 mm. Some tests under constant cyclic displacement conditions were performed with a span length between supports of 120 mm (longer than the standard), to enlarge the range for crack extension (see Table 1). Tests were performed at the mechanical testing laboratory of the University of Girona, which is Nadcap [32] (Non-metallic materials testing laboratory) and ISO17025 [33] accredited.

The fatigue tests were performed under displacement control, by applying a sinusoidal waveform at a frequency of 5 Hz and setting the ratio of minimum to maximum displacement per cycle (R) to $-10/(-3)$. The desired severity at the beginning of the test was defined by the ratio of the initial maximum cyclic energy release rate ($\mathcal{G}_{max,0}$) to the mean value of critical energy release rate ($\mathcal{G}_c$) measured by quasi-static tests carried out prior to the fatigue test on identical test specimens. Assuming that the behavior of the specimen was linear elastic, the selection of the initial minimum displacement ($\delta_{min,0}$) was related to $\mathcal{G}_{max,0}$ using Eqs. (5) and (6) and its derivative, and the initial crack length (a_0):

$$\delta_{min,0} = \frac{\left(m_{cc}(a_0)^3 + C_0\right)}{a_0}\sqrt{\frac{2B\mathcal{G}_{max,0}}{3m_{cc}}} \tag{14}$$

We established a maximum initial severity, $\mathcal{G}_{max,0}/\mathcal{G}_c$, of 0.55 to avoid the horizontal movement of the sample occurring for displacements below −3.5 mm. Other authors use mechanical restraints to avoid this [10] although this could affect the results.

The TestStar v3.5C control software for the MTS servohydraulic testing machine includes a "Calculated Channels" option that allows for internal variables, either external inputs or calculated through simple arithmetic operations, to be generated. It was used to compute the dynamic compliance, C^*, by processing the instantaneous signals of load and displacement in line with the methodology described in [11]. Next, the crack length was derived from the dynamic compliance using Eq. (6):

$$a = \sqrt[3]{\frac{C^* - C_0}{m_{cc}}} \tag{15}$$

One set of data (the dynamic compliance, C^*, the minimum cyclic load, P_{min}, and the number of cycles, N) was recorded every cycle and, as such, the crack length was calculated at the same monitoring frequency leading to a continuous $a(N)$ curve. Subsequently, the crack growth rate (da/dN) was obtained from the numerical derivative of the $a(N)$ curve. The recommended data reduction techniques for the ASTM standard [21] are the secant and the incremental polynomial methods. However, when these methodologies are applied to high frequency data acquisition curves, errors can occur because the dynamic compliance scatter might be too large compared to the increment in number of cycles between two successive data. For this reason, in this work the

Table 1
Initial conditions for the propagation tests. In the specimen identification, "V" stands for variable displacement tests and "C" stands for constant displacement tests.

Specimen ID	Initial load severity $\mathcal{G}_{max,0}/\mathcal{G}_c$ [–]	Initial crack length a_0 [mm]	Mid-span length L [mm]	Initial minimum displacement $\delta_{min,0}$ [mm]
01_V	0.50	30.0	50.00	−3.108
02_V	0.50	35.0	50.00	−3.075
03_V	0.50	38.0	50.00	−3.071
04_C	0.55	38.0	50.00	−3.356
05_C	0.40	38.0	50.00	−2.770
06_C	0.30	38.0	50.00	−2.543
07_C	0.25	45.0	60.00	−3.096
08_C	0.20	38.0	50.00	−2.104
09_C	0.18	45.0	60.00	−2.743
10_C	0.14	45.0	60.00	−2.347
11_C	0.12	45.0	60.00	−2.223

derivative was performed by linear regression of wider data sets, grouped so that the total increment of crack extension of each set was 0.1 mm [34].

Finally, da/dN was referred to the maximum energy release rate of the cycle normalized to the quasi-static critical value ($\mathcal{G}_{max}/\mathcal{G}_c$), or load severity. Taking Eq. (4) and the derivative of the compliance calibration (6), $\mathcal{G}_{max}$ reads:

$$\mathcal{G}_{max} = \frac{3m_{cc}\,P_{min}^2 a^2}{2B}, \tag{16}$$

where the crack length, a, is taken at the midpoint of the cycle.

Constant displacement tests were performed using eight different initial severities in order to cover a wider portion of the da/dN curve and the results were fitted together using the modified Paris' law from Eq. (8).

As mentioned in Section 1, the energy release rate does not evolve monotonically with the crack extension, but rather increases and then decreases under constant cyclic displacement, and with the maximum point (point 2 in Fig. 2a) always being located at $a = 0.7L$. Therefore, constant cyclic displacement tests were performed with initial crack length higher than $0.7L$, in order to avoid sweeping the same part of the crack growth rate curve twice (see Fig. 2b). In contrast, in variable cyclic displacement tests the initial crack length is not a limiting parameter because the dependence between the load severity and the crack length is monotonic. In this specific case, the authors chose different crack lengths in order to analyze the influence of the initial conditions on the resultant crack growth rate curve.

Table 1 indicates the initial conditions for each propagation test. The specimens labeled "V" were tested by applying the variable cyclic displacement methodology presented in this work and the specimens labeled "C" were tested under constant cyclic displacement conditions.

For the variable cyclic displacement tests, the "Calculated Channels" from the MTS TestStar v3.5C software allowed an internal variable to be calculated (in accordance with Eq. (13)) in real time. This variable was established as the continuous displacement set-point, δ_{min}.

Table 2 lists the parameters used for calculating of $\delta_{min}(N)$ (Eq. (13)). The Paris' law parameters, A and p, obtained in the da/dN data fitting resulting from tests 07_C, 09_C, 10_C and 11_C, were used to estimate the curve $\delta_{min}(N)$ for test 01_V. The results from tests 06_C and 08_C were added to the previous data to obtain A and p for tests 02_V and 03_V.

Constant cyclic displacement tests were performed on specimens with a mode I precrack, whereas the variable cyclic displacement tests were performed on specimens already tested under constant cyclic displacement (thus having a mode II fatigue precrack). The reason for this was to avoid the transient behavior observed at the onset of delamination for specimens with a mode I precrack, as described further in Sections 4 and 5.

4. Results

A typical crack growth rate curve (da/dN vs severity) in a specimen precracked under mode I and loaded under constant displacement amplitude exhibits three distinct stages (Fig. 4). As the severity decreases from the onset of the test, the curve sweeps from right to left. The first region is characterized by a growing crack growth rate as the severity decreases. Then, the largest region (i.e. the second region), consists of a smooth direct dependence between da/dN and severity. Finally, in the third region the crack tends to arrest with a higher slope than that seen in the second region. For these reasons discussed in the next section, the curve was truncated, neglecting the first and third regions. Only the mid-region was considered in the modified Paris' law calculation.

As variable displacement tests were performed on specimens already tested under mode II, their crack growth rate curves did not show the first region of Fig. 4. Fig. 5 compares the preselected and the experimental dependence between the severity and the crack length increment, confirming the new experimental methodology as being suitable to enlarge the range of severities explored in a single test.

The crack growth rate curve in Fig. 6 condensates the results obtained from the eleven tests performed in this study. All the tests were performed for the same load ratio, $R = -10/(-3)$, either under constant cyclic displacement or variable cyclic displacement control. The plot also includes the fitting of all the data from the

Table 2
Parameters used in the minimum variable displacement calculation, δ_{min}, using Eq. (13).

Specimen ID	Specimen width	Initial crack length	Estimated fatigue life constants (Eq. (8)), da/dN evaluated in mm/cycle		Compliance calibration parameters (Eq. (6))		Severity versus crack length constants (Eq. (1))	
	B [mm]	a_0 [mm]	A	p	m_{cc} [N^{-1} mm^{-2}]	C_0 [mm N^{-1}]	$m_{\mathcal{G}}$ [mm^{-1}]	n [–]
01_V	25.00	30.0	$6.192 \cdot 10^{-2}$	3.674	$3.193 \cdot 10^{-8}$	$2.608 \cdot 10^{-3}$	−0.030	1.400
02_V	25.00	35.0	$5.595 \cdot 10^{-2}$	3.695	$3.131 \cdot 10^{-8}$	$2.626 \cdot 10^{-3}$	−0.090	3.650
03_V	25.00	38.0	$5.595 \cdot 10^{-2}$	3.695	$3.188 \cdot 10^{-8}$	$2.594 \cdot 10^{-3}$	−0.225	9.050

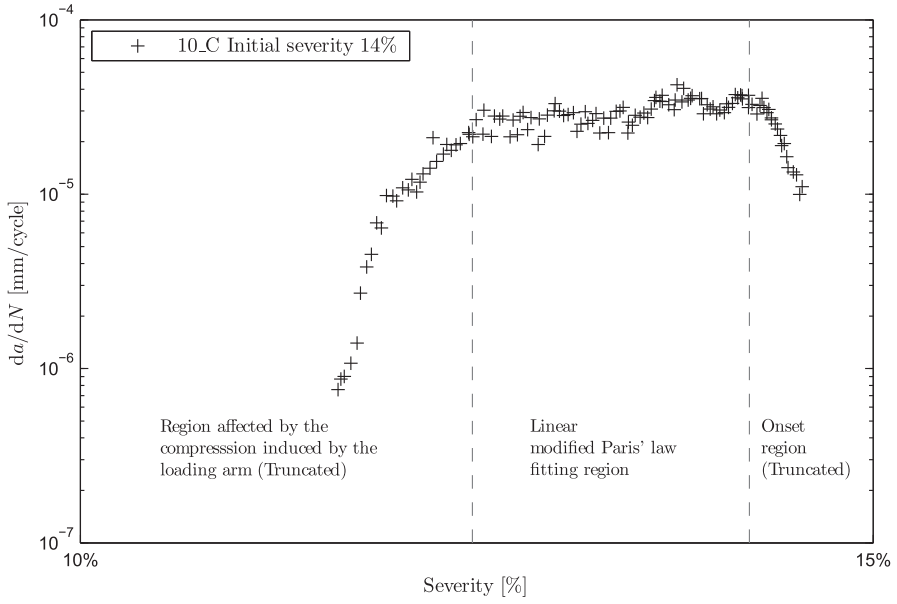

Fig. 4. Reduced fatigue crack growth rate data with the truncated regions in the modified Paris' law fitting from the constant cyclic displacement tests.

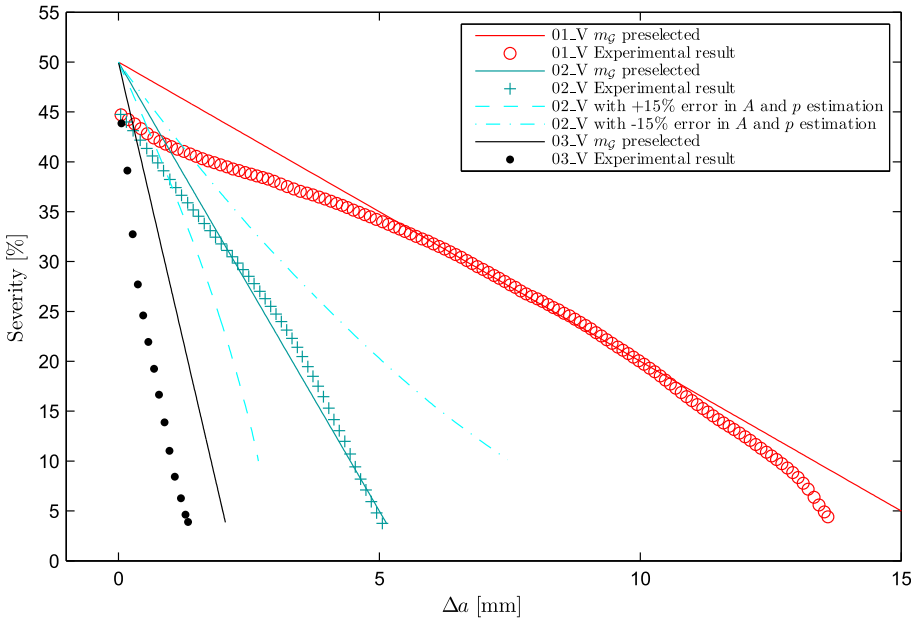

Fig. 5. Comparison between the preselected slope, $m_{\mathcal{G}}$, from the energy release rate versus the crack length curve and the experimental relationship $\frac{\mathcal{G}_{max}}{\mathcal{G}_c} - \Delta a$ obtained from the variable displacement tests. Dashed lines illustrate the $\frac{\mathcal{G}_{max}}{\mathcal{G}_c} - \Delta a$ relation obtained if the Paris' law parameters, A and p, used in the calculation of $\delta_{min}(N)$ in test 02_V, were predicted with an error of ±15%.

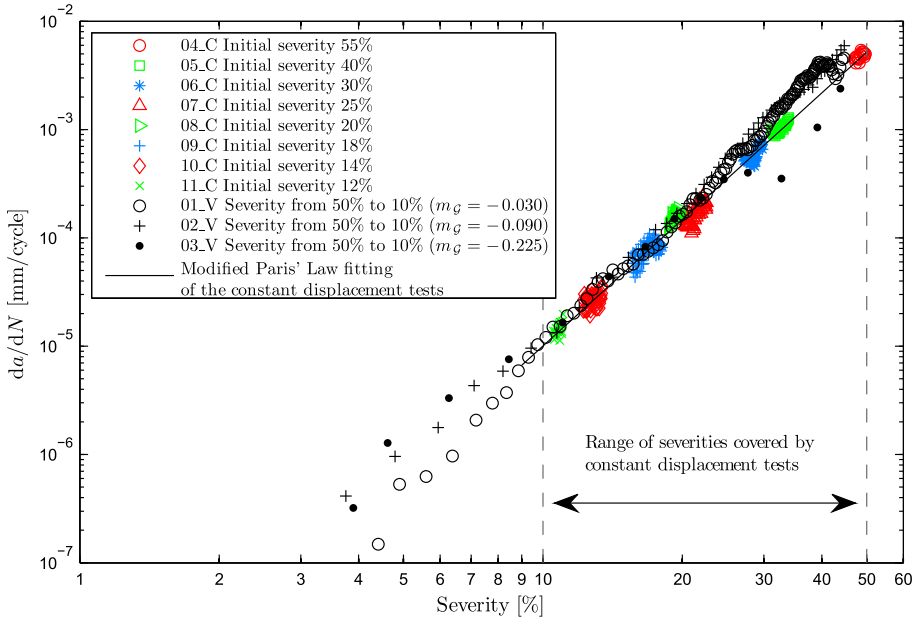

Fig. 6. Relation between crack propagation rate and peak energy release rate for $R = 0.3$. The results from both variable displacement ("V" labeled) and constant displacement ("C" labeled) tests are presented for comparison proposes.

Table 3
Fatigue life constants obtained from both variable displacement and constant displacement tests.

Specimen ID	Severity versus crack length slope (Eq. (1))	Obtained fatigue life constants (Eq. (8)), da/dN evaluated in mm/cycle	
	$m_{\mathcal{G}}$ [mm^{-1}]	A	p
01_V	−0.030	$1.975 \cdot 10^{-1}$	4.326
02_V	−0.090	$1.677 \cdot 10^{-1}$	4.168
03_V	−0.225	$7.342 \cdot 10^{-2}$	3.786
Modified Paris' law (Eq. (8)) fitting of the constant displacement tests' results		$7.636 \cdot 10^{-2}$	3.882

Table 4
Time employed in obtaining the crack growth rate curve for both variable and constant minimum displacement methodologies.

	Specimen ID	Total time (h)	Time 10–45% severity (h)
Variable displacement tests	01_V Severity from 50% to 10%	42.0	4.3
	02_V Severity from 50% to 10%	18.0	1.9
	03_V Severity from 50% to 10%	7.0	0.4
Constant displacement tests	04_C Initial severity 55%	0.2	
	05_C Initial severity 40%	1.3	
	06_C Initial severity 30%	2.6	
	07_C Initial severity 25%	4.0	
	08_C Initial severity 20%	8.8	
	09_C Initial severity 18%	15.5	
	10_C Initial severity 14%	48.1	
	11_C Initial severity 12%	89.1	
Total time employed in constant displacement testing		169.6	

constant cyclic displacement tests in accordance with the modified Paris' law (Eq. (8)).

The parameters of the modified Paris' law (Eq. (8)), the exponent, p, and the coefficient, A, are obtained from the linear fitting of the data plotted on log-log scales (Table 3).

The duration of each variable cyclic displacement test depends on the slope of the relation between the energy release rate and crack length, $m_{\mathcal{G}}$ (Fig. 5). Higher slopes tend to minimize the testing time. The total time employed in all tests (constant displacement and variable displacement) is specified in Table 4.

5. Discussion

The proposed experimental methodology for mode II testing in the 3-ENF configuration enables a chosen range of load severities to be swept while the crack grows in a predefined crack length increment. This is accomplished by varying the applied cyclic displacement as the number of cycles evolves. The $\delta_{min}(N)$ function depends on estimated Paris' law parameters (A and p), derived from the constant cyclic displacement tests. In spite of being just a rough estimation, the range of severities swept is close to the desired one and, in any case, much larger than what could be obtained from a constant displacement test. The consequence of using erroneous parameters is illustrated in Fig. 5 for the specimen 02_V. An error in A and p of $\pm 15\%$ leads to changes in the crack length increment needed to sweep the desired severity range. In any event, the severity range achieved would be much larger than that attained using a constant displacement test.

The variable cyclic displacement method leads to crack growth rate data practically indistinguishable from that resulting from the complete set of eight constant displacement tests. In particular, the Paris' exponent, p, obtained from variable cyclic displacement tests under steady growth conditions (severities from 10 to 30%), deviated from the log-linear fitting of the constant cyclic displacement tests results by +11.4%, +7.4% and −2.5% (specimens 01_V, 02_V and 03_V, respectively). No experimental data for severities higher than 45% could be obtained because of specimen horizontal movement. The agreement between the results from both methods, however, is expected to persist if this issue could be solved practically.

One of the main advantages of the new experimental methodology is the reduction of the time duration of the fatigue mode II test. The selection of the shedding rate, $m_{\mathcal{G}}$, determines the duration of the test. Table 4 exemplifies the time saved with this method. One single test performed with variable displacement to build the crack growth rate curve for a severity range between 10% and 45% is performed in 1.9 h (specimen 02_V), while the 8 constant displacement tests needed to sweep the same severity range require 169.6 h (80 times more if the times involved in setting up each of the tests is not considered).

The question arises of how fast the test can be carried out while still leading to the crack growth curve obtained in a constant displacement test. This question could be dealt with taking into account the formation of a failure process zone, FPZ, in front of the crack tip. While the FPZ for mode I delamination in CFRP is assumed to be so small as to be negligible in the data reduction of static interlaminar fracture toughness tests, the same does not apply for the FPZ in mode II tests [35]. Under mode II loading and for a given load severity, the crack growth rate would not reach its steady level until the FPZ is fully formed. In a variable displacement test, if the severity varies before the FPZ is fully formed, the crack growth rate would deviate from the steady crack growth rate for the actual severity being applied. This is more likely to happen as the shedding rate increases and that deviation would also be more important the stronger the variation of the FPZ with the load severity is.

Fig. 6 illustrates the crack growth rate curves obtained from the variable cyclic displacement tests for the three shedding rates, $m_{\mathcal{G}}$, explored in this study. The tests performed at low $m_{\mathcal{G}}$ lie close to the Paris' curve of constant cyclic displacement tests from the very first stages of the crack growth curve (higher severities), whereas the test performed at high $m_{\mathcal{G}}$ (03_V) tends to deviate from these curves in the region of high (30–45%) and low (<10%) severities, while in the region in between the agreement is complete. The deviation of specimen 03_V at the beginning of the test (high severities) corresponds to the transient stage from the FPZ of the precrack to the steady FPZ. On the contrary, at lower severities, below 10%, the deviation is attributed to a shedding rate too fast to permit the stabilization of the FPZ, leading to a faster crack growth than observed in constant cyclic displacement tests. The confirmation of these hypothesis and the study of the FPZ zone in fatigue tests as a function of the load severity deserves further investigation.

These facts highlight the impact the pre-cracking stage has on the initial measurements of the crack growth rate curves. In the first stage of the crack growth curve for constant displacement tests in Fig. 4 there is a clear evidence of the transient region between the FPZ of the precrack and the steady FPZ. Indeed, due to the fact that the constant displacement tests start from a mode I precrack (short FPZ), the crack grows more slowly than the steady rate until the mode II FPZ is fully formed.

In view of the foregoing, the variable cyclic displacement tests were performed on specimens tested under mode II cyclic loading, where the crack grew until the tip reached the zone affected by loading arm compression ("Region affected by the compression induced by the loading arm" in Fig. 4). In this region, the crack propagation tends to arrest, misrepresenting an artificial threshold. The FPZ formed in this situation (low severity), however, is different from the one expected at the beginning of the variable displacement tests (high severity). For that reason, a transient region in the variable displacement tests is expected. While this is not noticeable in specimens with low $m_{\mathcal{G}}$, it does span over several points for specimen 03_V.

The fact that the three crack growth curves obtained under variable cyclic displacement amplitude with different $m_{\mathcal{G}}$ coincide in the severity range between 30% and 10% indicates that the shedding rate is slow enough to lead to a fully developed FPZ, even with the highest $m_{\mathcal{G}}$ selected (Fig. 6). The prospect is that for a large enough $m_{\mathcal{G}}$, the crack growth curve would deviate from that of the constant displacement test. Following an equivalent rationale, the crack length increment can not be decreased arbitrarily if representative results are to be obtained. Fig. 5 shows that the same Paris' law curve is obtained for crack increments of 2 mm (specimen 03_V) or 14 mm (specimen 01_V). These constraints should be specifically considered when testing materials with expected large FPZ, as the case of adhesive joints is. The larger the expected FPZ, the slower the shedding rate should be and, likewise, the larger the crack increment to be traveled.

The comparison of the results from constant cyclic displacement tests reveals that the propagation rate does not depend on the span length (e.g. specimens 07_C and 08_C, with span lengths of 60 and 50 mm respectively, have similar da/dN at 20% severity). Thus, the same results are obtained with different crack lengths. This is an indication that, for the material studied, the crack growth rate is history independent under mode II test conditions when a steady crack growth is achieved (initial transient curves must be truncated, Fig. 4). This assertion is corroborated by the overlap among the crack growth rate curves obtained with the three variable displacement tests performed with different preselected gradients of energy release rate, $m_{\mathcal{G}}$ (see Table 3), again, once the FPZ is fully developed. Under this condition, the maximum difference in da/dN, for a given severity, between the data obtained from variable displacement tests and the fitting of all the data from constant displacement tests, amounts 0.3 decades. This is comparable to the scatter of the raw data from a single constant displacement test.

6. Conclusions

An automated procedure to obtain the log-linear region of a crack growth rate curve has been developed for an 3-ENF test for mode II fatigue delamination growth. The displacement applied,

$\delta(N)$, is calculated prior to initiating the fatigue test in order to achieve a constant negative energy release rate gradient throughout crack propagation. The continuous displacement shedding is conducted by implementing the calculated $\delta(N)$ curve in a computer-controlled testing system. This, in combination with the automated and continuous estimation of the crack length by means of the real time monitoring of the specimen's compliance, avoids the need of human intervention during the test.

The usefulness of this methodology has been exemplified with an experimental testing campaign in which the crack growth rate curve obtained is compared with the modified Paris' law fitting data from a batch of constant cyclic displacement tests.

The range of severities covered by a single test using the developed methodology spans from 0.45 to 0.1. Due to the specimen movement, the initial severity could not be higher than 0.50.

The time saved employing the methodology developed has been demonstrated (the example performed shows a reduction of 1/80) and how the duration of the test, which is determined by the shedding rate and the range of severities explored, is limited by the requirement of forming the complete failure process zone corresponding to the actual load severity is discussed.

Acknowledgements

This work has been partially funded by the Spanish Government (Ministerio de Economia y Competitividad) under contract TRA2015-71491-R and the European Union by the financial support of ERANet AirTN 01/2013 under the project entitled "Methodology to design composite structures resistant to intra- and interlaminar damage (static & fatigue)- MERINDA".

References

[1] SAE International. Polymer matrix composites: materials usage, design and analysis. Compos Mater Handbook Ser 2013;3:686–794.
[2] ASTM D 6115-97. Standard test method for mode I fatigue delamination growth onset of unidirectional fibre-reinforced polymer matrix composites; 2011.
[3] Dahlen C, Springer GS. Delamination growth in composites under cyclic loads. J Compos Mater 1994;28(8):732–81.
[4] Argüelles A, Viña J, Canteli AF, Bonhomme J. Fatigue delamination, initiation, and growth, under mode I and II of fracture in a carbon-fiber epoxy composite. Polym Compos 2010;31(4):700–6.
[5] Allegri G, Jones M, Wisnom M, Hallett S. A new semi-empirical model for stress ratio effect on mode II fatigue delamination growth. Compos Part A: Appl Sci Manuf 2011;42(7):733–40.
[6] Allegri G, Wisnom MR. A non-linear damage evolution model for mode II fatigue delamination onset and growth. Int J Fatigue 2012;43:226–34.
[7] Allegri G, Wisnom MR, Hallett SR. A new semi-empirical law for variable stress-ratio and mixed-mode fatigue delamination growth. Compos Part A: Appl Sci Manuf 2013;48(1):192–200.
[8] Al-Khudairi O, Hadavinia H, Waggott A, Lewis E, Little C. Characterising mode I/mode II fatigue delamination growth in unidirectional fibre reinforced polymer laminates. Mater Des 2015;66:93–102.
[9] Asp L, Sjogren A, Greenhalgh E. Delamination growth and thresholds in a carbon/epoxy composite under fatigue loading. J Compos Technol Res 2001;23(2):55.
[10] Brunner A, Stelzer S, Pinter G, Terrasi GP. Mode II fatigue delamination resistance of advanced fiber-reinforced polymer-matrix laminates: towards the development of a standardized test procedure. Int J Fatigue 2013;50:57–62.
[11] Renart J, Vicens J, Budhe S, Costa J, Mayugo JA. An automated methodology for mode II delamination tests under fatigue loading based on the real time monitoring of the specimen's compliance. Int J Fatigue 2016;82:634–42.
[12] ISO 15114:2014. Fibre-reinforced plastic composites – determination of the mode II fracture resistance for unidirectionally reinforced materials using the calibrated end-loaded split (C-ELS) test and an effective crack length approachs; 2014.
[13] Shindo Y, Takeda T, Narita F, Saito N, Watanabe S, Sanada K. Delamination growth mechanisms in woven glass fiber reinforced polymer composites under mode II fatigue loading at cryogenic temperatures. Compos Sci Technol 2009;69:1904–11.
[14] Davidson BD, Sun XU, Vinciquerra AJ. Influences of friction, geometric nonlinearities, and fixture compliance on experimentally observed toughnesses from three and four-point bend end-notched flexure tests. J Compos Mater 2007;41(10):1177–96.
[15] Brunner A, Murphy N, Pinter G. Development of a standardized procedure for the characterization of interlaminar delamination propagation in advanced composites under fatigue mode I loading conditions. Eng Fract Mech 2009;76:2678–89.
[16] Gillespie JW, Carlsson LA, Pipes RB. Finite element analysis of the end notched flexure specimen for measuring mode II fracture toughness. Compos Sci Technol 1986;27:177–97.
[17] Tanaka K, Tanaka H. Stress-ratio effect on mode II propagation of interlaminar fatigue cracks in graphite/epoxy composites. In: Composite materials: fatigue and fracture, 6th volume, ASTM STP 1285; 1997. p. 126–142.
[18] Matsubara G, Ono H, Tanaka K. Mode II fatigue crack growth from delamination in unidirectional tape and satin-woven fabric laminates of high strength GFRP. Int J Fatigue 2006;28(10):1177–86.
[19] Hojo M, Ando T, Tanaka M, Adachi T, Ochiai S, Endo Y. Modes I and II interlaminar fracture toughness and fatigue delamination of CF/epoxy laminates with self-same epoxy interleaf. Int J Fatigue 2006;28(10):1154–65.
[20] Hojo M, Tanaka K, Gustafson CG, Hayashi R. Effect of stress ratio on near-threshold propagation of delimitation fatigue cracks in unidirectional CFRP. Compos Sci Technol 1987;29:273–92.
[21] ASTM E647-13. Standard test method for measurement of fatigue crack growth rates. American Society for Testing and Materials (ASTM); 2013. p. 1–49.
[22] Saxena A, Schmidt D, Donald J, Hudak S. Computer-controlled decreasing stress intensity technique for low rate fatigue crack growth testing. J Test Eval 1978;6(3):167–74.
[23] Schmidt D, Donald J. Computer-controlled stress intensity gradient technique for high rate fatigue crack growth testing. J Test Eval 1980;8(1):19–24.
[24] Anderson TL. Fracture mechanics: fundamentals and applications. 3rd ed. CRC Press; 2005.
[25] Hojo M, Matsuda S, Fiedler B, Kawada T, Moriya K, Ochiai S, et al. Mode I and II delamination fatigue crack growth behavior of alumina fiber/epoxy laminates in liquid nitrogen. Int J Fatigue 2002;24:109–18.
[26] Paris PC. A rational analytic theory of fatigue. Trend Eng 1961;13:9–14.
[27] Forman FG, Shivakumar V, Cardinal JW, Williams L, McKeighan PC. Fatigue crack growth database for damage tolerance analysis. DOT/FAA/AR-05/15. US Department of Transportation, Federal Aviation Administration; 2005.
[28] Jones R, Stelzer S, Brunner AJ. Mode I, II and mixed mode I/II delamination growth in composites. Compos Struct 2014;110:317–24.
[29] ASTM D7905/7905M-14. Standard test method for determination of the mode II interlaminar fracture toughness of unidirectional fiber-reinforced polymer. American Society for Testing and Materials (ASTM); 2014. p. 1–18.
[30] Tanaka K, Kageyama K, Hojo M. Prestandardization study on mode II interlaminar fracture toughness test for CFRP in japan. Composites 1995;26(4):257–67.
[31] JIS K 7086-1993. Testing methods for interlaminar fracture toughness of carbon fibre reinforced plastics. Japanese Industrial Standards Group.
[32] AC7122/1 Rev B. Nadcap audit criteria for non metallic materials testing mechanical testing.
[33] ISO/IEC 17025. General requirements for the competence of testing and calibration laboratories; 2014.
[34] Stelzer S, Brunner AJ, Argüelles A, Murphy N, Cano GM, Pinter G. Mode I delamination fatigue crack growth in unidirectional fiber reinforced composites: results from ESIS TC4 round-robins. Eng Fract Mech 2014;116:92–107.
[35] Sarrado C, Turon A, Renart J, Urresti I. Assessment of energy dissipation during mixed-mode delamination growth using cohesive zone models. Composites Part A 2012;43(11):2128–36.